A novel technique to monitor ultrafast photoinduced chemical reaction dynamics at surfaces: The femtochemistry of methyl halide molecules adsorbed on oxides, metals and oxide supported metal clusters



Dissertation
zur Erlangung des Doktorgrades
Dr. rer. nat.
der Fakultät für Naturwissenschaften
der Universität Ulm

vorgelegt von
Mihai Emilian Vaida
aus Deva, Rumänien

2010

Amtierender Dekan: Prof. Dr. A. Groß

1. Gutachter: Prof. Dr. T. M. Bernhardt

2. Gutachter: Prof. Dr. H. Jones

Tag der Promotion: 21.07.2010

Contents

ABBREVIATIONS **7**

ABSTRACT **9**

1 INTRODUCTION AND MOTIVATION **11**

2 EXPERIMENTAL: GENERAL ASPECTS **15**

2.1 Vacuum apparatus **16**
2.1.1 Surface science chamber 18
2.1.2 Sample holder 19

2.2 Analytical tools **21**
2.2.1 Surface investigation by electron-based analytical methods 21
2.2.1.1 Low energy electron diffraction 22
2.2.1.2 Auger Electron Spectroscopy 25
2.2.1.3 Electron energy loss spectroscopy 26
2.2.2 Photoemission spectroscopy 27
2.2.3 Temperature programmed desorption 30
2.2.3.1 Kinetics of temperature programmed desorption 32
2.2.3.2 Redhead equation 33

2.3 Cluster sources **34**
2.3.1 Gold evaporator 34
2.3.2 Production of mass-selected Au clusters 35

2.4 Laser system **37**
2.4.1 Ti:Sapphire active medium 38
2.4.2 Femtosecond oscillator 38
2.4.3 Pulse amplification 41
2.4.4 Wavelength conversion 43
2.4.5 Pulse characterization 46
2.4.5.1 Spectral measurements 46
2.4.5.2 Pulse temporal profile 46

3 SURFACE FS PUMP-PROBE MASS SPECTROMETRY **49**

3.1 Time-of-flight mass spectrometry: General aspects **50**

3.2 SFsMS: Experimental realization **53**

3.3 Molecular adlayer preparation **54**

3.4 Fs-laser excitation and ionization of molecules at the surface **55**
3.4.1 Wavelength 55

3.4.2 Polarization ... 58
3.4.2.1 Polarization in direct surface photodissociation ... 64
3.4.2.2 Polarization in substrate mediated dissociation ... 65
3.4.3 Intensity ... 66
3.4.3.1 Pump intensity ... 66
3.4.3.2 Probe intensity ... 66

3.5 Mass, time, and velocity resolved measurements ... 69
3.5.1 Pump-probe schema ... 69
3.5.1.1 Surface photoexcitation ... 69
3.5.1.2 REMPI detection ... 71
3.5.2 Transient recording routine ... 71
3.5.3 Time zero determination ... 73
3.5.4 Evaluation of the SFsMS data ... 75
3.5.4.1 Potential energy diagram ... 75
3.5.4.2 Fitting procedure ... 77

4 SURFACE PREPARATION AND CHARACTERIZATION ... 79

4.1 MgO(100) on Mo(100) ... 80
4.1.1 Preparation of ultrathin MgO films on Mo(100) ... 80
4.1.2 Geometric structure of ultrathin MgO films on Mo(100) ... 83
4.1.3 PES of Mo(100) covered by ultrathin MgO(100) films of variable thickness ... 85
4.1.3.1 Excitation energy dependent photoemission ... 85
4.1.3.2 Coverage dependent photoemission ... 90

4.2 Gold films on a molybdenum single crystal surface ... 93
4.2.1 Preparation of Au films on Mo(100) ... 93
4.2.2 Structure of Au films grown on Mo(100) ... 97

4.3 Magnesia supported gold clusters ... 100
4.3.1 Fs-Laser photoemission from magnesia supported gold clusters ... 101
4.3.2 Estimation of the gold particle size ... 104

5 METHYL IODIDE ... 107

5.1 Methyl iodide on magnesia ... 108
5.1.1 Temperature programmed desorption ... 108
5.1.2 Real-time photoreaction dynamics ... 109
5.1.2.1 Unimolecular reaction ... 109
5.1.2.2 Bimolecular reaction ... 117
5.1.3 Influence of magnesia thin film layer thickness on the methyl iodide photochemistry ... 121
5.1.4 Influence of the MgO stoichiometry and composition on the methyl iodide thermal desorption and photodissociation ... 124

5.2 Methyl iodide on gold ... 131
5.2.1 Temperature programmed desorption and reaction ... 131
5.2.2 Photoemission spectroscopy ... 132
5.2.3 Methyl iodide photochemistry on gold ... 135
5.2.3.1 Methyl iodide photodissociation on a gold surface ... 135
5.2.3.2 Trapping of the I atoms at the surface subsequent to CD_3I photodissociation on Au ... 136

5.3 Methyl iodide on magnesia supported gold nanoparticles ... 141
5.3.1 Methyl iodide adsorption on magnesia supported gold nanoparticles ... 141
5.3.2 Photodissociation dynamics ... 142
5.3.3 Methyl iodide reactivity with very small gold clusters ... 144

5.4 Conclusions ... 146

6 METHYL BROMIDE 147

6.1 Methyl bromide on magnesia 148
6.1.1 Temperature programmed desorption 148
6.1.2 Real-time photodissociation dynamics 149
6.1.3 Influence of the magnesia film thickness on the methyl bromide photodissociation dynamics 155

6.2 Methyl bromide adsorption and photodissociation on gold 160
6.2.1 Temperature programmed desorption 160
6.2.2 Photodissociation dynamics 161

6.3 Methyl bromide adsorption and photodissociation on magnesia supported gold clusters 164
6.3.1 Temperature programmed desorption 164
6.3.2 Photodissociation dynamics 167
6.3.3 Gas-phase reactivity measurements 171

6.4 Conclusions 172

7 METHYL HALIDE ADSORPTION AND SURFACE FEMTOCHEMISTRY: COMPARISON AND CONCLUSIONS 175

7.1 Electronic structure 176

7.2 Adsorption behavior 176
7.2.1 Adsorption on MgO films on Mo(100) 177
7.2.2 Adsorption on Au films on Mo(100) 177
7.2.3 Adsorption on magnesia supported gold clusters 177

7.3 Photochemistry 178
7.3.1 Photochemistry on MgO films on a Mo(100) 178
7.3.1.1 8-10 ML MgO/Mo(100) 178
7.3.1.2 Mo(100) and 1-6 ML MgO/Mo(100) 179
7.3.2 Photochemistry on Au films on Mo(100) 180
7.3.3 Photochemistry on Magnesia supported gold clusters 180
7.3.3.1 Small gold clusters and nanoparticles 180
7.3.3.2 3D gold nanoparticles 180

7.4 Conclusions and future directions 183

ZUSAMMENFASSUNG 185

BIBLIOGRAPHY 187

CURRICULUM VITAE 205

LIST OF PUBLICATIONS 207

CONFERANCE CONTRIBUTIONS 209

ACKNOWLEDGEMENTS 213

Abbreviations

2D	Two dimensional
2PPS	Two-Photon Photoemission Spectroscopy
3D	Three dimensional
AES	Auger Electron Spectroscopy
AOM	Acousto Optical Modulator
BBO	β-Barium Borate
bcc	Body Centered Cubic
CCD	Charge Coupled Device
CORDIS	Cold Reflex Discharge Ion Source
CPA	Chirped Pulse Amplification
cw	Continuous Wave
DEA	Dissociative Electron Attachment
EELS	Electron Energy Loss Spectroscopy
E_F	Fermi Level
E_P	Primary Energy
EPR	Electron Paramagnetic Resonance
E_{VAC}	Vacuum Level
fcc	Face Centered Cubic
fs	Femtosecond
FWHM	Full Width at Half Maximum
GPIB	General Purpose Interface Bus

GVD	Group Velocity Dispersion
IR	Infrared
HREELS	High Resolution Electron Energy Loss Spectroscopy
L	Langmuir
LEED	Low Energy Electron Diffraction
LN_2	Liquid Nitrogen
MCP	Micro Channel Plate
MCS	Multi-Channel Scaler
MIES	Metastable Impact Electron Spectroscopy
ML	Monolayer equivalent
OPA	Optical Parametric Amplifier
PES	Photoemission Spectroscopy
PID	Proportional-Integral-Differential
rf	Radio Frequency
RGA	Residual Gas Analyzer
SFsMS	Surface Femtosecond Mass Spectrometry
SFM	Sum Frequency Mixing
SHG	Second Harmonic Generation
STM	Scanning Tunneling Microscopy
TPD	Temperature Programmed Desorption
THG	Third Harmonic Generation
TOF-MS	Time-of-Flight Mass Spectrometer
TOF-PES	Time-of-Flight Photoelectron Spectrometer
UHV	Ultra High Vacuum
UV	Ultraviolet

Abstract

The aim of this thesis was to measure the dynamics of chemical reactions of molecules adsorbed on solid surfaces in real-time by direct detection of reaction intermediates and products. To realize this goal a new experimental technique was developed. The novel experimental approach enables the time-resolved investigation of photoinduced surface reaction dynamics via multi-photon ionization of transition states, intermediates, and products directly at the surface in a pump-probe laser mass spectrometry schema.

To demonstrate the viability of the new technique, the photoinduced reaction dynamics of methyl iodide and methyl bromide molecules adsorbed at sub-monolayer coverage on (i) ultra-thin magnesia films, on (ii) a gold surface and on (iii) magnesia supported gold clusters and nanoparticles were investigated.

The employed surfaces were characterized by means of Auger electron spectroscopy, low energy electron diffraction, photoelectron spectroscopy and thermal desorption spectroscopy. In addition to these standard analytical techniques, femtosecond laser photoemission spectroscopy was employed for the first time to investigate the electronic structure of a refractory metal covered with ultrathin oxide films of variable thickness and to study gold clusters deposited on magnesia films.

Methyl iodide molecules adsorbed on a magnesia surface were photoexcited to the dissociative A-band and decomposed within about 300 femtoseconds. Subsequent to the methyl iodide dissociation and simultaneous with the desorption of the methyl fragments, the bimolecular reaction of the emerging ground state and spin-orbit excited iodine atoms on the surface was probed by detecting molecular iodine in the electronically excited B-state. These iodine molecules, however, were found to be metastable exhibiting surface-induced predissociation on the picosecond timescale.

On a gold surface and on magnesia supported gold nanoparticles the methyl iodide molecules experienced an ultrafast recapturing of the ground state before the C-I bond stretched considerably. Consequently, after excitation, the molecules almost instantaneously relaxed back into the ground state and the molecular dissociation was quenched.

The methyl bromide molecules adsorbed on a magnesia surface dissociated faster than the methyl iodide molecules. In addition, no bromine molecules were detected subsequent to methyl bromide photodissociation on magnesia.

In contrast to methyl iodide, methyl bromide molecules were found to dissociate on the gold surface and on magnesia supported gold nanoparticles. The time-resolved measurements revealed a perturbation of the electronic structure of the adsorbed methyl bromide mo-

lecules induced by the presence of gold. The magnitude of the perturbation was observed to change with the particle size.

Finally, the observation that no photoproducts of the methyl halides were detected for the smallest gold cluster sizes was explained by dissociative adsorption as verified by complementary experiments with gas-phase gold clusters.

1 Introduction and motivation

Femtochemistry is one of the most outstanding achievements in laser chemistry during the past decades and has been realized by applying ultrafast lasers to study chemical reactions [1-4]. Chemical bonds form, break or rearrange in the femtosecond time domain. The development of femtosecond time-resolved methods for the investigation of molecular dynamics was pioneered by Ahmed H. Zewail [5]. To investigate chemical reactions in real-time, generally a pump-probe configuration is applied. A femtosecond laser pulse - the pump - initiates a reaction, more exactly, it creates a non-stationary excited molecular state which is called wave packet. Subsequently, a second laser pulse - the probe - monitors the evolution of the wave packet as a function of time.

The most widely employed techniques to study ultrafast reaction dynamics are based on light detection (e.g., laser induced fluorescence or transient absorption), ion detection in conjunction with mass spectrometry, and electron detection (e.g., photoelectron spectroscopy) [1, 2]. In this way, a large variety of chemical reactions in the gas-phase, in liquids and also on well defined solid surfaces have been investigated.

Progress in surface science has contributed substantially during the past decades to the understanding of chemical reactions at gas-surface interfaces which are essential in materials research and heterogeneous catalysis [6]. The key to a molecular level perception of a bimolecular reactive encounter in the gas-phase, but also in condensed phase and on surfaces, is the knowledge about the structure and the dynamics of the transition state of a reaction which is potentially accessible via ultrafast time-resolved laser spectroscopy [5, 7-11]. In a seminal contribution in 1995 John C. Polanyi and Ahmed H. Zewail therefore proposed the investigation of surface transition state dynamics via direct detection of reaction intermediates and products in a femtosecond pump-probe schema similar to gas-phase femtochemistry investigations [12]. They considered the example of H_2S molecules which adsorb at low temperature on a LiF(100) surface in a well aligned geometry. The adsorbed geometry presents the collision complex for a photoinduced bimolecular photoreaction. Figure 1.1 displays the initial state geometry (at the zero of time t_0) of H_2S molecules on LiF(100) [12]. The initial distance between the colliding hydrogen atoms is r_1, the initial H-S distance is r_2, the collision angle is Θ ($\Theta = \sphericalangle$ (H - H)) and the collision distance with respect to a sulfur atom is b. An ultraviolet femtosecond laser pulse should trigger the reaction $H + H_2S_{(ad)} \rightarrow H_{2(g)} + HS_{(ad)}$ at the well-defined time zero configuration. Polanyi and Zewail termed this new approach that relies on a well defined reactant adsorption geometry *"surface aligned femtosecond photoreaction"*.

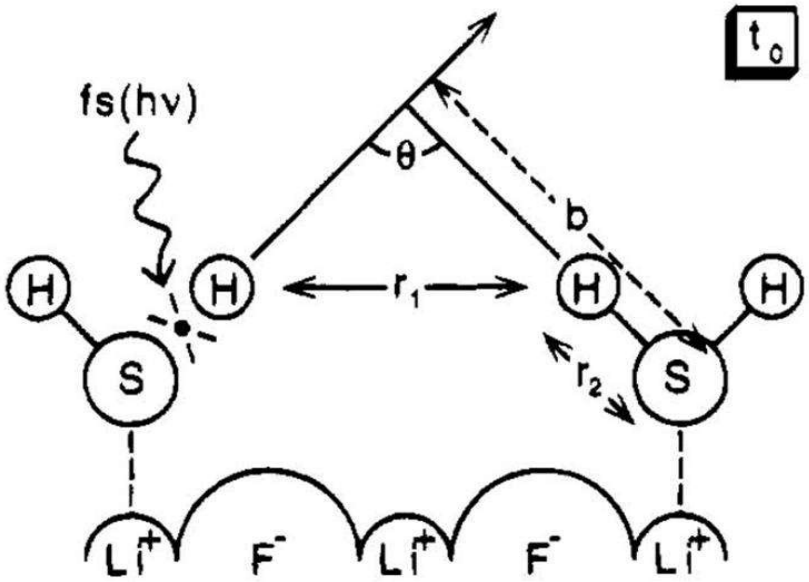

Figure 1.1 Surface aligned femtosecond photoreaction in H_2S adsorbed on LiF(100) as proposed by Polanyi and Zewail [12] (see text for more details).

A great deal of both, surface aligned reaction studies (not time-resolved) [13] as well as real-time surface femtochemistry investigations [14-17] employing, e.g., two-pulse correlation [18-20], sum frequency generation [21, 22], or two-photon photoemission [23-27], have provided insight into surface reaction dynamics. Nevertheless, the direct time- and mass-resolved detection of the transition state and the product formation dynamics of a bimolecular surface reaction as proposed by Polanyi and Zewail has not been realized so far.

The aim of the present work was to monitor ultra-fast chemical reaction dynamics of supported molecules on the basis of schema proposed by Polanyi and Zewail. For this purpose, a new experimental method, which combines femtosecond time-of-flight mass spectrometry with resonance enhanced multi-photon ionization, was developed in the framework of this thesis. The investigation of different reaction pathways was accomplished by real-time monitoring of the mass of different reaction products and intermediates as well as their relative kinetic energy content. In contrast to other surface femtochemistry approaches, the present experiment is clocking the surface reaction dynamics by direct detection of reaction intermediates and products through multi-photon ionization at the surface. To demonstrate the viability of this new experimental approach for the investigation of surface transition state dynamics, methyl iodide and methyl bromide molecules adsorbed on different substrates consisting of magnesia, gold, and magnesia supported gold clusters were employed as photochemical model systems. The choice of methyl halide molecules was guided by the fact that their photochemistry has been widely investigated in the past. The gas-phase photodissociation of methyl iodide via the electronically excited A-band had been extensively studied mostly in the frequency- (see the most recent contributions [28, 29] and references therein), but also in the time-domain [30-35].

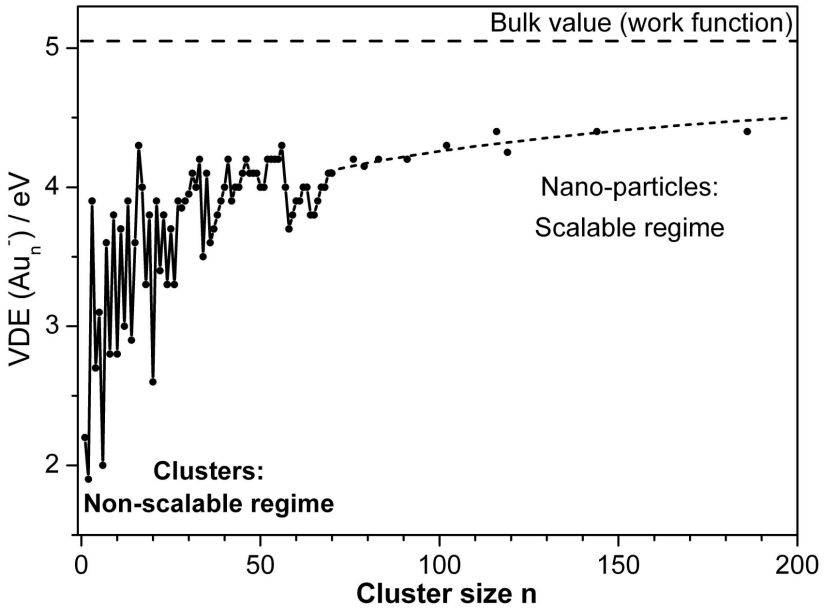

Figure 1.2 The vertical detachment energy of negatively charged gold clusters as a function of the number n of atoms in the cluster [36].

A great deal of theoretical contributions as well have been published due to the fact that methyl iodide represents a benchmark system for calculations on the fragmentation of a small polyatomic molecule in two electronic states (see also the most recent contributions [37-39] and references therein). The electronic structure [40, 41] and the gas-phase photodissociation of methyl bromide molecules via the A-band have been studied as well, but just in the frequency-domain [42-47].

Magnesium oxide as ultrathin film on a molybdenum single crystal was chosen as a substrate because it is only weakly interacting with the molecular adsorbates, it is relatively easy to prepare and transparent in the wavelength region of methyl iodide A-band. Photofragmentation (not time-resolved) of methyl iodide and methyl bromide molecules adsorbed on a magnesia single crystal surface have been investigated in detail experimentally [48-55] as well as theoretically [56-58]. However, no femtosecond time-resolved investigation has been published so far on magnesia supported methyl halide molecules.

Gold films grown on the molybdenum single crystal surface were chosen because the metallic substrate was expected to contrast the insulating MgO surface with respect to the methyl halide photochemistry. Furthermore the adsorption behavior of methyl iodide on gold has been characterized in the past as well [59].

Magnesia supported gold nanoparticles and small clusters were chosen as support to extend the photochemical investigation to a substrate-adsorbate interaction intermediate between the bare magnesia and the gold surface and because they represent more realistic model systems with respect to the application of the new femtosecond laser surface pump-probe mass spectrometry technique to catalytic reaction dynamics. Metal clusters are interesting because their physical and chemical properties can differ completely from those of the corres-

ponding bulk material [60, 61]. Furthermore, the properties vary strongly with the cluster size [36, 62-67]. Figure 1.2 shows the variation of the electron detachment energy of free negatively charged gold clusters as a function of the cluster size. When the dimension of the gold particles is gradually decreasing, their properties first change smoothly with the size. This is called the scalable regime, which extends form micro, and nanometer size gold aggregates down to particles consisting of about one hundred atoms. For gold particles smaller than about 100 atoms the electron detachment energy and in general all physical and chemical properties start to change discontinuously with size. In this regime, these small aggregates have mostly unpredictable, i.e. non-scalable properties and are termed clusters [66].

This thesis is structured as follows. In Chapter 2 a detailed description of the vacuum apparatus, of the analytical methods used in the present surface chemistry investigations as well as of the femtosecond laser system, including the generation and characterization of the laser pulses, is presented. Chapter 3 is dedicated to the description of the novel pump-probe laser mass spectrometry technique applied to monitor the photoreaction dynamics on the surface. In Chapter 4, the preparation and the characterization of the different substrates is described. Apart from the standard analytical techniques used to characterize the surface, femtosecond-laser photoemission spectroscopy was employed here for the first time to study the electronic structure of a refractory metal covered with an ultrathin oxide films of variable thickness and of metal clusters deposited on such oxide films. The adsorption and the photochemistry of methyl iodide and methyl bromide molecules on magnesia, gold and magnesia supported small gold clusters and nanoparticles are presented in Chapter 5 and 6, respectively. Conclusions and a comparative discussion of the results obtained for both investigated methyl halide molecules are presented in Chapter 7.

2 Experimental: General Aspects

The experiments presented in this thesis were carried out in a UHV surface science apparatus that was newly constructed in collaboration with Tobias Gleitsmann [68]. The employed analytical techniques consist of TDS, AES, LEED, EELS and PES. Furthermore, the investigations of ultrafast processes at the surface, i.e. the lifetime of the excited electronic states and the real-time photoinduced reactions at the surface were accomplished by femtosecond 2PPS and SFsMS (described in Chapter 3).

In addition to the UHV surface science chamber, a sputtering cluster source, which has the capability to produce small mass-selected metal clusters, an UHV chamber for gas-phase reaction kinetics measurements, and an ion guiding system that connects the cluster source to the surface and gas-phase investigation chambers, form the complete vacuum apparatus assembly.

In addition to the vacuum apparatus, an amplified femtosecond laser system, which generates light pulses with a duration down to 35 fs and a tunable wavelength between 235 and 3000 nm, is employed in conjunction with a pump-probe optical setup to measure ultrafast phenomena at surface.

2.1 Vacuum apparatus

The vacuum part of the experimental arrangement described in the present work is shown in Figure 2.1. It consists of a UHV chamber (Figure 2.1a part I) for the ultrafast surface reaction investigations, a cluster source (Figure 2.1a,b part II) which generates small, mass-selected metal clusters, a UHV chamber for gas-phase reaction kinetics investigations (Figure 2.1a,b part IV) [69], and an ion guiding system (Figure 2.1a,b part III), which connects the cluster source with the investigation chambers (Figure 2.1 part I and IV).

Almost all experiments presented in this work were performed in the surface science chamber on methyl halide molecules absorbed on surfaces consisting of magnesia, gold, and magnesia supported gold nanoparticles. As shown in Chapter 4 the gold nanoparticles were prepared in situ by gold evaporation. In few experiments, prior to methyl halide molecules adsorption, the magnesia surface was decorated with monomers, dimers, and trimers of gold, produced by the cluster source. For a better understanding of the processes on the surface, re-

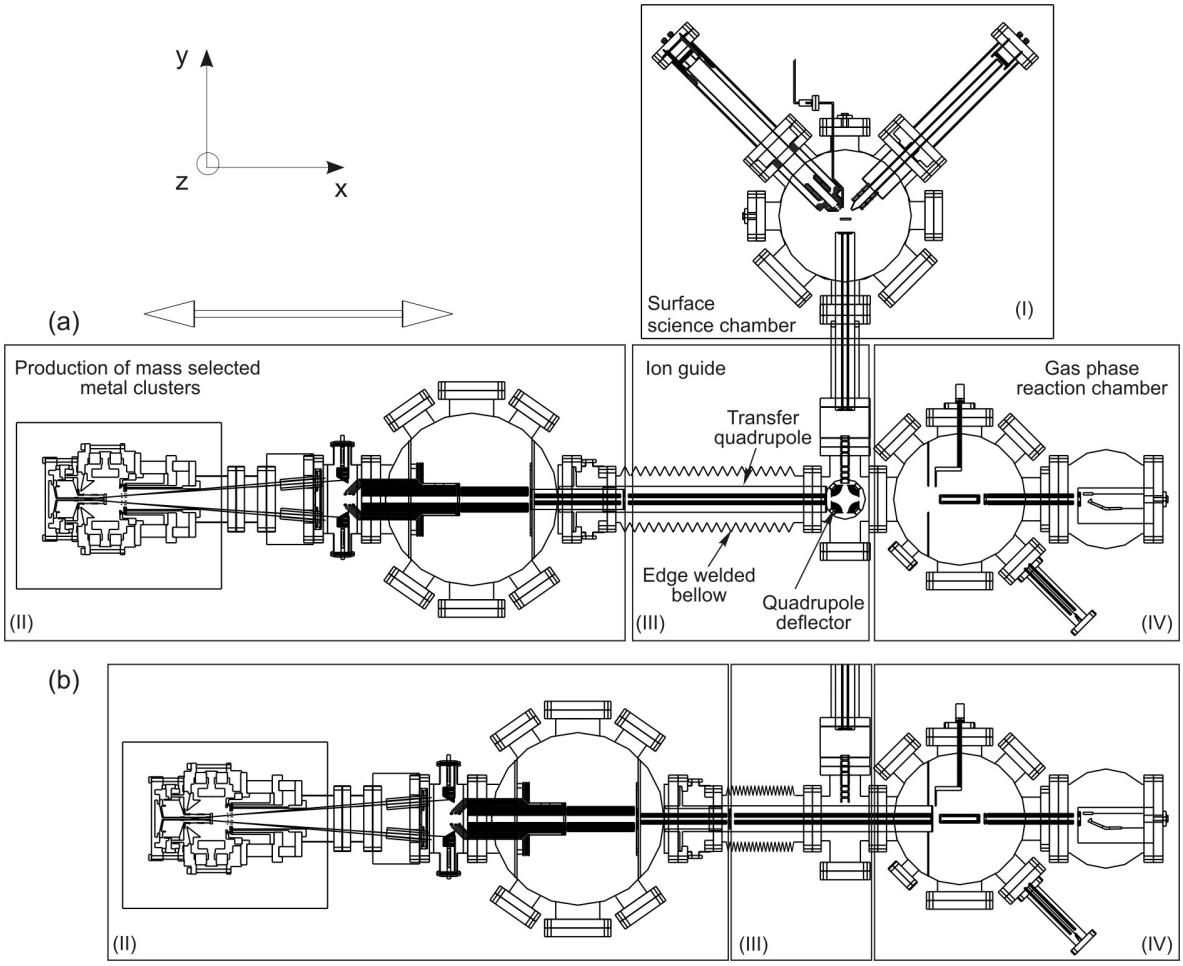

Figure 2.1 Schematic overview of the complete vacuum apparatus assembly. The cluster source and the ion guide are positioned for: (a) cluster deposition experiments; (b) gas-phase experiments (see text for details).

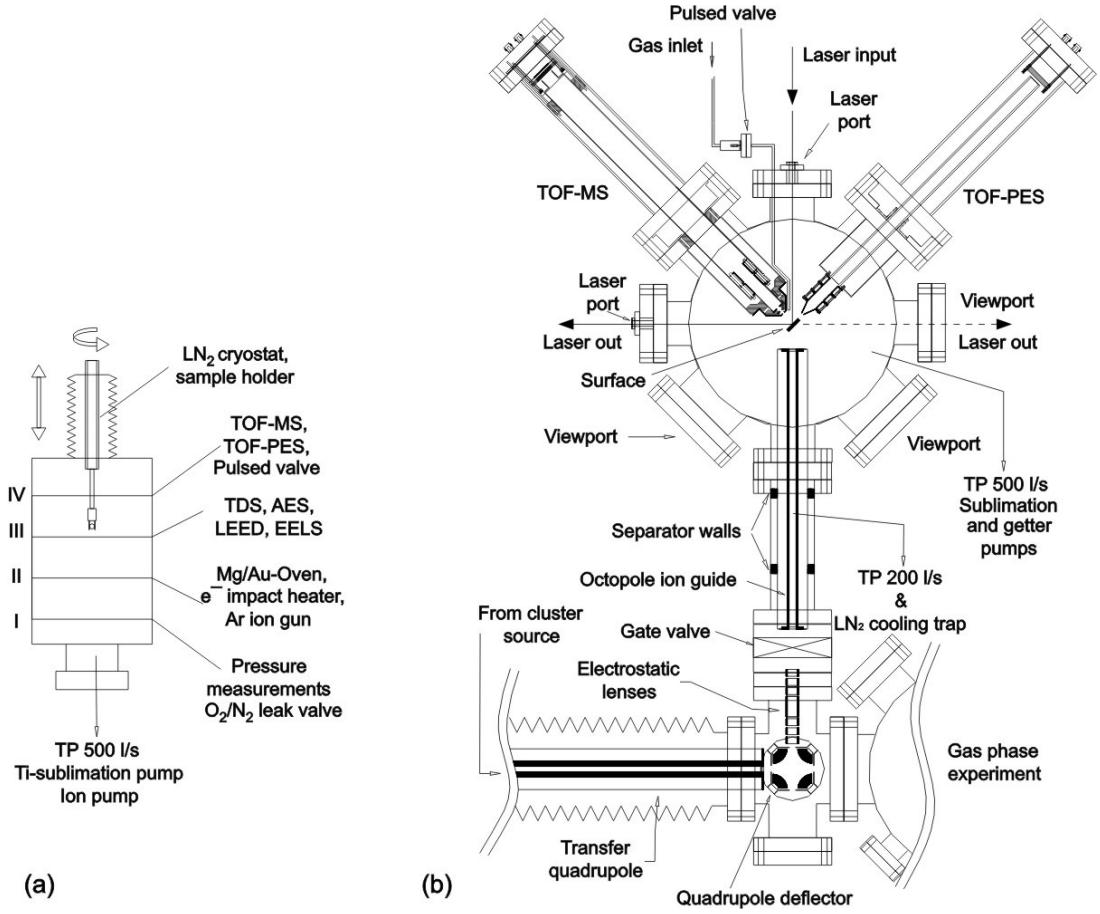

Figure 2.2 Schematic representation of the UHV surface science chamber. (a) Side view of the UHV surface chamber presenting the level arrangement of experimental tools. (b) The upper level of the UHV chamber together with the ion guide system used for mass-selected cluster deposition.

activity measurements with free small selected gold clusters and methyl halide molecules in the gas-phase were performed.

The cluster source and a part of the ion guiding system, i.e. the transfer quadrupole (cf. Figure 2.1 part II and III) are mobile. This was realized by mounting the entire cluster source and the transfer quadrupole on a linear double rail system so that this part of the apparatus can be shifted along the x-axis (see arrow in Figure 2.1). For the surface deposition experiments (cf. Figure 2.1a) the mass-selected metal cluster beam emerging from the cluster source is guided through a transfer quadrupole (x-axis) and is subsequently bent by 90° (y-axis) via a quadrupole deflector (cf. Figure 2.1 part III) to be directed toward the surface science chamber. For gas-phase experiments, the quadrupole deflector is retracted upwards from the ion guiding system with a z-axis translation mechanism under vacuum conditions. Subsequently, the cluster ion beam is guided directly into the gas-phase reaction chamber by the transfer quadrupole, which has been shifted together with the cluster source as shown in Figure 2.1b.

The entire vacuum system is differentially pumped. In this way, during the operation, a pressure difference of six orders of magnitude between the cluster production chamber

(10^{-2} mbar) and the gas-phase investigation chamber (10^{-8} mbar) is obtained. The surface science chamber is pumped down separately by turbo molecular pumps in conjunction with an ion and a titanium sublimation pump (base pressure $<1\times10^{-10}$ mbar) as described in the next section.

2.1.1 Surface science chamber

The UHV surface science chamber contains specific tools for surface preparation and characterization arranged on four levels as shown in Figure 2.2a. On the lowest level an oxygen and a nitrogen leak valve are positioned. They are used for magnesia thin film preparation and for the purging of the UHV chamber (cf. Figure 2.2a I).

The second level (cf. Figure 2.2a II), used for surface preparation, is equipped with a magnesium evaporator for magnesia thin film preparation and with an electron impact heater for surface cleaning. Also on the second level, a K-type thermocouple ending close to the center of the UHV chamber is employed as reference thermometer in contact with the surface for temperature calibration in the 100 K - 1200 K range.

The third level (cf. Figure 2.2a III) hosts a commercial LEED/AES device (OCI Vacuum Microengineering-BLD600IR) and a commercial quadrupole mass spectrometer (Thermo Onix-VGQ-100 amu), which has been adapted for temperature programmed desorption measurements. Also here an ion gauge for pressure measurement is placed.

The upper level (cf. Figure 2.2a IV) of the surface science chamber is presented in Figure 2.2b. A homebuilt time-of-flight mass spectrometer is used for the SFsMS measurements. A stainless steel tube (4 mm inner diameter) ending close to the surface is employed for gas admission prior to the photoreaction experiments. A homebuilt time-of-flight photoelectron spectrometer can be employed to obtain information about the electronic structure of the sample surface [68].

One sapphire laser port (18 mm diameter) mounted on the same flange as the gas admission tube permits the laser irradiation of the surface. As shown in Figure 2.2a (see also Section 2.1.2), the sample surface is attached to a manipulator and it can be translated and rotated to be positioned in front of each preparation tool and analytical instrument. Particularly for laser measurements employing the TOF-MS and TOF-PES, respectively, the sample surface is positioned in the front of the spectrometer and perpendicular to its axis. In this case the incidence and emergence angle of the laser light on the surface is 45°. For a precise adjustment of the incident laser beam on the surface a second sapphire laser port and a quartz view port are mounted each at 90° with respect to the input laser beam (cf. Figure 2.2b). When the incident laser beam irradiates the sample surface correctly, the emergent laser beam is reflected through the output windows and the shape of the beam profile can be observed.

The upper level also hosts an octopole ion guide used for deposition of mass-selected clusters. For this purpose the cluster ion beam emerging from the cluster source is bent by the quadrupole deflector, subsequently the beam divergence is corrected by a first electrostatic lens and then it is focused by the second electrostatic lens into the first quarter of the octopole ion guide (Figure 2.2b). The octopole guides the cluster ions toward the surface crystal inside

the UHV surface science chamber [70]. A gate valve mounted between the octopole ion guide and the electrostatic lens system is opened just during the cluster deposition.

The whole UHV surface science chamber is shielded by a μ-metal layer in order to minimize the effect of the external magnetic fields on the photoelectrons.

The base pressure of about 1×10^{-10} mbar in the surface science chamber is achieved in several steps. First, two turbo pumps with a total pumping rate of 700 l/s (TPU 510PMP and TPU 170, both Pfeiffer Vakuum), each pumped by a rotary vane pump (Edwards E2M2 and Balzer Duo 016B), are mounted directly at the UHV surface science chamber and underneath the octopole ion guide chamber, respectively. In order improve the pumping process, an ion getter pump (Physical Electronics IGP160, 160 l/s) and a water cooled titanium sublimation pump (ST22, AML TSP2) are also employed. To achieve the base pressure, the vacuum chamber is baked at 170°C for 48 hours by means of several heating tapes controlled by a PID regulator.

2.1.2 Sample holder

A Mo(100) crystal attached to a liquid nitrogen cryostat is mounted in the center of the UHV chamber. The crystal-cryostat assembly can be vertically translated to all vacuum chamber levels and horizontally rotated by 360^{0} by a mechanical manipulator. Furthermore, an xy-horizontal translation stage allows a movement of the assembly by ±15 mm from the mid-point. The crystal position can be reproduced with better then 0.02 mm and 0.5° accuracy.

The Mo(100) crystal (Mateck) has a diameter of 10 mm and a thickness of 2 mm. One side of the crystal is polished to a roughness of less than 0.03 μm and it is oriented with a precision better than 0.5°. In Figure 2.3 a schematic drawing of the crystal holder is presented.

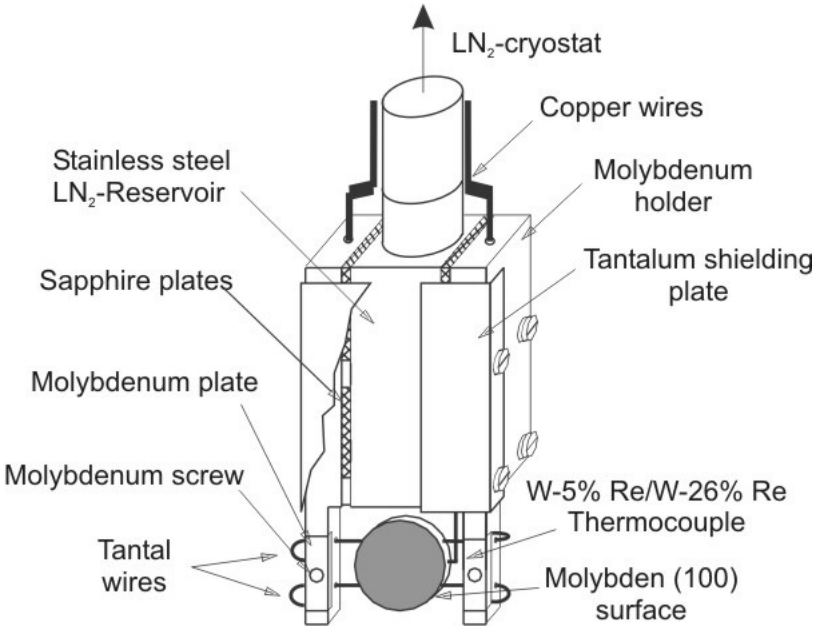

Figure 2.3 Schematic representation of the crystal holder.

Two slots cut into the upper and lower crystal edge are used to hold the crystal between two tantalum wires of 0.3 mm diameter (cf. Figure 2.3). The tantalum wires are fixed to two molybdenum holders by screwed molybdenum plates. Two sapphire spacers are located between the molybdenum holders and the stainless steel LN_2 reservoir. In this way, on one hand, a good thermal contact and on the other hand, an electrical isolation between the LN_2 reservoir and the molybdenum holders is achieved. The molybdenum holders are connected to a power supply (Lambda Z, UP10-40 up to 40 A) by means of two copper wires (1.4 mm in diameter) and two appropriate electric feedthroughs. By applying a current to the tantalum wires, the Mo(100) crystal can be resistively heated from the lowest temperature of 90 K up to 1300 K. A further heating up to 2000 K can be achieved by electron bombardment.

The temperature is measured with a W-5%Re/W-26% Re thermocouple introduced into a 0.7 mm hole on the crystal side. For the 90 - 1200 K temperature range the thermocouple was calibrated by means of a second Nickel-Chromium/Nickel thermocouple in contact with the crystal. The calibration accuracy was verified by TDS using the specific thermal desorption peaks for several absorbed molecules, i.e. CH_3Br, CH_3I, H_2O on MgO and Mg, MgO adsorbed on Mo(100). For temperatures higher than 1200 K, where the thermocouple presents a linear characteristic, the calibration curve was extrapolated linearly [71].

2.2 Analytical tools

2.2.1 Surface investigation by electron-based analytical methods

In electron-based analytical surface investigation techniques [72] the mean free path of electrons in a solid as a function of their kinetic energy plays a decisive role (see Figure 2.4). The characteristics of this curve are common for a large number of different materials. An investigation technique is surface sensitive, if the electrons to be detected can travel no more than a few atomic distances through the solid. As observed in Figure 2.4, the highest surface sensitivity is achieved when the surface is irradiated with electrons possessing a kinetic energy between 50 eV and 250 eV.

In numerous investigation methods used to study the structure and composition of a surface, a beam of electrons with well defined primary energy E_P impinging on the surface will produce the appearance of backscattered and emitted secondary electrons. These electrons leaving the surface can be divided into several groups:

- A fraction of the primary electrons are backscattered elastically. These electrons can interfere at crystalline surfaces due to their wave properties. In this way, the surface structure can be studied by LEED, a method which is similar to the X-ray diffraction technique, employed for single crystal surface analysis.
- Quasi-elastic electrons are the result of surface vibrations induced by the primary electrons. These electrons are investigated by HREELS.
- Primary electrons, which are losing their energy due to the collective excitation of the surface electrons (plasmon loss), are studied by EELS.

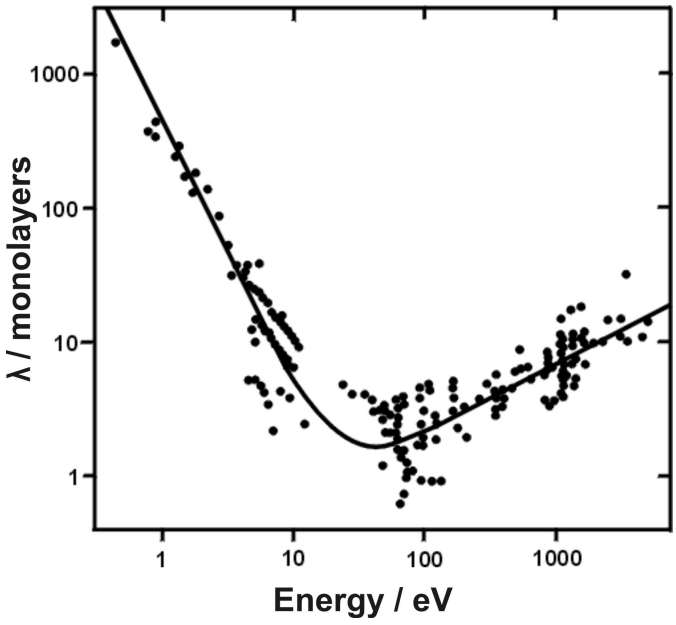

Figure 2.4 Mean free path of electrons in a solid as a function of their energy. From Seah and Dench [73]. The dots represent the measured data for a compilation of elements. The solid line is the least squares fit to the measured data over the complete energy range.

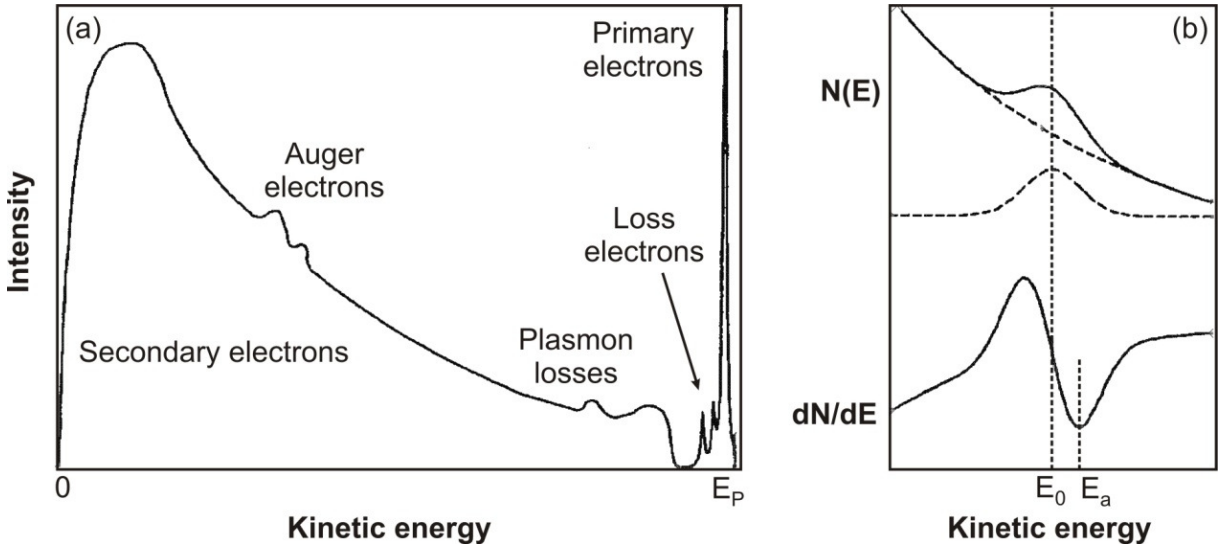

Figure 2.5 (a) Energy spectrum of electrons coming from a surface irradiated with a beam of primary electrons with a kinetic energy E_P. (b) The first derivative dN/dE facilitates the separation of the Auger peaks from the background. After J. W. Niemantsverdriet [74].

- Auger electrons created by the Auger effect [75, 76].
- A large fraction represents secondary electrons created by the collision of the primary electrons and the electrons bound in the solid.

Figure 2.5a shows a schematic energy distribution of the backscattered electrons as a function of their kinetic energy. Experimentally, in order to enhance the visibility of the Auger peaks, which are located on the background of the secondary electrons, Auger spectra are presented in the derivative mode. The kinetic energy of the Auger electrons corresponds to the center of the integral peak E_0, but they are usually reported at the negative excursion of the derivative E_a [74] (cf. Figure 2.5b).

2.2.1.1 Low energy electron diffraction

A commercial LEED/AES device (BLD600IR, OCI Vacuum Microengineering) was employed to study the surface composition and structure. In Figure 2.6 a schematic representation of the LEED/AES device is presented. It consists of a filament which produces electrons that are collimated by a Wehnelt cylinder and two electrostatic lenses. The electrons having the desired energy are passing a grounded drift tube and subsequently strike the sample surface at normal incidence. The backscattered electrons pass a grid system in which the first grid is grounded in order to avoid the electrostatic deflections of electrons by the potentials applied on the next electrodes. A negative potential, whose magnitude is slightly smaller than the primary energy of the electrons is applied on the second and third grid to repell the inelastically scattered electrons. Afterwards, the diffracted electrons cross a forth grid (grounded), hit a multichannel plate system, used for intensity amplification, and are detected on a fluorescent screen. The diffraction images are visualized through a viewport and recorded by a CCD camera.

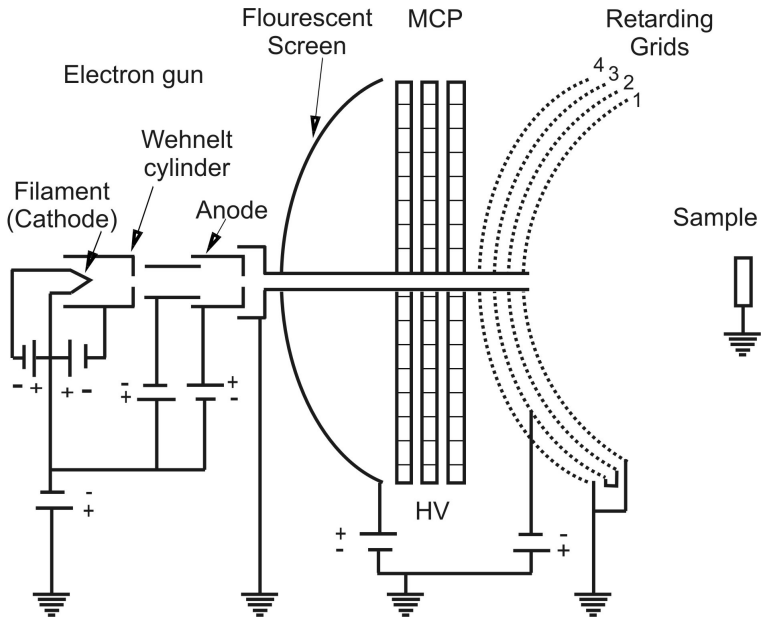

Figure 2.6 Schematic representation of the LEED-AES-EELS device

LEED was used in the present work to investigate the surface geometry itself and the geometry of adsorbed layers that form a periodic structure on the substrate. Typically, the employed energy of the primary electrons was between 35 eV and 200 eV, which coincides with the minimum of the mean free path in solids.

Considering the wave nature of the electrons, the basis for the interference of electrons at a periodic surface structure is the de Broglie equation:

$$\lambda = \frac{h}{m_e v} = \frac{h}{\sqrt{2 m_e E_P}} \tag{2.1}$$

where:

λ is the wavelength of the electrons
h is the Plank constant
m_e is the mass of electron
E_P is the kinetic energy of the electron

When a wave scatters at a periodic array, constructive interference take place, if the scattered waves from neighboring lattice points have path differences of multiple of wavelength λ

$$\sin\alpha = \frac{n\lambda}{a} = \frac{nh}{\sqrt{2 m_e E_P}}, \; n = 0, 1, 2, \tag{2.2}$$

in which:

α is the angle between the scattered electrons and the surface normal
n is the order of diffraction
a is the distance between two neighboring atoms

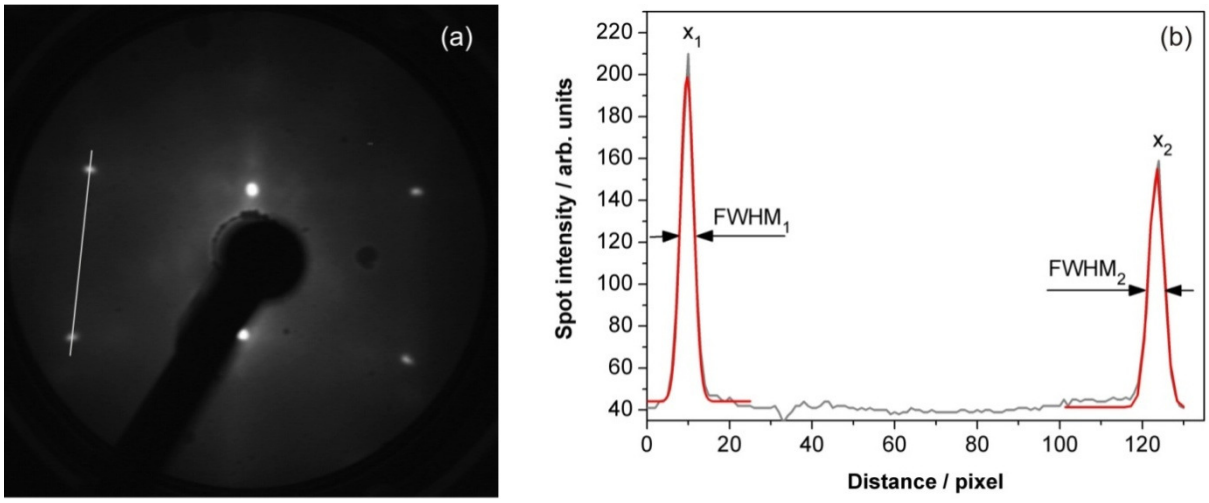

Figure 2.7 (a) LEED image of a clean Mo(100) surface. (b) Intensity profile of two adjacent spots from (a) used for the determination of the transfer width of the diffractometer (E_P = 80 eV).

Due to the inverse relationship between interatomic distances and the directions in which constructive interference between the scattered electrons occurs, the separation between the LEED spots is large when the interatomic distance is small and vice versa. The LEED pattern has the same form as the reciprocal lattice.

The transfer width (t_w) plays an important role for the LEED evaluation of domain structures, i.e. the case were the periodic sequence of the elementary cell of the surface structure do not cover the whole surface area irradiated by the primary electron beam. t_w arises due to the imperfections of the primary electron beam, i.e. the energy spread, lateral extensions, and limited parallelism. If the diameter of a domain structure is smaller than t_w, the LEED image will contain effects due to the superposition of the amplitudes of the electron waves scattered from different domains, which results in spot broadening, spot splitting or formation of streaks. If the diameter of a domain structure is bigger than the transfer width, the LEED image presents a superposition of spots originating from the interface phenomena caused by the separate regions with uniform periodicity. Typically, the transfer width values are between 5 and 10 nm and vary with the electron energy [77].

The transfer width for a given energy of the primary electrons can be experimentally estimated from a LEED image recorded from a surface, whose structure is periodic over distances larger than t_w, using the equation:

$$\frac{P_{FWHM}}{a^*} = \frac{a}{t_w} \tag{2.3}$$

where:

P_{FWHM} is the mean value of the full width at the half maximum of the LEED spots,
a^* is the distance between two adjacent spots,
a is the lattice constant.

In Figure 2.7a, a LEED image recorded from a Mo(100) surface with primary electrons having the energy of 80 eV is presented. In Figure 2.7b, the intensity profiles of two adjacent spots from Figure 2.7a are plotted. The FWHM of the LEED spots were deduced by fitting the peaks in Figure 2.7b with a Gaussian function (red curves, $FWHM_1 = 3.2$ pixel, $FWHM_2 = 3.4$ pixel). For this LEED image (Figure 2.7), the transfer width of the diffractometer was estimated to be about 10 nm at $E_P = 80$ eV (cf. Figure 2.7b and relation (2.3)).

2.2.1.2 Auger Electron Spectroscopy

Auger electron spectroscopy is used in surface science to obtain information about the chemical composition in the 5 to 20 Å depth region near the surface. AES is carried out by exciting the sample with a beam of primary electrons with a kinetic energy between 1 and 10 keV. These electrons ionize the sample atoms in one of the core states. The relaxation of the sample atoms is realized by filling the core hole with an electron from a higher shell. The energy is either liberated as an X-ray photon or in an Auger process (discovered in 1925 by Pierre Victor Auger [75]) by the emission of a Auger electron. These processes are illustrated in Figure 2.8 for the case of an atom excited in a K level. An electron from the L_{III} level jumps into the core hole, consequently a quantum of characteristic X-ray is emitted (see Figure 2.8a). In Figure 2.8b the core hole is filled by an outer electron and the surplus energy is transmitted in a non-radiative process to a second electron, which leaves the atom with a characteristic kinetic energy (Auger process).

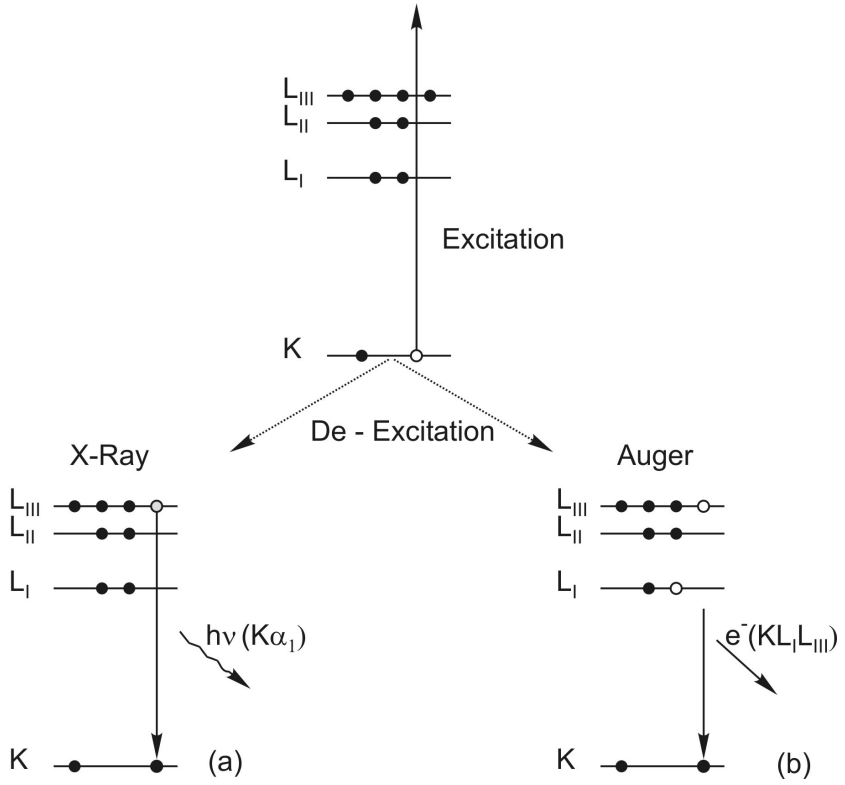

Figure 2.8 De-excitation of an atomic core hole, giving rise to: (a) X-Ray emission; (b) Auger electron emission.

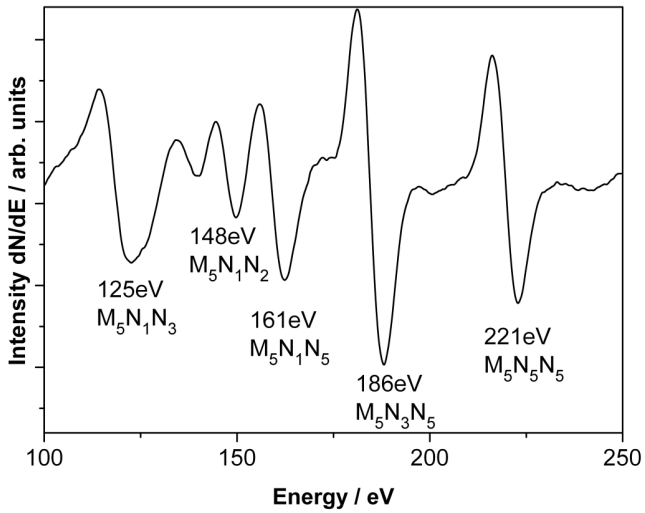

Figure 2.9 Typical Auger electron spectrum recorded from a clean Mo(100) surface (E_P=2000 eV). The corresponding Auger transitions are noted for each peak in the figure.

For AES a source of primary electrons, a sample, an analyzer and a detector system is needed. The instrumentation used in the present work for AES was presented in Figure 2.6. Following the sample excitation by the primary electrons (E_P = 2 kV), the Auger electrons are analyzed by ramping the applied retarding potential on the second and third grid of the spectrometer. The electrons are detected on the MCP used as Faraday cup. Afterwards the electron signal is amplified by means of a Lock-In amplifier.

AES was employed in the present work qualitatively in order obtain information about the samples cleanliness, to study the magnesia oxidation on the molybdenum single crystal substrate, and also quantitatively in order to calibrate the deposition rate of the magnesia and gold evaporators for thin film deposition. In Figure 2.9, a typical Auger electron spectrum recorded from a clean Mo(100) surface together with the corresponding electronic transitions is presented.

2.2.1.3 Electron energy loss spectroscopy

EELS is a surface sensitive technique in which the energy loss of the primary electrons is used to study the electronic structure of the surface. In our experiment the energy loss of the primary electrons has been measured by means of the LEED and AES instrumentation (cf. Figure 2.6). For the EELS measurements, the kinetic energy of the primary electrons was between 100 and 500 eV.

The losses can be divided in five categories:

- Core electron excitation
- Excitation of the valence electrons
- Plasmon losses
- Extended loss fine structure
- Vibrational excitation (investigated just by HREELS)

2.2.2 Photoemission spectroscopy

Based on the photoelectric effect [78], fs-laser photoemission is employed to investigate the electronic structure of the substrates, to study the changes that arise after thin films deposition, and to understand the photoinduced chemical reactions at the surface.

In Figure 2.10 a schematic representation of the time-of-flight photoelectron spectrometer is presented. A standard TOF-PES consists of a surface sample, a free field drift tube, and a detector. In this work, the sample surface was positioned 5 mm apart of the TOF-PES entrance with the surface normal parallel to the spectrometer axis. The entrance electrode of the spectrometer has a conical form with a center hole of 2.9 mm diameter. In this way, mostly the electrons emitted parallel to the spectrometer axis are analyzed. In order to collimate the electrons to be analyzed and in the same time to improve the transmission of the spectrometer, an electrostatic lens system is mounted between the entrance electrode and the drift tube, which was, however, grounded in the present experiments. The photoelectrons were amplified by a factor of 10^6 - 10^7 via a micro-sphere plate arrangement at the end of the field free double-wall μ-metal drift tube. Subsequently, the electron signal was collected on a metal anode. In order to avoid the alteration of the photoelectron measurements by external magnetic fields, additionally, the inner part of the whole UHV chamber was covered with a μ-metal wall. The vacuum housing of the ToF-PES was constructed of μ-metal, and a cylindrical μ-metal shield was installed around the spectrometer entrance and electrostatic lenses.

The photoemission experiments were performed with the excitation wavelengths relevant to our pump-probe experiments of adsorbed methyl halide molecules (263 - 266 and 333 nm) and with the second harmonic of the laser fundamental (400 nm). In Figure 2.11, a schema of the experimental arrangement used for the photoemission experiments with fs-laser pulses is presented. A fast photodiode (818-BB-21 Newport) mounted directly in the third harmonic generator converts the laser pulse into an electrical signal, which is used by the MCS electronics[1] as a trigger pulse (START). For a straightforward understanding of the

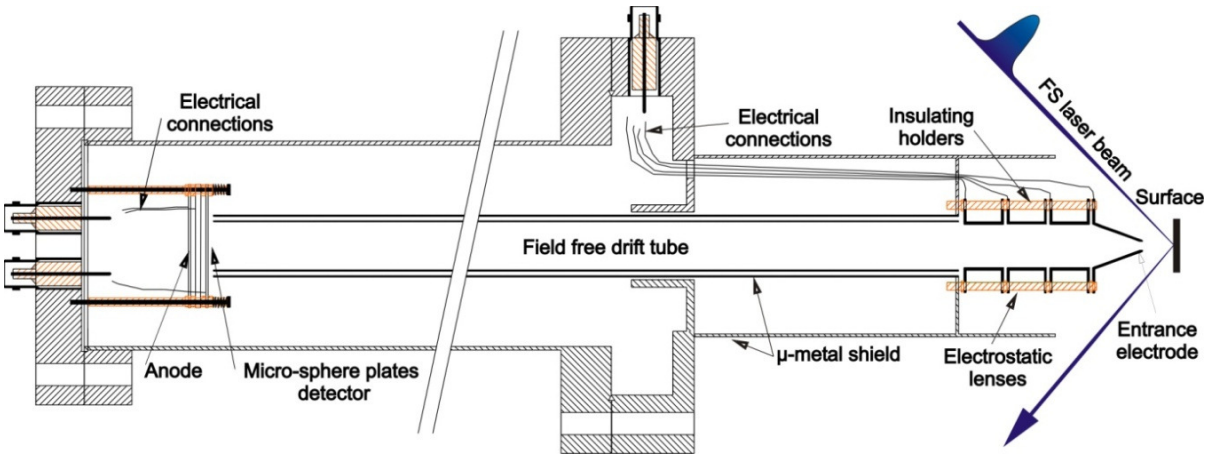

Figure 2.10 Schematic drawing of the time-of-flight photoelectron spectrometer.

[1] The MCS electronics (P7887 from FAST Com Tec) is a PCI (peripheral component interconnect) board and was employed in conjunction with a single core 3 GHz personal computer.

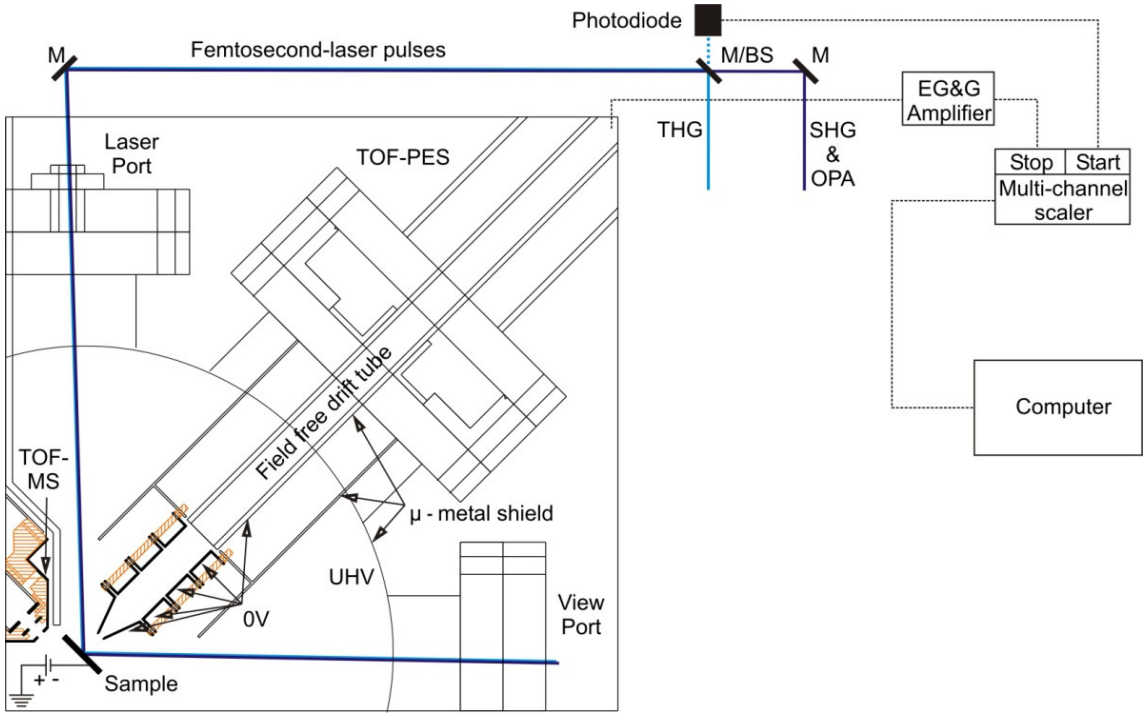

Figure 2.11 The experimental arrangement used for femtosecond photoemission experiments.

working principle, in Figure 2.11 the photodiode is illustrated outside of the THG, but the correct location is presented in Figure 2.23.

The photoemission signal from the detection anode of the TOF-PES is amplified by a factor of 10 by means of a fast amplifier (EG&G Ortec VT 120) and subsequently used as STOP signal for the MCS electronics. The MCS electronics has a time resolution of 250 ps and the ability to detect multiple events for every START pulse.

A small bias of typically 3-5 V was applied to the surface in order to prevent cutting off the low energy electrons due to the work function difference between the substrate and the spectrometer. The laser beam incidence angle was about 45° and the irradiated surface area was about 2 mm^2. In order to avoid spectral broadening due to space charge effects, the laser intensity was carefully adjusted and the count rate was kept at small values (below 100 counts/s at 1 kHz laser repetition rate). Usually, the photoemission spectra were recorded at 90 K by summing the photoelectron signal of 10^5 laser pulses.

In Figure 2.12, the potential distribution between the Mo(100) surface and the time-of-flight photoelectron spectrometer is displayed schematically. The sample and the spectrometer exhibit the work functions Φ and Φ_{sp}, respectively. The spectrometer is grounded. Applying a negative potential U_{bias} to the sample, the Fermi energy of the sample E_F can be varied (raised) with respect to the Fermi energy of the spectrometer $E_{F,sp}$ and consequently, E_{vac} is varied, too. If both, the sample and the spectrometer, are at the same potential, their Fermi energies coincide. As the binding energy of an electron in a solid is related to the Fermi energy, upon absorption of a photon its kinetic energy E_{kin} above the sample is:

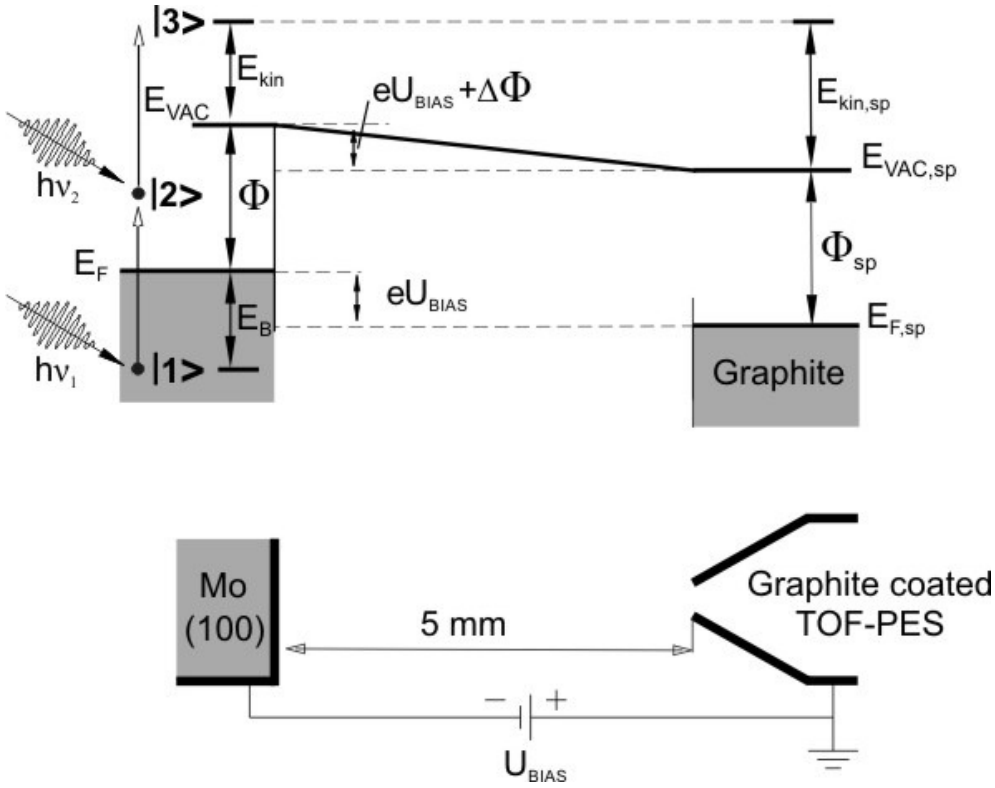

Figure 2.12 Energy level diagram for 2PPS. An electron is excited from the initial state |1> to an intermediate state |2> due to a $h\nu_1$ photon adsorption. From the |2> state, the electron is ejected from the material into the final state |3> after the absorption of a second photon $h\nu_2$.

$$E_{kin} = h\nu - E_B - \Phi, \tag{2.4}$$

where hν is the photon energy for one photon photoemission, or $h\nu = h\nu_1 + h\nu_2$ in the case of two-photon photoemission as illustrated in Figure 2.12.
The measured kinetic energy, as determined by the spectrometer is:

$$E_{kin,sp} = h\nu - E_B + eU_{BIAS} - \Phi_{sp}. \tag{2.5}$$

The electrons originating from the Fermi level ($E_B = 0$), posses the maximum kinetic energy:

$$E_{kin,sp_{(max)}} = h\nu + eU_{BIAS} - \Phi_{sp}. \tag{2.6}$$

The measured minimum kinetic energy value is:

$$E_{kin,sp_{(min)}} = \Phi + eU_{BIAS} - \Phi_{sp}. \tag{2.7}$$

The width of the spectrum ΔE is therefore given by:

$$\Delta E_{kin} = E_{kin,sp(max)} - E_{kin,sp(min)} = h\nu - \Phi\ . \tag{2.8}$$

Thus, the work function of the sample can be determined from the width of the photoemission spectrum and the energy of the exciting photon(s):

$$\Phi = \Delta E_{kin} - h\nu. \tag{2.9}$$

Due to the fact that the spectrometer is coated with graphite, ($\Phi_{sp} = \Phi_{graphite} = 4.45$ eV [79]) the spectrometer calibration and the determination of the initial and intermediate energy states in 2PPS experiments is possible. The kinetic energy of the electrons in the spectrometer is determined from the time-of-flight t, using the equation:

$$E_{kin} = \frac{m_e \cdot l^2}{2(t - t_0)^2}, \tag{2.10}$$

where:

m_e is the electron mass

l is the length of the field free region (l = 541 mm)

t_0 is the initial time corresponding to the moment when the electron is emitted.

The initial time t_0 can be determined by recording a series of photoelectron spectra for different U_{BIAS}. After the subtraction of the U_{BIAS} from the E_{kin}, the photoemission spectra are plotted and t_0 is varied until the spectra overlap [68, 80]. In the end, in order to convert the time-of-flight spectrum into an energy spectrum, the intensity (dN/dt) is also rescaled (to dN/dE_{kin}) according to:

$$\frac{dN}{dE_{kin}} = \frac{dN}{dt} \cdot \left| \frac{dt}{dE_{kin}} \right| = \frac{dN}{dt} \cdot \frac{(t - t_0)^3}{m_e \cdot l^2} = \frac{dN}{dt} \sqrt{\frac{m_e \cdot l^2}{8}} \cdot E_{kin}^{-\frac{3}{2}}. \tag{2.11}$$

2.2.3 Temperature programmed desorption

A commercial quadrupole mass filter (mass range from 1 to 100 amu, VGQ 100 Thermo ONIX) mounted on a retractable flange is used as differentially pumped thermal desorption spectrometer as well as a RGA. The spectrometer setup in both operation modes is schematically depicted in the Figure 2.13. In the TPD mode the mass filter is enclosed in a stainless steel tube. The sample surface is positioned about 4 mm apart from the skimmer entrance, with the surface normal parallel to the spectrometer axis. The skimmer is biased with a negative voltage in order to avoid electron stimulated desorption induced by the electrons originating from the ionizer. A stationary ring (ionizer cover) covers the rectangular opening in the housing tube (dashed line in Figure 2.13a) at the ionizer region. Differential pumping is accomplished by several holes in the housing on the detector side of the mass filter. For RGA measurements, the mass filter housing tube can be retracted from the crystal. The ionizer is not covered anymore in this position, and therefore exposed to the vacuum chamber through

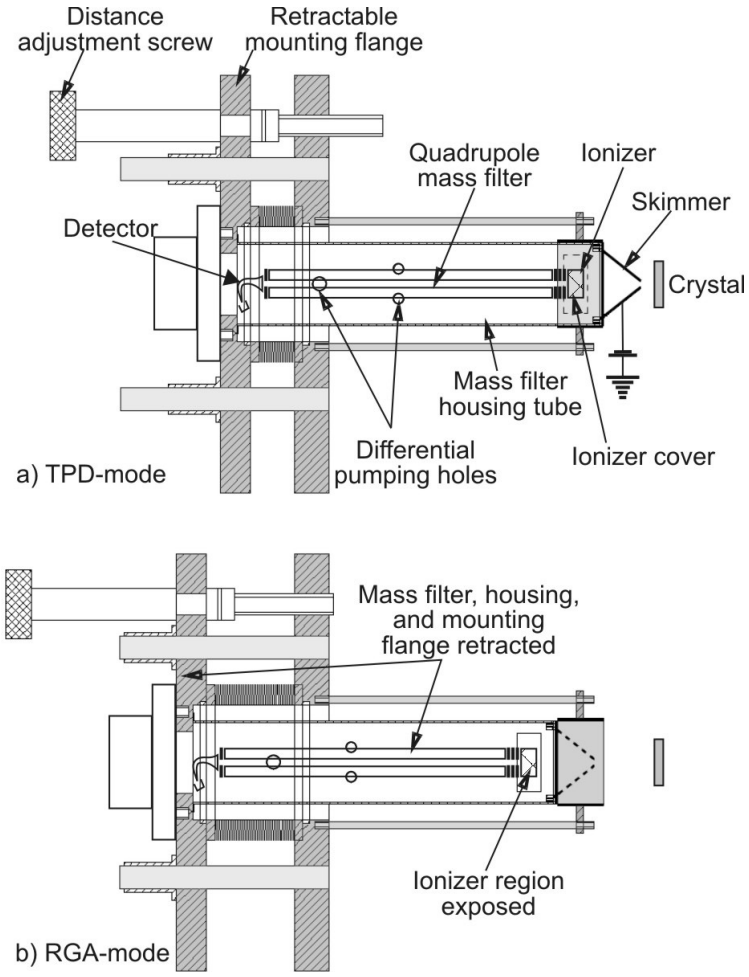

Figure 2.13 Schematic representation of the quadrupole mass filter assembly used for (a) Temperature programmed desorption; and (b) residual gas analysis.

the large rectangular opening in the housing tube (cf. Figure 2.13b). In this way, the residual gas pressure inside the chamber can be monitored.

TPD is used in surface science to study the desorption of gases from surfaces in vacuum. It does not give information about the surface structure or chemical composition, but it is able to indicate the presence of surface defects through their influence on the desorption temperature of the adsorbate molecules as will be shown later for the case of MgO thin films on Mo(100) (Chapter 5).

In the TPD measurements, the surface sample temperature is ramped uniformly according to:

$$T = T_0 + \beta t \tag{2.12}$$

in which

T is the surface temperature

T_0 is the initial temperature

t is the time

β is the heating rate, equal to dT/dt

by a PID controller implemented into a self-writen LabView program. The same LabView program reads the surface temperature as well as accomplishes the mass spectrometer signal acquisition.

2.2.3.1 Kinetics of temperature programmed desorption

The kinetics of TPD is usually described by the Polanyi-Wigner equation:

$$r = -\frac{d\theta}{dt} = \nu\theta^n e^{-\frac{E_{des}}{kT}}, \tag{2.13}$$

in which

r is the desorption rate,
θ is the molecular coverage of the adsorbate in monolayers equivalent,
ν is the frequency factor (typical values: 10^{12} - 10^{14} Hz),
E_{des} is the desorption energy,
k is the Boltzmann constant.

The Arrhenius form of the equation (2.13) facilitates its physical interpretation. The desorption energy is the barrier of desorption and thus a measure of the strength of the bond between the adsorbate and the surface, while the frequency factor is identified with the vibrational frequency of the surface bond of the adsorbed species. The θ^n term contains information about the desorption mechanism, analogous to the concentration factors in chemical kinetics expressions. For example, molecular species which desorb upon recombination of dissociated fragments usually exhibit second order (n = 2) desorption kinetics, while desorption of molecules which adsorb molecularly (undissociated) on a substrate is described by first order (n = l) desorption kinetics. At multilayer coverages, the desorption order is zero (up to the desorption maximum). This is a reflection of the fact that removal of the top molecular layer reveals an identical molecular layer and not a bare substrate surface. Fractional order desorption kinetics have also been observed when desorption primarily takes place at the perimeter of islands or clusters [81, 82].

Equation (2.13) describes the desorption rate as a function of the time t. Because TPD profiles are usually presented as plots of desorption rate vs. surface temperature it is more convenient to express the rate in terms of the surface temperature T. Using the chain rule, the equation (2.13) can be rewritten as:

$$-\frac{d\theta}{dt} = -\frac{d\theta}{dT}\cdot\frac{dT}{dt} = \nu\theta^n e^{-\frac{E_{des}}{kT}} \tag{2.14}$$

For a linear temperature ramp ($T = T_o + \beta t$), as for the experiments described here, this results in:

$$-\frac{d\theta}{dt} = \frac{\theta^n\nu}{\beta} e^{-\frac{E_{des}}{kT}} \tag{2.15}$$

If the value of θ is well known, then equation (2.15) contains three unknowns: n, ν and E_{des}. The value of n can often be determined by comparing the shapes of the TDS traces for various initial coverages. For instance, if E_{des} and ν are constant for a given coverage and temperature, first order kinetics yields a temperature of maximum desorption that is constant with the initial coverage. Zero order kinetics gives TPD signals whose leading edges coincide and whose peak positions shift to higher temperatures with increasing initial coverage, while second-order desorption leads to TPD signals whose peak positions shift to lower energy with increasing initial coverage.

When E_{des} and ν are not constants, the interpretation of the desorption order is more problematical. For first order desorption kinetics, in which E_{des} decreases smoothly with coverage, the temperature of maximum desorption intensity decreases with coverage. Such behavior is specific for repulsive interactions between the adsorbed molecules as can be seen for the case of methyl halides adsorbed on magnesia.

The frequency factor ν may be extracted from the leading edge of the TPD profile, without any assumption about the desorption energy. More commonly, ν is assumed to be constant over the TPD peak with a value in the range 10^{12}-10^{14} Hz. The actual value may be based on the nature of the adsorbate bond; vibrational frequencies in the range 10^{13} - 10^{14} Hz would be expected for chemically bound species (in general). Frequencies of the order of 10^{12} Hz would be more likely for physisorbed species. If the desorption energy is assumed not to be constant, then the frequency factor should not be a constant as well.

2.2.3.2 Redhead equation

TPD is used most commonly in surface science to estimate of the energy barrier of desorption. In the case of first order desorption, the desorption energy can be obtained from the peak temperature of the TPD profile by the method of Redhead [83]. For this method, E_{des} is assumed to be constant with coverage and temperature. When n = l. in (2.15), the TPD peak profile is described by the first derivative of (2.15):

$$\frac{dr}{dT} = r\left(\frac{E_{des}}{kT^2} - \frac{\nu}{\beta}e^{-\frac{E_{des}}{kT}}\right), \tag{2.16}$$

where r is the desorption rate ($r = -d\theta/dT$). Setting the previous equation to zero, the rate of desorption is a minimum when r = 0 (i.e., when T = 0 or θ = 0) and a maximum when:

$$\frac{E_{des}}{kT_{max}} - \frac{\nu}{\beta}e^{\frac{E_{des}}{kT_{max}}} = 0. \tag{2.17}$$

Where T_{max} is the temperature of the maximum desorption intensity. The above equation can be written as:

$$\frac{E_{des}}{kT_{max}} = \ln\left(\frac{\nu T_P}{\beta}\right) + \ln\left(\frac{kT_{max}}{E_{des}}\right). \tag{2.18}$$

E_{des} can be calculated by using the Redhead equation:

$$\frac{E_{des}}{kT_{max}} = \ln\left(\frac{\nu T_P}{\beta}\right) - 3.64. \tag{2.19}$$

The Redhead equation is approximately correct for first order desorption. It is often applied to determine E_{des} from a single spectrum. One must however choose a value for ν.

2.3 Cluster sources

In this work, experiments on methyl halide molecules adsorbed on gold nanoparticles and on mass-selected gold clusters on magnesia thin films were performed. For this purpose, a gold evaporator mounted inside of the UHV chamber was employed for the gold nanoparticle production. For the generation of monodispersed gold clusters, an external cluster source coupled to the UHV surface science chamber by means of an ion guiding system was used.

2.3.1 Gold evaporator

Gold nanoparticles are grown by gold evaporation from a homemade evaporator. In Figure 2.14 a schematic representation of the gold evaporator is presented. It consists of an Au ribbon (Alfa, 99.998%) placed inside of a loop made of tantalum wire (0.3 mm diameter). During the evaporation a current of 7.7 A is applied on the tantalum wire. The ends of the tantalum wire are introduced in two tantalum holders with a diameter of 2.1 mm. The tantalum holders are gripped in the terminal part of two copper rods (8 mm diameter) used also for current supply. In order to evaporate Au just in one defined direction, a stainless steel cylinder with a circular opening of 10 mm encloses the evaporator.

For the deposition, the substrate held at 90 K is positioned 10 mm apart from the gold oven. During the evaporation the pressure inside the UHV chamber reaches a maximal value of 2×10^{-9} mbar. The evaporator is initially carefully out gassed and gives stable deposition rates over extended periods of time. The deposition rate is calibrated by means of AES as will be described in Chapter 4.

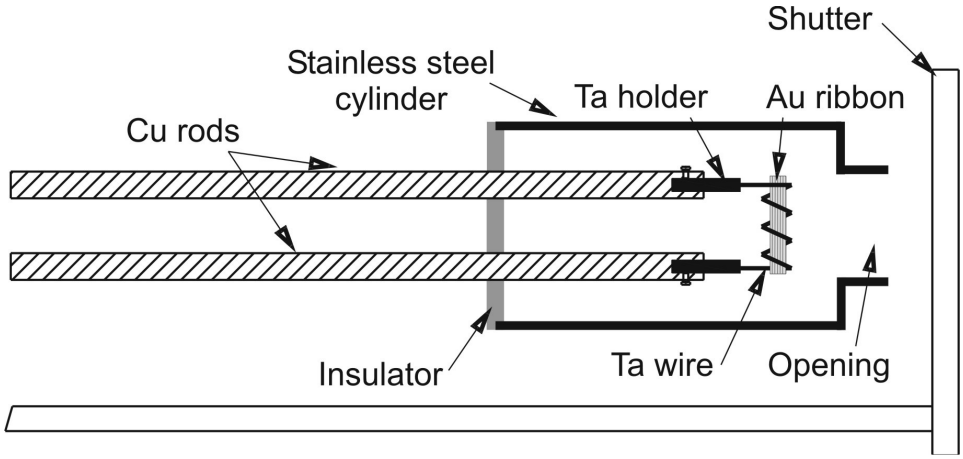

Figure 2.14 Schematic draw of the gold evaporator.

2.3.2 Production of mass-selected Au clusters

Gold clusters are produced by simultaneous sputtering of four Au targets (99.995%) with accelerated xenon ion beams. The xenon ion beams of typically 12 keV kinetic energy and about 2 mA are generated by a modified CORDIS [84] (see Figure 2.15a). The cathode, for primary electron generation, is placed within the extraction chamber and consists of six tantalum filaments, suspended on a tantalum disc. A current of 180 A and a voltage of 6 V is applied to the filaments. The emitted electrons are accelerated toward the anode by a potential difference of 50 V and ionize the Xe atoms on their pathway. Consequently, a plasma is obtained and it is confined in the center of the extraction chamber by means of a magnetic field produced by 18 Co-Sm permanent magnets, which are placed behind the anode. Subsequently, four Xe^+ ion beams are extracted by means of a three element electrostatic lens. Each beam is deflected by an angle of 5° with respect to the symmetry axis of the cluster source and hit a metal target after 450 mm pathway. Due to the sputtering process, positively or negatively cluster ions are produced. The primary cluster ions exhibit a considerable spread in kinetic energy, which is undesirable for further experiments. Therefore, the sputter source is coupled with a first helium filled quadrupole ion guide called the "phase-space-compressor"

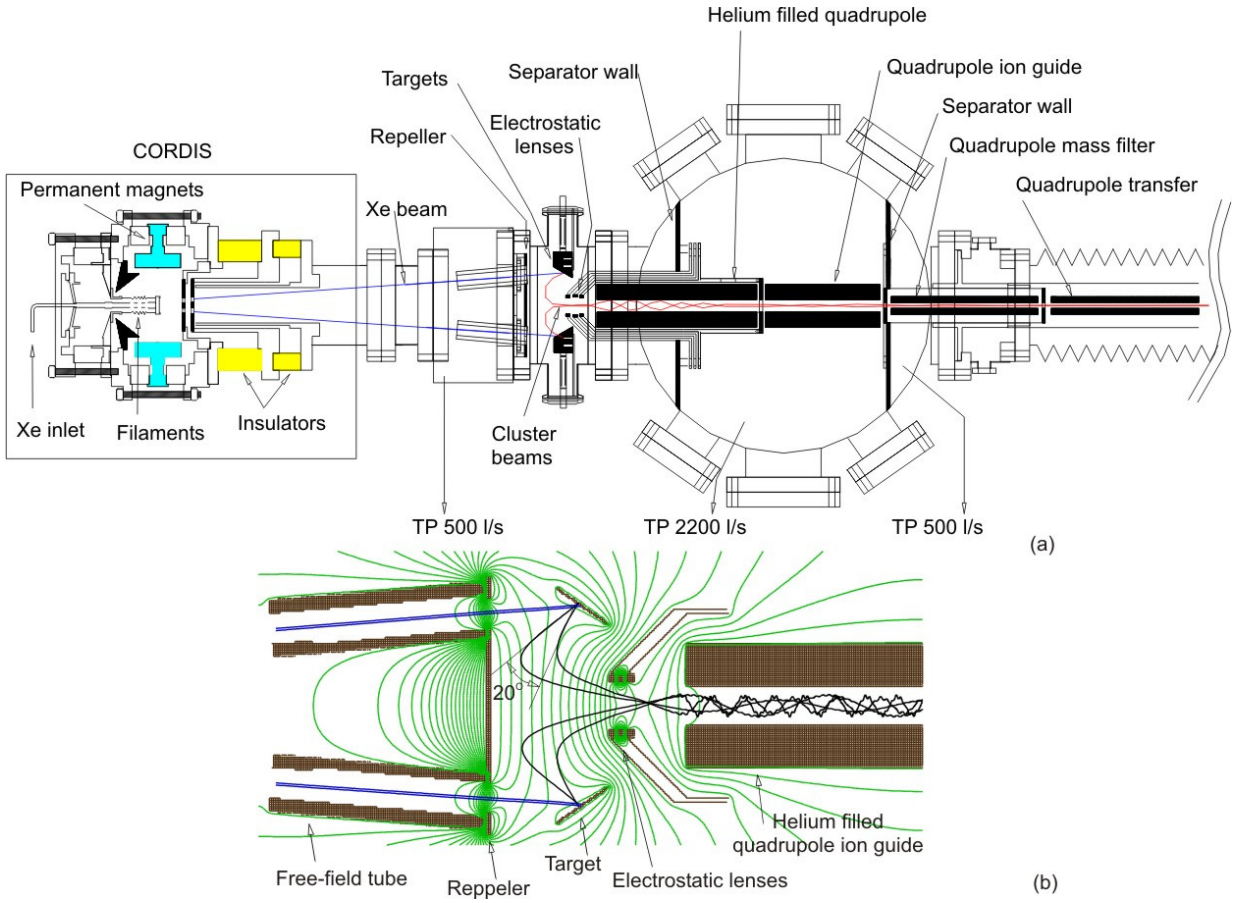

Figure 2.15 (a) Schematic illustration of the cluster source; (b) SimION simulation illustrating a longitudinal cross-section image of the cluster production chamber together with the Xe, and the metal cluster ion trajectories, respectively.

[85-87]. Inside the phase-space-compressor the cluster ions are collimated and thermalized through collisions with helium buffer gas, allowing the generation of clusters with relatively low kinetic energy and a narrow energy spread. Figure 2.15b presents a longitudinal cross-section image of a 3D-SimION[2] simulation of the ion trajectories in the cluster production chamber. The Xe ion beams (blue lines in Figure 2.15b) produced by the CORDIS are guided toward the targets through four field free tubes arranged under a 5° angle with respect to the symmetry axis. Subsequent to the collision of the Xe ions with the targates two positively charged particles starting from each target are simulated (black lines in Figure 2.15b). They have the same mass and the same origin and start under an angle of 20° with respect to each other. The kinetic energy of the particles differs by 5 eV. The ions are subsequently reflected by the potential applied to the repeller plate and are collimated by three electrostatic lenses at the input of the phase-space-compressor. Varying the origin and the starting angle (not shown in the present simulation) a cluster beam with an energy spread larger than 25 eV can be steered into the phase- space-compressor. Note that the trajectories of the ions inside of the phase-space-compressor were calculated without taking into consideration the interaction with the buffer gas. Each collision with He atoms will change the trajectory and will reduce the kinetic energy of the cluster. After thermalization, a kinetic energy spread of less than 2.5 eV is measured in experiment.

The pressure inside the phase-space-compressor is measured directly by a Pirani detector. The highest cluster ion intensity at the narrowest energy distribution was achieved for a helium pressure of 6×10^{-2} mbar. The ion beam is further guided by a quadrupole ion guide, which is free of helium, into a quadrupole mass-filter used to record and to optimize the cluster ion distribution prepared by the sputter source and to select one particular clusters size. Subsequently, the cluster ions are guided by a transfer quadrupole either to the gas-phase experiment or to the surface deposition experiment. In this transfer quadrupole the clusters can be further thermalized by means of collisions with helium buffer gas.

The cluster source is differentially pumped by means of three turbo molecular pumps. The first turbo molecular pump (Pfeiffer 500 l/s) evacuates the region up to the first quadrupole, mostly residual xenon gas. The second and third turbo molecular pump with a pumping capacity of 2200 l/s (Pfeiffer) and 500 l/s (Pfeiffer), respectively, evacuate the mass filter and the transfer quadrupole. If xenon (6.5×10^{-2} mbar) is admitted to the CORDIS and helium (6×10^{-2} mbar) in the phase-space-compressor, the pressure at the exit of the transfer quadruopole is around 5.1×10^{-5} mbar.

Using this cluster source a continuous, positively or negatively charged cluster ion current between few tens of pA and few nA, depending on the cluster size, can be produced.

[2] SimION is a software package primarily used to calculate electric fields and the trajectories of charged particles in those fields when given a configuration of electrodes with voltages and particle initial conditions.

2.4 Laser system

In order to monitor the ultrafast, photoinduced reaction dynamics of methyl halide molecules at the surface and to characterize the surface samples by means of photoelectron spectroscopy, an amplified femtosecond laser system generating ultrashort laser pulses was employed. In Figure 2.16 a schematic representation of the laser system is shown. The femtosecond laser light was produced by a Ti:Sapphire oscillator (Spectra Physics Tsunami) continuously pumped by a 6 W Nd:YVO_4 laser (Spectra Physics Millennia). Pulse amplification was carried out by a Nd:YLF laser (Spectra Physics Empower) pumped Ti:Sapphire amplifier (Spectra Physics Spitfire XP). In order to obtain the appropriate wavelength for each experiment, 60% of the total intensity from the amplifier output is used to seed two optical parametric amplifiers (Spectra Physics OPA 800C). Only one OPA was employed in the present experiment. According to the technical requirements of the OPA, the infrared input beam diameter was reduced by a homebuilt telescope. The rest of the intensity was used for the second and third harmonic generation by means of a homebuilt third harmonic generator (tripler). For pump-probe experiments, a computer controlled delay stage was used to vary the length of the laser beam path, hence to control the delay between the pump and the probe laser pulses.

The wavelength of the laser beams were measured by means of an optical spectrometer (Spectra Physics OSM100). For the measurement of the laser pulse duration, a beam splitter that reflects 1% of the incident intensity was employed to steer the amplified infrared laser pulses into an autocorellator (AC, Spectra Physics PulseScout).

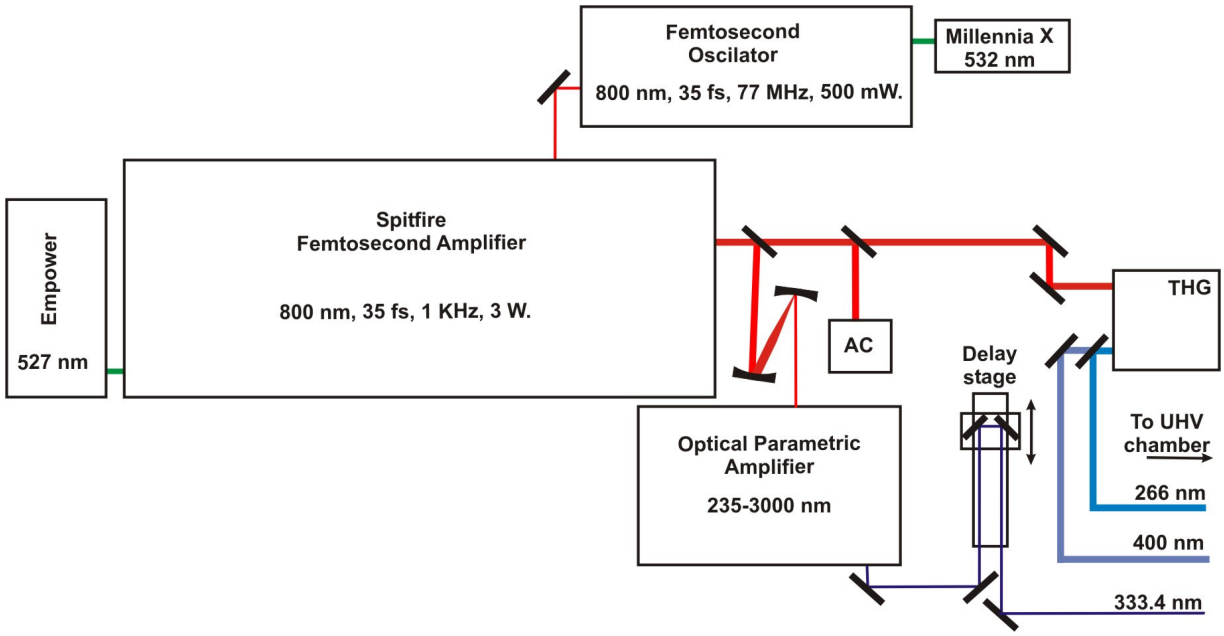

Figure 2.16 Layout of the femtosecond laser system. The wavelengths as well as the most important laser parameters are indicated in the figure.

2.4.1 Ti:Sapphire active medium

Both the femtosecond oscillator and the femtosecond amplifier make use of a Ti:Sapphire crystal as active laser medium. Titanium-doped sapphire (Ti:Sapphire) is a extensively used gain medium for tunable lasers and femtosecond solid-state lasers. The first spectroscopic measurements and the laser performance of Ti:Sapphire were reported by Moulton [88, 89].

The Ti^{3+} ion is responsible for the laser effect of Ti:Sapphire. In the sapphire (Al_2O_3) crystalline environment the electronic ground state of the Ti^{3+} is split into a pair of vibrational broadened levels as shown in Figure 2.17a. The absorption occurs over a broad range of wavelengths from 400 to 600 nm. The fluorescence occurs from the lower vibrational levels of the excited state (^2E_g) to the upper vibrational levels of the ground state ($^2T_{2g}$). The upper state lifetime is about 3 µs [90]. The fluorescence occurs between 600 nm and 1 µm. This makes the Ti:Saphire crystal a suitable material for constructing laser active media to generate broadband femtosecond pulses. The long wavelength side of the absorption band overlaps with the short wavelength end of the emission spectrum. Therefore, the laser action is only possible at wavelengths longer than 660 nm. Additionally, the tuning range is affected by mirror coatings, losses in the laser cavity, pump power, and pump mode quality [91]. In Figure 2.17 the energy level structure of Ti^{3+} in Al_2O_3 crystal field together with the absorption and emission spectra of a Ti:Sapphire crystal are presented.

2.4.2 Femtosecond oscillator

In the femtosecond oscillator an intense pumping laser beam having a Gaussian profile propagates through the Ti:Sapphire crystal. Due to the non-uniform power density distribution of the Gaussian beam, the refractive index of the Ti:Sapphire changes across the beam profile, being larger in the center than at the edge (Kerr lens effect). In the free-running regime, the laser oscillates simultaneously over all the resonance frequencies of the cavity.

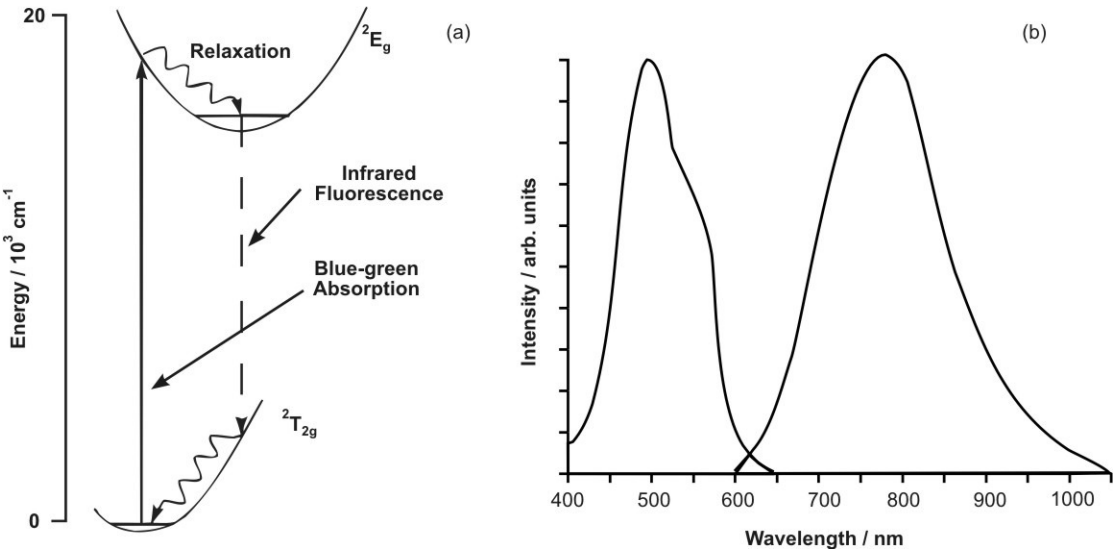

Figure 2.17 (a) Energy level structure and (b) absorption and emission spectra of Ti:Sapphire

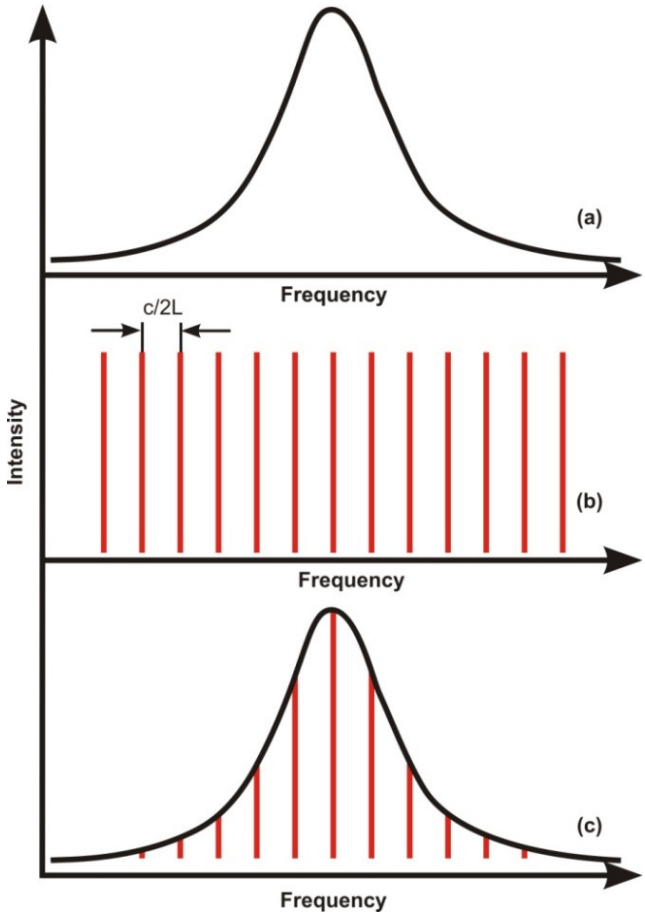

Figure 2.18 The Mode-locking principle. (a) The laser gain; (b) the cavity longitudinal mode structure; (c) the amplified modes.

These frequencies make up the set of the longitudinal modes of the laser. By means of the Kerr-lens effect, the most strongly focused frequencies are further amplified. To lock the laser modes implies to organize the competition between the modes in such a way that the relative phase stays constant. In this way all the waves of different frequencies will interfere constructively at one point, resulting in a very intensive and ultrashort light pulse. The mode-locking occurs due to the Kerr-lens effect induced in a nonlinear medium by the beam itself and the phenomenon is known as Kerr-lens mode-locking.

For a simple plane mirror resonator the allowed modes are those for which the separation distance of the mirrors L is an exact multiple of half the wavelength of the light (Figure 2.18b), such that:

$$\Delta\upsilon = \frac{c}{2L} \tag{2.20}$$

where:

$\Delta\upsilon$ is the frequency separation between two adjacent modes

c is the speed of light

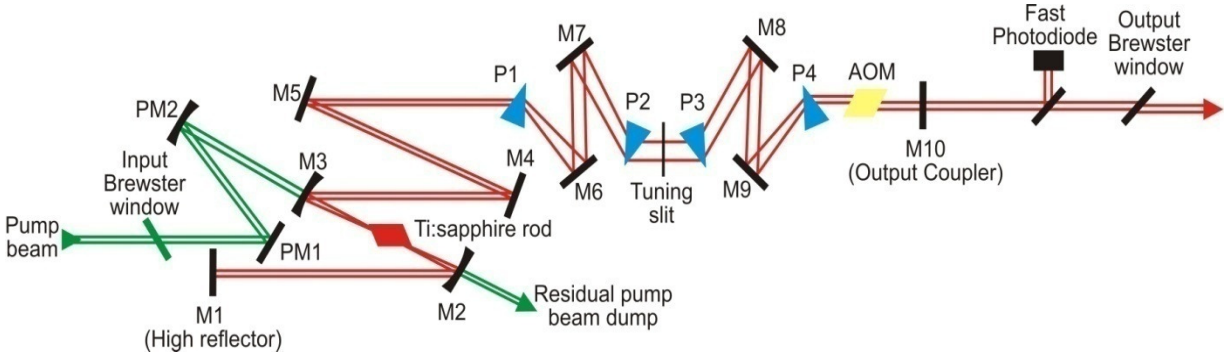

Figure 2.19 Layout of the Ti sapphire femtosecond oscillator. PM1, PM2 pumping mirrors, M1-M10 infrared mirrors, P1-P4 prisms.

The pulses of light produced in mode-locked regime, when the laser modes constructively interfere (see Figure. 2.18c) appear separated by the time interval:

$$\tau = \frac{2L}{c} \tag{2.21}$$

where:

τ is the time taken for light to make exactly one round trip of the laser cavity

The number of modes, which are in the oscillating phase, i.e. the wider the bandwidth, the shorter the laser pulse duration, determines the duration of a laser pulse.

For the initiation of the mode-locking regime, two methods are used: passive mode-locking and active mode-locking. Passive mode-locking is achieved in practice by perturbing a prism inside the laser cavity. Consequently, the modulation of the radiation inside the laser cavity is automatically synchronized to the cavity round trip frequency. For active mode-locking, as in the present experiment, a standing wave AOM is introduced in the laser cavity and is controlled from an external rf signal. The AOM modulates the modes at a frequency close to the intermode frequency interval. Consequently, a coupling between each mode and the sidebands created by the modulation of its neighboring modes is realized. The phase of the modes can than be locked onto each other.

The Millennia VI laser employed in the present experiment for the pumping of the femtosecond oscillator works as follows. A diode laser is used to end-pump a neodymium doped yttrium vanadate (Nd:YVO_4) active medium. The resulting 1064 nm output is converted to 532 nm (maximum 6 W) through frequency doubling in a temperature tuned lithium triborate (LBO) nonlinear crystal.

The optical path in the femtosecond oscillator is presented in Figure 2.19. For the compensation of the positive GVD in the oscillator, four prisms are employed. The fast photodiode is used to record the repetition rate of the laser, which is subsequently used to control the AOM. The output wavelength can be adjusted by means of the tuning slit.

The typical output parameters of the femtosecond oscillator are:

Wavelength:	800 nm
Bandwidth:	60 nm
Pulse duration :	35 fs
Repetition rate:	77 MHz
Power:	500 mW

2.4.3 Pulse amplification

The amplification of femtosecond laser pulses is realized again with a Ti:Sapphire crystal. During the propagation of an intense laser beam through a Ti:Sapphire crystal non-linear processes such as self-focusing occur. Thus, permanent damage of the gain medium can happen. Consequently, for the amplification of femtosecond laser pulses it is necessary to limit the peak power of a pulse in the Ti:Sapphire crystal to less than 10 GW/cm^2 [92]. The CPA technique allows a Ti:Sapphire crystal to amplify pulses beyond this peak power, while keeping the power density in the amplifier below the damage threshold of the crystal. In Figure 2.20 the CPA technique is schematically represented. For CPA realization, the laser pulse which has to be amplified is stretched out in time prior to introducing it into the gain medium using a pulse stretcher. After the stretching process the laser pulse becomes positively chirped, that is, the high-frequency component lags behind the low frequency component, and has a longer duration than the original pulse by a factor of 10^3 to 10^5. Then the stretched pulse, whose intensity is sufficiently low with respect to the damage threshold of the gain medium, is amplified. For the amplification a pump laser provides a synchronous energy pulse to the Ti:Sapphire crystal to excite it just prior to the arrival of the stretched seed pulse. The seed pulse produces the stimulated emission, which amplifies the pulse by a factor of 10^6 or more. Finally, the amplified laser pulse is recompressed back to the original pulse width.

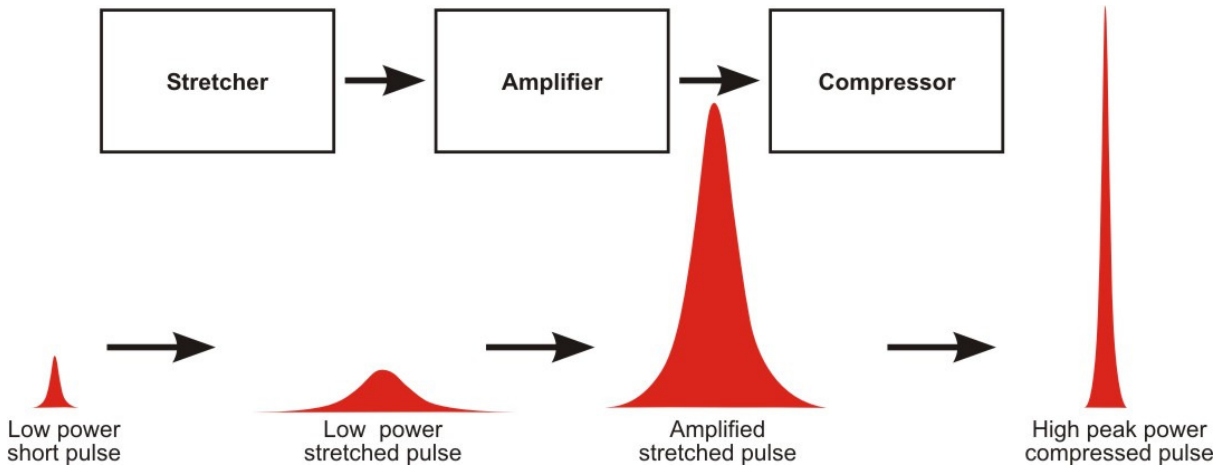

Figure 2.20 Chirped pulse amplification technique.

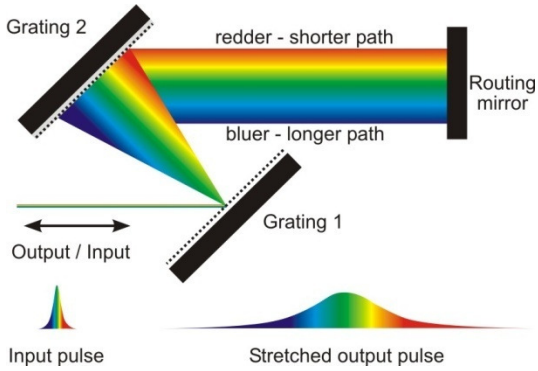

Figure 2.21 Principle of a pulse stretching using positive GVD.

For the stretching or compression of a laser pulse a diffraction grating or a pair of diffraction gratings are used. By means of a diffraction grating, the wavelength components of a laser pulse are spatially separated (dispersion). In a stretcher the grating and the routing mirror can be chosen so that the bluer frequency components of the spectrum travel farther than the redder components, causing the redder frequency components to exit the stretcher first. In the compressor, the spatially spread beam is flipped so that the redder components have to take the long path, thereby allowing the bluer frequency to catch up. In Figure 2.21 a scheme of a pulse stretcher is presented. The same optical components can be used to compress a laser pulse.

The laser pulse amplification in the present setup is realized by means of a regenerative amplification technique. This implies the trapping of a laser pulse in the laser cavity until it reaches the highest intensity. Using a Pockels cell and a broad band polarizer the trapping and dumping of a laser pulse is achieved. The Pockels cell consists of a birefringent crystal, which changes the polarization of the light passing through when a high voltage is applied to it. The Pockels cell is initially set to be equivalent to a quarter wave plate. When a pulse is in the resonator, the voltage on the Pockels cell is switched so that it becomes equivalent to a half-wave plate. The pulse stays in the cavity until it reaches the saturation, and a second voltage step is applied to the Pockels cell to extract the pulse from the resonator. In Figure 2.22 the optical paths in the Spitfire regenerative amplifier are presented. The pulse stretcher, the regenerative amplifier and the pulse compressor are marked in the figure. For the selection of one laser pulse from the MHz seed train at the 1 kHz repetition rate of the pump laser an extra-cavity Pockels cell is employed. The pumping of the amplifier is achieved by the second harmonic (527 nm, up to 20 mJ) of a nanosecond, Q-switched neodymium-doped lithium yttrium fluoride (Nd:YLF) laser (Empower in Figure 2.16).

The typical output parameters of the amplifier are:

Wavelength:	800 nm
Bandwidth:	60 nm
Pulse duration :	35 fs
Repetition rate:	1 KHz
Power:	3.5 W

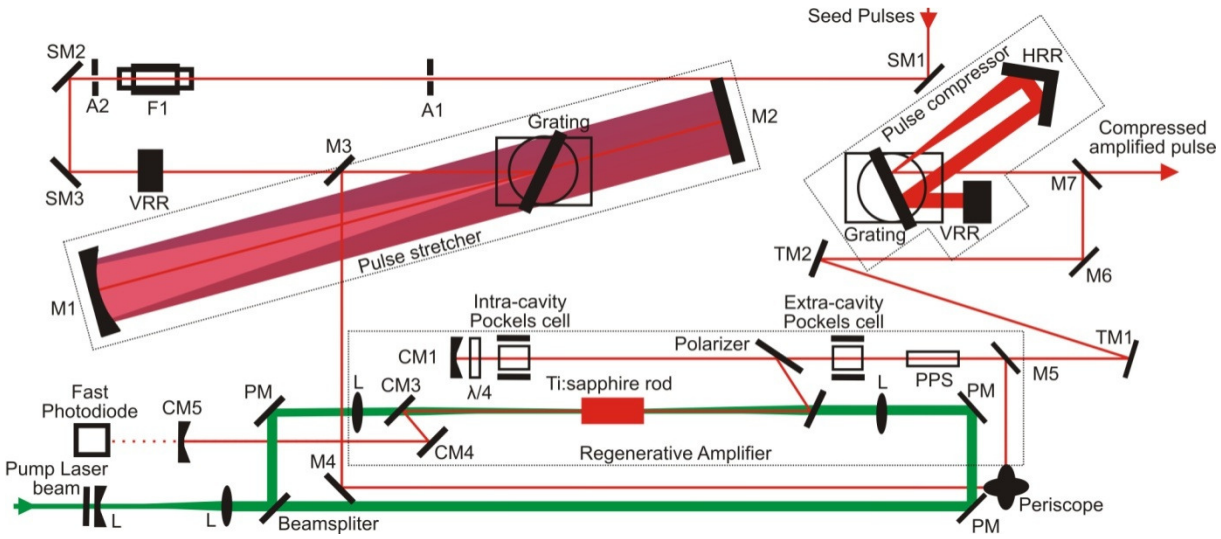

Figure 2.22 The optical paths in the regenerative amplifier (A-apertures, SM-seed beam mirrors, M-mirrors, CM-cavity mirrors, PM-pump beam mirrors, TM-telescope mirrors, PPS-polarizer, L-lenses, HRR and VRR-stretcher/compressor mirrors).

2.4.4 Wavelength conversion

In order to obtain the appropriate wavelengths required for the time-resolved photoinduced chemical reaction of supported methyl halide molecules a homebuilt third harmonic generator (tripler) and an OPA are employed.

For THG, the fundamental wavelength is split in two beams where one arm is doubled (SHG) in a 0.3 mm thin BBO type I crystal with a diameter of 10 mm and the cutting gle $\theta = 29.2°$. In the doubling crystal two photons with the same frequency can be effectively "combined" and give rise to a single photon with twice the frequency and half the wavelength of the initial photons. In type I crystals the two mixing photons should have the same polarization, whereas in type II crystals the photons to be mixed should be orthogonally polarized. The second harmonic conversion efficiency grows linearly with increasing pump intensity, so that the frequency doubled wave intensity grows with the square of the pump intensity. In our experiment the second harmonic conversion efficiency is about 40%. For THG production a second 0.3 mm thin BBO type I crystal with a diameter of 10 mm and the cutting gle $\theta = 44.3°$ is employed. The frequency tripling is realized by mixing the original pump wave and the frequency doubled part of it in the second BBO crystal (SFM). The THG efficiency could reach up to 10 % of the initial pumping beam. In Figure 2.23 the third harmonic generator is represented schematically. An 800 nm laser beam enters into the tripler. Dichroic mirrors (DM1 - DM3) separate/combine the laser beams of different wavelengths. After BBO1 the 400 nm laser beam has the polarization orthogonal on the polarization of the 800 nm laser beam. A half-wave plate rotates the polarization of the 800 nm laser beam prior to the THG in the BBO2 (type I). The temporal overlap of the 400 nm and the 800 nm laser pulses prior to THG is achieved by a mechanical delay stage. A fast photodiode mounted inside of the tripler produce the trigger pulse in the experiments employing time-of-flight spectrometry.

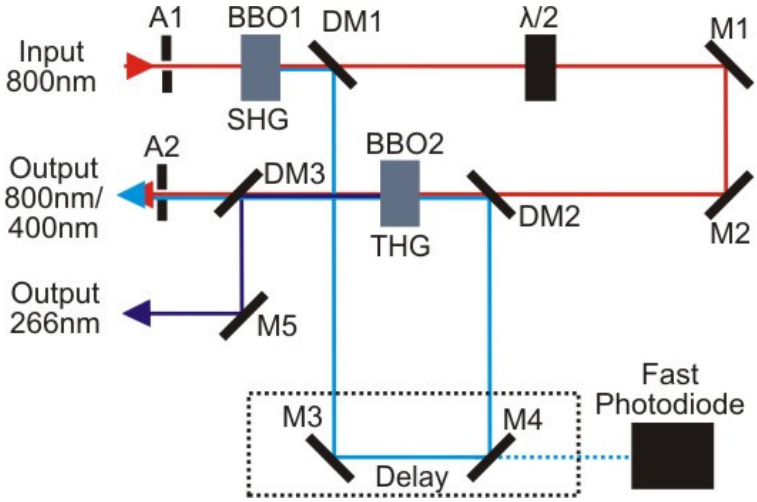

Figure 2.23 Diagram of the homebuilt third harmonic generator employed for the production of the pump laser pulses (see text for more details).

The typical output parameters of the tripler are:

Wavelength:	266 nm
Bandwidth:	1.5 nm
Pulse duration :	70 fs
Repetition rate:	1 kHz
Power:	up to 10% of the pump beam

The OPA employed in this work has the capability to convert the fundamental Ti:Sapphire output to light with a wavelength ranging from 250 nm to 3 µm by means of white light continuum generation and optical parametric amplification. In contrast to SHG, in parametric generation a photon having the frequency ω_P (pump) splits to produce two photons, one with the frequency ω_S (signal) and one with the frequency ω_I (idler). Energy conservation determines the generated frequency or wavelength, i.e., [93]

$$\omega_P = \omega_S + \omega_I \tag{2.22}$$

or

$$\frac{1}{\lambda_P} = \frac{1}{\lambda_S} + \frac{1}{\lambda_I}. \tag{2.23}$$

Efficient conversion requires the best phase match conditions:

$$\Delta\mathbf{k} \equiv \mathbf{k}_P - \mathbf{k}_S - \mathbf{k}_I = 0 \tag{2.24}$$

or

$$\frac{n_P}{\lambda_P} = \frac{n_s}{\lambda_S} + \frac{n_i}{\lambda_I}, \tag{2.25}$$

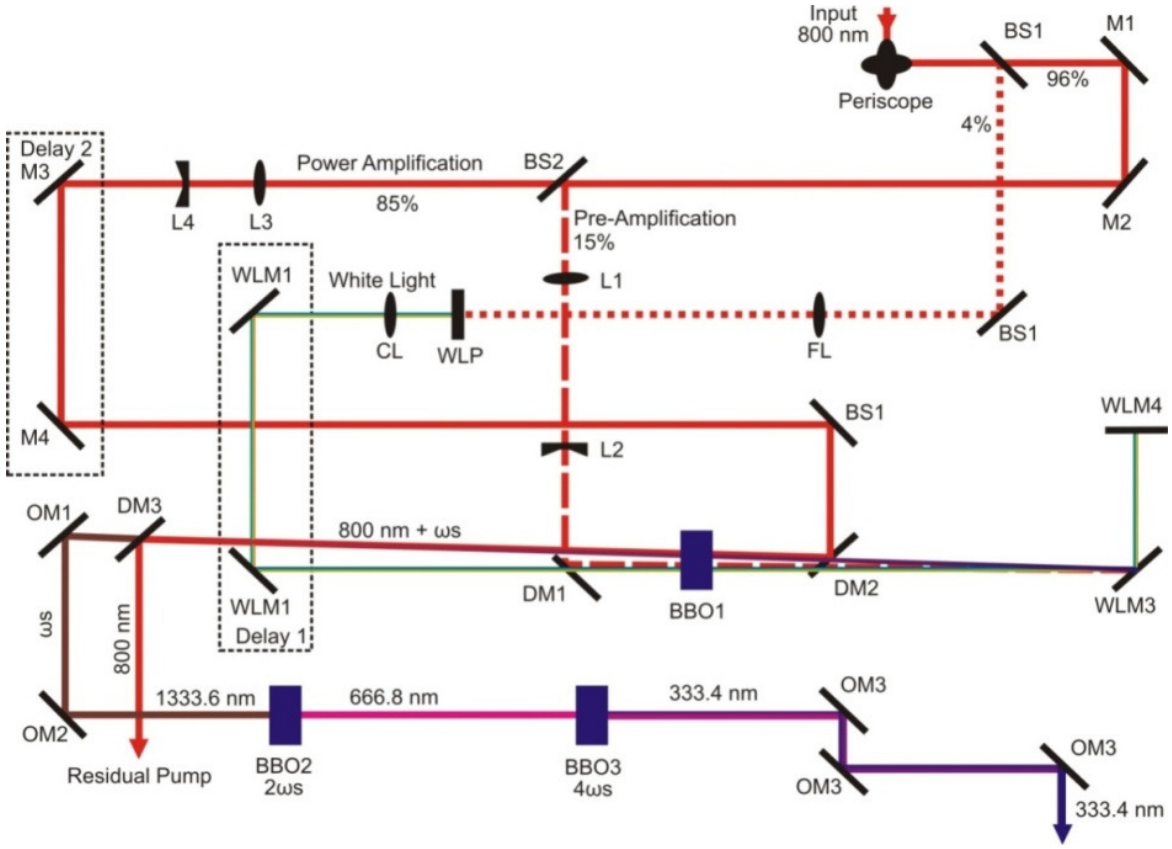

Figure 2.24 Schema of the optical parametric amplifier employed for the production of the probe pulses. Notations: BS-beam splitter, M-mirror, WLM-white light mirror, DM-dicroic mirror, OM-output mirror, L-lens, WLL-white light lens.

where: n_P, n_s, n_i are the refractive indexes of the nonlinear crystal for each wavelength and $\mathbf{k}_P$, $\mathbf{k}_S$, $\mathbf{k}_I$ are the wave vectors of each beam. By changing the crystal angle, n_P, n_s, n_i and $\mathbf{k}_P$, $\mathbf{k}_S$, $\mathbf{k}_I$ are changed and consequently the wavelength can be tuned.

The amplification of the signal or idler intensity is realized through the interaction of one of these beams (seed beam) with the fundamental of the Ti:Saphire in a type I BBO crystal. Figure 2.24 shows the optical path in the OPA configured to produce the wavelength of 333.4 nm, which is employed for the ionization of the methyl radicals (by means of (2+1) REMPI). A first beam splitter (BS1) separates 4% from the total intensity from the 800 nm input beam to produce the seed beam through white light generation into a sapphire plate (white light plate - WLP). The remaining intensity (96%) is split again (BS2) in two beams used for the pre-amplification (15%) and amplification (85%) of the seed beam inside BBO1 crystal. Two mechanical delay stages accomplish the temporal overlap of the seed, pre- and final amplification laser pulses in the BBO1. The BBO1 is positioned to amplify the signal wave at 1333.6 nm. Subsequent to the separation from the pump beam by dicroic mirrors, the signal wave beam is doubled in the BBO2 crystal to produce 666.8 nm. This beam is doubled again in the BBO3 crystal to produce 333.4 nm, which is separated from the other wavelengths by using appropriately coated mirrors. The output power of the OPA depends on the

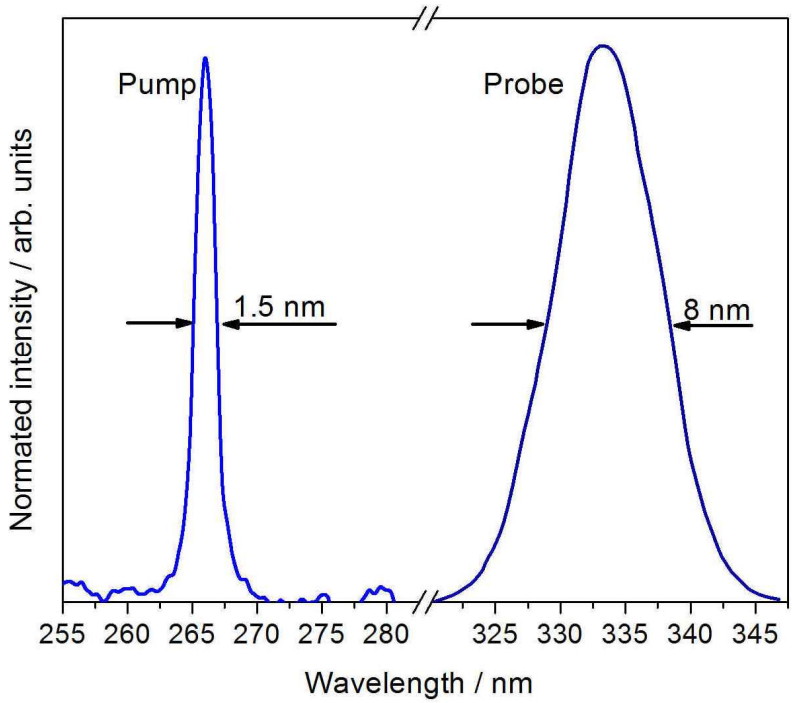

Figure 2.25 Output spectra of the pump and probe laser beams.

output wavelength, input power and pulse duration. The typical parameters of the OPA tuned to 333.4 nm are:

Wavelength:	input: 800 nm	output: 333.4 nm
Bandwidth:	input: 55 nm	output: 8 nm
Pulse duration :	input: 50 fs	output: 70 fs
Repetition rate:	input: 1 KHz	output: 1 kHz
Power:	input: 650 mW	output: 6 mW

2.4.5 Pulse characterization

2.4.5.1 Spectral measurements

The central wavelength as well as the bandwidth of the employed laser pulses were determined by means of a commercial optical spectrometer (Newport OSM100). The light to be analyzed was directed into the spectrometer housing box by an optical fiber. It is spectrally decomposed by a diffraction grating (600 Lines/cm). The light spectrum is detected by a linear CCD detector and visualized on a computer. The spectrometer has a spectral window from 250 to 850 nm, and a resolution of 0.3 nm. In Figure 2.25 the output wavelength spectra of the pump and the probe laser beams employed in the present investigation are shown.

2.4.5.2 Pulse temporal profile

In order to measure the time duration of the femtosecond laser pulses the autocorrelation technique was employed. In Figure 2.26 a schematic representation of an autocorrelator is

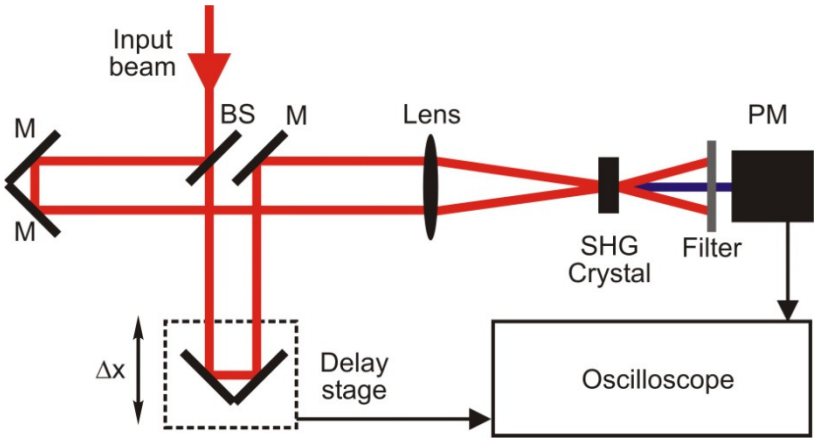

Figure 2.26 Schematic illustration of the autocorrelator. Notations: M-Mirror, BS-beam splitter, PM-photomultiplier.

presented. The incoming femtosecond laser beam (cf. red line in Figure 2.26) is split in two beams of identical intensity. On one arm an adjustable optical delay stage is used. Similar to a Michelson interferometer the beams are recombined into a BBO crystal for second harmonic generation. The intensity of the SHG beam (cf. blue line in Figure 2.27) is proportional to the pulse overlap within the crystal.

The intensity of the SHG signal, measured as a function of the delay time Δt between the pulses, produces a correlation function, which depends on the width of the incoming pulses $\Delta\nu$. If the incoming waves have the intensities $I(t)$ and $I(t-\tau)$, then the autocorrelation function is:

$$A(\tau) = \int_{-\infty}^{\infty} I(t)I(t-\tau)\,dt \tag{2.26}$$

The relation between the pulse width $\Delta\nu$ and the autocorrelation width $\Delta\tau_A$ depends on the shape of the pulse as shown in Table 2.1

Shape	I (t)	$\Delta\nu\cdot\Delta t$
Gausian	$\exp(-(4\ln 2)t^2/\Delta t^2)$	0.441
Hyperbolic secant	$\mathrm{sech}^2(1.76/\Delta t)$	0.315
Lorentian	$1/(1+2t/\Delta t)^2$	0.221
Exponential	$\exp(-(\ln 2)t/\Delta t)$, $(t \geq 0)$	0.11

Table 2.1 Autocorrelation width and spectral bandwidth for various pulse shapes take from [94]. Δν and Δt are FWHM quantities.

3 Surface fs pump-probe mass spectrometry

Time-of-flight mass spectrometry in conjunction with femtosecond-laser resonance enhanced multiphoton ionization is used here for the first time in a new approach to monitor the ultrafast chemical reaction dynamics of supported molecules. The mass-resolved investigation of different reaction pathways is accomplished by direct real-time monitoring of the different reaction products and intermediates as well as their relative kinetic energy content. In contrast to other surface femtochemistry approaches such as two pulse correlation [18-20], sum frequency generation [21, 22], and two-photon photoemission [23-27], the present experiment is clocking the surface reaction dynamics by direct detection of reaction intermediates and products through multiphoton ionization at the surface.

This chapter gives a detailed account of the experimental arrangement and of the novel technique employed to monitor the methyl halide reaction dynamics at the surface.

3.1 Time-of-flight mass spectrometry: General aspects

Time-of-flight mass spectrometry is an analytical tool in which ions are separated by an electric field according to their mass-to-charge ratio. The simplest TOF spectrometer consists of an ion source and a detector located at the opposite end of a field free drift region. In a TOF-MS bunches of ions are accelerated by a static electric field of known strength. Consequently, an ion acquires the same kinetic energy as any other ion with the same charge starting at the same location with similar initial kinetic energy. The resulting velocity of the ions after exiting the acceleration field depends on the mass-to-charge ratio. Therefore, the time-of-flight of an ion that needs to pass the accelerating field and the subsequent field free drift region to reach the detector situated at a well defined distance depends also on the mass-to-charge ratio (light ions reach higher velocities than the heavier ions).

When an ion is accelerated in an electric field, its potential energy E_{pot} is converted to kinetic energy E_{kin}

$$\begin{aligned} E_{pot} &= E_{kin} \\ qU &= \frac{1}{2}mv^2 \end{aligned} \tag{3.1}$$

where:

q is the charge
U is accelerating voltage
m is the ion mass
v is the ion velocity

The velocity of the ion after acceleration will be constant since it moves in a field free region. Measuring the time-of-flight t and knowing the length of the drift tube D the velocity of the ion v, can be calculated as follow:

$$v = \sqrt{\frac{2qU}{m}} = \sqrt{\frac{2qEs}{m}} \tag{3.2}$$

where

E is the electric field strength
s is the length of the acceleration field

Consequently the relation between the time-of-flight and the mass can be deduced (using v = D/t):

$$t = D\sqrt{\frac{m}{2qU}} \tag{3.3}$$

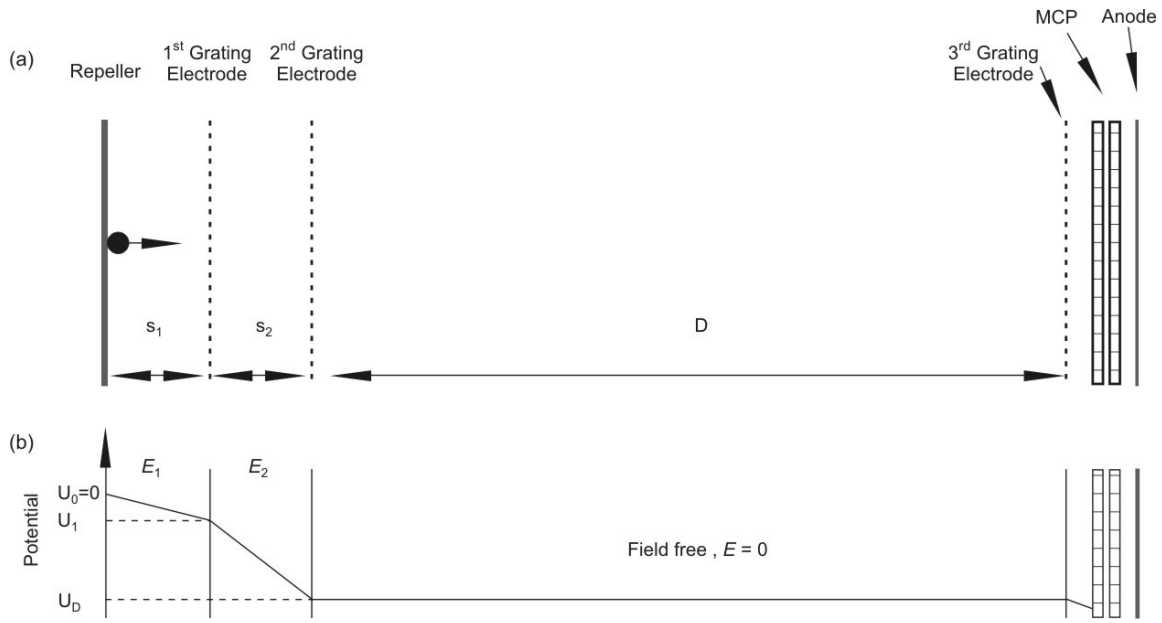

Figure 3.1 (a) Schematic representation of a linear time-of-flight mass spectrometer with two acceleration regions. (b) The magnitude of the electric fields in the time-of-flight mass spectrometer.

Equation (3.3) reveals that the time-of-flight of an ion varies with the square root of its mass-to-charge ratio.

In the present work, a homebuilt [95] Wiley/McLaren-type time-of-flight mass spectrometer [96] with two accelerating fields is employed. This type of TOF-MS has superior ability to resolve masses despite an initial spatial distribution of the ions (space resolution) and can reduce the time spread introduced by the initial kinetic energy distribution (energy resolution).

In Figure 3.1 a schematical drawing of a Wiley/McLaren-type TOF-MS with two accelerating regions is presented. The ions are thought to be generated directly at the repeller electrode. In the example of Figure 3.1, a bias voltage U_1 is applied to the first spectrometer electrode and creates a static electric field E_1 (first acceleration region) between the grounded repeller and this first spectrometer electrode. A second acceleration of the ions is accomplished by the voltage U_D applied to the second electrode and to the field free drift region itself. E_2 represents the electric field strength in the second acceleration region. In the end, the ions pass the field free drift region and are detected according to their mass to charge ratio and to their initial kinetic energy.

The total time-of-flight of an ion in the mass spectrometer is a sum of the flight time in the first acceleration region t_1 in the second acceleration region t_2 and in the drift tube t_D:

$$t(s) = t_1 + t_2 + t_D. \tag{3.4}$$

The flight time in the first acceleration region can be obtained by integrating the equation (3.2):

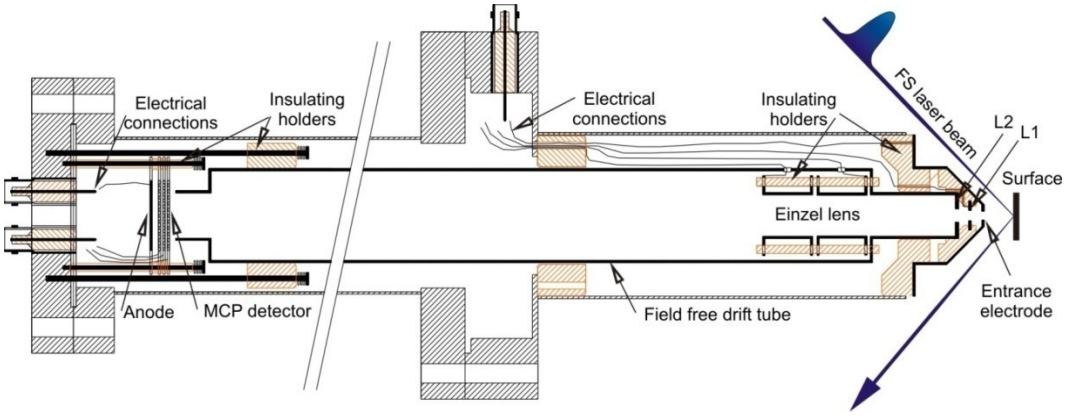

Figure 3.2 Schematic drawing of the Wiley-McLaren type time-of flight mass spectrometer.

$$t_1 = 2s_1\sqrt{\frac{m}{2qE_1s_1}}, \tag{3.5}$$

were $\sqrt{m/(2qE_1s_1)} = 1/v_1$ and v_1 represents the velocity of the ions after the first acceleration region. The velocity of the ions after the second acceleration region can be calculated from their kinetic energy ($E_1s_1 + E_2s_2$):

$$v_2 = v_D = \sqrt{2q/m(E_1s_1 + E_2s_2)} \tag{3.6}$$

Because E_1 is a homogenous electric field, the time-of-flight of the ions in the second acceleration region can be calculated using the mean velocity $(v_1+v_2)/2$ [95]:

$$t_2 = \sqrt{\frac{m}{2q}}\left(\frac{2s_2}{\sqrt{E_1s_1 + E_2s_2} + \sqrt{E_1s_1}}\right) \tag{3.7}$$

The time-of-flight in the drift tube up to the detector is calculated from equation (3.6):

$$t_D = \sqrt{\frac{m}{2q}}\left(\frac{D}{\sqrt{E_1s_1 + E_2s_2}}\right) \tag{3.8}$$

In Figure 3.2 a schematic drawing of the TOF-MS employed in the present work is presented. On the surface, subsequent to a photoinduced reaction, the intermediates and the final products are ionized by a laser pulse (ionization region). The first accelerating voltage U_1 is applied to the entrance electrode. Between the entrance electrode and the second accelerating electrode (L2) an electrostatic lens (L1) is used to homogenize the second accelerating field. The einzel lens is used for a supplementary collimation of the ions. The ion bunches are amplified and transformed into an electric signal by means of two micro-channel plates situated at the end of the drift tube. The output signal from the TOF-MS is analyzed either by means of a 500 MHz oscilloscope (LECROY 9350CL) or by the MCS electronics (FAST P7887).

3.2 SFsMS: Experimental realization

In order to monitor the ultrafast chemical reaction dynamics of supported molecules, a novel experimental procedure was employed. In Figure 3.3 its experimental realization is schematically illustrated. The TOF-MS was employed to measure the mass and the relative kinetic energy content of the reaction products. The grounded support surface was positioned perpendicular to the spectrometer axis. The distance between the surface sample and the first spectrometer electrode was 8 mm. The accelerating voltage U_1 applied to the first TOF-MS electrode (see the insert in Figure 4.1) was adjusted either to improve the mass- or the energy-resolution of the spectrometer. The pump and probe laser beams were combined by means of a dichroic mirror and subsequently are directed onto the surface. The two laser beams collinearly irradiated the surface, slightly focused, at an angle of approximately 45°. The output signal from a photodiode was used to trigger the MCS electronics. A mechanical shutter blade was used to control the surface irradiation by the laser light. Methyl halide molecules were dosed onto the surface by means of a computer controlled, UHV compatible pulsed magnetic

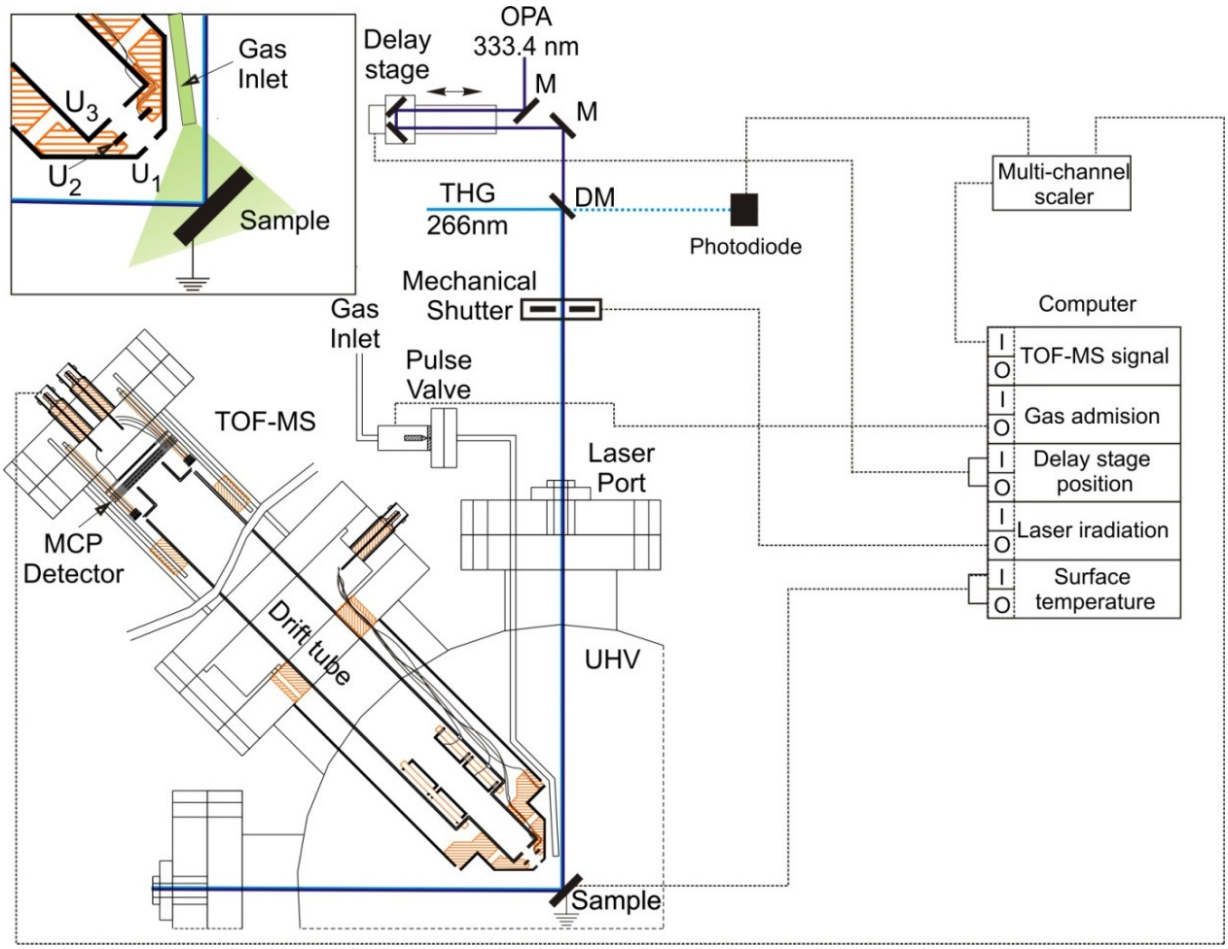

Figure 3.3 Schematic representation of the experimental arrangement used for the investigation of ultrafast surface reactions (see text for more details). The inset shows a magnified view of the TOF-MS head presenting the potentials applied to the electrodes.

valve (General Valve Series 99) that is connected to a stainless steel tube (4 mm inner diameter). The distance between the end of this tube and the sample surface was 20 mm. The control of the gas admission, the delay stage position, the laser irradiation, and the surface heating current was accomplished by means of a self-written software developed in the LabVIEW environment running on a personal computer. Simultaneously, using the same software, the surface temperature and the data from TOF-MS were acquired. A block schema illustrating the input and output functions of the PC-LabView software is also presented in Figure 3.3.

3.3 Molecular adlayer preparation

The methyl halide molecules CH_3I, CD_3I, and CH_3Br, (all Sigma-Aldrich >99.5%) were investigated. Methyl iodide and methyl bromide were transferred into a UHV compatible, homebuilt, stainless steel cylinder and were additionally purified by several freeze-pump-thaw cycles. The methyl halide molecules were dosed onto the surface by means of the pulsed valve connected to the stainless steel tube as shown in Figure 3.3. In this way, a well defined quantity of molecules could be dosed onto the surface in a very short time because, locally, in the vicinity of the tube, the pressure was higher during the molecule admission compared to the rest of the UHV chamber. As a consequence, the pumping of the non-adsorbed molecules after the molecule admission was achieved within a few seconds for doses reported in the present work.

The calibration of the pulsed valve was accomplished by means of TPD. In the calibration procedure, the surface sample was first positioned about 30 cm lower in the UHV chamber with respect to the molecule admission tube. Operating the pulsed valve at a constant frequency for a certain time period, a well defined partial pressure of molecules was established in the UHV chamber. By varying this admission time period, different coverages of molecules were dosed onto the surface. The molecule deposition on the MgO/Mo(100) film was performed with the substrate held at 90 K. For every preparation a TPD spectrum was recorded.

In the second step of the pulsed valve calibration procedure, the surface was positioned to record TOF mass spectra. A distinct quantity of molecules (defined by the pulsed valve opening time and the number of gas pulses) was dosed onto the MgO/Mo(100) film at 90 K. Subsequently, a TPD spectrum was recorded and the integrated area as well as the temperature of maximum desorption intensity are compared with the previously recorded TPD spectra obtained in the first step. In this way, the pulsed valve parameters were obtained that correspond to the desired surface coverage. Typically, coverages of 0.25 ML methyl iodide were achieved by 50 pulses at 20 Hz with an opening time of 600 μs. For this coverage a pressure of about 4×10^{-9} mbar was usually detected by the ion gauge.

3.4 Fs-laser excitation and ionization of molecules at the surface

In surface photochemistry investigations, the important light parameters are wavelength, intensity and polarization. In time-resolved photochemical studies, the duration of the laser pulses define the temporal resolution of the experiment. These parameters can be varied in the experiment and their role will be discussed in the following.

3.4.1 Wavelength

The energy of a photon is defined by:

$$\epsilon = h\nu \tag{3.9}$$

where:

h is the Plank constant[3] and

ν is the light frequency ($\nu = c/\lambda$).

The energy of the light is an essential variable, which sets limits on energetically allowed processes. The transition rate (probability of transition per unit time) for a single particle is described by Fermi`s Golden rule:

$$\mathcal{R}_{12} = \frac{\pi e}{mh\nu} |\langle f|\mathbf{E}\boldsymbol{\mu}|i\rangle|^2 \delta \tag{3.10}$$

where:

m is the mass of the electron,

e is the charge of the electron.

i, f are the initial and the final states,

E is the electric field vector,

μ is the transition dipole momentum,

δ is the density of the final states

$\langle f|\mathbf{E}\boldsymbol{\mu}|i\rangle$ is the matrix element of the perturbation **Eμ** between the final and initial states

The Fermi`s Golden rule will be used in this chapter to describe the direct molecular photodissociation.

As already explained, a first laser pulse is employed to dissociate the adsorbed methyl halide molecules; subsequently, a second laser pulse detects the reaction products by ionization at the surface. For the dissociation step two pathways are assumed here:

(i) direct photodissociation, when the light excites strictly the adsorbed molecule or molecule-substrate complex, leading to non-thermal chemical change;

(ii) substrate excitation, when the photon is adsorbed by the substrate and the resulting excited electrons or holes (hot carriers) induce non-thermal adsorbate chemistry.

[3] $h = 4.13566733\times10^{-15}$ eV·s

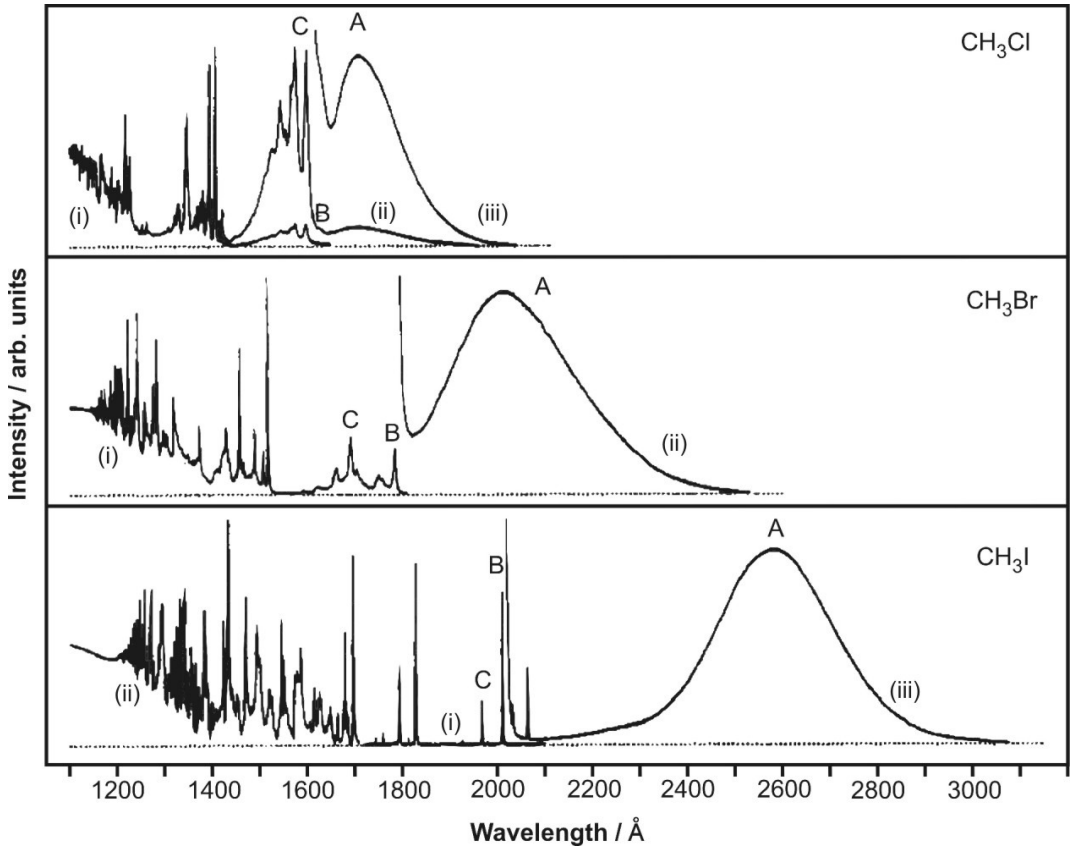

Figure 3.4 Electronic absorption spectra of the free methyl halide molecules in the 1050 - 3100 Å spectral region taken from reference [97]. For CH_3Cl the pressures in the absorption cell were: (i) 35 pmHg, (ii) 515 pmHg, and (iii) 5.76 mmHg. For CH_3Br the pressures were: (i) 27 pmHg and (ii) 8.3 mmHg. For CH_3I the pressures were (i) 5.3 pmHg,(ii) 16.5 pmHg, and (iii) 5.0 mmHg. The dashed line in each spectrum is the base line. The capital letters mark the A-band and the lowest energy s-Rydberg states B and C.

In Figure 3.4 the adsorption spectra of free CH_3X (X=Cl, Br, I) molecules in the 1050-3100 Å spectral range are presented. For a direct photodissociation of the methyl halide molecules the excitation of the A-band (indicated by A in Figure 3.4) is required. The heavier the halogen atom mass the lower the methyl halide dissociative A-band energy. According to the gas-phase data (Figure 3.4), at 266 nm just CH_3I can be directly photodissociated on the surface by means of single photon adsorption. However, the presence of a metallic substrate might induce perturbations of the electronic structure of the ground- and the excited-states of the adsorbates. This is valid even when the adsorbate is weakly bound directly to a metallic surface or to a thin insulating layer deposited on a metallic substrate, i.e. magnesia thin films on Mo(100). As a consequence, transitions in adsorbate molecules have been observed to be broadened by 0.1 - 1 eV and they might be either blue-shifted or red-shifted with respect to their gas-phase energy [98-101]. In this case, the equation (3.10) has limited applicability. Besides the electronic perturbation of the adsorbates, a metallic support surface can induce

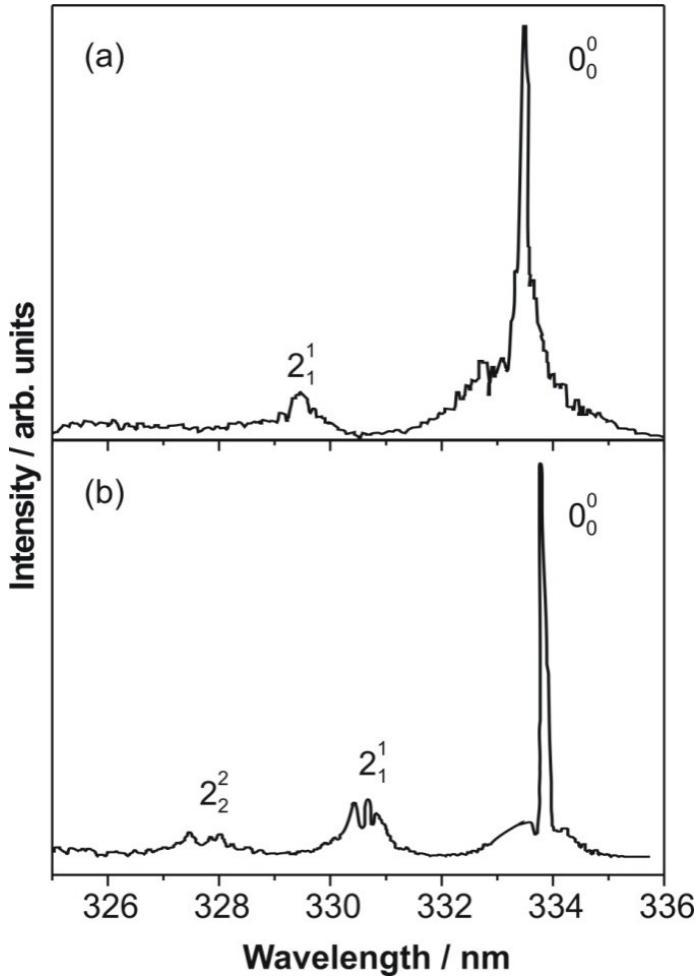

Figure 3.5 Gas-phase (2+1) REMPI spectra of: (a) CH_3; and (b) CD_3. Adapted from Hudgens et al. [102].

new electronic states that could be involved in UV adsorption [103]. Excitation involving these new electronic states leads to a wavelength response quite different from the gas-phase.

If a chemical reaction is promoted by means of surface excitation as expected in the case of the adsorbates on a metal surface, three distinct processes occur:

(i) photo-excitation of the electrons in the bulk substrate;

(ii) migration of the hot carriers to the surface;

(iii) attachment of the hot carriers to the adsorbates accompanied by formation of excited adsorbate states.

The attachment rate is established by the energy of the adsorbate orbitals, the energy of the excited electrons or holes and by the tunneling barrier.

Also for the ionization of the reaction products specific wavelength are required. The methyl detection is achieved by means of (2+1) REMPI at 333.4 nm (CH_3I) and 333.9 nm (CD_3I). Figure 3.5 shows the gas-phase (2+1) REMPI spectra of both CH_3 and CD_3 radicals. Details concerning the REMPI of the methyl fragments are presented in Section 3.4.3.2. Other

reaction products were also detected with 333.4 nm light by multiphoton non-resonant ionization.

3.4.2 Polarization

In classical electrodynamics the light is defined as an electromagnetic plane wave with orthogonal electric and magnetic field vectors perpendicular to the propagation direction. In a non adsorbing medium the instantaneous value of the electric field vector is given by the time dependent solution of Maxwell`s equation as:

$$\mathbf{E} = \mathbf{E}^0 e^{i(\omega t - \frac{2\pi n}{\lambda}\mathbf{s}\cdot\mathbf{r})}, \tag{3.11}$$

where:

$\mathbf{E}^0$ is the wave amplitude,
ω is the angular frequency,
λ is the wavelength,
$\mathbf{r}$ is the position vector,
$\mathbf{s}$ is a unit vector in the propagation direction,
t is the time,
n is the refraction index (n = c/v, c –light velocity in vacuum, v – wave phase velocity).

A light wave traveling in an absorbing medium is described by

$$\mathbf{E} = \mathbf{E}^0 e^{i(\omega t - \frac{2\pi n}{\lambda}\mathbf{s}\cdot\mathbf{r})} e^{-\frac{2\pi\kappa}{\lambda}\mathbf{s}\cdot\mathbf{r})}, \tag{3.12}$$

where κ is the extinction coefficient of the medium.

The light polarization is defined by the direction of the electric field vector. The electric fields are in the plane of incidence for p-polarized light and normal to the plane of incidence for s-polarized light[4]. In Figure 3.6 the electric field vectors corresponding to the propagation of s- and p-polarized light in a three-phase-system composed of vacuum, 10 ML thin (2 nm) magnesia film, and molybdenum substrate are illustrated. The angle of incidence is ϕ_1 for the light beam propagating from vacuum (phase 1) to MgO. The angle ϕ_2 inside MgO can be calculated using the Snellius-Descartes law ($\sin\phi_1/\sin\phi_2 = n_1/n_2$), where $n_1 = 1$ and $n_2 = 1.75$ [104] are the refractive indices of the vacuum and MgO, respectively. The optical properties of each phase itself are specified by the refractive index n, by the extinction coefficient κ and by the magnetic permeability of the material μ.

The reflective properties of the interface between the transparent magnesia (phase 2) and the metallic absorbing molybdenum (phase 3) are determined by the Fresnel coefficients of the reflection r_{P23} and r_{S23} (for s- and p-polarization), which are obtained using the Maxwell equations with the proper boundary conditions [103, 105, 106]:

[4] s - *senkrecht*, German for perpendicular

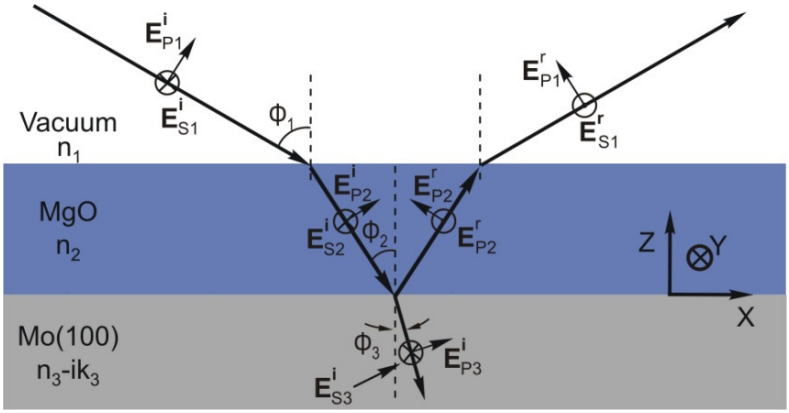

Figure 3.6 Electric field vectors in a three-phase-system. The superscripts i and r are used for incident and reflected beams. The subscripts P and S denote parallel and vertical light polarization, respectively, while the number indices (1, 2, 3) indicate the first (vacuum), the second (MgO) and the third phase (Mo). The direction of the electric field vectors perpendicular to the plane of incidence is symbolized by ⊗ (into the paper plane) and the anti-parallel direction ⊙.

$$r_{P23} = \frac{E^i_{P2}}{E^i_{P3}} = \frac{-n_3^2\cos\phi_2 + n_2\sqrt{n_3^2 - n_2^2\sin^2\phi_2}}{n_3^2\cos\phi_2 + n_2\sqrt{n_3^2 - n_2^2\sin^2\phi_2}} \tag{3.13}$$

$$r_{S23} = \frac{E^i_{s2}}{E^i_{s3}} = \frac{-n_2\cos\phi_2 - \sqrt{n_3^2 - n_2^2\sin^2\phi_2}}{n_2\cos\phi_2 + \sqrt{n_3^2 - n_2^2\sin^2\phi_2}}, \tag{3.14}$$

where the refractive index of the Mo is complex and defined as $n_3 = n_3 - i\kappa_3$. At 330 nm $n_3 = 3.04$ and $\kappa = 3.31$ [107]. In the following we explicitly elaborate on the multi-photon ionization wavelength employed in this study. The absolute phase change which occurs due to the reflection at the MgO/Mo interface for either p- or s-polarized light (indicated by the sub-script 'P,S' in the following) can be calculated according to:

$$\delta_{P,S\,23} = \arg(r_{P,S\,23}) = \tan^{-1}\left[\frac{\mathrm{Im}(r_{P,S\,23})}{\mathrm{Re}(r_{P,S\,23})}\right]. \tag{3.15}$$

The Fresnel coefficients r_{P12} and r_{S12} as well as the phase shifts δ_{P12} and δ_{S12} for both polarizations at the vacuum/MgO interface can be derived accordingly, yet the actual calculation is simpler, because n_1 and n_2 are real numbers in this case. In Figure 3.7 the phase shifts as a function of the angle of incidence upon external reflection of s- and p-polarized UV light at the vacuum/Mo interface is shown. Both s- and p-polarized waves change the phase continuously upon reflection. At an angle of incidence of 45°, as in the present experiment, the

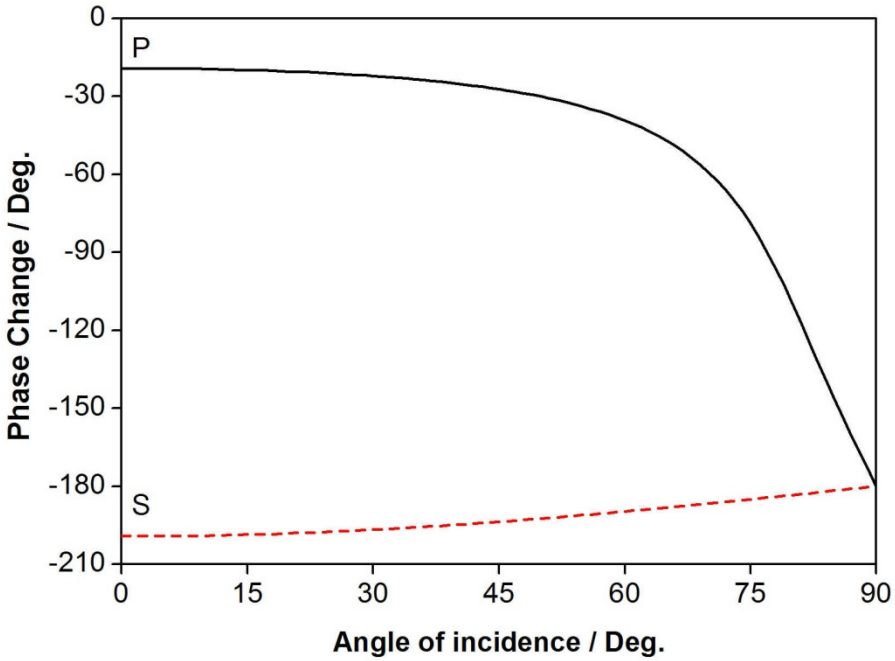

Figure 3.7 Phases change as a function of the angle of incidence upon external reflection of p- and s-polarized UV wave at vacuum/Mo interface.

s- and p-polarized wave have a phase change of -199.25° and -26.8°, respectively. At grazing incidence both waves suffer a phase change of 180° upon reflection.

For the complete three phase system consisting of vacuum, MgO film, and Mo substrate, the Fresnel coefficients are given by [105, 108]:

$$r_{P,S\,123} = \frac{r_{P,S\,12} + r_{P,S\,23}e^{-i2\beta}}{1 + r_{P,S\,12}r_{P,S\,23}e^{-i2\beta}} \quad , \tag{3.16}$$

where β represents the phase change that occurs during one traversal of the Mg film phase of thickness d.

$$\beta = \frac{2\pi n_2 d\cos\phi_2}{\lambda} \tag{3.17}$$

Finally, the reflectivity of the complete three-phase system is given by (for both polarizations, respectively):

$$R_{P,S\,123} = \left|r_{P,S\,123}\right|^2 \tag{3.18}$$

Applying equations (3.12) to (3.17), the reflectivity of the Mo substrate covered by 10 ML (d = 2 nm) MgO, $R_{P,S\,123}$, has been calculated. In addition, for comparison, also the reflectivity of a bare Mo surface, $R_{P,S\,13}$, has been calculated by setting d = 0 in equation (3.17).

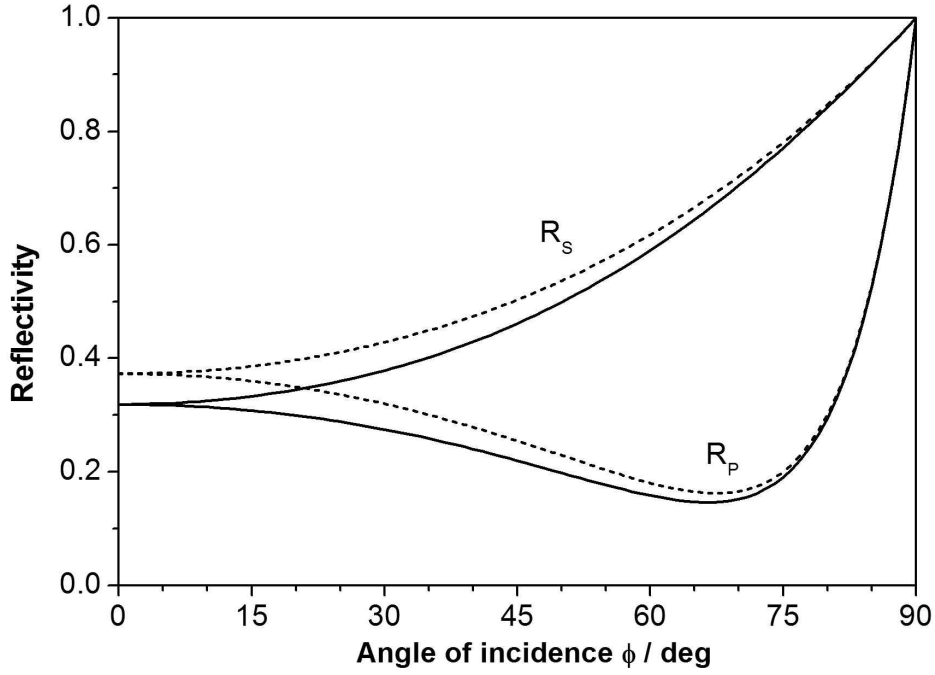

Figure 3.8 Reflectivity of bare Mo substrate (dashed line) and Mo covered by 10 ML MgO film (solid line) as a function of the angle of incidence.

Figure 3.8 displays the reflectivity as a function of the angle of incidence ϕ_1 for both, s- and p-polarization. R_S (for MgO/Mo and Mo, respectively) increases monotonically from its minimum value at $\phi_1 = 0°$ to unity at $\phi_1 = 90°$. R_P (for MgO/Mo and Mo, respectively) exhibits a minimum at the pseudo-Brewster angle, but for $\phi_1 = 0°$ and $\phi_1 = 90°$ it has the same values as R_s. At 45° incidence and p-polarization, as in the present experiment, the bare Mo surface reflects about 25% of the incident light, while the MgO covered Mo surface reflects 22%.

The mean-square electric field strength in a two and multi-phase system have been derived by Hansen [109]. For the calculation of the relative standing wave field in front of the Mo surface, i.e., the mean-square of the electric field strength (standing wave field) in the vacuum (phase 1) in front of the Mo surface $\langle E_{S,P\,1}{}^2 \rangle$ relative to the mean-square of the incident electric field strength $\langle E^i_{S,P\,1}{}^2 \rangle$, the following equations from Hansen's derivation have been employed:

$$\frac{\langle E_{S1}{}^2 \rangle}{\langle E^i_{S1}{}^2 \rangle} = 1 + R_S + 2\sqrt{R_S}\cos\left[\delta_S + 4\pi\left(\frac{z}{\lambda}\right)\xi_1\right], \tag{3.19}$$

$$\frac{\langle E_{Px1}{}^2 \rangle}{\langle E^i_{P1}{}^2 \rangle} = \cos^2\phi\left\{1 + R_P - 2\sqrt{R_S}\cos\left[\delta_S + 4\pi\left(\frac{z}{\lambda}\right)\xi_1\right]\right\}, \tag{3.20}$$

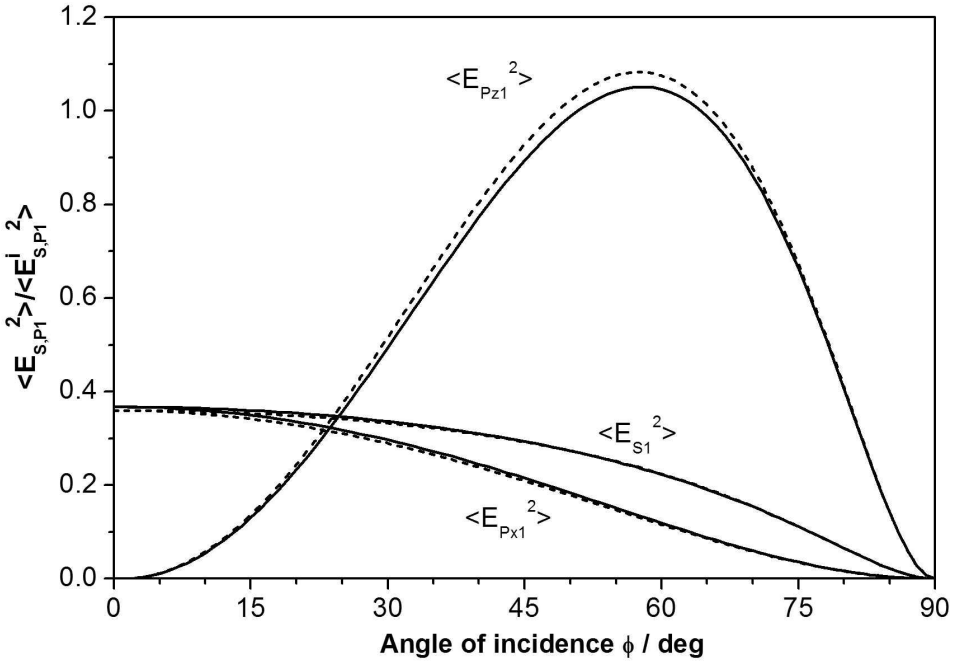

Figure 3.9 Angular dependent electric field intensity at the surface for p and s-polarized light: (dashed line) bare Mo surface; (solid line) Mo covered by 10 ML MgO film.

$$\frac{\langle E_{Pz1}{}^2\rangle}{\langle E_{P1}^{i}{}^2\rangle} = \sin^2\phi\left\{1 + R_P + 2\sqrt{R_S}\cos\left[\delta_S + 4\pi\left(\frac{z}{\lambda}\right)\xi_1\right]\right\}, \tag{3.21}$$

where:

z is the distance from the Mo surface

ξ_j is an angle dependent quantity ($\xi_j = n_j \cos\phi$) and j is represents a given phase

Equations (3.19) to (3.21) can also be used to calculate the standing wave field in the vacuum phase in front of the magnesia covered molybdenum surface. In this case it should be taken into account that R_S and R_P represent the reflectivities $R_{P,S\,123}$ of the MgO/Mo(100) system calculated by means of equation (3.18).

Figure 3.9 shows the variation of the standing wave field directly at the surfaces (z = 0) of Mo and MgO/Mo as a function of the angle of incidence for s- and p-polarization. For s-polarization the surface electric field intensity $\langle E_{S1}{}^2\rangle$ decreases monotonically to zero with increasing incidence angle. The same holds for the x component of the electric field intensity in the case of p-polarization $\langle E_{Px1}{}^2\rangle$. The z component of the electric field intensity $\langle E_{Pz1}{}^2\rangle$ is zero at normal incidence, reaches a maximum at 58° and returns to zero at grazing incidence. In contrast to the case of incident infrared light, where $\langle E_{S1}{}^2\rangle$ and $\langle E_{Px1}{}^2\rangle$ are in general at metallic surfaces zero for all angles [105], for UV light, as in the present investigation, these components are yet of sufficient magnitude to interact with the adsorbed species.

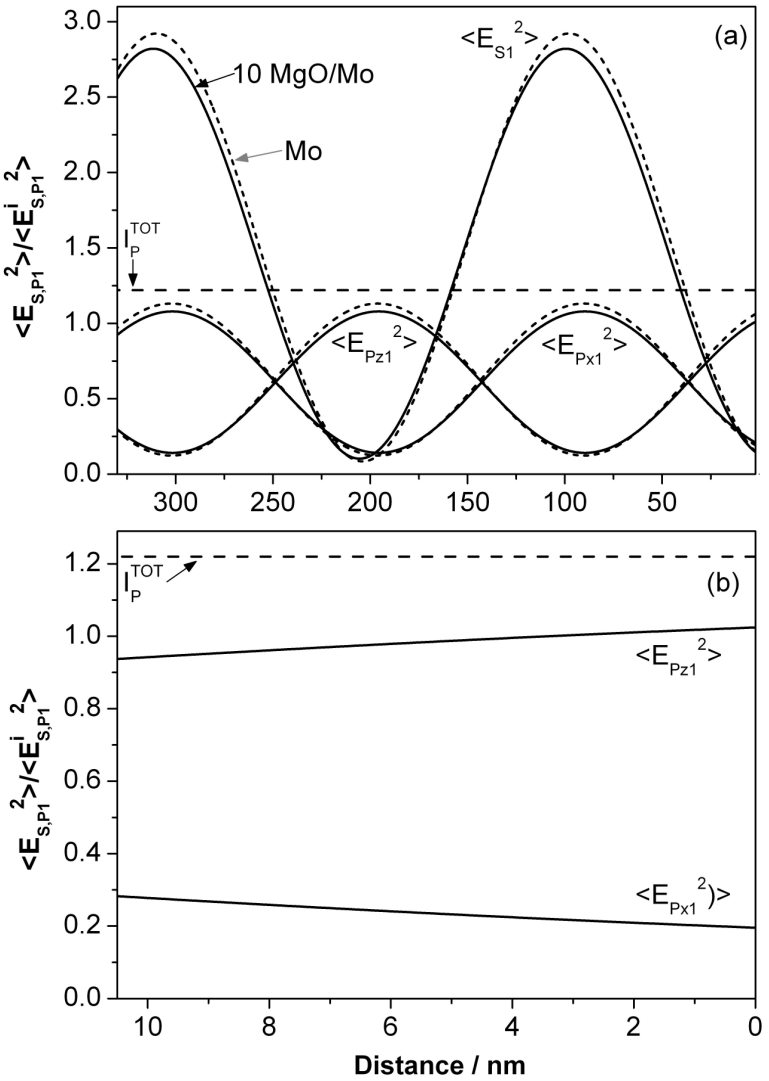

Figure 3.10 Spatial variation (z-distance dependence) of the standing wave field in front of the substrate system at an angle of incidence of 45°. (a) Relative mean-square of the electric field strength in the standing wave in front of the substrate system (dashed line: bare Mo; solid line 10 ML MgO on Mo) up to distances on the order of the probe wavelength. I_P^{TOT} indicates the magnitude of the constant total light intensity at the surface for incident p-polarized light. (b) Close-up of the near-surface region of the magnesia covered molybdenum substrate.

For the Mo surface covered by the 10 ML ultrathin MgO film, the z component of the electric field intensity $\langle E_{Pz1}{}^2 \rangle$ (solid line in Figure 3.9) is 3.4% smaller at 45° incidence compared to bare Mo surface (dashed line). $\langle E_{S1}{}^2 \rangle$ and $\langle E_{Px1}{}^2 \rangle$ are less than 1% lower for all angles of incidence after covering the Mo surface by the MgO film.

Figure 3.10a shows the variation of the standing wave field as a function of distance from the MgO/Mo(100) and the bare substrate. The mean square of the electric fields for both, the bare Mo surface and MgO/Mo, as well as the total light intensity I_P^{TOT} (for p-polarized light and the MgO/Mo surface as employed in this experiment) have been calculated for the

vacuum phase at 45° incidence. The periodic oscillation of the electric field intensity components with increasing distance from substrate are due to the interference that occurs between the incident and the reflected part of the light. The s-polarized component increases with z and reaches a maximum at 96.6 nm distance from the bare Mo surface and at 98.0 nm distance from the MgO/Mo surface. The separate components of the incident and the reflected p-polarized light interfere with each other, producing also a standing wave field in the front of the surface. The standing waves formed by the x and the z components of the p-polarized light are in antiphase (cf. Figure 3.10a). Spatially, an interference node of one component coincides with the antinode of the other component. In contrast to s-polarization, the total intensity for p-polarized light I_P^{TOT}, i.e., the sum of $\langle E_{Px1}^2 \rangle$ and $\langle E_{Pz1}^2 \rangle$, does not exhibit a spatial variation as can be seen from Figure 3.10. Close to surface, where we expect that the ionization of the reaction products occurs, only a slight variation of the electric field intensities are observed as apparent from Figure 3.10b. Only p-polarized light in interaction with the MgO/Mo surface system, as employed in the experiment, are considered in Figure 3.10b. The $\langle E_{Pz1}^2 \rangle$ component decreases by 6.3% within the first 10 nm distance from the MgO film, whereas the $\langle E_{Px1}^2 \rangle$ component increases by the same amount. Thus, as stated above, the total light intensity I_P^{TOT} is constant along the surface normal. Due to the relative intensity variation of $\langle E_{Pz1}^2 \rangle$ and $\langle E_{Px1}^2 \rangle$, the direction of the electric field vector in the standing wave field above the surface at incident p-polarized light changes from 10° tilt angle with respect to the surface normal directly at the MgO surface to 16° tilt angle at 10 nm distance.

3.4.2.1 Polarization in direct surface photodissociation

In direct optical excitation of the adsorbates, the dissociation cross section $\sigma_{P,S}$ (for both polarizations, respectively) is determined by:

$$\sigma_{P,S} \sim |\boldsymbol{\mu}\mathbf{E}|^2 \tag{3.22}$$

Equation (3.22) is a simplified version of Equation (3.10). For an adsorbed molecule with a unit transition dipole oriented as in Figure 3.11, for s-polarization:

$$|\boldsymbol{\mu}\mathbf{E}|^2 = \langle E_S^2 \rangle \sin^2\theta \sin^2\varphi \tag{3.23}$$

and for p-polarization

$$|\boldsymbol{\mu}\mathbf{E}|^2 = \langle E_{PX}^2 \rangle \sin^2\theta \cos^2\varphi + \langle E_{PZ}^2 \rangle \cos^2\theta + \langle E_{PX} E_{PZ} \rangle \sin\theta \cos\theta \cos\varphi \tag{3.24}$$

where $0° \leq \theta \leq 360°$ and $0° \leq \varphi \leq 360°$.

The photodissociation rates for s- and p-polarization for surfaces with C_4 rotational symmetry as in the case of Mo(100) and MgO(100) are given by [103, 106]:

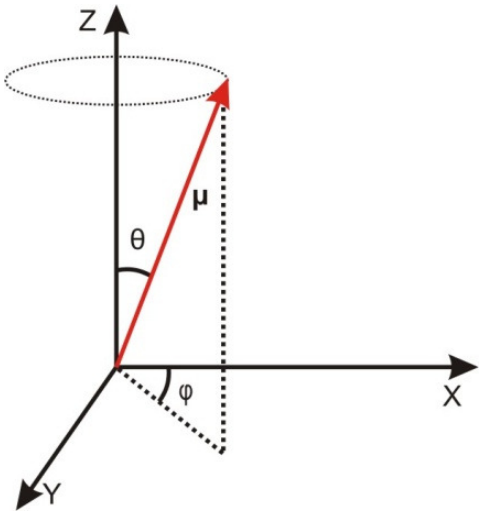

Figure 3.11 Geometry of the transition dipole of an adsorbed molecule at a surface

$$\sigma_s \sim 0.5\sin^2\theta_0\langle E_S^2\rangle \tag{3.25}$$

$$\sigma_P \sim 0.5\sin^2\theta_0\langle E_{PX}^2\rangle + \sin^2\theta_0\langle E_{PZ}^2\rangle, \tag{3.26}$$

where θ_0 and ϕ_0 are the coordinates of a fixed dipole, $0° \leq \theta_0 \leq 360°$ and $0° \leq \phi_0 \leq 360°$.
For surfaces with C_1 symmetry as expected on magnesia films that exhibit defects as steps and kinks:

$$\sigma_{P,S} \sim E_\mu^2 \tag{3.27}$$

For s- and p-polarized light:

$$\sigma_s \sim \langle E_\mu^2\rangle = \langle (E_S\sin\theta\sin\varphi)^2\rangle \tag{3.28}$$

$$\sigma_P \sim \langle E_\mu^2\rangle = \langle \left(E_{PX}\sin\theta\sin\varphi + E_{pZ}\cos\theta\right)^2\rangle \tag{3.29}$$

3.4.2.2 Polarization in substrate mediated dissociation

The photolysis cross section in substrate mediated excitation is determined by the concentration of hot carriers at the surface. For both s- and p-polarization the photolysis cross section can be in generally written as:

$$\sigma_{P,S} \sim A_{P,S}\rho(\varphi), \tag{3.30}$$

where:

$A_{P,S}$ is the absorption coefficient ($A_{P,S} = 1 - R_{P,S}$)
$\rho(\phi)$ is the a function of incidence angle φ [103].

Equations (3.28) to (3.30) illustrate that the use of polarized light at different angle of incidence can provide insights into the excitation mechanisms of the adsorbates, i.e. direct photoexcitation versus surface-electron mediated excitation in a surface photochemistry investigation [103, 106]. The importance of light polarization for the ionization-detection step will be discussed in conjunction with the methyl REMPI.

3.4.3 Intensity

Besides the wavelength and the polarization, the intensity of the light is also an essential parameter, which is defined as the energy falling on a unit area per unit time. Concerning the real-time surface investigation technique presented in this work, in this section the importance of the light intensity for both pump and probe laser beams is discussed.

3.4.3.1 Pump intensity

In direct excitation processes involving a single-photon, e.g., the dissociation of CH_3I on MgO, the rate equation can be written:

$$k \sim I\sigma C \tag{3.31}$$

where:

I is the intensity

σ is the cross section of the process

C is the adsorbate concentration

Equation (3.31) is of first order in both I and C

In hot carrier mediated processes, power laws with fractional order [110], first order [111] and higher orders [112], have been reported in the literature. In a DEA processes promoted by a single photon, the dissociation rate is proportional to the concentration of hot carriers reaching the surface. According to Fermi`s Golden rule, (cf. equation (3.10)), the concentration of nascent hot carriers is proportional to the number of absorbed photons. The hot carrier concentration reaching the surface is proportional to the nascent hot carriers. Thus, a first-order power law is expected.

3.4.3.2 Probe intensity

The detection of the reaction products is achieved by multiphoton ionization at the surface. Therefore, multiphoton processes have to be considered in the discussion of the probe intensity effects. Moreover, in this section the role of the laser polarization in the REMPI process is discussed.

Different selection rules apply to a multiphoton transition compared with a single-photon transition. Consequently, new excited states and vibrations can be accessed by multiphoton transitions that are not allowed for a single photon transition. Typically, the cross section for multiphoton processes is $10^{-50}cm^4s$ for a two-photon adsorption and $10^{-82}cm^6s^2$ for a three photon adsorption [113]. Due to these small numbers, it is apparent that high laser intensities should be applied in order to achieve a significant transition probability. To realize the

methyl radical detection, a (2+1) REMPI process is employed [102, 114, 115]. At 333.4 nm, a resonant two-photon transition occurs from the $2p^2A_2^{''}$ ground state to the $3p^2A_2^{''}$ Rydberg state of CH_3. Subsequently, a third photon having the same wavelength ionizes the excited CH_3^* radical. For the detection of the CD_3 radical, the same (2+1) REMPI process occurs, but at a wavelength of 333.9 nm (cf. Figure 3.5).

In order to describe the production of ions in resonant multiphoton ionization processes, rate equations are used [116-118]. For (2+1) REMPI of the methyl radical we can write:

$$Me + 2h\nu \overset{k_1}{\rightarrow} Me^* + h\nu \overset{k_2}{\rightarrow} Me^+, \tag{3.32}$$

where k_1 is the two-photon excitation rate to the $3p^2A_2^{''}$ Rydberg state and k_2 is the single photon ionization rate from $3p^2A_2^{''}$. The rates coefficients in s^{-1} are given by

$$k_1 = \sigma^{(2)}(\omega)\left(\frac{I}{\hbar\omega}\right)^2 \tag{3.33}$$

$$k_2 = \sigma_{ion}(\omega)\frac{I}{\hbar\omega} \tag{3.34}$$

where:

$\sigma^{(2)}$ is the generalized two-photon adsorption cross-section (cm^4 s),

I is the laser intensity (W/cm^2),

ω is the laser angular frequency (s^{-1}),

σ_{ion} is the excited state ionization cross-section (cm^2).

The two-photon adsorption cross-section $\sigma^{(2)}$ may be expressed as the product of the line-shape-independent cross section $\sigma_0^{(2)}$, which depends only on the properties of the methyl radical, i.e. the line shape function $g(\omega)$ and a photon statistical factor $G^{(2)}$ (see Ref. [117] for more details):

$$\sigma^{(2)} = \sigma_0^{(2)} g(\omega) G^{(2)} \tag{3.35}$$

The lineshape-independent cross section is obtained from perturbation theory by [116]:

$$\sigma_0^{(2)} = (2\pi)^3\left(\frac{e^2}{\hbar c}\right)^2 (\hbar\omega)^2 P^2 \tag{3.36}$$

where:

$$P = \sum_{K} \frac{\langle f|p\hat{\mu}|m\rangle\langle m|p\hat{\mu}|i\rangle}{E_i - E_k + \hbar\omega} \tag{3.37}$$

i, m, f are the initial, intermediate and final states
E_i, E_m are the energies of the initial and intermediate states
p is the light polarization
$\hat{\mu}$ is the electric dipole operator

From equation (3.37) it can be seen that the laser polarization can influence the transition probability. Indeed, polarization dependent multiphoton ionization spectroscopy has been extensively employed to obtain information about the symmetry of the intermediate excited states. In gas-phase where the molecules have an arbitrary orientation, a change in the ion signal intensity can be measured, depending on the symmetry of the excited state, when the light polarization is changed from linear to circular.

The use of polarization to determine the symmetry of a two-photon transition have been first described by McClain [119] and others [120, 121] and have been applied to different molecules [122-125]. Molecular alignment upon scattering and desorption from a surface has been studied by means of multiphoton ionization with linear polarized light [126, 127]. The alignment of the CD_3^+ fragment using (2+1) REMPI via the 4Pz Rydberg state following the A-band gas-phase photodissociation has been measured at room temperature [128]. Janssen et al. have measured the intensity of the ^{5}P(3) transition of the ^3p_z-$X0_0^0$ band of the CD_3 radical subsequent to the methyl iodide A-band dissociation employing (2+1) REMPI as a function of the laser polarization [115]. The highest methyl signal intensity has been detected when the polarization of the dissociation and the detection laser beams were parallel with respect to each other. The methyl signal presented a minimum when the polarizations have been perpendicular to each other. An absolute intensity variation of the methyl signal of about 8.5% has been observed by rotating the polarization of the detection laser beam. The polarization of the third photon that ionizes the excited methyl radical should not influence the REMPI probability. However, similar gas-phase investigations that probe the CH_3 0_0^0 Q branch by means of (2+1) REMPI at 333.4 nm show that the polarization has almost no influence on the CH_3^+ signal intensity [30, 129].

Finally, it can be concluded that the orientation of the laser beam polarization employed to detect the methyl radical by means of (2+1) REMPI at 333.4 nm (333.9 nm) does not affect the total ion intensity as long as the 0_0^0 Q branch is accessed. The decisive variables are the laser intensity and wavelength.

[5] P(3) probes K = 1 and 2

3.5 Mass, time, and velocity resolved measurements

In this section the novel methodology applied to study the real-time dynamics of methyl halide molecules adsorbed on different surfaces is described. As an example, the particular case of deuterated methyl iodide adsorbed on thin magnesia films is discussed.

3.5.1 Pump-probe schema

3.5.1.1 Surface photoexcitation

In order to monitor the real-time fragmentation dynamics of the methyl iodide molecules adsorbed at submonolayer coverage on the MgO/Mo(100) surface, the following pump-probe schema is applied. The pump laser pulse is centered at a wavelength of 266 nm to electronically excite the adsorbed CD_3I molecules to the A-band by means of direct one photon adsorption (see, e.g., [29-31, 33-35, 37, 38, 130] and references therein). Due to the transition of

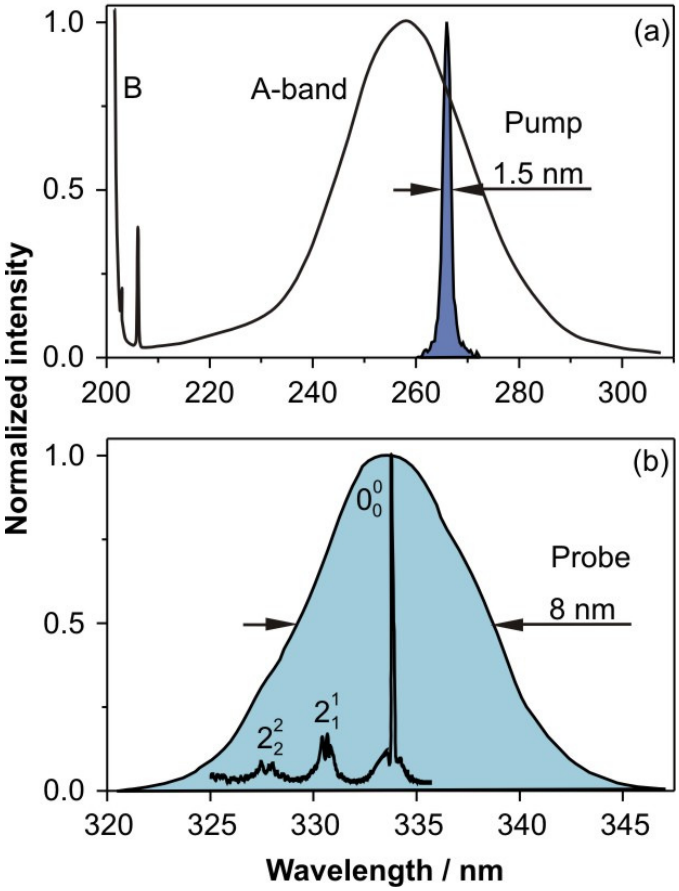

Figure 3.12 (a) Single photon adsorption spectrum (A-band) of methyl iodide near the region of excitation by the pump pulse adapted from Reference [97]*). The peak highlighted in blue represents the measured pump laser beam spectrum employed for the methyl iodide dissociation. (b) Two-photon resonant ionization spectrum of CD_3 radicals (adapted from Reference* [102]*) displaying the three vibronic transitions in the probe wavelength region. The measured spectrum of the probe laser beam is represented by the spectrum highlighted in light blue.*

a nonbonding 5pπ iodine electron to the σ* antibonding C-I orbital the methyl iodide molecule will dissociate (see also the discussion in Chapter 5).

In Figure 3.12a the measured spectrum of the pump laser beam is presented. The one photon absorption spectrum of methyl iodide in the A-band region [97] is also displayed in Figure 3.12a. Subsequently, the probe pulse detects the methyl fragments through multiphoton ionization. The detection scenario will be discussed in the next section.

For the direct photoexcitation of the adsorbed molecules the p-polarization of the pump pulse is particular important. Only in this case, as discussed in Section 3.4.2 (see also Figure 3.10a), the direction of the electric field vector directly in front of the surface is oriented mainly along the surface normal (z-direction) and coincides with the alignment of the C-I axis (see discussion in Section 5.1), i. e. the transition dipole moment of the molecules (the excitation to the A-band is a parallel transition).

In previous photodissociation experiments with methyl iodide adsorbed at submonolayer coverage on MgO(100) single crystal surfaces the direct photoexcitation has been shown to be the exclusive excitation mechanism [131, 132]. In the present experiments, an ultrathin magnesia film on Mo(100) has been employed instead of a magnesia single crystal. Still, all experimental evidence indicates that the direct photoexcitation clearly dominates over a surface mediated process (see Section 3.4.2). These two possible processes, direct and surface mediated excitation, are commonly distinguished by monitoring the angle of incidence dependence of the photodissociation product yield for s- and p-polarized incident light, respectively (see Section 3.4.2). This dependence should be determined by the substrate absorption (1-R), where R is given in Figure 3.8, for a substrate mediated process. In contrast, in case of the direct excitation mechanism, the standing wave field intensity as depicted in Figure 3.9 should determine the photoproduct yield. However, it is not possible in the present experimental arrangement to perform measurements other than close to 45° angle of incidence. Nevertheless, the methyl product yield at this orientation is strongly enhanced for p- vs. s-polarized light and thus favoring a direct excitation mechanism because this mechanism is considerably more pronounced for p-polarized light compared to s-polarized light (cf. Figures 3.8 and 3.9), yet further angular dependent data are necessary for an unambiguous identification.

More importantly, reversing pump and probe, i.e., excitation with 333.9 nm and time-delayed detection with 266 nm, does not yield a methyl ion signal at all. This strongly supports the direct photoexcitation mechanism because at 333.9 nm the A-band absorption cross section of methyl iodide is marginal compared to 266 nm (see Figure 3.12). In addition, we did also carry out similar experiments with adsorbed methyl bromide molecules on MgO/Mo(100) (cf. Chapter 6). The A-band of CH_3Br is considerably blue-shifted compared to CD_3I, far beyond 266 nm (cf. Figure 3.4). In this case no single photon dissociation of CH_3Br is detected at 266 nm excitation wavelength as expected in a surface mediated process. Summarizing all the evidence, it is concluded that the major contribution to photodissociation of methyl iodide on MgO/Mo(100) is due to direct photoexcitation of the adsorbed molecules via the A-band absorption (see also discussion in Chapter 5).

3.5.1.2 REMPI detection

Subsequent to the A-band dissociation, the probe pulse at a central wavelength of 333.9 nm is employed to sensitively detect the methyl fragments through (2+1)-REMPI [30, 31, 102]. As previously discussed (cf. Section 3.4.3.2), two photons are employed for excitation from the $2p^2A_2^{''}$ ground state to the $3p^2A_2^{''}$ Rydberg state, followed by absorption of a third photon to ionize the methyl fragments. Figure 3.12b displays the probe laser beam spectrum together with the (2+1) REMPI transitions of CD_3I around 333 nm [102]. Due to the bandwidth of 8 nm (FWHM), the probe pulse is able to excite simultaneously the 0_0^0, 2_1^1, and 2_2^2 vibronic transitions (cf. Figure 3.12b).

It should be emphasized that our experiment probes the dynamics of neutral products emerging from photoexcitation and dissociation at the surface. The REMPI process occurs only when the electronic states of the methyl fragment involved in the resonant transitions are not perturbed, neither by the iodine fragment nor by the substrate. Consequently, the real-time evolution of the REMPI probability reflects the dynamics of the methyl liberation from the iodine and surface force fields.

As previously discussed, the light polarization has almost no influence when the CH_3 0_0^0 Q-branch is probed by means of (2+1) REMPI [30, 129]. However, when the pump laser beam is p polarized and the probe laser beam polarization is changed to s, no photofragments are detected due to the interference node that appear at surface (cf. Figure 3.10a). This confirms the multi-photon ionization of the reaction products at surface.

3.5.2 Transient recording routine

To monitor in real-time the methyl iodide dissociation dynamics at submonolayer coverage on the magnesia ultrathin films, the following transient recording routine (illustrated in Figure 3.13) is applied while the MgO/Mo(100) surface is positioned in the front of the TOF-MS (as shown in Figure 3.3) and cooled to 90 K. (i) An initial coverage of 0.25 ML to 0.5 ML CD_3I is dosed onto the surface with the pulsed valve while the laser is blocked by a computer controlled mechanical shutter (see Figure 3.3) so that no methyl signal can be detected by the mass spectrometer as indicated in Figure 3.13. (ii) A short pumping brake of a few seconds follows. (iii) Subsequently, the laser shutter is opened and the mass peak of interest (methyl cation in Figure 3.13) is detected and summed over 2500 to 5000 laser shots at one fixed pump-probe delay time. A complete mass spectrum recorded at a pump-probe delay time of 130 fs is shown in Figure 3.14.

After 2500 to 5000 laser shots, depending on the initial coverage, essentially all molecules are dissociated and desorbed from the irradiated surface area. Subsequently the laser beams are blocked again and the surface is covered with an identical amount of molecules as before. During the following short pumping brake the pump-probe delay time is adjusted and the described data acquisition procedure is repeated for a new pump-probe delay time.

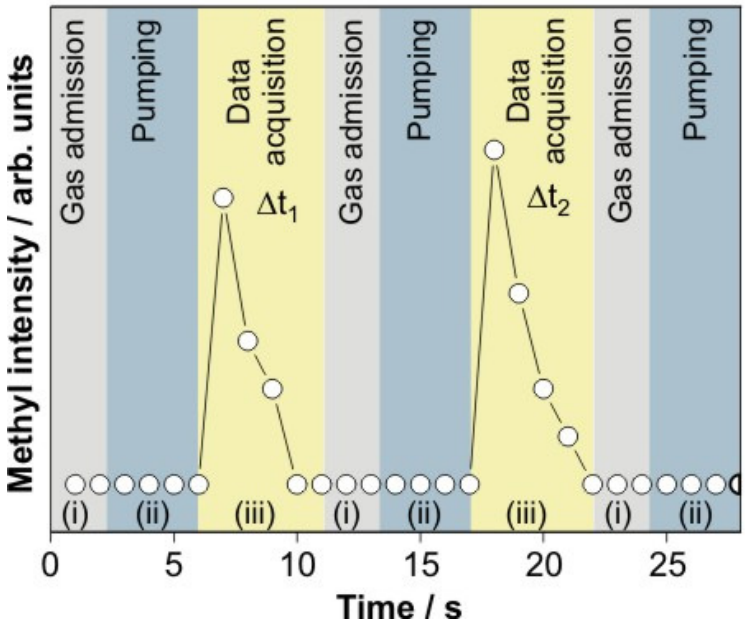

Figure 3.13 Transient recording routine: (i) Methyl iodide is admitted to the surface by the pulsed valve. During the admission time the laser beam is blocked; (ii) the non-adsorbed molecules are pumped and the delay time between the pump and the probe laser pulses is adjusted. The laser beam is blocked also during this period; (iii) the surface is exposed to laser light and the methyl mass peak intensity is integrated until all molecules are dissociated/desorbed from the irradiated area. The initial surface coverage in this experiment was 0.5 ML and the laser exposure time 5 s (5000 laser pulses).

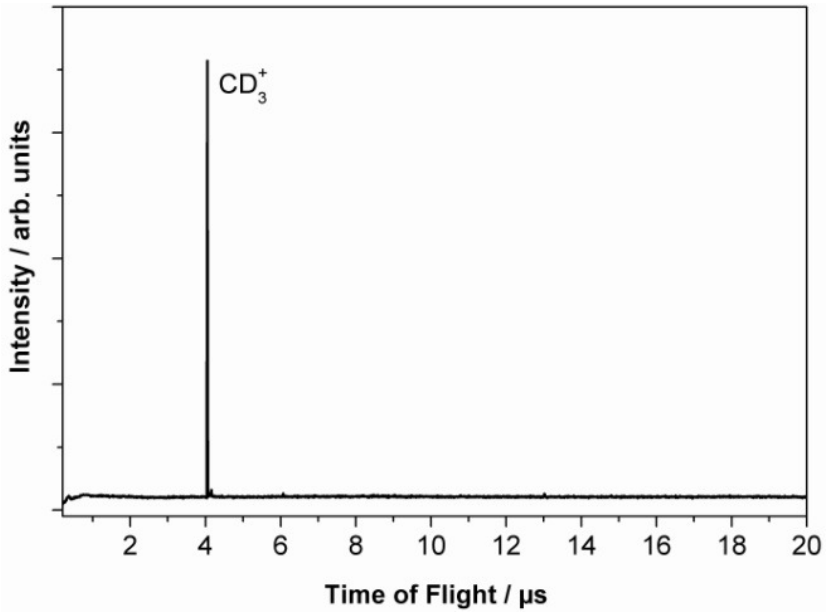

Figure 3.14 Time-of-flight pump-probe laser ionization mass spectrum obtained from 0.25 ML methyl iodide adsorbed on 10 ML MgO/Mo(100) with 130 fs pump-probe delay time. The spectrum has been obtained by summing the ion signals from 105 laser pulses. The surface temperature was 90 K.

3.5.3 Time zero determination

The determination of the zero time delay between the excitation and detection laser pulses has a central importance in all time-resolved pump-probe experiments. To measure the pump-probe cross correlation function and hence to determine the zero time delay for the surface pump-probe fs-laser mass spectrometry experiment, transient two-photon photoemission is employed. For this purpose the molybdenum surface is covered by a thin film of gold and placed in the same position as during the pump-probe mass spectrometry experiments (cf. Figure 3.3). A gold film is utilized because of its comparably high work function (about 5 eV [133]) which is larger than the energy of a single pump or of a single probe photon at 266 or 333.9 nm, respectively. During the measurement of the transient photoemission signal, the surface is biased at -10 V. The photoemission current from the gold surface is detected on the TOF-MS entrance electrode and measured by means of a commercial pico-Ampèremeter (Keithley Instruments). The intensities of both pump and probe beam are carefully adjusted to obtain equal photoemission currents from each separate laser beam.

The data in Figure 3.15a show the integral photoemission yield from a 12 ML thick gold film on Mo(100) as a function of the pump-probe delay time. The peak of this photoemission transient defines the time zero of the experiment with an accuracy of ±16 fs (standard deviation of the peak position of the Gauss fits of several subsequent measurements). The cross-correlation width (FWHM) of this transient is determined by a Gaussian fit to amount to 176 fs. However, this cross correlation width is considerably larger than expected from the laser pulse width that has been extrapolated from the amplifier output autocorrelation measurement to be about 80 fs (taking into account the influence of all dispersive elements in the optical pathway). This temporal broadening can be attributed to two factors: (i) A power broadening due to space charge repulsion effects induced by an excess in laser intensity used in this measurement and (ii) the influence of the lifetime of the electronic states of the substrate which can be probed with the applied laser wavelengths. Reducing the laser power to obtain an electron emission rate of less than 0.1 per laser pulse eliminates effect (i). Furthermore, by kinetic energy resolved detection of the emitted electrons (2PPS with a time-of-flight photoelectron spectrometer described in Section 2.2.2) the obtained transient electron dynamics can be compared to previously published lifetimes of electronic excitations on gold surfaces [134].

Figure 3.15b displays the respective time-resolved two-photon photoemission obtained from the same gold film as in Figure 3.15a recorded with the photoelectron spectrometer [133, 135, 136]. The open circles are the experimental data obtained by integrating the complete photoemission spectrum. The FWHM of this transient is 155 fs, i. e. less than in Figure 3.15a due to the elimination of space charge effects at reduced laser power. The open squares in Figure 3.15b are the detected time- and energy-resolved photoemission intensity at 0.6 eV intermediate state energy above the Fermi energy ($E_i - E_F$). Deconvolution of this transient into a single exponential decay component and a Gaussian autocorrelation pulse profile [137] (Section 3.5.4.2) yields an excited state lifetime of 165 ±14 fs, if a laser pulse width of

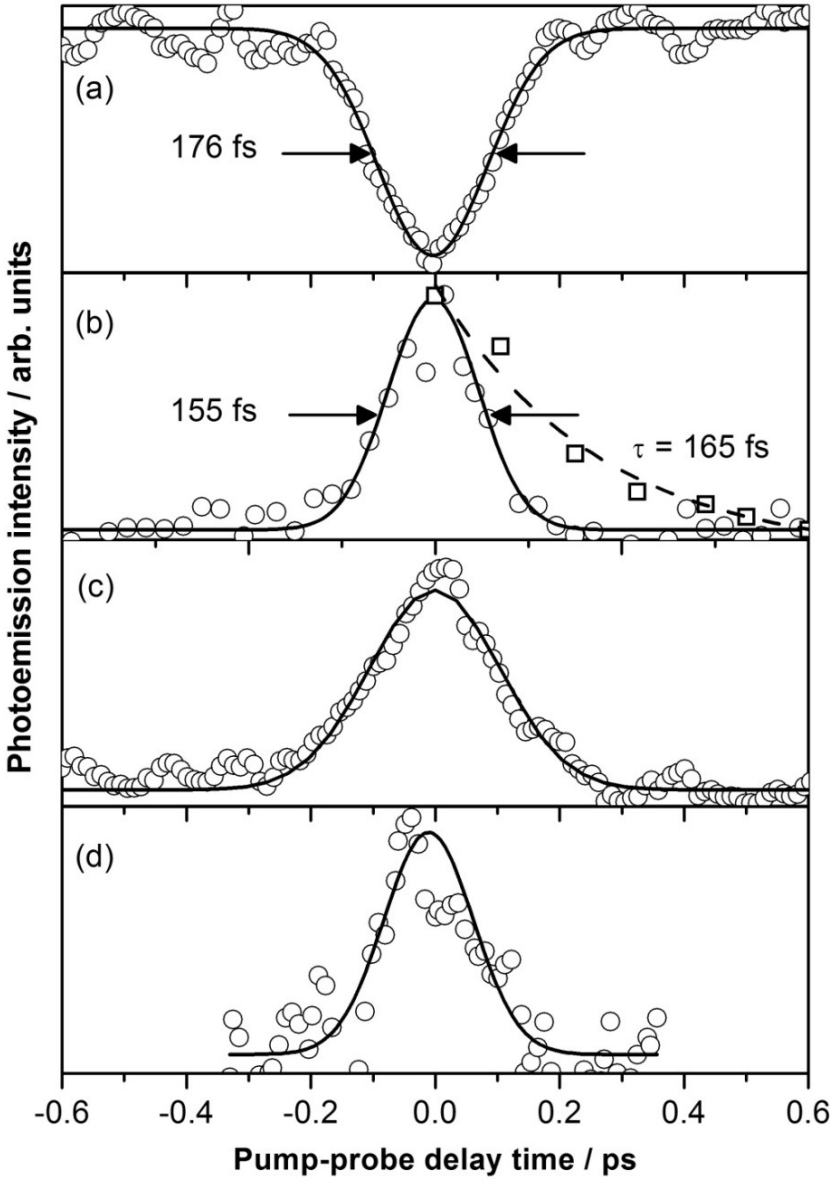

Figure 3.15 Determination of zero pump-probe laser time delay via transient two-photon photoemission. (a) Integral two-photon photoemission yield from a gold film on Mo(100) recorded with a pico-Ampèremeter on the TOF-MS entrance electrode (cf. Figure 3.3). Open circles represent the experimental data (average of five single transients); the solid line is a Gaussian fit to the data. (b) Two-photon photoemission transient signals recorded with a time-of-flight photoelectron spectrometer at reduced laser power [133, 136]. Open circles represent the experimental integrated photoemission intensity; the solid line is a Gaussian fit to the data. The open squares are experimental two-photon photoemission intensity data obtained at 0.6 eV intermediate state energy above E_F; the dashed line is a fit of a single exponential decay convoluted with a Gaussian cross correlation function to these data. (c) Transient measurement of positive charge carriers with a pico-Ampèremeter while the laser beams are directed onto the TOF-MS entrance electrode (average of six single transients). (d) Integral two-photon photoemission yield from the Mo(100) single crystal surface recorded with the pico-Ampèremeter on the TOF-MS entrance electrode.

80 fs is assumed. This result compares very favorably with the about 172 fs reported for an Au(111) surface in the same energy range previously [134].

A more convenient method to determine the zero time delay for the surface pump-probe fs-laser mass spectrometry experiment on a daily basis consist in recording the transient holes signal on the TOF-MS entrance electrode (stainless steel). For this purpose the laser beams are slightly deflected to illuminate this electrode. In order to measure the transient current intensity of the positive charge carriers, the TOF-MS entrance electrode is negatively biased (-10 V). The resulting transient is shown in Figure 3.15c. The center of the transient peak structure exactly coincides with the time zero defined in the photoemission experiment with the gold surface and can thus be used for its convenient determination.

A third possibility to obtain the zero delay time consists in measuring the two-photon photoemission yield from the molybdenum single crystal substrate. The corresponding signal is depicted in Figure 3.15d. Also in this case, the peak of the transient structure coincides with the zero time delay defined in the gold photoemission experiment. However, the two-photon photoemission signal from the Mo(100) surface is comparably weak due to the fact that the 266 nm laser pulse already generates a strong single photon contribution to the photoemission because of the lower (4.5 eV [138]) work function of molybdenum.

3.5.4 Evaluation of the SFsMS data

Transient signals recorded using procedure presented in Section 3.5.2 from methyl iodide and methyl bromide adsorbed on different substrates are presented in Chapters 5 and 6. For the evaluation of reaction dynamics on the surface mass spectra recorded at different reaction times, transient measurements of the intermediates and of the reaction products, power dependence measurements and the available potential energy curves of the investigated molecules are employed.

3.5.4.1 Potential energy diagram

In Figure 3.16 a schematic representation of the potential energy diagram for the simplest case of a free diatomic molecule is illustrated. This figure can be also used to explain the photodissociation dynamics of a quasi-diatomic molecule as methyl iodide. In Figure 3.16 a pump pulse (λ_1, dotted arrow) excite the AB molecule and prepares a wave packet on the repulsive V_1 potential. Finally the molecule dissociate into A and B. The curved arrows (cf. Figure 3.16) represent the wave packet propagation. In order to find the dissociation time of the AB molecule, the probe pulse (λ_2, dashed arrows) which is tuned to sensitively detect the B fragment by means of REMPI is delayed with respect to the pump pulse. In the same time the excited $AB^{*‡}$ complex could adsorb probe photons to reach the cation state(s). The excited $AB^{*‡}$ complex become ionized (AB^{*+}) after the adsorption of two probe photons. Subsequently the AB^{*+} complex dissociate due to the V_2 potential leading to $A + B^+$. The dynamics of the transition states $AB^{*‡}$ and of the final product B could be monitored at the same time by varying the pump-probe delay time and monitoring the B^+ fragment intensity.

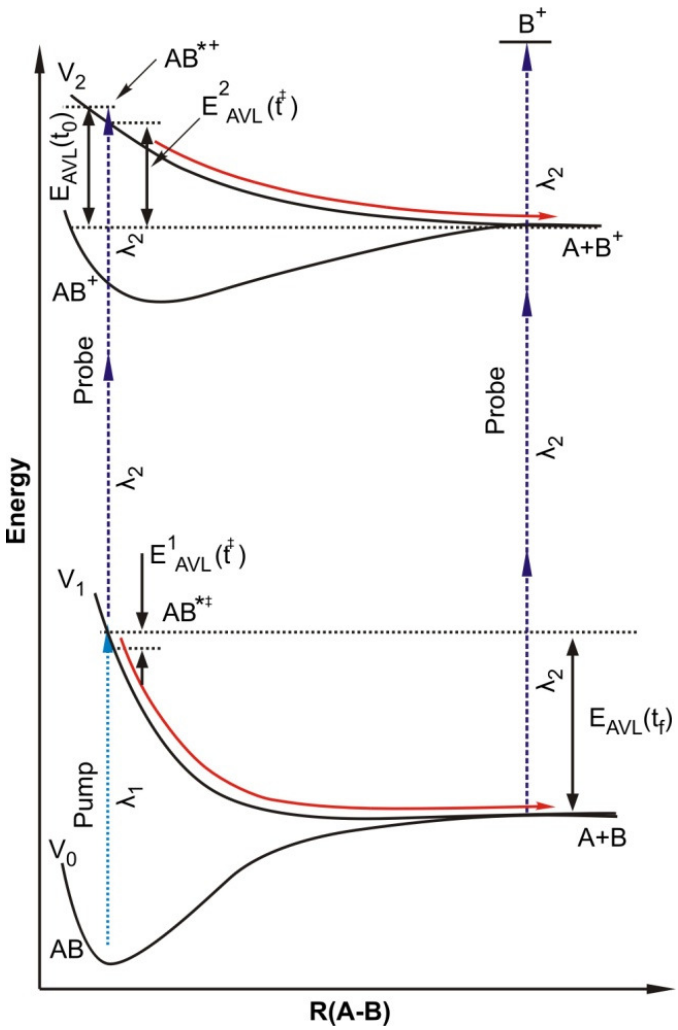

Figure 3.16 Illustration of the femtosecond pump-probe scheme used for the investigation of the methyl halide photodissociation dynamics (see text for more details).

More information concerning the reaction dynamics can be obtained my monitoring the relative kinetic energy of the B^+ fragment in real-time. At zero time delay the kinetic energy of the B^+ fragment is determined by the total energy $E_{AVL}(t_0)$ on the V_2 potential. When the reaction is finished the kinetic energy of the B^+ fragment $E_{AVL}(t_f)$ is determined by the energy released from AB^* dissociation. At intermediate time delay, when the energy of the probe pulse is still enough to ionize the $AB^{*‡}$ complex the total kinetic energy of the B^+ fragment is given by the energy gained $E^1_{AVL}(t^‡)$ in the neutral complex AB^* during the wave packet evolution from t_0 to $t^‡$ and by the energy $E^2_{AVL}(t^‡)$ from the excited ionic potential V_2.

In conclusion, the dissociation dynamics of the AB molecule can be studied exactly by monitoring the intensity of the mass signal and the relative kinetic energy of the B^+ fragment as a function of the pump-probe delay time.

3.5.4.2 Fitting procedure

In order to determine the time constant of a given dynamic process, the measured transient data are fitted with the appropriate molecular response function (in general an exponential rise or decay function) convoluted with the laser autocorrelation function.

Here, the simplest case of a photoinduced unimolecular first order reaction is considered, where the educt A decomposes exponentially after laser irradiation to the reaction products B and C:

$$A \xrightarrow{k} B + C \tag{3.38}$$

The molecular response function decays exponentially with the reaction rate coefficient k as follows:

$$M(t) = A_0 \cdot e^{-kt}, \tag{3.39}$$

where t is the reaction time and A_0 is the initial intensity of the educt A.
As previously mentioned, the laser pulse durations involved in the photoinduced process have to be also taken into account. If the temporal shape of the pump and probe laser pulses is approximated by a Gaussian function, the resulting autocorrelation function G(t) is given by:

$$G(t) = \frac{1}{\sqrt{2\pi}\sigma_G} \cdot e^{-\frac{t^2}{2\sigma_G^2}}, \tag{3.40}$$

where σ_G is the measured laser pulse duration.
The convolution of the single exponential decay function with the laser autocorrelation function gives the desired signal function $S(t_D)$:

$$S(t_D) = \int_{-\infty}^{+\infty} M(t) \cdot G(t_D - t) dt, \tag{3.41}$$

where t_D is the pump-probe delay time.
Integrating the equation (3.41), the implemented fit function is obtained:

$$S(t_D) = A_0 \cdot \frac{1}{2} e^{\frac{\sigma_G^2 k^2}{2}} \cdot e^{kt_D} \left[1 - \operatorname{erf}\left(\frac{\sigma_G k}{\sqrt{2}} - \frac{t_D}{\sigma_G \sqrt{2}}\right)\right], \tag{3.42}$$

4 Surface preparation and characterization

Ultrathin metal oxide films on metal single crystal substrates have become an extensively investigated research subject in recent years [139, 140]. This interest is due to their importance to a wide range of applications, including magnetic tunneling junctions [141], chemical sensors [142], and nanoscale model systems in heterogeneous catalysis [143]. Because of their finite thickness of only a few atomic monolayers, electron tunneling through the film into the metal substrate is possible and, hence, scanning tunneling microscopy and electron spectroscopic methods can be applied to investigate the geometric and the electronic structure of these films, even if they are composed of wide band gap insulating materials such as magnesium oxide [144]. With respect to surface chemistry and heterogeneous catalysis MgO ultrathin films on Mo(100) are particularly appealing due to their good chemical and thermal stability, their simple rock salt structure, and their amenability to high temperature treatment because of the high refractory metal support [145-147]. Nanoparticle model catalysts could be prepared by thermal evaporation or by mass-selected deposition of metal clusters on the insulating magnesia film.

In this work, the employed surfaces consist of ultrathin MgO films grown on a Mo(100) single crystal surface, Au films grown on Mo(100), and magnesia supported Au nanoparticles and mass-selected Au_N (N = 1, 2, 3) clusters. These substrates are employed as support for the investigation of methyl halide photoinduced reactions.

In this chapter, the surface preparation and characterization methods are presented. As analytical tools AES, LEED, EELS and TPD were employed to characterize the surface. Besides these standard analytical techniques, fs-PES has been employed here for the first time to study the electronic structure of a refractory metal covered with ultrathin oxide films of various thickness. Furthermore, the potential of fs-PES for the investigation metal clusters on oxide films is demonstrated. Fs-PES is sensitive enough to detect a change in the electronic structure of the magnesia supported gold clusters, even if the Au coverage is varied by just 0.01 ML.

4.1 MgO(100) on Mo(100)

4.1.1 Preparation of ultrathin MgO films on Mo(100)

For the preparation of the magnesia films, a homebuilt Mg metal evaporator was employed. It consists of a magnesium ribbon placed inside a coil of a 0.4 mm thick tantalum filament [148]. The MgO ultrathin films were prepared, according to the procedure reported in the literature [146-148], by evaporation of magnesium metal in an atmosphere of 2×10^{-7} mbar of oxygen. During the deposition, the Mo(100) crystal was held at 600 K [149]. The Mg evaporation rate of 0.15 ML/min was determined by a combination of TPD and AES investigation of Mg layers deposited directly onto the Mo(100) surface. In Figure 4.1, Mg TPD spectra recorded from Mo(100) as a function of the magnesium evaporation time are shown. After 10 s Mg evaporation, two desorption peaks appeared above 600 K (cf. Figure. 4.1a). The origin of these desorption peaks was attributed to submonolayer desorption. The evolution of the desorption peak above 600 K with increasing the Mg coverage reflects a strong repulsion between the atoms at submonolayer coverage [147]. For Mg evaporation times longer than 30 s, a new desorption peak below 600 K, which has the shape characteristics of zero-order desorption (cf. Section 2.2.3) appeared (Figure 4.1b-c) [147]. This new desorption peak was attributed to the Mg multilayer desorption.

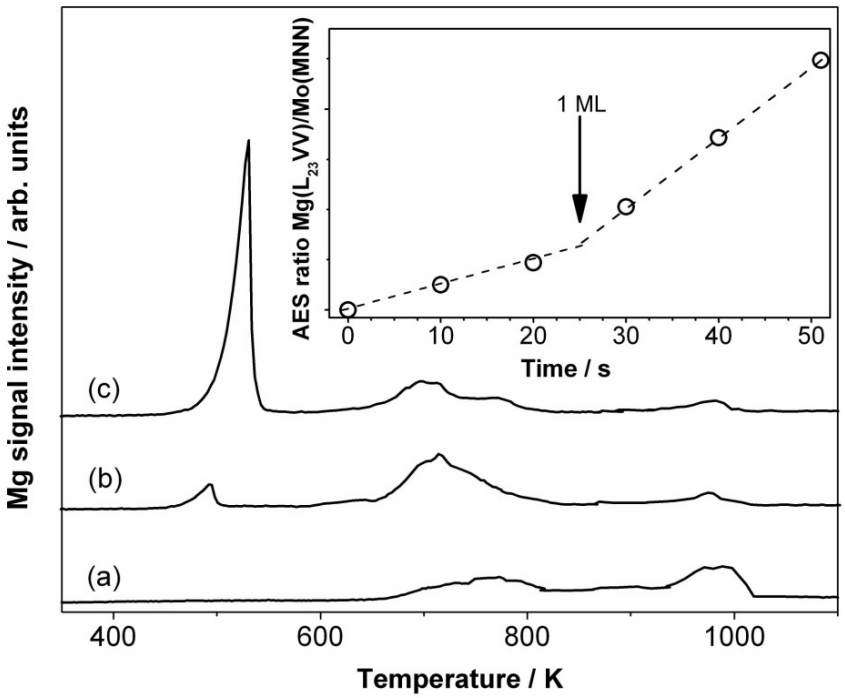

Figure 4.1 TPD desorption spectra as a function of magnesium coverage: (a) 10 s; (b) 30 s; (c) 70 s. The inset shows the Mg ($L_{23}VV$) to Mo(MNN) AES ratio as a function of the Mg evaporation time.

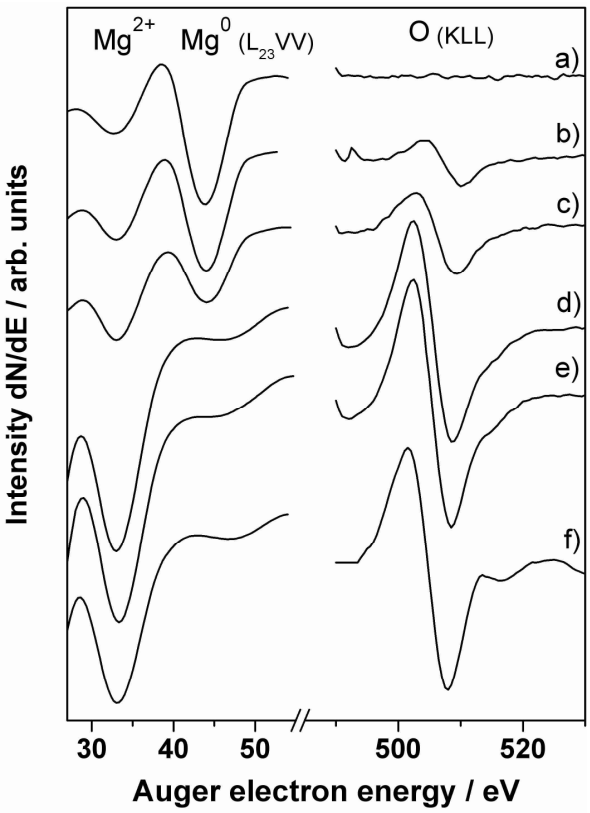

Figure 4.2 Auger electron spectra of MgO films grown on Mo(100) as a function of the oxygen background pressure (E_P = 2000 eV): (a) 0.7×10^{-8} mbar; (b) 1.3×10^{-8} mbar; (c) 3.3×10^{-8} mbar; (d) 7.3×10^{-8} mbar; (e) 1.0×10^{-7} mbar; (f) 2.5×10^{-7} mbar. All MgO films were synthesized at 360 K and had the same thickness of 5 ML.

The inset in Figure 4.1 shows the Mg/Mo AES ratio as a function of the magnesium evaporation time. A gradual increase of the magnesium evaporation time on the molybdenum surface leads to a brake-point in the intensity ratio of the Mg(L_{23}VV) AES signal at 44 eV to the Mo(MNN) AES signal at 186 eV, which coincides with the appearance of the multilayer peak in the TPD spectra (cf. Figure 4.1) and corresponds to the exact amount of Mg needed for the completion of the first Mg layer on Mo(100). Assuming that the sticking probability of Mg atoms adsorbed on Mo(100) is unity during the growth of MgO films, the thickness of the MgO films can be determined from the calibrated Mg evaporation rate.

The oxidation of the Mg overlayer during the MgO film growth was also investigated by means of AES. For this purpose, Auger spectra were recorded from 5 ML Mg films oxidized during the growth employing different oxygen background pressures. The results are displayed in Figure 4.2. During the Mg deposition the substrate temperature was kept at 360 K and the Mg evaporation rate was 0.5 ML/min. An increase of the oxygen background pressure reduces the Auger peak at 44.0 eV, while a new peak at 32 eV successively increases. The peak at 44 eV is assigned to the Mg^0 (L_{23}VV) Auger transition and corresponds to metallic magnesium, while the second peak is attributed to the Mg^{2+} (L_{23}VV) Auger transition due to the formation of MgO [150, 151]. Both peaks coexist without changing their position

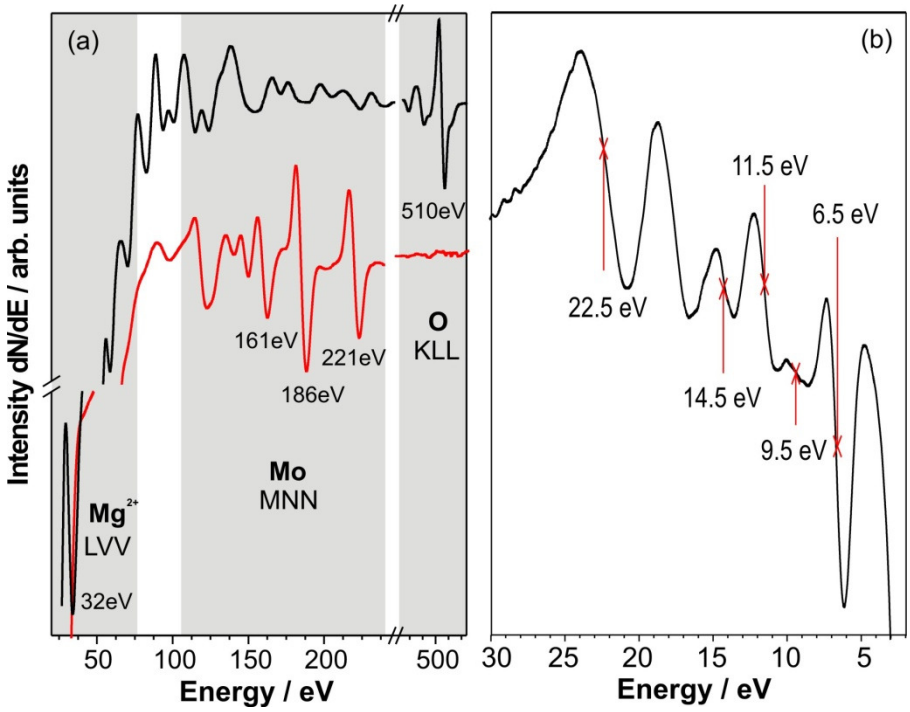

Figure 4.3 (a) Auger electron spectra taken from a clean Mo(100) surface (black line) and from a 10 ML MgO film on Mo(100) (red line) (E_P = 2000 eV). The characteristic Auger transition for magnesium, molybdenum and oxygen are noted in the figure. (b) Electron energy loss spectrum of a 10 ML MgO film on Mo(100) (E_P = 100 eV).

on the energy scale up to an oxygen background pressure of 5×10^{-8} mbar (cf Figure 4.2a-c). The peak at 510 eV corresponds to the O (KLL) Auger transition and its intensity increases by increasing the oxygen background pressure. A fully oxidized MgO film is reached for pressures larger than 7×10^{-8} mbar which coincides with the disappearance of the Auger transition at 44 eV. A further increase in the oxygen background pressure does not influence the magnesia composition as can be seen in Figure 4.2.

In Figure 4.3a Auger electron spectra recorded from a clean Mo(100) surface and from a 10 ML MgO film on Mo(100) are shown. The clean Mo(100) surface shows just the MNN transitions in AES. At 10 ML MgO coverage, the intensity of the Mo(MNN) Auger peaks is strongly reduced, and new transitions characteristic to oxidized magnesium and to oxygen appear at 32 eV and 510 eV, respectively.

In Figure 4.3b an electron energy loss spectrum recorded from a 10 ML MgO film on Mo(100) is displayed. The electron energy losses are calculated from the kinetic energy of the primary electrons (100 eV). The loss at 22.5 eV is assigned to a plasmon excitation corresponding to the collective excitation of the O 2p electrons. The losses at 17.5, 14.5, 11.5, 9.5 are attributed to the O-to-MgO interionic transitions [152]. The 6.5 eV loss is attributed to a surface related interband transition since its energy is less than the band gap in MgO (7.8 eV). It has been demonstrated experimentally [153] that the 6.5 eV loss is enhanced at low primary energies and at gracing incidence, indicating that is of surface origin.

4.1.2 Geometric structure of ultrathin MgO films on Mo(100)

In agreement with the previous reports by Goodman et al. and Freund et al. [146, 147, 154, 155], we found that the MgO films grow epitaxially on the Mo(100) surface. The (100) face of MgO is parallel and rotated by 45° with respect to the (100) face of Mo(100), which means that the MgO[110] direction is along the Mo[100] direction. The molybdenum has a bcc crystal structure with a lattice constant of 3.15 Å. In contrast, the distance between the Mg atoms of MgO (fcc structure) is 2.98 Å. Consequently, the mismatch between the molybdenum and magnesia primitive cells is 5.4% [146, 154, 155].

In this work the structure of ultrathin magnesia films grown on Mo(100) was investigated by means of LEED. Figure 4.4 shows LEED images recorded from a clean Mo(100) surface and from a 10 ML MgO ultrathin film on Mo(100) as well as the corresponding ball models of these surface structures. Initially, the clean Mo(100) surface exhibits a sharp (1x1) diffraction pattern in LEED.

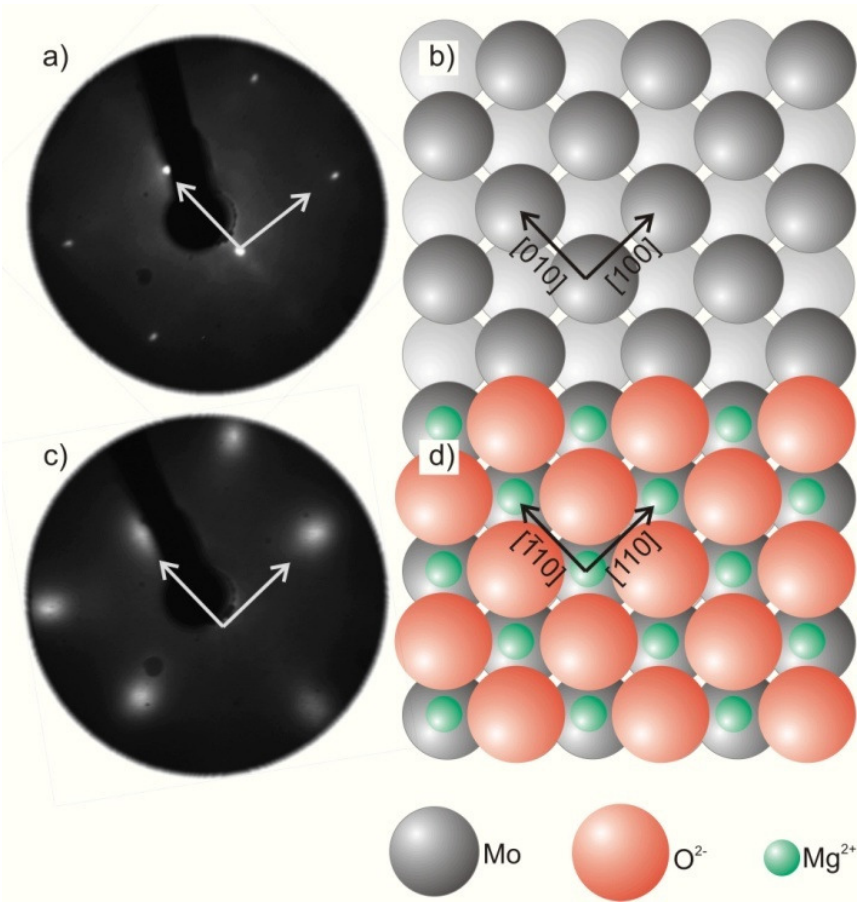

Figure 4.4 Morphology of Mo(100) and MgO(100)/Mo(100): (a) LEED image recorded from a clean Mo(100) surface (E_p = 87 eV; T_{surf} = 90 K); (b) model of the Mo(100) surface. The dark gray spheres represent the upper layer while the light gray spheres represent the second layer of molybdenum atoms. (c) LEED image obtained from 10 ML MgO(100) on Mo(100) (E_p = 87 eV; T_{surf} = 90 K); (c) model of an MgO monolayer on the Mo(100) surface.

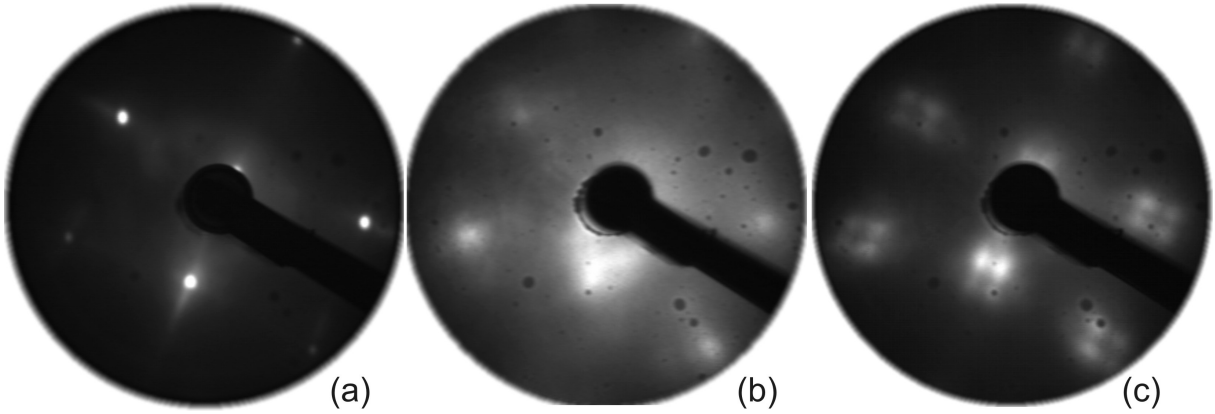

Figure 4.5 LEED images recorded from: (a) Mo(100) surface; (b)10 ML MgO film grown on Mo(100) at 600 K; (c) 10 ML MgO film grown on Mo(100) at 600 K and subsequently annealed at 1210 K for 3 min. The magnesia deposition rate in (b) and (c) was 0.15 ML/min, and the oxygen background pressure was 1.2×10^{-7} torr. All LEED images were recorded at T_{surf} = 90 K and E_p = 87 eV.

After the deposition of 10 ML MgO the diffraction pattern is not changed, which reflects the epitaxial growth of the oxide film, but the LEED spots becomes broader, in accordance with earlier observations [146]. Neither a lower magnesium deposition rate nor the growth of the films at elevated oxygen pressures (>1.2×10^{-7} torr) do significantly influence this overlayer LEED pattern. The MgO films present long-term stability and can be used also at elevated temperatures as high as 1000 K.

A change appears in the LEED patterns when the magnesia films are annealed at elevated temperatures above 1200 K. Figure 4.5 shows the LEED patterns of the Mo(100) substrate and of a 10 ML MgO film on Mo(100) before and after annealing at 1200 K. The LEED spots split and distinct crosses appear around each fundamental spot oriented along the [110] direction when the magnesia films are annealed at temperatures around 1200 K (cf. Figures 4.5c). This observation is in agreement with previous reports of Freund and coworkers. [154-156]. Similar results have also been reported for magnesia films grown on Fe(100) [157] and Ag(100) single crystal surfaces [158, 159] and were attributed to the formation of a mosaic structure spanned between a dislocation network that relaxes the strain in the oxide layer. The size of the LEED spot crosses depends on the inclination angle of the tilted regions [154].
As shown by Yan et al. [160], F centers appear on the MgO films annealed at elevated temperatures. Therefore, in this work defective MgO films produced by thermal annealing have been employed to investigate the adsorption and the photoreaction dynamics of methyl iodide molecules (Chapter 5).

The thermal annealing procedure employed in this investigation (also applied to obtain Figure 4.5c) consists in a fast heating of the sample to 1000 K with a heating rate of up to 5 K/s and a subsequent slow further temperature increase to about 1200 K with a rate of 0.3 - 0.5 K/s. We observed that a fast annealing (5 K/s) directly to 1200 K leads to a non-controllable preparation of the samples, due to the desorption of a significant part of the magnesia film as evidenced by post-annealing AES measurements [133].

Based on the previous results, the standard procedure employed for the MgO films preparation for the SFsMS experiments consists in Mg evaporation with a rate of 0.15 ML/min. During the Mg evaporation, the surface temperature and the oxygen background pressure are kept at 600 K and 2.5×10^{-7} mbar, respectively. In few preparations, a further annealing above 1180 K was applied to these films to produce defective surfaces (cf. Chapter. 5).

4.1.3 PES of Mo(100) covered by ultrathin MgO(100) films of variable thickness

In order to completely exclude the influence of adsorbates on the photoemission spectra, the surface sample was flash heated just before recording a spectrum (to 700 K in the case of a MgO/Mo(100) preparation and to 1200 K for the clean Mo(100) substrate). All photoemission spectra were recorded at 90 K by summing the photoelectron signal of 10^5 laser pulses.

The photoemission spectra are displayed on the electron kinetic energy scale. The energy of the final electronic state E_{final} is given by: $E_{final} = E_F + \Phi + E_{kin}$, with E_F representing the Fermi energy, Φ the surface work function, and E_{kin} the electron kinetic energy. The onset of the kinetic energy scale ($E_{kin} = 0$ eV) is set to the half-maximum of the lowest-energy edge of the spectra [92]. The presence of a shoulder at this lowest-energy edge in some spectra, however, leads to a rather large error in the deduced work function values (±0.15 to ±0.2 eV). The surface work function is obtained from the width of the reported spectra (which is here equal to the maximal kinetic energy $E_{kin,max}$), according to $\Phi = h\nu - E_{kin,max}$, with $h\nu$ being the total excitation energy, (one or two photon, respectively) (cf. Section 2.2.2).

In the following, the kinetic energy distribution of the photoelectron emission from a Mo(100) surface due to femtosecond laser irradiation will be presented as a function of the excitation energy and of the thickness of a covering MgO(100) ultrathin film. Excitation schemes will be derived on the basis of power dependence measurements and the determined work function change due to increasing magnesia layer thickness will be compared to theoretical predictions [161, 162].

4.1.3.1 Excitation energy dependent photoemission

The left column of Figure 4.6 displays the measured photoemission spectra obtained from a bare Mo(100) surface. At 4.71 eV excitation energy (Figure 4.6a, 263 nm center wavelength), a single narrow emission peak is observed extending from 0 to 0.4 eV electron kinetic energy. The power dependence of the emission at this wavelength indicates a one photonic transition as schematically depicted in the level diagram of Figure 4.7a (process I). From the width of this peak, the surface work function is determined to amount to 4.3 ±0.2 eV, which is in reasonable agreement with the reported literature value of 4.53 ±0.02 eV for the (100) surface of Mo [138].

At 3.72 eV excitation energy (333 nm), the Mo(100) spectrum changes considerably as can be seen from Figure 4.6b. Not only the emission range extend now up to electron kinetic energies of 3.05 eV, but the emission intensity is also reduced, as apparent from the increased noise level although the laser intensity has been increased by more than a factor of 10.

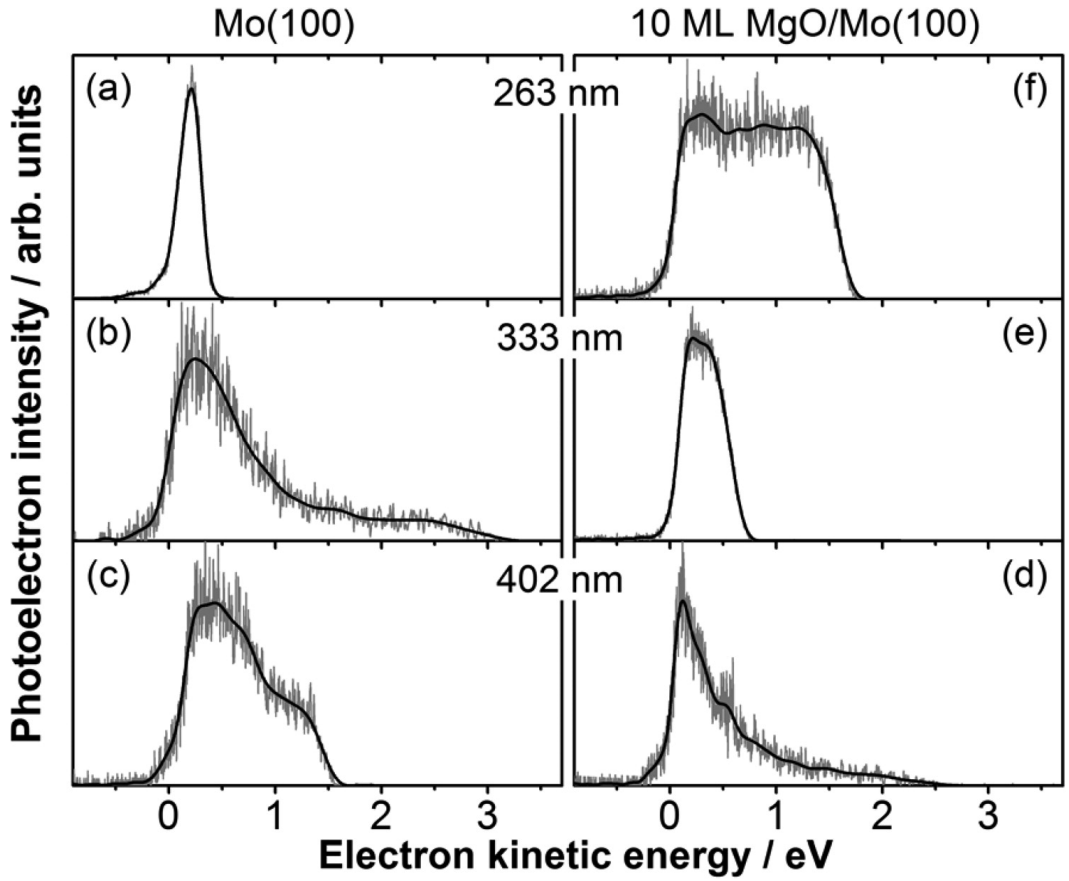

Figure 4.6 Femtosecond-laser photoemission spectra obtained at excitation wavelengths of 263, 333, and 402 nm from a bare Mo(100) surface (a-c) and from a Mo(100) surface covered by a 10 ML MgO(100) ultrathin film (d-f). Thin grey lines represent the experimental data; bold black lines were obtained by applying a low pass FFT filter to the data. The laser pulse energies employed to obtain the spectra were (a) 0.4 nJ, (b) 52 nJ, (c) 62 nJ, (d) 7 nJ, (e) 0.1 nJ, and (f) 0.1 nJ

The emission is clearly due to a two-photon excitation as depicted schematically in Figure 4.7a (process II). A surface work function of 4.4 ±0.2 eV is deduced from the width of this spectrum. Two-photon photoemission from bare Mo(100) is also observed at 3.09 eV (402 nm) excitation energy as shown in Figure 4.6c and schematically indicated in Figure 4.7a (process III).

The shape of this spectrum agrees favorably with previously reported two-photon photoemission spectra from polycrystalline molybdenum samples recorded at similar excitation energies [163].The work function corresponding to the width of this spectrum amounts to 4.5 ±0.2 eV and is thus also in agreement with the literature value [138].

Covering the molybdenum surface with an ultrathin film of magnesia is known to considerably reduce the work function of this surface [164]. For ionic oxides like MgO, this effect is particularly pronounced because of the electrostatic “compression” effect [165, 166].

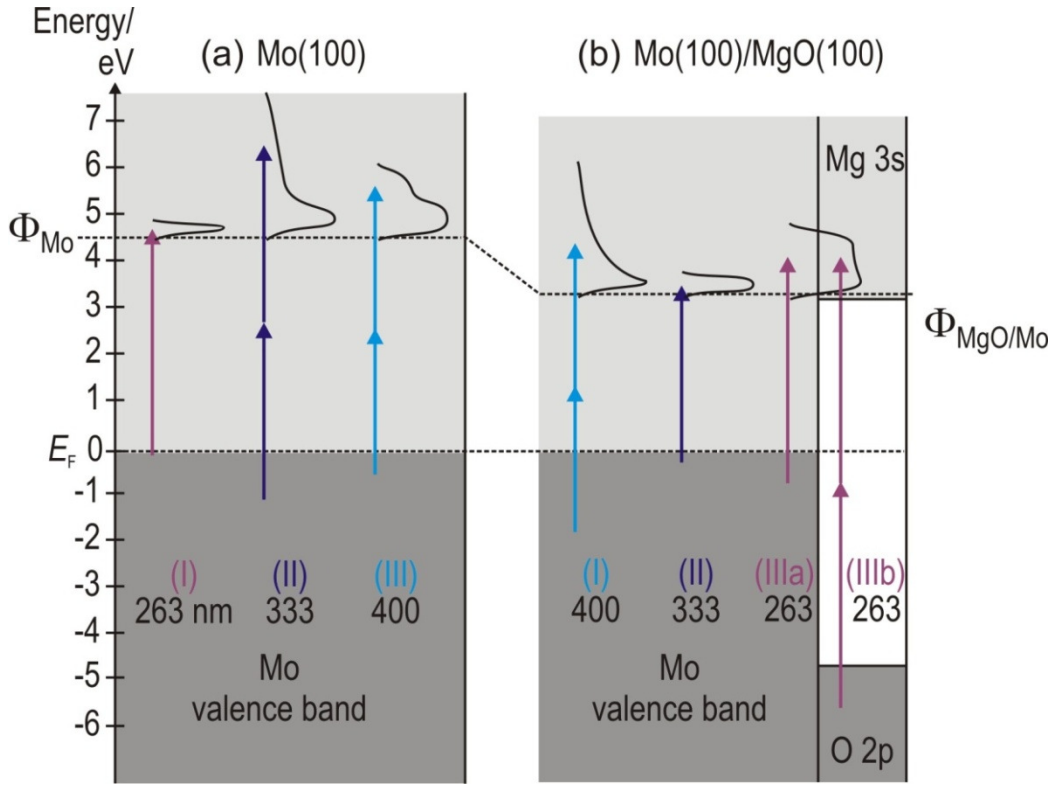

Figure 4.7 Schematic energy level diagram illustrating the assignment of the different excitation processes that lead to the observed photoemission signals of Figure 4.6: (a) for the bare Mo(100) surface and (b) for the 10 ML MgO(100) ultrathin film on Mo(100) at the three different excitation wavelengths.

In this mechanism, the oxide layer reduces the electronic charge spill over from the metal surface. As a consequence, the metal electrons are polarized toward the surface and the work function decreases [165]. For stoichiometric 10 ML MgO films on Mo(100) work function values around 2.7 to 3.5 eV have been reported [164, 167]. For the (100) surface of an MgO crystal a value of 2.7 eV was measured by vacuum ultraviolet photoemission spectroscopy (UPS (He I)) and MIES [164]. In the same investigation, the bandgap at the MgO(100) surface was determined to amount to 6.7 eV with the MgO O2p valence band starting around 4.5 eV below the Fermi level, as indicated in the schematic level diagram in Figure 4.7b [164, 168, 169]. Therefore, single photon photoemission from MgO should not be observed at the excitation energies employed in the present investigation. The fs-laser photoemission spectra obtained here from a 10 ML MgO(100) ultrathin film are shown in Figure 4.6d,f.

The corresponding power dependencies of the photoemission intensity for the different excitation wavelengths are depicted in a double logarithmic representation in Figure 4.8. The lowest excitation energy of 3.09 eV (402 nm) is neither sufficient for a single nor for a two-photon electron emission from MgO. Nevertheless, a photoemission spectrum is observed with electron emission up to kinetic energies of about 2.7 eV, as shown in Figure 4.6d. The power dependence of this photoemission signal (cf. Figure 4.8) indicates a two-photon transition (slope $n = 2.15 \pm 0.21$). A potential explanation for this photoemission is MgO surface

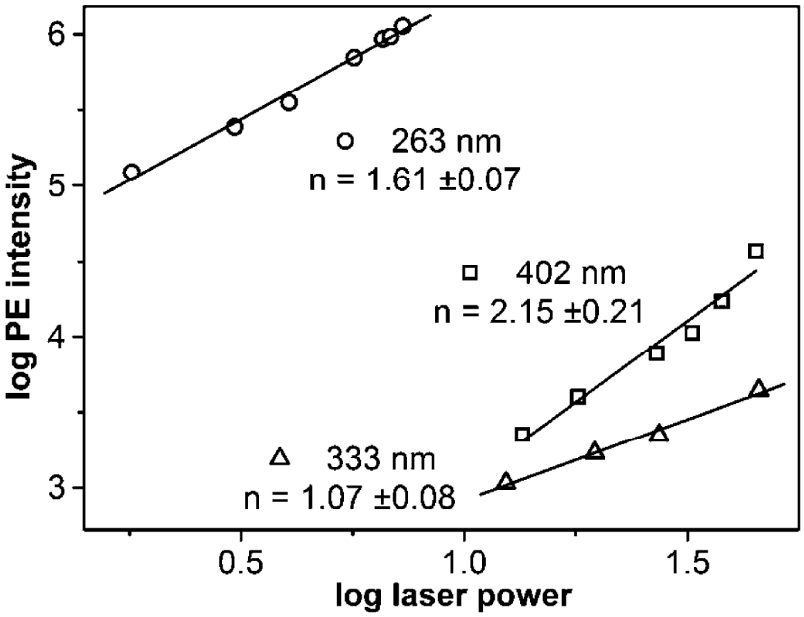

Figure 4.8 Power dependences of the integral photoemission signals obtained from the 10 ML MgO film on Mo(100) for the different excitation wavelength (cf. Figure 4.6d–f). See text for details.

imperfection, which might induce defect states within the MgO band gap [167]. However, detailed studies of MgO films prepared under various conditions show that the preparation procedure does not notably influence the spectrum in Figure 4.6d, as long as no oxygen vacancies (F-centers) are generated [68]. These results, in conjunction with the wavelength dependence of the photoemission presented below, lead us to the conclusion that this electron emission (Figure 4.6d) has to be assigned to originate from the valence band of the molybdenum substrate as illustrated by process I in Figure 4.7b, with only minor contributions from MgO imperfections. The magnesia film lowers the surface work function to 3.5 ±0.2 eV as deduced from the width of the photoemission spectrum in Figure 4.6d. A further effect of the magnesia layer is a reduced emission intensity in the high kinetic energy part of the spectrum (electrons originating from energies close to the Fermi level) as is apparent from the spectrum in Figure 4.6d which is compared with the two-photon photoemission spectra from bare Mo(100) in Figure 4.6b,c.

Figure 4.6e shows the photoemission spectrum from 10 ML MgO/Mo(100) obtained with 333 nm (3.72 eV). The power dependence in Figure 4.8 indicates a single photon excitation mechanism (cf. Figure 4.7b, process II), thus supporting the assignment of this emission signal to electrons originating from the molybdenum valence band as well.

Finally, the photoemission spectrum due to 263 nm (4.71 eV) excitation is shown in Figure 4.6f. The corresponding power dependence in Figure 4.8 is not as unambiguous as for the other excitation energies and exhibits a slope of $n = 1.61 \pm 0.07$. A potential interpretation might consider two excitation mechanisms contributing to this emission signal: (i) Single photon photoemission of electrons from the molybdenum valence band (process IIIa in Figure 4.7b). To this end, the spectrum might be compared to the two-photon photoemission

spectrum in Figure 4.6c that covers the same initial state energy range. (ii) Two-photon photoemission of electrons originating from the MgO O2p valence band states which are accessible for 9.42 eV (2×4.71 eV) two-photon excitation (process IIIb in Figure 4.7b). The vacuum ultraviolet photoemission spectra (UPS (He I)) from MgO ultrathin films indicate a steep increase in photoelectron emission intensity at energies covering the begin of the oxygen valence states of magnesia [164]. UPS (He I) and MIES data reported in the literature [164] for MgO films of comparable thickness to those investigated here, however, do not indicate any electron emission from states between the Fermi energy and the onset of the O2p valence band and thus clearly reflect the wide band gap insulating nature of such ultrathin films. Also, scanning tunneling spectroscopy (STS) investigations of MgO layers on Ag(100) indicate that the ultrathin magnesia films can be considered perfect insulators, if they consist of 3 ML or more [139, 169]. In this respect, it is quite surprising that the major contributions in our fs photoemission spectra have apparently to be assigned to electrons originating from the molybdenum substrate d band states. However, it is important to note that, whereas MIES and STS are strictly surface sensitive analytical methods, the penetration depth of light in the vacuum ultraviolet (UPS He(I), 21.2 eV) and also in the ultraviolet spectral range (3 - 4.7 eV) employed in the present study is considerably larger than the thickness of the MgO film thickness [72] enabling the excitation of the Mo metal substrate in both cases. Therefore, to find an explanation for the fact that electron emission from the MgO-covered Mo substrate is observed at energies close to the Fermi level in the present investigation, but not in UPS (He I) studies, the electron transport function, i.e., primarily the mean free path of electrons in solids as a function of their kinetic energy, is considered [72]. Electrons liberated by UPS (He I) excitation from molybdenum valence band states in the energy range of the MgO band gap possess kinetic energies around 14 - 18 eV. In contrast, the kinetic energy of the electrons assigned to originate from Mo(100) d band states in the present investigation ranges between 0 and 2.5 eV (cf. Figure 4.6d-f). The mean free path of 14 - 18 eV electrons is only 2 - 4 ML, and these electrons emitted by vacuum UV (He I) irradiation are thus most likely stopped within the 10 ML MgO overlayer on Mo. Electrons with kinetic energies around 1 - 2 eV, however, have a mean free path of more than 100 ML [72]. Therefore, these low energy electrons emitted by the fs-laser irradiation are able to pass the ultrathin MgO film and are detected in the photoemission spectra of Figure 4.6d-f. This interpretation does also account for the reduced emission intensity in the “higher kinetic energy” (1 - 2.5 eV) part of the 10 ML MgO spectrum in Figure 4.6d compared to the emission spectra from bare Mo(100) in Figure 4.6b,c that covers a similar electron kinetic energy range because in this energy range, the electron mean free path is a very steep function of the kinetic energy.

4.1.3.2 Coverage dependent photoemission

Fs photoemission spectra that have been obtained by successively increasing the magnesia film thickness monolayer by monolayer are displayed in Figure 4.9 for excitation wavelengths of 263 and 333 nm. The spectra recorded from 1 ML MgO on Mo(100) are rather similar to the spectra of the bare metal surface. Also, the surface work function remains almost unchanged as apparent from the width of the spectra.

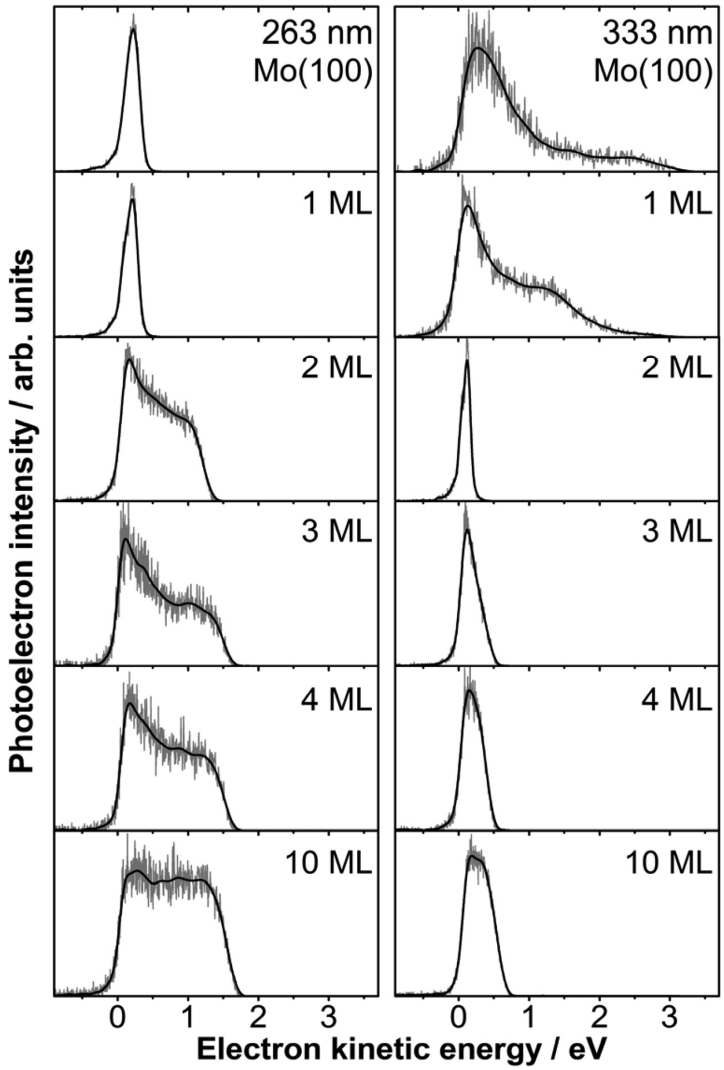

Figure 4.9 Fs-laser photoemission spectra obtained for different MgO layer thickness. Left column: 263 nm excitation wavelength. Right column: 333 nm excitation wavelength. The topmost spectra were recorded from the bare Mo(100) surface (cf. Figure 4.6). The MgO(100) layer thickness of the subsequent spectra is as indicated. Thin grey lines represent the experimental data; bold black lines were obtained by applying a low pass FFT filter to the data. The laser pulse energies employed to obtain the spectra at 263 nm excitation wavelenght are: 0.4 nJ for Mo and 1 ML MgO, 0.1 nJ for >1 ML MgO; at 333 nm excitation wavelength: 52 nJ for Mo and 1 ML MgO, 4 nJ for 2 ML, 0.3 nJ for 3 ML, and 0.1 nJ for >3 ML MgO.

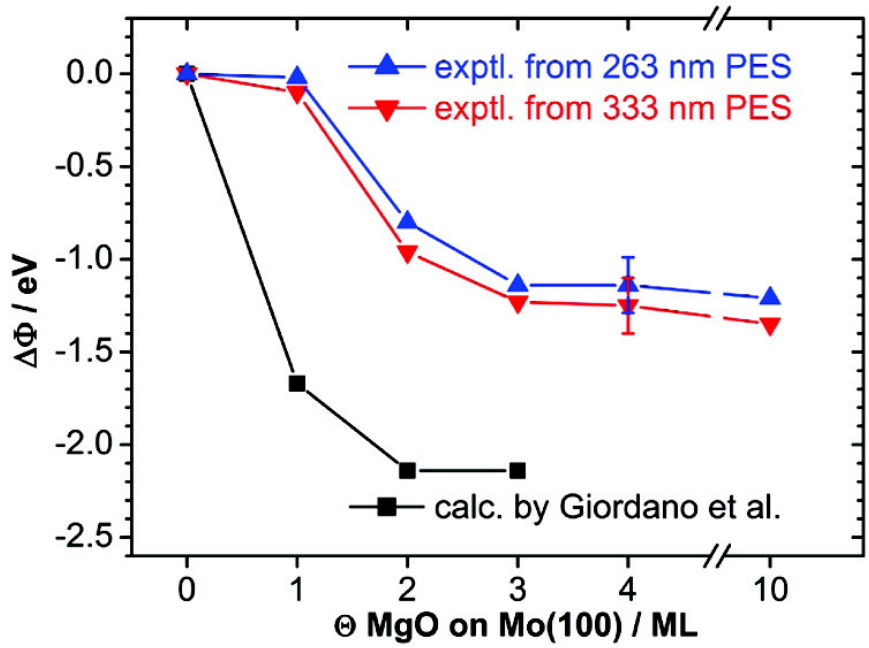

Figure 4.10 Change of the electronic work function Δφ of the Mo(100) surface as a function of the number of MgO(100) overlayers Θ. The experimental data obtained with 263 nm (blue triangles) and 333 nm (red upside-down triangles) excitation wavelength, respectively, are compared to calculated values reported in Reference [161] (black squares). Representative experimental error bars are shown at 4 ML coverage.

At 2 ML MgO coverage, however, the kinetic energy distribution of the photoemission considerably changes. This change is due to a reduction of the surface work function by about 1 eV. As a consequence, the 263 nm emission spectrum starts to contain contributions from the two-photon excitation of MgO O2p valence electrons as discussed above. In contrast, the 333 nm photoemission spectrum narrows because single photon emission of Mo valence band electrons becomes amenable for excitation with 3.72 eV photons (and dominates in the spectrum) at the reduced work function. For coverages larger than 2 ML up to 10 ML the photoemission spectra are rather similar with only slight changes in appearance for 263 nm excitation (Figure 4.9). These differences might tentatively be assigned to an increasing contribution of the two-photon emission from MgO valence band states with increasing layer thickness, as observed in UPS measurements on ultrathin magnesia films on Fe(100) [170].

The relative changes of the surface work function, ΔΦ, as a function of the MgO layer thickness Θ, deduced from the spectra in Figure 4.9, are plotted in Figure 4.10 together with the theoretically predicted values from the work of Pacchioni and co-workers [161].

In the theoretical prediction, Φ decreases up to an MgO film thickness of 2 ML by 2.1 eV compared to the bare Mo(100) surface and remains constant afterward. The experimental results of the present investigation confirm the rapid decrease of Φ with the deposition of the first few monolayers. However, in the experiment, Φ decreases up to an MgO film thickness of 3 ML by only about 1.3 eV compared to the bare Mo(100) surface and remains constant afterward. Thus, the observed maximum decrease in the surface work function due to an ultrathin magnesia overlayer is considerably smaller than theoretically predicted (cf. Fig-

ure 4.10). It has to be noted, however, that the work function of metal oxide surfaces is known to be extremely sensitive to the preparation procedure and the analytic method [142].

Furthermore, the very first magnesia ML changes Φ only slightly in the experiment. Φ starts to decrease considerably with the second MgO layer, whereas, theoretically, already the first ML is predicted to lower Φ considerably. The reason for the difference in the influence of the first MgO monolayer on the electronic structure of the surface can be explained by an imperfect geometric arrangement of this layer in the experiment. Previous LEED and scanning tunneling microscopy (STM) investigations of MgO(100) on Mo(100) indicate that after deposition of approximately one monolayer, the film still exhibits large holes, confined by nonpolar [100] and polar [110] oriented edges [147, 154]. The incompleteness of the first monolayer (90% fractional coverage) governed by patches with 2 ML thickness has also been observed for MgO on Ag(100) [171]. After deposition of 2 ML MgO, the metal surface is completely covered with MgO [154, 169]. With the deposition of the second monolayer, MgO films on Mo(100) were furthermore found to exhibit a distinct moiré-type superperiodic structure comprising tilted MgO facets [154, 156]. At even larger coverages (> 5 - 7 ML), the formation of a mosaic structure has been observed that is spanned between a dislocation network which relaxes the strain in the oxide layer (due to 5% lattice mismatch between Mo(100) and MgO(100)). A mean domain size of 55 Å has been reported for the mosaic structure [154, 156]. A similar mosaic pattern has also been observed for MgO growth on Ag(100) (3.1% lattice misfit) [158]. Above 7 ML film thickness, the oxide was found to gradually flatten and the global roughness to decrease, indicating flat and defect-poor surface structure [154]. However, these structural transformations at coverages above 2 ML are not reflected in the photoemission spectra recorded in the present investigation.

The coverage dependent photoemission results are also corroborated by UPS experiments of MgO on Fe(100) [170]. In these experiments, very little modification is seen in the emission close to the Fermi energy (between 0 and 3.5 eV electron binding energy) for low coverages of 0.5, 1, and 2 ML MgO. The major modification at these coverages consists in the appearance of an intense emission centered at approximately 5.5 eV, which is characteristic of highly hybridized O2p and Mg3s valence band states of the MgO film. Furthermore, it is interesting to note that while photoemission experiments yield information about the integral surface work function, Kelvin probe force microscopy measurements on cleaved single crystal MgO(100) surfaces reveal local work function differences with deviations of up to 1.5 eV for low-coordinated sites like steps, kinks, and corners and, even more importantly, for metal ion vacancies with locally increased electronic charge [172].

4.2 Gold films on a molybdenum single crystal surface

For the investigation of photoinduced reaction dynamics of methyl halide molecules on metallic supports, an Au surface was chosen. For this purpose, Au films were grown on Mo(100). These films were prepared with a low Au deposition rate of 0.0125 ML/min. The small deposition rate was chosen because the gold source was also employed for the generation of magnesia supported Au nanoparticles (cf. Section 4.3), which required a high accuracy and reproducibility in preparing nanoparticles by deposition of low Au coverages. Such small deposition rates have a central influence on the surface structure periodicity. Unfortunately, no reports are available regarding gold films grown on Mo(100) at low deposition rates. Thus, no direct comparison is possible between the literature and the surface structures obtained in the present work. The only Au/Mo(100) surface structure investigation was performed for Au coverages up to 0.5 ML [173]. However, Pd, Cu, Ag and Au present similar structural features when deposited on the refractory metal supports. Therefore, the structure of the Au films on Mo(100) obtained in this work will be compared to those obtained for other noble metals deposited on Mo(100).

4.2.1 Preparation of Au films on Mo(100)

Prior to the gold film deposition, the surface was cleaned by heating the Mo(100) crystal to 2000 K by means of electron bombardment. Subsequently, the surface temperature was ramped down to 1000 K. In order to avoid the surface contamination, the Mo crystal was held at 1000 K by resistive heating until the background pressure was restored ($< 5\times10^{-10}$ mbar). Subsequently the surface was cooled down to the deposition temperature of 400 K.

For gold deposition, the evaporator presented in Section 2.3 was employed. The gold evaporator was initially outgased and gives stable deposition rates over extended periods of time. In order to ensure the constant evaporation rate, prior to each deposition, the Au oven was preheated for 15 min. Subsequently, the substrate was positioned 10 mm apart from the gold source and the support was held at 400 K. The gold evaporation was performed at normal incidence. The maximum background pressure in the UHV chamber reached throughout the gold evaporation process was less than 2×10^{-9} mbar.

The deposition rate was calibrated by monitoring the intensities of the Auger transitions of Au N_7VV at 69 eV and Mo $M_5N_3N_5$ at 186.5 eV during direct evaporation of Au onto Mo(100) for different deposition times. Figure 4.11 displays an Auger electron spectrum recorded from 2 ML Au evaporated onto Mo(100). As reference, an Auger electron spectrum recorded from a clean Mo(100) surface is presented as well. After evaporation of 2 ML gold, the intensity of the molybdenum MNN Auger transitions are slightly diminished, while the new peak at 69 eV becomes dominant. The inset in Figure 4.11 shows the Au to Mg Auger intensity ratio as a function of Au deposition time. A gradual increase of the gold coverage on the molybdenum surface led to a brake-point in the intensity ratio of the Au (69 eV) to Mo (186.5 eV) Auger transitions, which coincided with the exact amount of gold needed to complete the first Au layer on Mo(100). The brake point in the Au/Mo AES ratio appeared after a

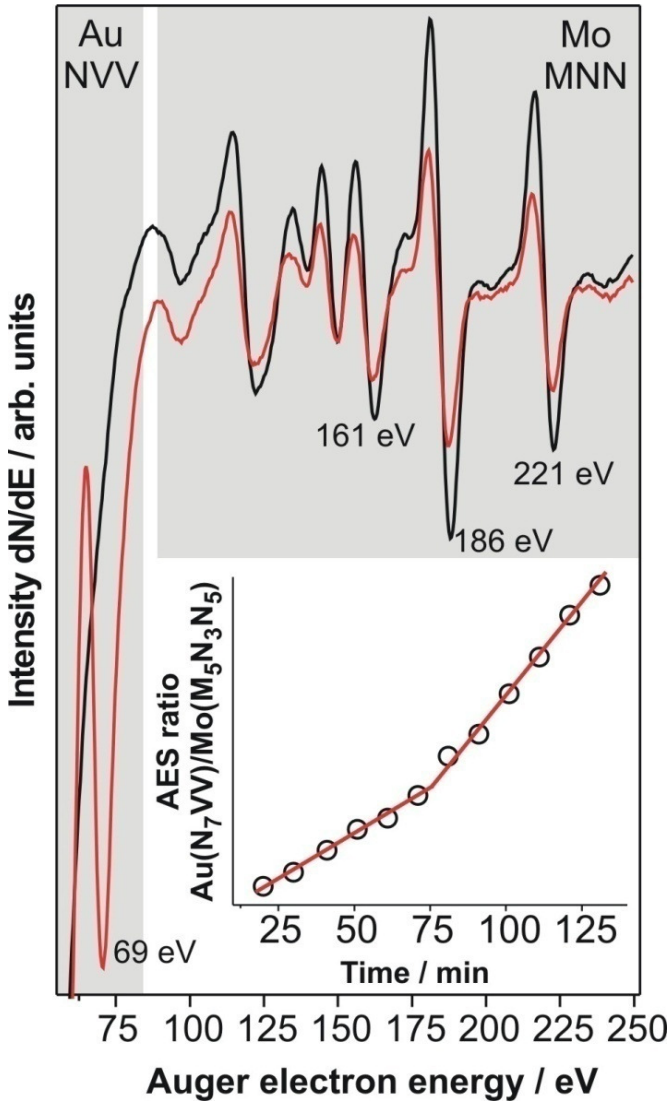

Figure 4.11 Auger electron spectra recorded from clean Mo(100) surface (black curve) and from a 2 ML Au film on Mo(100) (red curve). The inset shows the Au(N_7VV) to Mo($M_5N_3N_5$) AES ratio as a function of Au deposition time. The break point in the AES ratio plot corresponds very closely to the initial appearance of the Au multilayers.

deposition time of 80 min indicating a deposition rate of 0.0125 ML/min.

The electronic structure of the Au overlayer was analyzed by means of fs-laser photoemission spectroscopy. Figure 4.12 displays the photoemission spectra recorded at 333 nm and 263 nm excitation wavelength. The sample surface consisted of a 10 ML Au film on Mo(100). In order to completely exclude the influence of adsorbates on the photoemission spectra, the surface sample was flash heated to 800 K just before recording a spectrum. The photoemission spectra were recorded at 90 K by summing the photoelectron signal of 10^5 laser pulses. Both spectra in Figure 4.12 were plotted on the initial state energy scale ($E_F = 0$)

The measured photoemission spectra (Figure 4.12) exhibit similar features as the 2PPS spectra that have been previously obtained by Cao et al. from an Au(111) surface [134]. The flat part at the high energy side (0 to -2 eV) represents the photoemission from Au 6s elec-

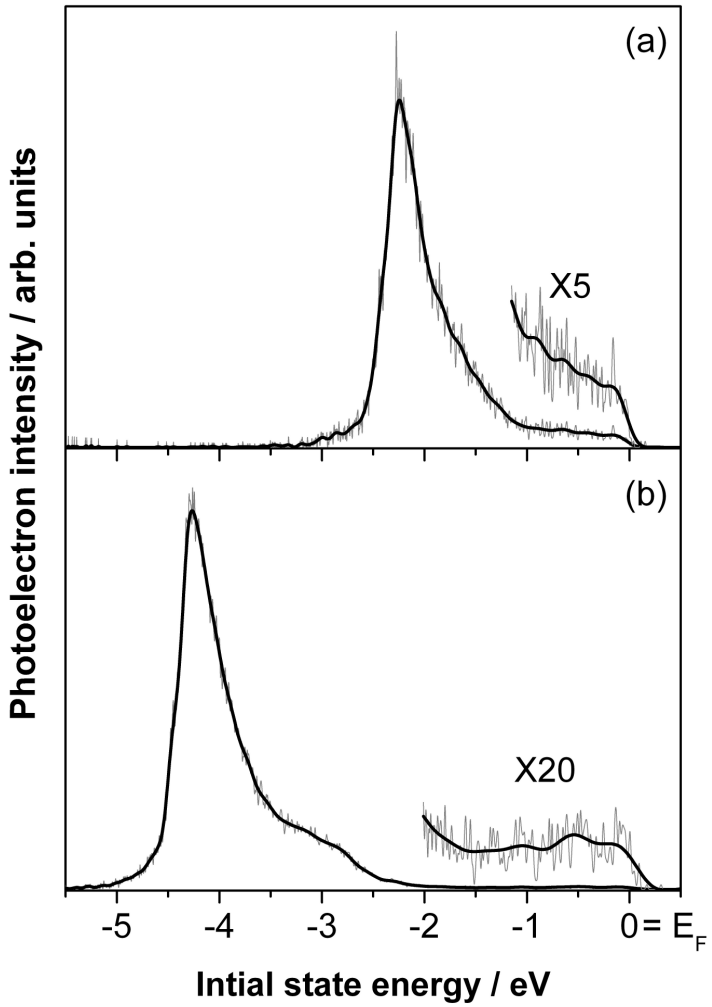

Figure 4.12 Fs-laser photoemission spectra obtained from 10 ML Au grown onto Mo(100) at excitation wavelengths of: (a) 333 nm and (b) 263 nm. Thin grey lines represent the experimental data; bold black lines were obtained by applying a low pass FFT filter to the data. The laser pulse energies employed to obtain the spectra were 130 nJ at 263 nm excitation and 300 nJ at 333 nm excitation, respectively. The high energy part of the spectrum is presented separately and is multiplied by a factor of: (a) 5; (b) 20.

trons (s-p band). The photoemission feature between -2 and -3 eV is attributed to the upper d bands [174], while the peak starting at -3.5 eV is assigned to the Au $5d_{5/2}$ bands [174].

The surface work function Φ is determined from Φ = 2hν - W, where W is the width of the spectrum and $h\nu$ is the excitation energy (cf. Section 2.2.2). The work functions deduced from Figure 4.12 are 5.03 ±0.2 eV and 5.02 ±0.2 eV at the excitation wavelengths of 333 nm and 263 nm, respectively. These values are within 0.2 eV of that previously published by Hansson et al. (5.22 ±0.04 eV) [175].

Finally, the shape of the two-photon photoemission spectra of the 10 ML gold film on Mo(100) (Figure 4.12) are discussed. As this system also has not been investigated before by fs-laser photoemission, the pertinent features will be discussed here in some detail. Although the general appearance of the spectrum is quite similar to that obtained previously with the

same method from an Au(111) surface [134], the strong decrease in photoemission intensity with increasing electron kinetic energy is rather striking. Several reasons might be responsible for the deviation in the photoemission intensity distribution:

(i) Apparently, also in this case, the fs-laser photoemission spectrum constitutes a convolution of the photoemission from the gold overlayer and from the molybdenum substrate. It is, however, hard to decide to which extent both metals contribute to the observed photoemission.

(ii) If the shape of the spectrum is assumed to largely reflect the electronic band structure of gold, then the low intensity part at the high kinetic energy side can be assigned to the two-photon photoemission from the Au 6*s* electrons (*s*-*p* band), which has a comparably low density of states. In contrast, the pronounced peak at lower energy originates from electrons emitted from the Au 5d band with a considerable larger density of states [134].

(iii) The lifetime of the excited states is considerably larger for states close to the Fermi energy E_F and decreases rapidly with increasing distance in energy to E_F [134]. Thus, a two-photon photoemission process involving intermediate electronic levels near E_F and leading to photoelectrons with low kinetic energy has a considerably higher probability than two-photon photoemission via intermediate states high above E_F that leads to photoelectrons with high kinetic energy.

(iv) In the kinetic energy range around 1 to 5 eV the electron mean free path in materials is a very steep function of the kinetic energy [72]. Therefore, the photoelectrons with the lowest kinetic energies that are emitted by the fs-laser irradiation might easily penetrate from deep in the bulk metal to the vacuum, whereas the higher energy electrons in the -2 to 0 eV range are considerably attenuated. This energy dependence of the electron mean free path, thus, also strongly contributes to the observed photoemission intensity distribution with particularly high emission intensities at very low electron kinetic energies.

4.2.2 Structure of Au films grown on Mo(100)

In this section, the investigation of the structure of Au films consisting of 1 ML and of 10 ML Au on Mo(100) by means of LEED is presented. Depending on the growth parameters, i.e. the deposition rate, the deposition temperature, and the annealing temperature, gold films with different structure can be obtained on Mo(100). A similar strong dependence of the thin film structure on the growth parameters was reported for different transition metals deposited on single crystal refractory metal substrates, e.g., Pd/Nb(110) [176, 177], Pd/Ta(110) [177, 178], Pd/Mo(110) [179], Pd/W(110) [180], Cu/W(100) [173, 181], Ag/W(100) [173, 181, 182], Ag/Mo(100) [173, 181], Au/W(100) [173], Au/Mo(100)[173], Au/Mo(110)[183]. The only exception so far, is the fact that Pd, Cu, Ag, and Au exhibit comparable features when they are adsorbed at submonolayer coverage on Mo(100) [173, 184, 185]. However, at multilayer coverage, the surface structure of these films depends strongly on the growth parameters as previously mentioned.

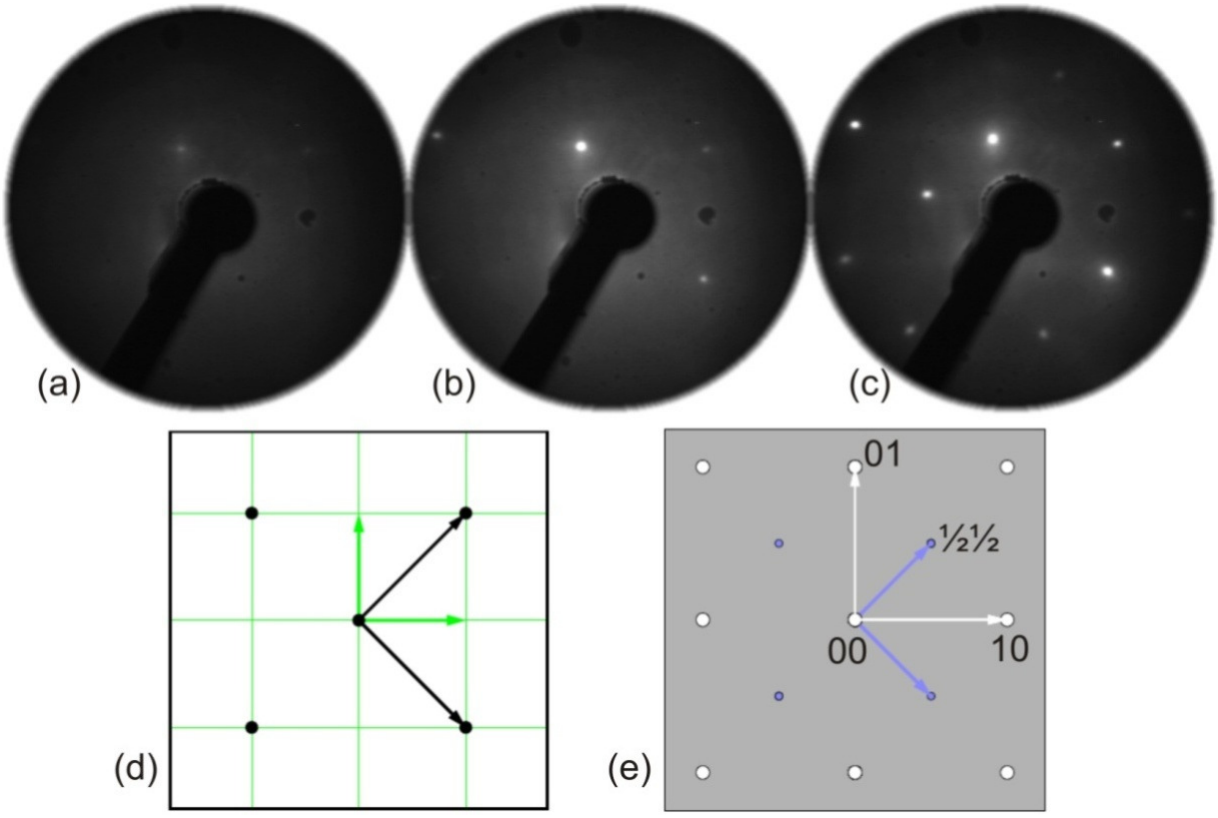

Figure 4.13 LEED images recorded from: (a) 1 ML Au on Mo(100); (b) 1 ML Au on Mo(100) annealed at 800 K for 1 min; (c) 1 ML Au on Mo(100) annealed at 1000 K for 1 min. The LEED patterns were recorded by E_P = 87 eV. Simulation of c(2×2) Au/Mo(100) structure: (d) real lattice: the black points represent the Au atoms adsorbed on the Mo substrate (thin line squares); (e) reciprocal lattice: the substrate spots are represented by the open circles while the Au spots are represented by the filled circles.

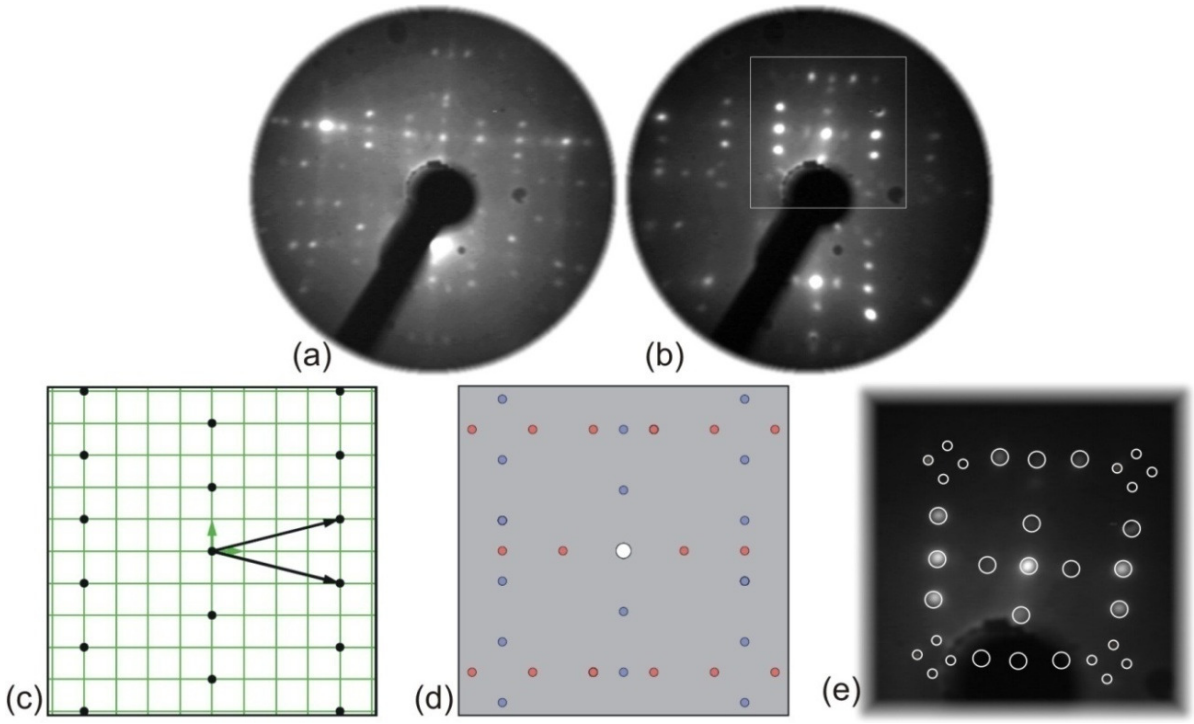

Figure 4.14 LEED images recorded from: (a) 10 ML Au on Mo(100), $E_P = 87\ eV$; (b) 10 ML Au on Mo(100) annealed at 1000 K for 10min, $E_P = 30\ eV$. Simulation of c(8×2) Au/Mo(100) structure: (c) Real lattice: the black points represent the Au atoms adsorbed on the Mo substrate (thin line squares); (d) Reciprocal lattice: the 00 reflex is represented by the open circle while the Au domain spots are represented by the filled circles. (e) Enlarged view into the domain structure marked in (b). For the sake of clarity the diffraction spots were marked with open circles.

In this work, gold is evaporated with a rate of 0.0125 ML/min on the Mo(100) substrate held at 400 K. Figure 4.13a-c shows LEED images recorded at 90 K from 1 ML gold coverage at different annealing temperatures. As can be seen, the freshly prepared surface (Figure 4.13a) appears amorphous because just a pale spot originating from the 00 reflex appears in LEED. After 1 min annealing time at 800 K, the diffraction pattern corresponding to the (1×1) Mo(100) structure can be observed in Figure. 4.13b.

Further annealing at 1000 K for 10 min leads to the appearance of a c(2×2) structure in the LEED image as can be seen in Figure 4.13c for the 1 ML Au on Mo(100) preparation. A simulation of the c(2×2) LEED pattern employing the software LEEDpat 2.2[6] is shown in Figure 4.13d,e. A similar c(2×2) structure was reported for Cu and Ag adsorbed at submonolayer coverage on Mo(100) as well, and was in this case attributed to a surface rearrangement [181, 186]. Later investigations showed that the c(2×2) structure appears also for 0.5 ML Au/Mo(100) and it was attributed to the formation of a surface alloy in this case [187, 188]. First principle calculations show that a c(2×2) substitutional surface alloy is energetically favored compared to overlayer structures [184]. Charge transfer from the Mo substrate to the

[6] PC-based software tool to visualize and analyze LEED patterns of substrates and overlayers (developed at Fritz-Haber-Institut, Berlin, 2009).

adatoms is responsible for stabilizing the c(2×2) vacancy array, in which the adatoms are incorporated. Furthermore, the atomic radius of Au (1.44Å) is comparable with the atomic radius of Mo (1.39Å), which allows Au atoms to insert within the surface layer and to form a planar alloy structure.

As previously reported by Man et al., the alloy forms within terraces when the deposited Au atoms exchange with Mo atoms in the surface layer [188]. The displaced Mo atoms join with Au atoms to form alloy islands concurrently. Consequently, flat initial surfaces convert into a two-level alloy surface. The alloy formation on the Mo(100) substrate was observed at higher temperature preparations, i.e. after deposition or annealing at elevated temperatures. Surface alloy formation at room temperature was also reported for fcc (100) substrates, e.g., Au [189] and Pd [190] on Cu(100), Mn on Pd(100) [191], and Au on Mn(100) [192]. The alloy formation at room temperature or at lower temperatures in this cases implies that the exchange barrier on the fcc (100) surface is smaller than on the bcc Mo(100) surface. The difference between the formation kinetics on a bcc Mo(100) and a fcc (100) metal surfaces is consistent with the difference in the substrate bulk cohesive energy that is 6.82 eV/atom for Mo as compared to 2.95 eV/atom for Ag, 3.49 eV/atom for Cu and 3.89 eV/atom for Pd [193].

A further increase in the Au coverage on the Mo(100) substrate induces another structural change of the surface. Figure 4.14a,b shows the diffraction pattern obtained from a 10 ML Au film on Mo(100). The freshly prepared surface appears amorphous, similar to the 1 ML preparation (cf. Figure 4.13a). After 1 min annealing at 1000 K, a new structure appears in the LEED image, which becomes more apparent when the annealing time is increased to 10 min (Figure 4.14b). In Figure 4.14c,d a LEEDpat 2.2 simulation of a c(2×8) Au/Mo(100) structure is shown. The simulated c(2×8) structure resembles the marked structure presented in Figure 4.14b (see also Figure 4.14e).

LEED and low energy electron microscopy investigations demonstrate for the case of Pd adatoms adsorbed on the Mo(100) that a change from a c(2×2) to a c(2×8) structure occurs by increasing the Pd coverage above 0.7 ML [184]. The c(2×8) structures was observed just for a deposition rates below 0.033 ML/min at substrate temperatures larger than 800 K, whereas at a higher deposition rate the surface structure is significantly changed. The Pd/Mo(100) c(2×8) structure persists at coverage of 2.5 ML. The surface structure at coverages higher than 2.5 ML Au was not reported.

A detailed analysis of the LEED pattern obtained in the present work reveals a more complicated structure. Nevertheless, the obtained surface structure at 10 ML Au coverage could be attributed to a degenerate c(2×8) structure as observed by Wu et al. [184]. The LEED patterns presented in Figure 4.14 are perfectly reproducible and are not influenced by a further thermal treatment of the surface, i.e. a higher preparation temperature or a longer annealing time.

4.3 Magnesia supported gold clusters

Magnesia supported gold clusters are employed to cover the particle size range with properties intermediate between the insulating magnesia and the metallic gold surface with respect to the investigation of methyl halides photoreaction dynamics at different surfaces.

In principle, two different techniques are used in order to deposit clusters onto a surface. The first method makes use of a diffusion process. Atoms evaporated from the gas-phase are initially trapped to the nucleation sites on the surface. The growth of clusters results from the diffusion between the nucleation centers and the subsequent association of free atoms and trapped ones [194]. In the second method, clusters are prepared in the gas-phase, and then they are mass-selected either by means of a quadrupole mass filter or by a time-of-flight spectrometer and are finally deposited on the surface (cf. Chapter 2). When the clusters are deposed on surfaces under soft-landing conditions, i.e. $\leq$ 1 eV/atom, they are likely to remain intact and fragmentation is avoided [148, 167, 195].

Depending on the preparation procedure, i.e. the deposition rate, the oxygen background pressure, the deposition, and the annealing temperatures, subsequent electron sputtering or alkaline metals deposition, the magnesia films could contain defects as: steps, kinks adatoms and vacancies. Experiments in conjunction with theoretical calculations have shown that the Au atoms and clusters are strongly adsorbed at oxygen vacancies [165, 196]. It was demonstrated experimentally by means of STM that the oxygen vacancy are preferably located at the steps, terraces and corners on magnesia [197]. They have different charge states: 0, +1, +2 [149, 197].

Concerning magnesia supported gold clusters, a number of investigations have been performed to get insights into the adsorption energy and the charge state of the Au clusters adsorbed on the MgO surface. Experiments in conjunction with theoretical calculation [194, 198-201] have shown that the adsorption energy of Au clusters is the smallest on an MgO single crystal, increases on F centers on an MgO single crystal, and is even larger for adsorption on MgO thin films on Mo(100). The largest adsorption energies have been determined for F centers on MgO thin films on Mo(100). On a single MgO crystal the Au clusters or nanoparticles are neutral, but they could become charged through partial electron transfer from a magnesia oxygen vacancy [202-204]. The partial charge of the supported Au clusters increases from a substrate consisting of a thin MgO films on Mo(100) to the F centers on a MgO(100) single crystal to the F centers on MgO thin films on Mo(100) [198]. A further increase is observed, if the MgO film thickness on the Mo(100) substrate is decreased [205, 206].

In this work, gold nanoparticles were prepared via vapor deposition from the gas-phase onto MgO films held at 90 K. The Au deposition rate was calibrated by monitoring the AES ratio of the Au (69 eV) to the Mo (186.5 eV) peak intensities during direct evaporation of Au on Mo(100), as described in Section 4.2. A small deposition rate, i.e. 0.0125 ML/min was used in order to have a high accuracy and reproducibility in preparing Au nanoparticles.

4.3.1 Fs-Laser photoemission from magnesia supported gold clusters

The magnesia supported gold clusters were investigated by means of femtosecond laser photoelectron spectroscopy. Figure 4.15 shows the fs-laser photoemission spectra recorded from MgO/Mo(100) substrates covered with varying amounts of gold (up to 0.25 ML). From pre-

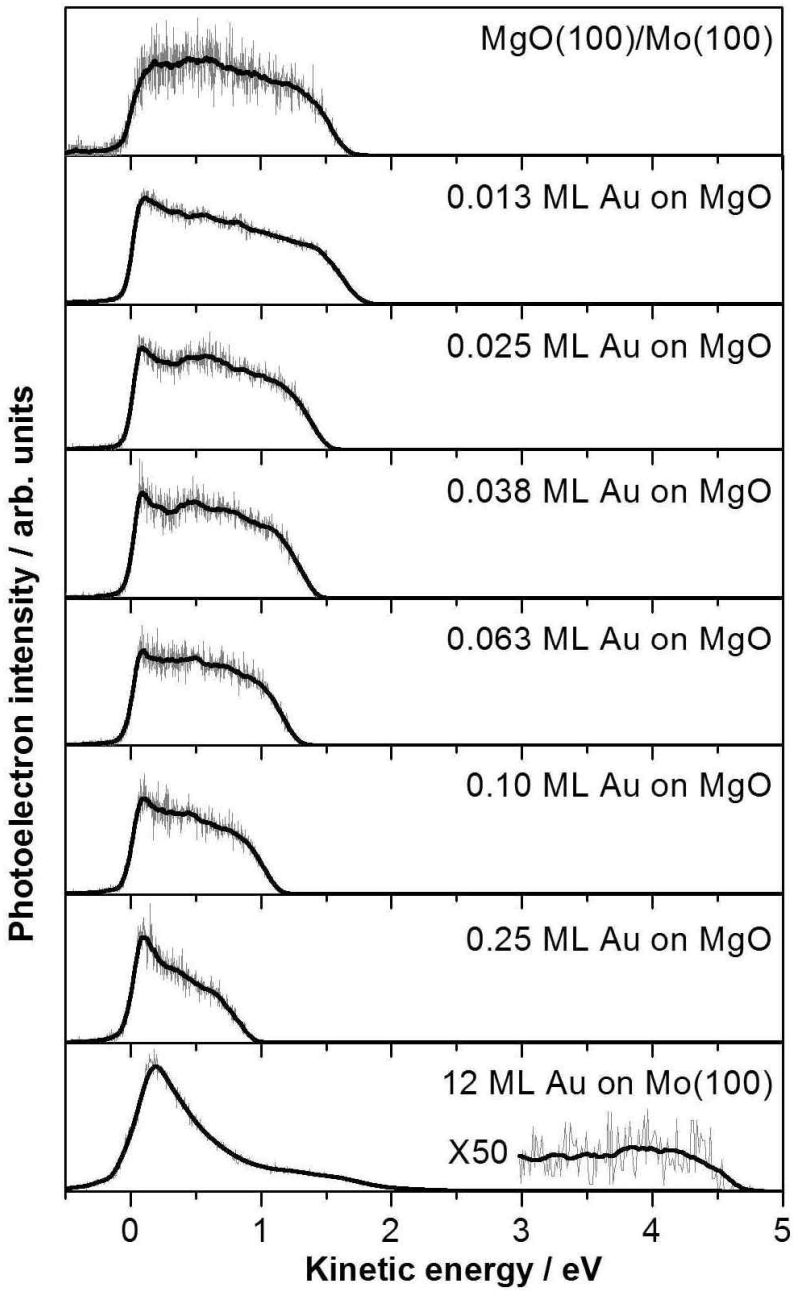

Figure 4.15 Fs-laser photoemission spectra recorded at 266 nm excitation wavelength from magnesia supported gold clusters for various nominal gold coverages as indicated. Also shown are the photoemission spectra obtained from a bare MgO(100)/Mo(100) substrate and from a gold film (12 ML Au/Mo(100)). Thin gray lines represent the experimental data; bold black lines were obtained by applying a low pass FFT filter to the data.

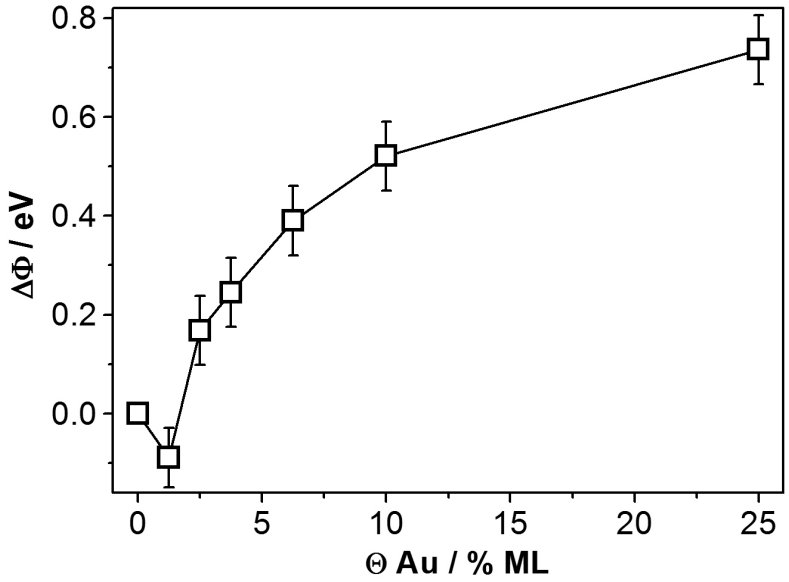

Figure 4.16 Change of the work function of the MgO/Mo(100) substrate with increasing gold coverage. Lines are drawn to guide the eye.

vious investigations it is known that under these conditions gold nano-clusters are formed which grow in size with increasing gold coverage [194, 201]. Also shown for comparison in Figure 4.15 (bottom graph) is the photoemission spectrum from an extended gold film on Mo(100).

Laser power dependence measurements suggest that the 266 nm photoemission from the bare and the gold covered MgO/Mo(100) substrates contain both, single photon photoemission from the Mo substrate *d* band as well as two-photon photoemission from the magnesia O2*p* valence band states (the measured exponent of the power dependence is 1.61 ±0.07. For a detailed discussion, please see Section 4.1.3 and Ref. [136]). Because of the single photon excitation contribution it has to be concluded that the work function of the gold covered MgO/Mo(100) substrates is below the excitation laser energy (4.7 eV).

At the lowest investigated nominal gold coverage of 0.013 ML a slightly broader spectrum is observed compared to the bare magnesia surface indicating a lowering of the surface work function due to the gold deposition. However, with further increasing gold coverage, the photoemission spectra progressively narrow reflecting a gradually increasing surface work function. This work function change $\Delta\Phi$ relative to the bare magnesia thin film is plotted in Figure 4.16.

In contrast, the photoemission from the Au film on Mo(100) is clearly due to a two-photon excitation. The work function of the gold film was determined to be 5.0 ±0.2 eV which compares well with the literature value of 5.22 ±0.04 eV that has been measured for the Au(100) surface [175] (see Section 4.2).

The work function of a Mo(100) surface amounts to 4.53 eV [138]. If this surface is covered by several monolayers of magnesia the surface work function is considerably reduced

[136, 164]. Different experimental methods yielded work function values for a magnesia film of about 10 ML thickness on Mo(100) ranging from 2.7 to 3.5 eV [135, 136, 164].

The work function of the 10 ML MgO film on Mo(100) determined in the present work amounts to 3.2 ±0.2 eV (top graph in Figure 4.15), i.e., about 1.3 eV lower than the work function of the Mo substrate. Deposition of gold on this MgO film initially leads to a slight decrease in the surface work function which, however, subsequently increases again monotonically with increasing cluster size, i.e., nominal gold coverage (see Figure 4.16).

A similar behavior of $\Delta\Phi$ as a function of the metal coverage has been previously observed for other magnesia supported metals that posses outer *s* electrons like, e.g. copper and silver [207, 208]. In these cases, the initial work function minimum was observed at 0.1 ML coverage of copper and at 0.05 MLE coverage of silver, respectively. In the present investigation of gold on MgO(100) a work function minimum is apparent around 0.013 ML.

As explanation for the initial decrease of the work function the interaction of the metal clusters with regular and low-coordinated surface oxygen ions was inferred [208]. Two contributions to the bonding can be distinguished in this case: (i) the polarization by the surface Madelung potential and (ii) the covalent interaction through mixing of the *s* and *d* orbitals of the deposited metal with the 2*p* orbital of the surface oxygen, whereby the latter was found to be comparably small. Thus, the metal polarization was claimed to primarily account for the observed decrease of the surface work function during the initial metal deposition. Accordingly, a decrease of the polarization of the metal charge cloud with increasing coverage was proposed as reason for the occurrence of the work function minimum and subsequent rise [208]. Interestingly, gold atom possess a smaller polarizability compared to silver and copper [209] which might be related to the appearance of the work function minimum at lower metal coverages in the case of gold.

In the molecular adsorption and photodissociation experiments a sample with 0.13 ML gold coverage was employed. In this case the surface work function was about 0.5 eV higher than that of the bare MgO/Mo(100) substrate.

It has however to be noted that the photoemission spectra only reflect the integral surface properties and that the local surface work function varies, in particular on and in the vicinity of the metal clusters. In the case of palladium clusters on MgO, e.g., recent Kelvin probe microscopy measurements revealed that the local work function on the clusters exceeds that of the magnesia substrate in average by 2.4 eV [172]. Such variations in the local electronic properties are expected to strongly influence also the photoreaction dynamics of adsorbate molecules.

Finally, the bottom graph of Figure 4.15 displays, for comparison, the two-photon photoemission spectrum of a 10 ML gold film on Mo(100). This spectrum has been described in detail in Section 4.2.

4.3.2 Estimation of the gold particle size

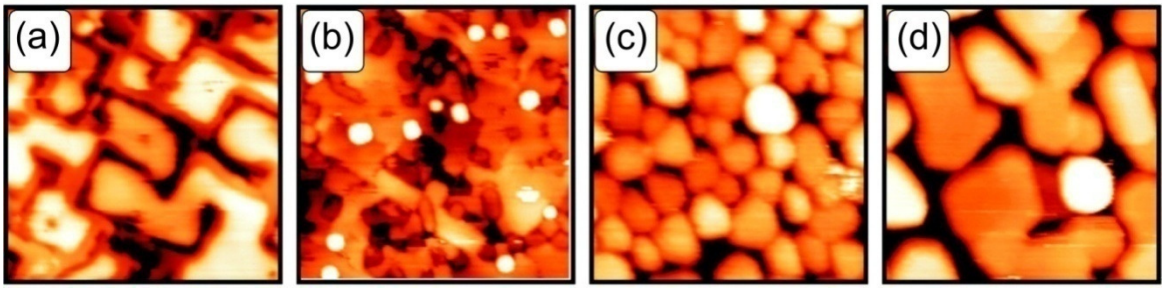

Figure 4.17 STM images (50×50 mn^2) recorded form (a) 7 ML MgO/Mo(100) and from 7 ML MgO/Mo(100) covered with different amounts of Au: (b) 0.06 ML; (c) 0.6 ML; (d) 2.5 ML. Images taken from Ref. [194].

No analytical tools for a direct determination of the Au particles size on MgO films are available in our laboratory. However, by comparison of our preparations with similar experiments reported in the literature, an estimation of the gold particle size was possible. Freund and coworkers grew Au nanoparticles by thermal evaporation on magnesia thin films with different thicknesses and at different temperatures [194, 201]. They investigated their surface preparations by means of STM. Figure 4.17 displays a series of STM images recorded from a 7 ML MgO film on Mo(100) and from gold particles grown on a 7 ML MgO film on Mo(100). The Au deposition was performed at room temperature. For 0.06 ML Au coverage, small bilayer aggregates preferentially along step edges were observed (cf. Figure 4.17b). The formation of 3D compact particles was reported for Au coverages above 0.5 ML (cf. Figure 4.17c). A further increase of the Au coverage to 2.5 ML guided to the formation of large crystalline islands (cf. Figure 4.17d).

Gold particles grown by deposition of 0.035 - 0.05 ML Au were also investigated by means of STM at various substrate temperatures on a magnesia film with a thickness of 8 ML [201]. For a substrate temperature of 10 K, just Au atoms were observed in STM. Upon annealing of the surface at 210 K the appearance of flat bilayer Au particles with a diameter of about 3 nm was observed. A further annealing at 300 K caused the appearance of 3D compact Au particles, which exhibited a larger height that the ones observed after the 210 K annealing process.

Concerning the growth of Au nanoparticles on MgO thin films, a recent investigation of Freund and coworkers employing temperature dependent EPR measurements has shown that the Au atoms become mobile at temperatures above 125 K [210]. In this report the highest investigated gold coverage was 0.05 ML and the substrate consisted of a 20 ML MgO film on Mo(100).

Based on the STM and EPR investigations presented above, an estimation of the Au particle size on MgO/Mo(100) at 90 K can be performed. For 0.013 ML to 0.06 ML coverage mostly Au atoms are expected on the surface. For coverages above 0.25 ML, certainly 3D compact particles are expected. The exact Au coverage required to produce 3D particles at 90 K has not been reported.

In the framework of this thesis, in few experiments gold monomers, dimers, and trimers, were produced by the cluster source (see Section 2.3) and deposited at 90 K under soft-landing conditions on 8 ML thin MgO films grown on Mo(100). The highest gold coverage was kept under 0.02 ML in order to avoid the particle agglomeration and subsequently formation of bigger Au clusters. Under these preparation conditions it was demonstrated that the clusters keep their initial gas-phase composition on the surface [148, 195].

5 Methyl iodide

The novel method of surface femtosecond pump-probe mass spectrometry described in Chapter 3 was applied to monitor the ultrafast photoinduced chemistry of methyl iodide molecules adsorbed on magnesia, gold and magnesia supported gold clusters. The methyl iodide adsorption behavior on the different substrates was characterized by means of temperature programmed desorption spectroscopy.

In addition to the unimolecular dissociation of methyl iodide, a bimolecular reaction leading to the formation of molecular iodine was observed on magnesia thin films. The real-time dynamics of both uni- and bimolecular reaction was studied with time-, mass-, and velocity-resolution. Most interestingly, a considerable influence of the magnesia layer thickness and stoichiometry, i.e. the presence of surface defects, on the observed reaction dynamics could be identified.

In contrast to methyl iodide adsorbed on insulating magnesia films, no photodissociation products were observed from methyl iodide adsorbed on metallic gold films and on magnesia supported gold nanoparticles This was interpreted in terms of an ultrafast recapturing of the ground state after photoexcitation and before the C-I bond stretched considerably, i.e., the molecular dissociation was quenched.

Neither molecular thermal desorption nor photodissociation fragments were detected from methyl iodide adsorbed on small mass-selected gold clusters consisting of just few atoms (Au_N, N=1, 2, 3) deposited on magnesia films. This was assigned to a very strong CD_3I-Au interaction that led to molecular fragmentation upon adsorption.

5.1 Methyl iodide on magnesia

5.1.1 Temperature programmed desorption

Figure 5.1 displays TPD spectra recorded after dosing of different amounts of CH_3I onto an MgO/Mo(100) film at 90 K substrate temperature to characterize the adsorption behavior. Methyl iodide is known to adsorb molecularly on the MgO(100) single crystal surface and to desorb without decomposition [211].

As mentioned in Section 2.2.3, our TPD spectrometer is limited to a mass range from 1 to 100 amu, therefore the spectra in Figure 5.1 show the methyl peak resulting from the ionizer fragmentation of methyl iodide molecules [212]. Molecular desorption is confirmed by simultaneously monitoring the CD_3^+ and I^{2+} signals, which have an identical appearance

The maximum of the CH_3I desorption signal in Figure 5.1 shifts with increasing coverage to lower temperatures indicating a desorption activation energy that decreases with increasing coverage. On single crystal MgO [211] the similar temperature dependence was interpreted in terms of a repulsive adsorbate-adsorbate interaction due to an adsorbate structure with the CH_3I symmetry axis and hence the permanent dipole moment of the molecules aligned parallel to each other and parallel to or slightly tilted from the surface normal.

No evidence for methyl iodide dissociation subsequent to adsorption on MgO/Mo(100) substrate are found. No reaction products as ethane, which could form subsequent to methyl iodide dissociation on the surface are observed.

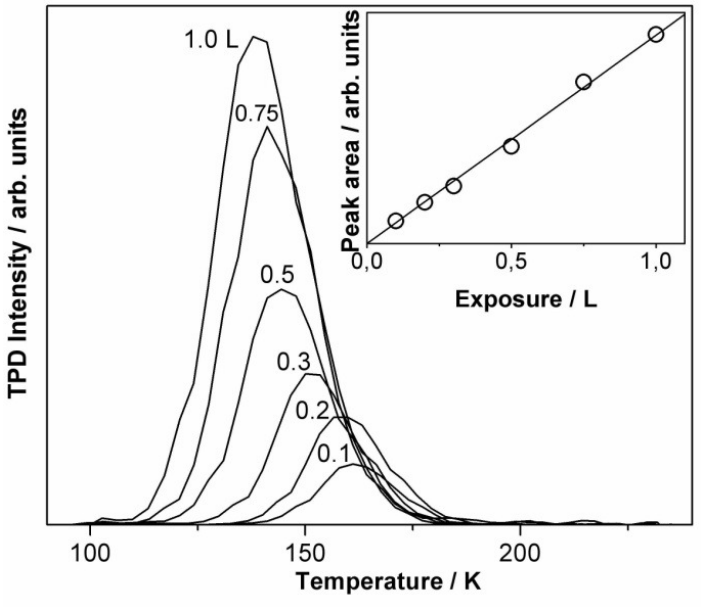

Figure 5.1 TPD spectra of submonolayer CH_3I on MgO(100)/Mo(100) ultra-thin films (10 ML thickness). The spectra were obtained with a heating rate of 2 K/s. The numbers indicated at the spectra represent the CH_3I exposure in units of Langmuir (1 L = 0.25 ML [211]). The inset shows the linear correlation of the TPD peak area with the exposure illustrating the constant sticking coefficient.

5.1.2 Real-time photoreaction dynamics

5.1.2.1 Unimolecular reaction

As already mentioned, the methyl iodide molecule dissociate upon photoexcitation of a non-bonding 5pπ iodine electron to the σ* antibonding C-I orbital (A-band). In Figure 5.2 the relevant potential energy curves of the methyl iodide ground state and A-band are depicted [38]. As the exact influence of the surface on the methyl iodide potentials is not known and because the methyl iodide molecules do only weakly bind to the magnesia surface [58], the shown gas-phase potentials are assumed to be almost unperturbed by the surface to a first approximation.

The A-band dissociation of CH_3I after 266 nm excitation is prompt and involves primarily two dissociative excited electronic states denoted as $^3Q_{0+}$ and $^1Q_1$ by Mulliken [213] (cf. Figure 5.2). It leads to methyl fragments and iodine atoms in the ground and the spin-orbit

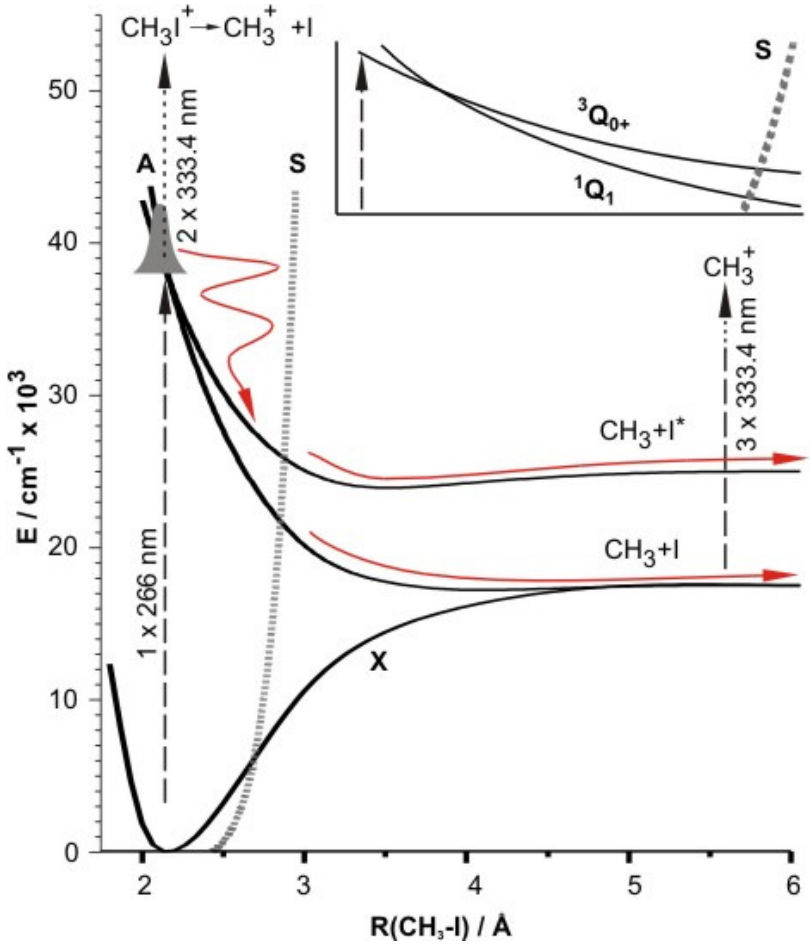

Figure 5.2 Potential energy diagrams of free methyl iodide [38, 39]. The solid arrows illustrate the propagation of the wave packet. The dashed arrows represent the excitation and the detection laser pulses (detection energies not drawn to scale). The potential S reflects the Lennard-Jones interaction between the methyl group and the magnesia surface [214]. The inset shows a magnification of the methyl iodide A-band excitation region.

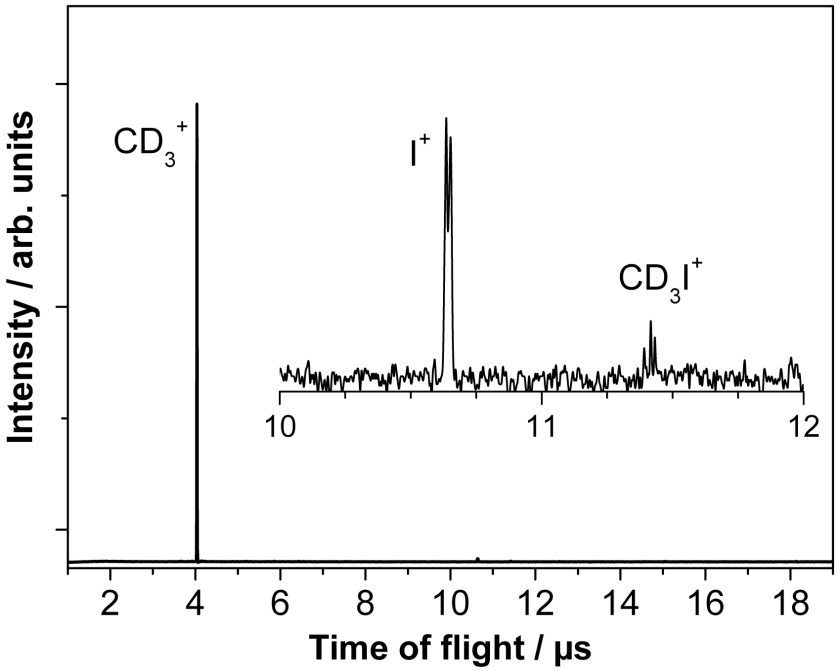

Figure 5.3 Time-of-flight mass spectrum obtained from methyl iodide adsorbed on 10 ML MgO/Mo(100) at 130 fs pump-probe delay time. The inset presents a magnified view of the mass spectrum between 10 and 12 µs flight time.

excited state. The initial excitation near 266 nm is largely to the $^3Q_{0+}$ state which correlates diabatically with CH_3 and the excited $^2P_{1/2}$ state of iodine (I*). At a C-I bond distance of about 2.35 to 2.40 Å the $^3Q_{0+}$ potential crosses the $^1Q_1$ potential, which leads to the $^2P_{3/2}$ ground state of iodine. An experimental gas-phase I($^2P_{3/2}$) yield of about 30% [215] points toward an efficient coupling between the $^3Q_{0+}$ and $^1Q_1$ states. Most of the energy available to the products is found in the translational degrees of freedom with only minor excitation of the CH_3 umbrella bending mode [216].

First gas-phase time-resolved investigations of CH_3I photodissociation dynamics via A-band employing femtosecond pump-probe technique in conjunction with mass spectrometry were performed by Zewail and coworkers [34, 35]. A dissociation time of 120 fs could be established for the CH_3 + I* channel by monitoring the I^+ signal intensity by means of (2+1) REMPI detection at 304 nm. The escape of the wavepacket from the $CH_3I^{*‡}$ transition state Franck-Condon region was determined to be faster than 50 fs [35, 217].

Recent gas-phase investigation performed by Bañares and coworkers employing femtosecond pump-probe spectroscopy in conjunction with velocity map imaging have monitored several well defined channels of the C-I bond breakage of the CH_3I molecule via A-band excitation by detecting the methyl radical via (2+1) REMPI at 333.5 nm [30, 31]. Bañares and coworkers, found that the CH_3I dissociation yielding vibrationless methyl radicals as well as ground and spin-orbit excited iodine atoms occurs in 40 fs and 80 fs, respectively. The CH_3I dissociation yielding the iodine fragments in the ground state and vibrational excited methyl radicals ($CH_3(1_1^1)$) occurs in 135 fs.

Figure 5.3 shows a time-of-flight mass spectrum obtained at 130 fs pump-probe delay time from methyl iodide adsorbed at submonolayer coverage on MgO/Mo(100). Besides an intense methyl ion peak, small peaks corresponding to iodine atoms and methyl iodide molecules are present. The large difference between the peaks intensities is attributed to the resonant detection of the methyl group versus the multiphoton non-resonant detection of the iodine atom and the methyl iodide molecule.

Transients were obtained by monitoring the methyl signal intensity for CH_3I and CD_3I adsorbed on MgO/Mo(100). Figure 5.4a shows the result for CH_3I molecules on MgO/Mo(100) measured with a probe laser power of 70 mW/cm². The transient signal exhibits a steep rise starting at zero delay time with a maximum reached around 130 fs. It subsequently decays but does not reach the initial value measured at negative delay times again. Instead, a small but clearly apparent offset is observed which stays constant at longer positive delay times. Fitting of an exponential 'rise and decay'-model (with subsequent offset) to the experimental data gave similar time constants of $\tau_1 = \tau_2 = 90$ fs for the rise and the decay component of the observed peak, respectively (cf. Section 3.5.4.2). The transient signal obtained for CD_3^+ at comparable laser conditions is displayed in Figure 5.4b. The appearance is identical to the CD_3^+ signal in Figure 5.4a: a peak followed by a signal offset at positive delay times. Fitting of the 'rise and decay'-model to the peak structure also resulted in identical time constants as in the non-deuterated case. No clear indication for the expected isotope mass effect of about 20% on the dynamics could be detected within the accuracy of the time resolution in the present experiment.

Figure 5.4c shows the transient CD_3^+ signal recorded with the same pump power as above, but with the probe power increased to 600 mW/cm². While the peak structure at short delay times is still present, the offset at longer delay times is now considerably enhanced and exhibits an exponential rise. The strong probe pulse energy dependence of this latter rising signal supports its attribution to the resonant ionization ((2+1)-REMPI) of methyl fragments resulting from the A-band dissociation. Power dependent measurements indeed confirmed the three photon transition. In contrast, for the peak structure at early delay times a quadratic (two photon) intensity dependence on probe pulse energy was observed pointing toward a completely different origin of these methyl ions. Figure 5.5 shows the power dependence measurements performed on the pump laser pulse and on the probe laser pulse at 130 fs and at 3 ps corresponding to peak and exponential rise structure.

The fitting of a 'rise and decay'- in conjunction with a 'delayed exponential rise'-model to the transient in Figure 5.4c resulted in similar rise and decay time constants for the peak as in Figures 5.4a and 5.4b. For the exponential rise at longer delay times, a time constant of $\tau_3 = 680 \pm 50$ fs with an initial coherent delay of $\Delta t_0 = 170$ fs was obtained from the fitting procedure. The two separate components of the fit, peak and delayed rise, respectively,

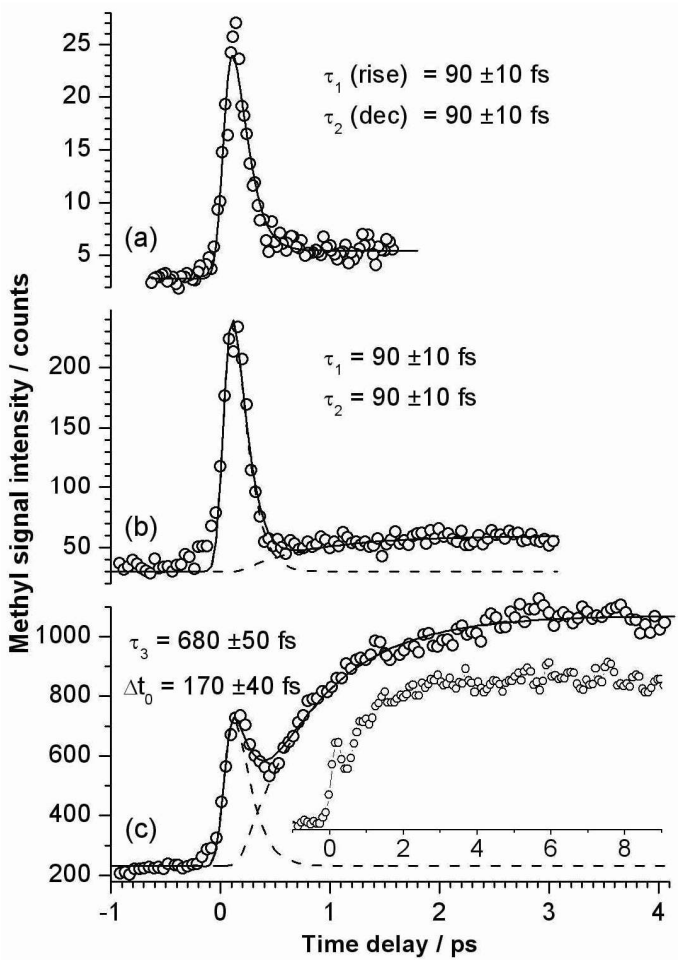

Figure 5.4 Transients obtained by monitoring the methyl cation signal as a function of the pump-probe delay time. Each data point of one single transient represents the sum over the ion count yield from 2500 pump and probe laser exposures to a 0.25 ML methyl iodide preparation. For each transient shown ten single transients were averaged to improve the signal-to-noise ratio: (a) CH_3I transient obtained with 1 mW/cm² pump and 70 mW/cm² probe laser power. The solid line is the best fit of an exponential 'rise and decay'-model (with offset at long delay times) to the experimental data yielding the indicated time constants τ_1 and τ_2. (b) CD_3I transient obtained with comparable laser conditions (pump: 2 mW/cm²; probe: 70 mW/cm²). The solid line is the best fit of the sum of the exponential 'rise and decay'- and the 'delayed exponential rise'-model to the experimental data. The separated components corresponding to the two models are indicated by the dashed lines. The indicated time constants τ_1 and τ_2 result from the fitting of the 'rise and decay'-model. The time constant and delay of the 'delayed exponential rise'-component were taken from the fitting of the data in (c) with adjusted amplitude. (c) CD_3I transient obtained with 600 mW/cm² probe laser power (pump power: 2 mW/cm²). The solid line is the best fit of the 'rise and decay'/'delayed exponential rise'-model to the experimental data. The dashed curves represent the separated components corresponding to the two models. The obtained time constants for τ_1 and τ_2 were the same as in (a) and (b). The initial coherent delay Δt_0 and the time constant τ_3 of the 'delayed exponential rise'-component are indicated in the graph. The insert is the same transient as in (c), but measured for longer pump-probe delay time.

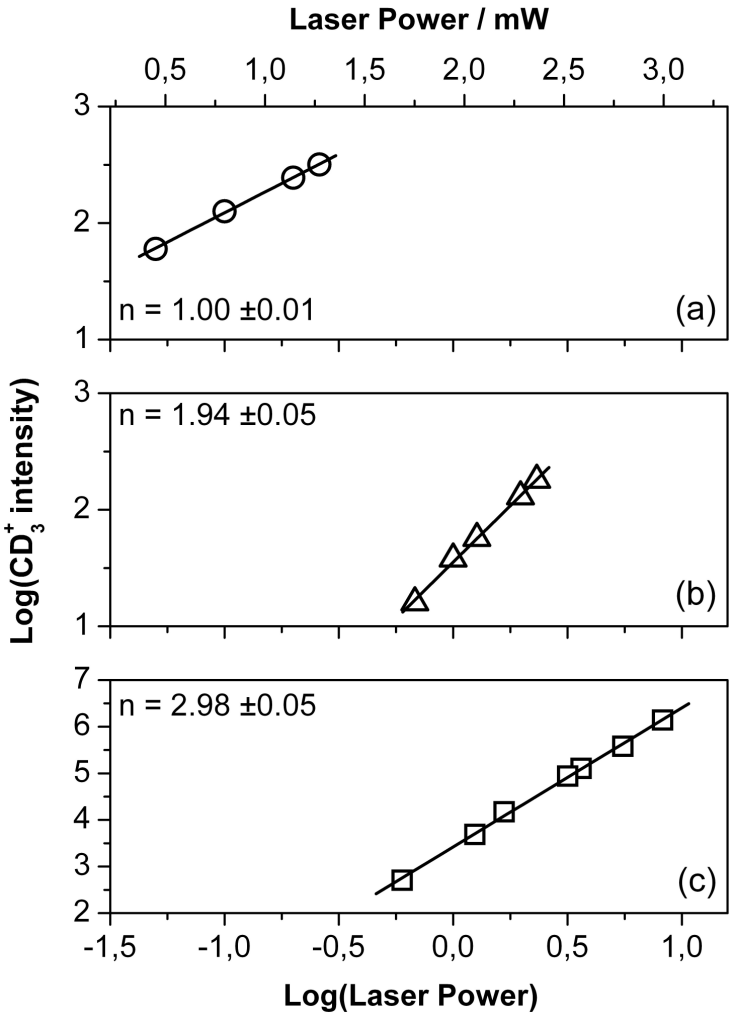

Figure 5.5 Dependence of the methyl cation signal on the laser power: (a) Pump laser beam intensity variation (130 fs pump-probe delay time; 2500 fs (not shown) is similar). (b) Probe laser beam intensity variation at 130 fs pump-probe delay time; (c) Probe laser beam intensity variation at 2500 fs pump-probe delay time.

are indicated by the dashed lines in Figure 5.4c. Identical fitting parameters with adjusted amplitudes also fitted the transient CD_3^+ signal obtained at lower probe laser power (see dashed curves in Figure 5.4b).

A similar appearance of the transient data consisting of a peak structure followed by an exponential rise, however, with completely different time constants, was reported previously for the gas-phase dissociation of methyl iodide [35]. In the gas-phase investigations, the peak structure was attributed to the dynamics of the dissociating excited transition state of methyl iodide, $CH_3I^{*\ddagger}$, which was directly ionized by the probe pulse immediately after A-band excitation. Subsequent, rapid decomposition of the CH_3I^{+}* ion leads to the observed CH_3^+ fragment. In contrast, the delayed rise of the transient signal was attributed to the direct REMPI detection of the emerging neutral fragments (I [35, 217] or CH_3 [30, 31]) reflecting the dynamics of their liberation from the force field of each other in coherent motion along

the dissociative potential energy surfaces (cf. Figure 5.4c). Because of the similar appearance of the measured methyl transient signal (cf. Figure 5.4), our interpretation is based on the gas-phase explanation of the molecular dynamics of transition state and emerging fragments, respectively. On the basis of this assignment and by considering the potential energy diagram of methyl iodide (Figure 5.2) an interpretation of the measured reaction times of the methyl iodide surface reaction will be proposed in the following discussion.
First, the peak structure with the rise and decay time constants of 90 fs, apparent in all observed transients (cf. Figure 5.4), will be discussed. In accordance with the gas-phase interpretation, the peak structure is assigned to the ionization of the excited methyl iodide before complete decomposition according to the schema:

$$CH_3I_{ads} \xrightarrow{266\ nm} CH_3I^{*\ddagger}{}_{ads} \xrightarrow{2 \times 333.4\ nm} CH_3I^{+*} \rightarrow CH_3^{+} + I \qquad (5.1)$$

The peak structure of the methyl ion signal therefore reflects the passage of the wave packet initially launched on the $^3Q_{0+}$ state through the transition state Franck-Condon region of the two-photon ionization (cf. Figure 5.2). The methyl iodide cation thus generated immediately decomposes leading to the observed methyl ion signal

In the direct gas-phase dissociation the $CH_3I^{*\ddagger}$ transition state was detected instantaneously after excitation and decayed faster than 50 fs [35, 130, 217]. In the case of methyl iodide adsorbed on MgO, however, a 90 fs rise is observed with a maximum signal around 130 fs followed by a 90 fs decay. This indicates that the presence of the magnesia surface has a fundamental impact on the dynamics of the transition state: (i) It influences the excited electronic state structure of methyl iodide so that the optimal Franck-Condon window for $CH_3I^{*\ddagger}$ detection is reached only after 130 fs. (ii) The process of methyl iodide dissociation is considerably delayed by the presence of the surface. This indicates a strong inelastic interaction of the $CH_3I^{*\ddagger}$ transition state with the surface prior to decomposition. (iii) Would the methyl iodide molecules be adsorbed with the iodine facing the magnesia surface [51, 54], the dissociation of $CH_3I^{*\ddagger}$ would lead to the prompt ejection of the light methyl fragments resulting in a time constant for the $CH_3I^{*\ddagger}$ decay identical to the gas-phase [56-58]. Thus, the observed dynamics strongly point toward an adsorption structure with the methyl heading toward the surface. This is further supported by the measured dynamics of the methyl fragments emerging from the A-band dissociation, which will be presented in the following.

The second part of the discussion will be concerned with the delayed exponential rise that is particularly apparent at high probe laser flux (cf. Figure 5.4c). It is assigned, again in accordance with the gas-phase interpretation, to the (2+1) REMPI detection of methyl radicals emerging from the A-band dissociation of the adsorbed methyl iodide molecules according to the schema (cf. Figure 5.2):

$$CH_3I_{ads} \xrightarrow{266\ nm} CH_3I^{*\ddagger}{}_{ads} \rightarrow CH_3 + I/I^* \xrightarrow{(2+1) \times 333.4\ nm} CH_3^{+} + I/I^* \qquad (5.2)$$

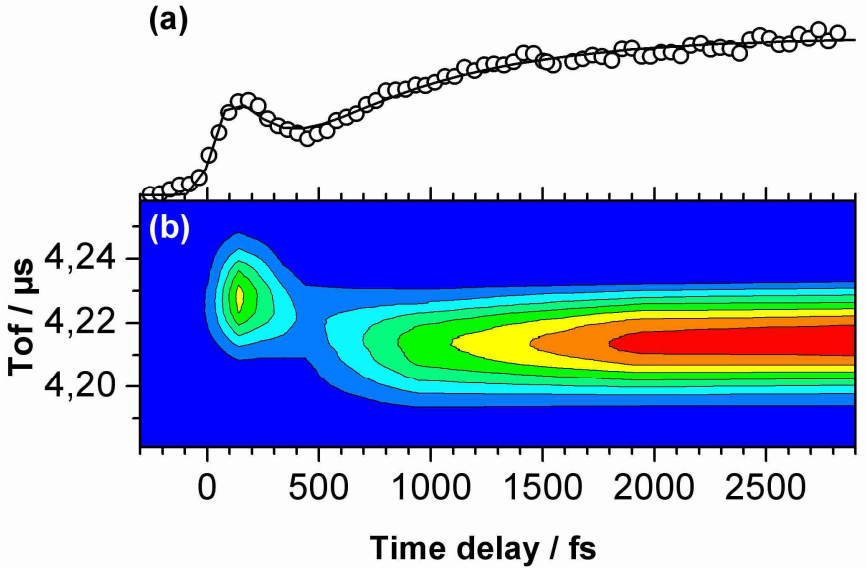

Figure 5.6 Time-, mass-, and velocity-resolved detection of CD_3^+. (a) Integrated mass signal intensities as a function of the pump-probe delay time (same transient as in Figure 5.4c). (b) Contour representation of the mass signal intensities as a function of the reaction time and of the time-of-flight in the mass spectrometer (color coded, ranging from 0% (blue) to 100% (red)). The laser parameters were the same as in Figure 5.4c.

The initial coherent delay of Δt_0 = 170 fs (cf. Figure 5.4c) of this part of the methyl ion signal reflects the liberation of the methyl fragments from the molecular force field and from the force field of the magnesia surface. Gas-phase investigations showed a 120 fs coherent delay in the methyl fragment appearance [30, 31]. Because of the considerably prolonged coherent delay observed here, the direct ejection of methyl as in the free molecule can be ruled out. Instead, the data are again in favor of a CH_3I adsorption structure with the methyl facing the magnesia substrate. The extended time needed for the liberation of the methyl thus reveals the effect of the magnesia surface that manifests itself in the trapping of the $CH_3I^{*\ddagger}$ transition state. The subsequent growth of the methyl signal with a time constant of τ_3 = 680 fs (Figure 5.4c) is consequently interpreted as the average life time of all trajectories leading from the transition state to the release of the methyl fragment. For the free molecule, due to the strongly repulsive nature of the dissociation and thus well focused wave packet, this rise is instantaneous [31, 35]. At the surface, however, the wave packet spreads due to the inelastic interaction with the surface. The corresponding trajectories therefore include the motion of methyl toward the surface leading to the inelastic collision and the recoil away from the surface followed potentially by a collision with the slowly moving, heavy iodine atom. This interaction with both, the surface and the iodine atom, was predicted theoretically and was termed as 'chattering' motion [56-58]. The scenario might proceed until the methyl trajectory is rotated away from the iodine trajectory far enough so that the fragment can escape.

In addition to the mass-resolved detection, it was also possible to measure the relative initial velocities of the methyl fragments emerging from the CD_3I photodissociation on mag-

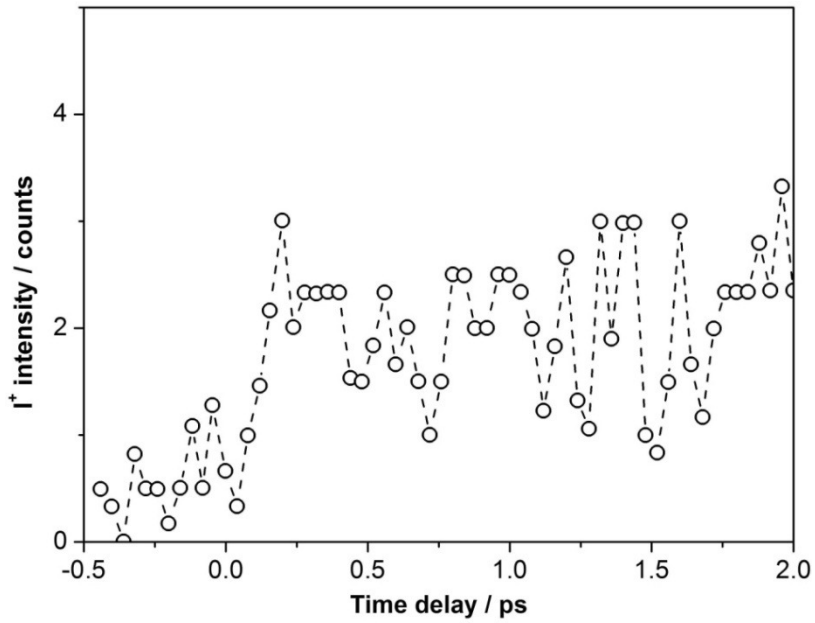

Figure 5.7 Transient obtained by monitoring the iodine cation signal from CD_3I dissociation as a function of the pump-probe delay time (pump pulse: 266 nm, 2 mW/cm²; probe pulse: 333.9 nm, 600 mW/cm²). For the shown transient ten single transients were averaged to improve the signal-to-noise ratio.

nesia. This was realized, as explained in Chapter 3, by decreasing the voltage on the first acceleration electrode of the mass spectrometer (directly opposite to the surface) by a factor of 4 compared to the setting for optimal mass resolution. In this way, the shape and relative position of a peak corresponding to a particular ion mass reflect the initial kinetic energy distribution of these ions [35, 218]. Besides the integrated mass signal intensity as a function of the pump-probe delay time presented in Figure 5.6a, a contour plot of the methyl ion mass signal as a function of both, the pump-probe delay time and the ion flight time in the mass spectrometer is displayed in Figure 5.6b. A longer ion flight time corresponds to a smaller initial ion velocity or initial kinetic energy, respectively. Clearly, the peak and the delayed exponential rise structures originate from methyl ions with different initial kinetic energy. This is again a strong indication that two different elementary processes are responsible for the observed transient evolution of the methyl signal in agreement with equations (5.1) and (5.2).

The liberated methyl radicals would be expected to appear with two different initial kinetic energies corresponding to the two dissociation channels along the $^3Q_{0+}$ and the $^1Q_1$ potentials, respectively (cf. Figure 5.2). However, this difference is not resolved in the data of Figure 5.6b which might be due to the energy loss during the interaction with the surface. In contrast, the heavy iodine atoms are assumed to remain almost immobile during the dissociation time period and might be released in the spin-orbit excited as well as the electronic ground state.

In Figure 5.7 displays the integrated atomic iodine mass signals as a function of the pump-probe time delay. Due to the non-resonant detection of the iodine atoms, this mass signal is considerably smaller than the methyl mass signal (cf. the mass spectrum in Figure 5.3).

Therefore, the signal to noise ratio in the transient evolution of this mass peak is considerably reduced as can be seen from Figure 5.7 and it is not possible to reliably fit a kinetic model to these data. Nevertheless, in contrast to the methyl radical, the transient I^+ signal appears to exhibit a fast rise starting at about zero time delay, with a maximum intensity reached within a few hundred fs. Subsequently, this transient signal stays at constant intensity for longer time delays. The assumption that the methyl iodide adsorbed on magnesia with the methyl group facing to the surface is strongly supported by the transient signal in Figure 5.7. The fast appearance of the I^+ signal would not be possible when the methyl iodide molecule adsorbs with the iodine end heading to the magnesia surface.

5.1.2.2 Bimolecular reaction

A time-of-flight mass spectrum obtained after photodissociation of CD_3I molecules with a 266 nm fs-laser pulse (pump) and 2 ps time-delayed ionization of the emerging neutral fragments with a 333.9 nm fs-laser pulse (probe) is depicted in Figure 5.8. Apart from the methyl peak that is also present in the mass spectrum at shorter reaction times, a new prominent peak corresponding to molecular iodine appears. Minor signals are attributed to iodine atoms and to methyl iodide molecules. In this section the formation dynamics and the detection of the iodine molecules subsequent to methyl iodide A-band dissociation on the magnesia surface will be discussed.

Figure 5.9a displays the real-time evolution of the integrated I_2 mass signal intensity. The open symbols again represent the experimental data. No iodine molecules are detected up to a reaction time of about 200 fs. Afterwards, the signal rises exponentially, reaches a maximum value at 1.2 ps and remains constant up to 3 ps. The flight time and the time delay dependence of this I_2 signal is shown in Figure 5.9b.

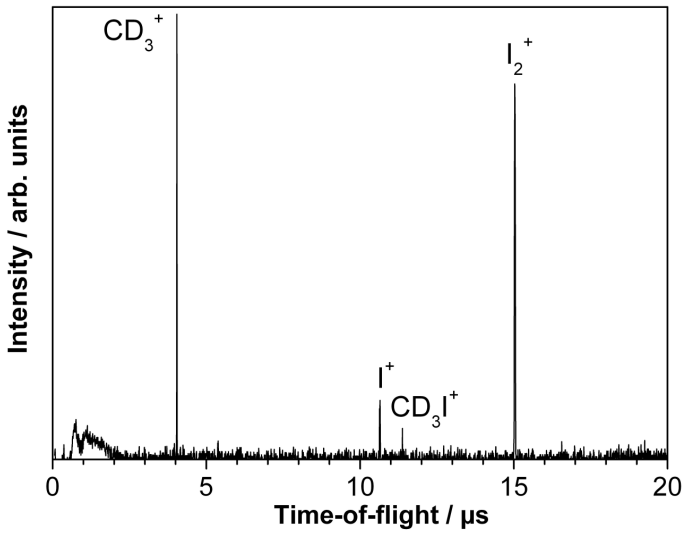

Figure 5.8 Time-of-flight mass spectrum recorded at a pump-probe delay time of 2 ps (pump pulse: 266 nm, 2 mW/cm²; probe pulse: 333.9 nm, 600 mW/cm²). The surface sample consists of 0.25 ML CD_3I adsorbed on 10 ML MgO film on Mo(100).

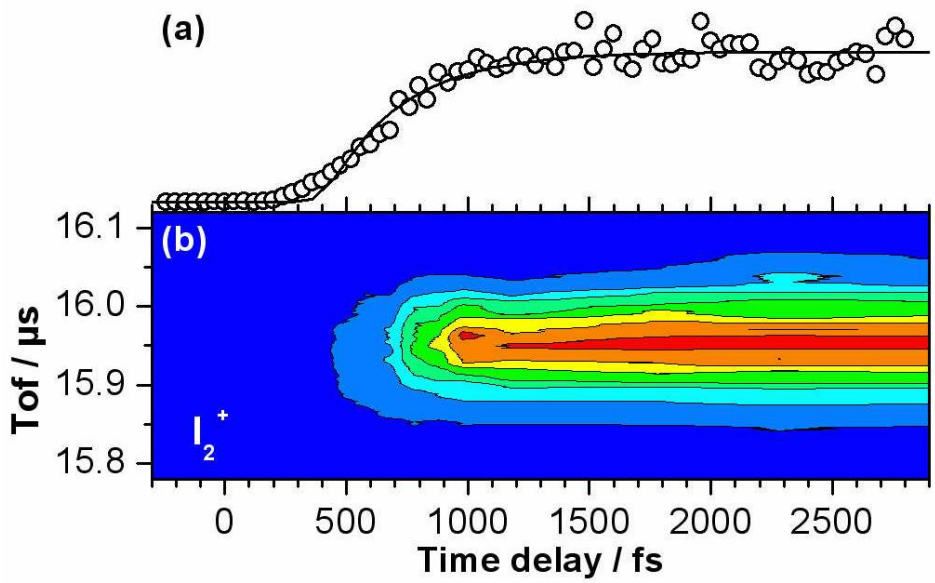

Figure 5.9 Time-, mass-, and velocity-resolved signals of I_2^+. (a) Integrated mass signal intensities as a function of the pump-probe delay time. (b) Contour representations of the mass signal intensities as a function of the reaction time and of the time-of-flight (TOF) in the mass spectrometer (color coded, ranging from 0% (blue) to 100% (red)).

Apparently, the corresponding kinetic energy distribution of I_2 does not change notably with reaction time. Fitting an exponential growth model (solid line in Figure 5.9a) to the data yields a rise time constant of $\tau_1(I_2) = 310 \pm 30$ fs.

Probe laser power dependence measurements (inset in Figure 5.11) demonstrate that the I_2^+ signal is due to a two-photon ionization process. However, the X- and A-states of I_2 are not accessible for two-photon ionization with 333.9 nm. Thus, it is most likely that the I_2^+ signal originates from the ionization of iodine molecules in the electronically excited B-state.
Figure 5.10 illustrates the relevant potential energy curves of the methyl iodide and the iodine molecule [38, 39, 90]. $I_2(B)$ might be formed in a bimolecular reaction of emerging spin-orbit excited I* with ground state I atoms (indicated by the dashed red arrow connecting the CD_3I with the I_2 potentials in Figure 5.10). However, pump power dependent measurements of the I_2 signal indicate the predominance of a single photon excitation mechanism for the bimolecular reaction.

In previous gas-phase experiments with methyl iodide clusters, a four-center bimolecular reaction had been proposed to account for the observed I_2 formation [34]. In this mechanism two adjacent methyl iodide molecules act as reaction center with the photoexcitation leading to a cooperative nuclear motion of both C–I bonds via a transition state of the form $[CD_3\text{-}I^*\text{-}I\text{-}CD_3]^{\ddagger}$ finally resulting in the elimination of $I_2(B)$. The transient data of Figures 5.9a and b thus are interpreted to reflect the real-time dynamics of the bimolecular interaction of I* with I via a favorable surface aligned geometry that enables the four-center transition state. The fastest release of I_2 molecules in this reaction is observed within 200 to 300 fs. The

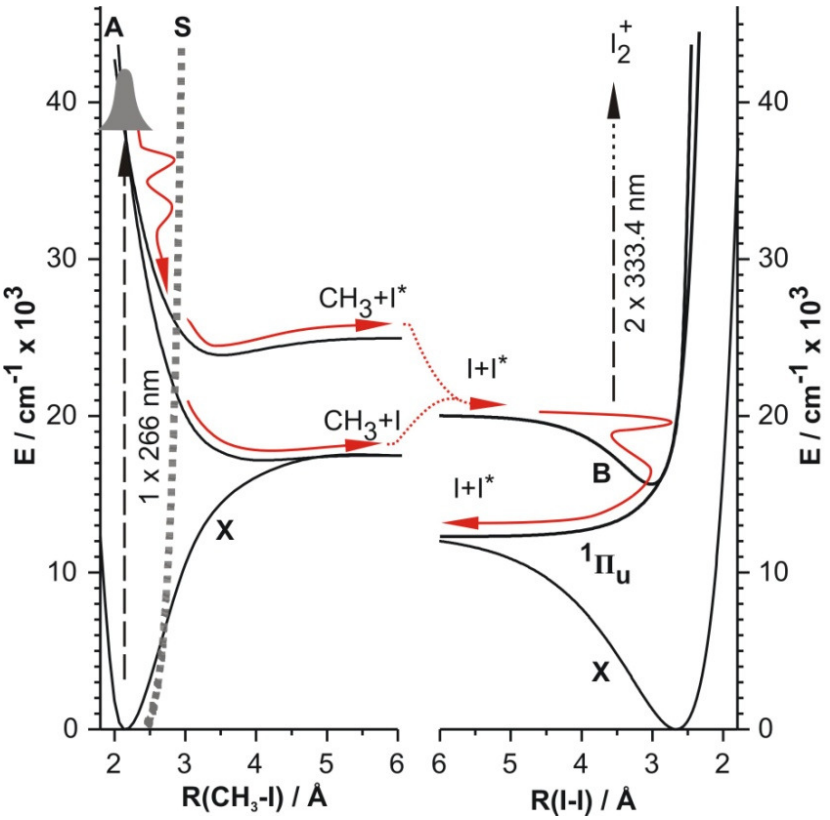

Figure 5.10 Potentials of CD_3I (left) and I_2 (right) adapted from Ref. [38, 39, 90]. The solid arrows illustrate the propagation of the wave packet. The dashed arrows represent the excitation and the detection laser pulses (detection energies not drawn to scale). The potential S reflects the Lennard–Jones interaction between the methyl group and the magnesia surface [214].

average time constant for all trajectories leading from the bimolecular transition state to I_2 is represented by the 310 fs rise of the molecular iodine signal.

Molecular iodine is bound in the B-state (cf. Figure 5.10) and the radiative lifetime of the molecule in this state is on the order of microseconds [219]. In the present experiment, however, a decay of the I_2^+ signal is observed starting after several ps with a decay time constant of $\tau_2(I_2) = 5.0 \pm 0.3$ ps. Figure 5.11 illustrates the I_2^+ transient recorded up to 40 ps. This decay is attributed to a non-adiabatic coupling between the B-state and a $^1\Pi_u$ dissociative state (Figure 5.11) induced by the presence of the surface in the vicinity of iodine molecule (breaking of the $D_{\infty h}$ molecular symmetry) which leads to predissociation on the ps timescale. A similar behavior was experimentally evidence in a gas-phase investigation in which argon embedded iodine molecule were excited in the B-state [220]. The value of the predissociation time constant depends on the coupling between the B-state and the $^1\Pi_u$ dissociative state, which is influenced the surrounding medium. As a result, only ground state iodine atoms are

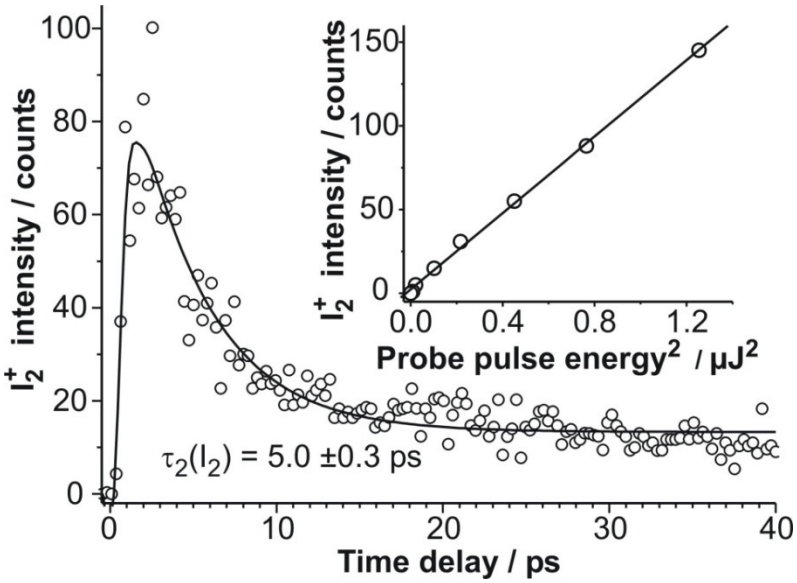

Figure 5.11 Intensity of the I_2 signal at longer pump-probe delay times. Open circles represent the experimental data; the solid line is the fit of a kinetic exponential decay model. The laser parameters were the same as for the transients presented in Figure 5.9. Inset: Intensity of the I_2^+ signal as a function of the probe pulse energy at 2 ps delay time.

released after several ps. Interestingly, this also provides a new mechanism for the previously observed pronounced and puzzling I* quenching in surface photodissociation experiments [132]. A further interesting detail of the I_2^+ transient is the small but apparent offset in the signal intensity at long delay times in Figure 5.11 (< 20% of the maximum signal amplitude). This offset might indicate a second contribution to the molecular iodine signal and it might also correlate with the I_2^+ signal at 200 to 400 fs delay time in Figure 5.9a that does not perfectly match to the fitted exponential rise model (solid line). A speculative explanation for this additional contribution to the I_2^+ signal might be found in ground state (or A-state) molecular iodine ionized in a three photon non-resonant process that does not show up in the overall power dependence at the peak I_2^+ intensity (inset in Figure 5.11) because of the small amplitude of this contribution. As can be seen from the potentials in Figure 5.10 (left side), ground state iodine atoms are also released due to the conical intersection in the A-band of methyl iodide. The interaction of $I(^2P_{3/2})$ with an adjacent CD_3I in the surface aligned geometry can lead to the formation of $I_2(X)$ (see right side of Figure 5.10) probably prior to $I_2(B)$, and is not subject to predissociation which would explain the signal offset at long delay times in Figure 5.11.

It can be concluded that the influence of the insulating surface on the bimolecular reaction dynamics manifests itself in: (i) providing an additional energy dissipation pathway for the bimolecular reaction to proceed; (ii) breaking the molecular symmetry of the $I_2(B)$ state to enable predissociation and thus opening a new channel for I* de-excitation at the surface.

5.1.3 Influence of magnesia thin film layer thickness on the methyl iodide photochemistry

In this section, the influence of the MgO film thickness on the photodissociation dynamics of adsorbed methyl iodide molecules is presented. Figure 5.12 displays a series of time-of-flight mass spectra recorded from the photodissociation of CD_3I adsorbed on magnesia films with different thicknesses and on bare Mo(100). As described in the previous section, CD_3^+ and I_2^+ reaction products were detected after the A-band photodissociation of CD_3^+I adsorbed on 8 ML MgO films on Mo(100) (see Figure 5.12a). Both products were still detected on a substrate consisting of 4 ML thin MgO film on Mo(100), but with an apparently reduced I_2^+ intensity (Figure 5.12b). When the MgO film thickness was lowered to less than 3 ML the CD_3^+ intensity remains roughly constant, but no iodine molecules are detected anymore (Figure 5.12c shows the signal obtained from the bare Mo(100) surface).

The physical and chemical properties of an adsorbate can be influenced by a variation in thickness of the supporting oxide film on the metal substrate. It was demonstrated that small gold clusters adsorbed on magnesia films with a thickness of 1-3 ML become partially negatively charged due to an electron transfer from the metal substrate [205, 206]. As a consequence, not only the electronic, but also the geometric structure can be drastically influenced. No charging of adsorbates was observed for thicker films. Similar effects are expected also when methyl halide molecules are adsorbed on these supports. Consequently, on a 1-3 ML MgO/Mo(100) surface either the iodine molecule formation does not occur or the detection is not possible anymore.

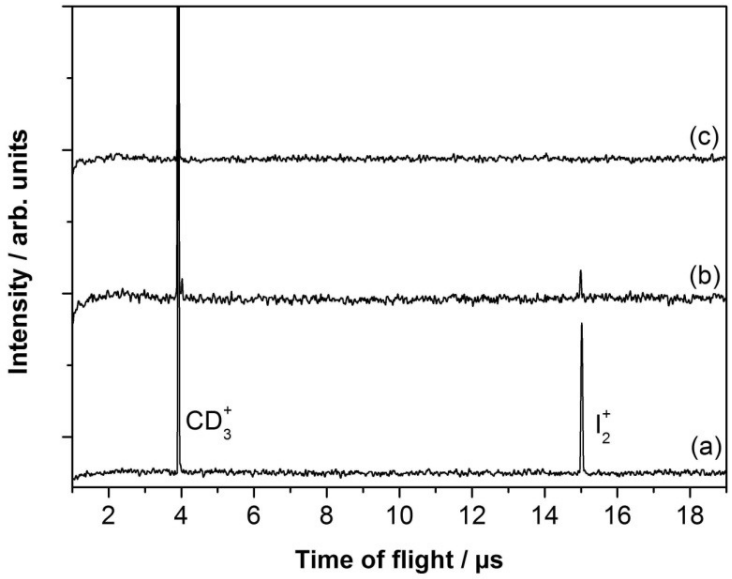

Figure 5.12 Time-of-flight mass spectra recorded from CD_3I adsorbed on a molybdenum surface and on magnesia thin films with different thicknesses: (a) 8 ML MgO/Mo(100); (b) 4 ML MgO/Mo(100); (c) bare Mo(100). All spectra were recorded at 90 K and 2 ps pump-probe delay time (266 & 333.9 nm).

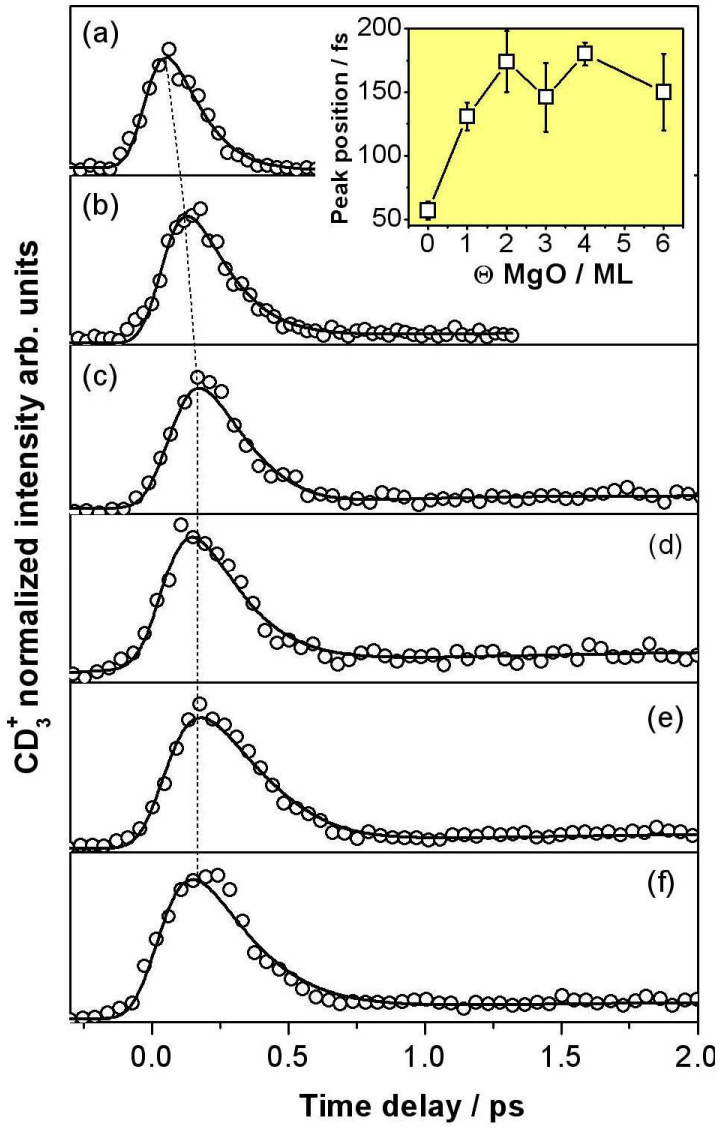

Figure 5.13 Time-resolved dissociation dynamics of CD_3I molecules adsorbed on (a) the bare Mo(100) surface and on MgO films with variable thickness grown on Mo(100) (b) 1 ML; (c) 2 ML; (d) 3 ML; (e) 4 ML; (f) 5 ML; (g) 6 ML (pump pulse: 266 nm, 2 mW/cm^2; probe pulse: 333.4 nm, 400 mW/cm^2). Open circles represent the experimental data. The solid line is the best fit of the 'rise and decay with a delayed exponential rise'-model to the experimental data. The dashed line, drawn to guide the eye, indicates the shift of the peak maximum. Inset: Position of the peak maximum in the methyl transient data as a function of magnesia film thickness. The shown error bars results from the accuracy of the fitting procedure.

On the bare Mo(100) surface the only observed reaction product was CD_3^+. In contrast to methyl iodide adsorbed at submonolayer coverage on noble metals like Pt [103] and Au (cf. Section 5.2) where the photodissociation is quenched due to a strong coupling between the excited states of the molecule and the substrate, on Mo(100) the methyl iodide molecule can be photodissociated.

The absence of the iodine molecule from the mass spectrum in Figure 5.12c could be caused by the methyl iodide adsorption geometry on the Mo(100). On different metallic surfaces the methyl iodide molecule is chemisorbed with the iodine end pointing toward the surface [59, 221]. Consequently the trapping of the iodine atom on the surface is probable. The possibility of the I_2 formation on the Mo(100) surface cannot be ruled out. However, its detection by means of ionization at surface could be hindered, if the molecules interact to strongly with the substrate.

In Figure 5.13 transients obtained by monitoring the methyl cation signal as a function of the pump-probe delay time from surface samples consisting of methyl iodide adsorbed on magnesia films of various thicknesses are displayed. The weak methyl signal intensity at reaction times longer than 1 – 3 ps (offset) is caused by the low probe laser intensity.

In this experiment the shift of the peak maximum and the relative intensity of the methyl transient signal at longer delay times were monitored as a function of magnesia film thickness. On the Mo(100) surface the CD_3 transient signal does not exhibit an exponential growth part at longer delay times under any pump or probe laser conditions. It just consists of a peak structure centered at 58 ±10 fs.

On a 1 ML thick magnesia film grown on Mo(100) the peak structure shifts from 58 ±10 fs to 125 ±20 fs. Moreover, a small offset appears in the methyl signal at longer delay times. A further shift of the peak and an increase of the methyl signal offset at longer delay times are observed on 2 ML MgO. As apparent from Figure 5.13, for magnesia films with 3 – 6 ML thickness no significant change of the transient signals is detected anymore and the signal agrees well with the one recorded under similar laser conditions on a 10 ML MgO film (see Figure 5.4a and b). The inset in Figure 5.13 summarizes the observed shift of the methyl transient peak maximum as a function of the magnesia film thickness.

According to the discussion in Section 5.1.2, the peak signal can be assigned to the detection of the dissociating transition state of the excited methyl iodide molecules according to equation (5.1). If this applies also to the methyl iodide molecules adsorbed on molybdenum, then the shift of the peak maximum to earlier delay times confirms a different interaction of the CD_3I molecules with the metal surface compared to the MgO film. In addition, it might indicate a different adsorption geometry that enables a faster release of the methyl fragments like, e.g., the iodine atom facing the molybdenum substrate. A halogen-down adsorption geometry is commonly observed for methyl halide adsorption on metal surfaces, as indicated above [221, 222].

As previously mentioned, independent on the laser parameters, the methyl transient signal does not exhibit an offset at later pump-probe delay times on the Mo(100) surface. Moreover, we observed that the irradiation of CD_3I on Mo(100) with the probe laser beam (333.9 nm) only leads to the formation of CD_3^+ fragments. Note that on magnesia films no CD_3^+ signal can be observed after irradiation of the adsorbed CD_3I molecules with 333.9 nm, independent on laser intensity. According to these observations and taking into account the methyl detection mechanism described by equation (5.1) it can be concluded that the CD_3I

molecules adsorbed on Mo(100) can be excited into a dissociative cationic state after the simultaneous absorption of three photons at 333.9 nm. This is only possible when the electronic structure of the adsorbed molecules is perturbed by the Mo(100) substrate in a way that the A-band and the cationic states of CD_3I are shifted to lower energies. The absence of the CD_3^+ offset at later pump-probe delay times observed in the case of CD_3I molecules adsorbed on Mo(100) can be explained by high CD_3^+ background signal produced by the probe beam at 333.9 nm alone.

Clearly, except for 1 ML MgO on Mo(100), where the magnesia film does not yet completely cover the metal substrate (see Section 2.2), the layer thickness does not notably influence the observed reaction dynamics. However, the dynamics resulting from electronic excitation and subsequent multiphoton ionization should be extremely sensitive to changes in the electronic level structure of the adsorbed molecules. Thus, in the case of CD_3I adsorbed on magnesia ultrathin films, no indications for an electronic coupling of the molecules to the underlying molybdenum substrate, which would lead to e.g., charging effects, could be detected in this experiment. In this respect it would be very interesting to investigate the dissociation and desorption dynamics of adsorbate molecules with large electron affinity, like NO_2, for which a considerable charging at the ultrathin film surface has been predicted [223, 224].

5.1.4 Influence of the MgO stoichiometry and composition on the methyl iodide thermal desorption and photodissociation

As explained above (Chapter 3), the MgO(100) surface is inert, irreducible, non-polar and relatively easy to prepare. However, this surface becomes chemically reactive once defects are generated. Several methods to create defects on magnesia thin films have been reported: electron bombardment [225-227], thermal annealing [160, 225, 228], Ar^+ bombardment [225, 229], addition of Li atoms [228, 230-232], and subsequent deposition of Mg [229]. Defect-rich magnesia surfaces are also generated, if the magnesium metal evaporation rate is very fast during the growth process of the MgO films so that not all Mg surface atoms are fully oxidized [233, 234].

In principle, the defects consist of steps, kinks, and isolated vacancies. The vacancies (F centers) are mainly responsible for the reactive character of the magnesia surface. When an oxygen atom leaves the magnesia surface, electrons can be trapped in the vacancy. Depending on the charge, the vacancy is termed F, F^+, or F^{2+}, which corresponds to the removal of a neutral O atom, of an O^-, or of an O^{2-} anion, respectively.

Experimentally, various analytical methods have been employed to investigate F centers on magnesia ultrathin films like, e.g., electron energy loss spectroscopy [228], electron spin resonance [149, 197, 234], scanning tunneling microscopy and spectroscopy [149, 235], as well as infrared vibrational spectroscopy [233] and temperature programmed desorption [225, 233] of adsorbed molecules like, e.g., NO. In addition, there is an extensive theoretical literature available on various aspects of defects in magnesia ultrathin films [165, 236, 237]. In the present investigation the defects were produced by electron bombardment or by anneal-

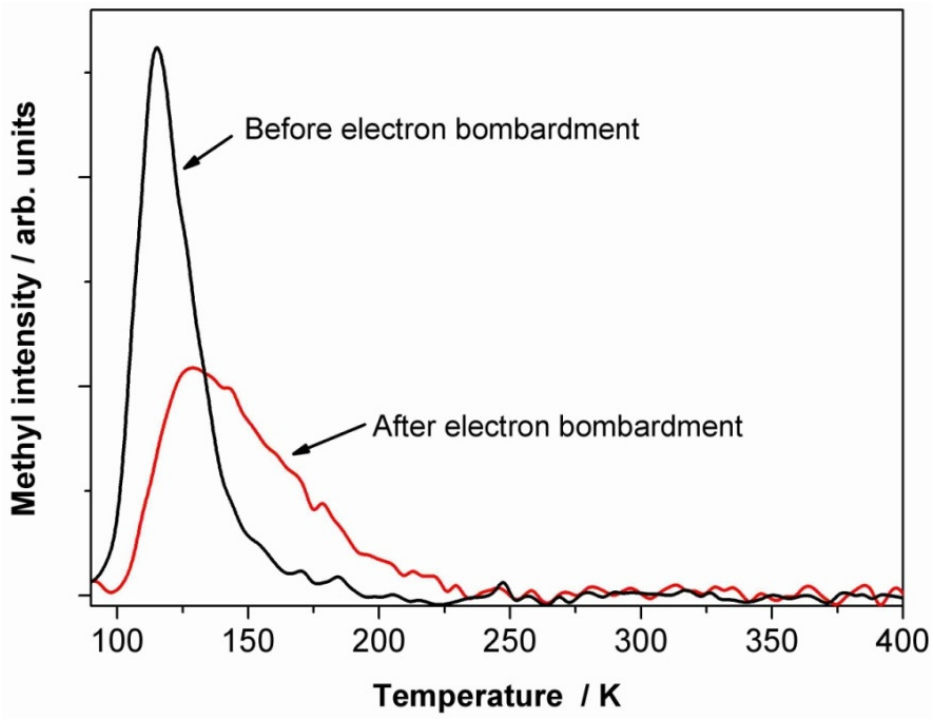

Figure 5.14 Thermal desorption spectra of 0.5 ML CD_3I adsorbed on defect poor (black spectrum) and defect rich (red spectrum) MgO films on Mo(100)

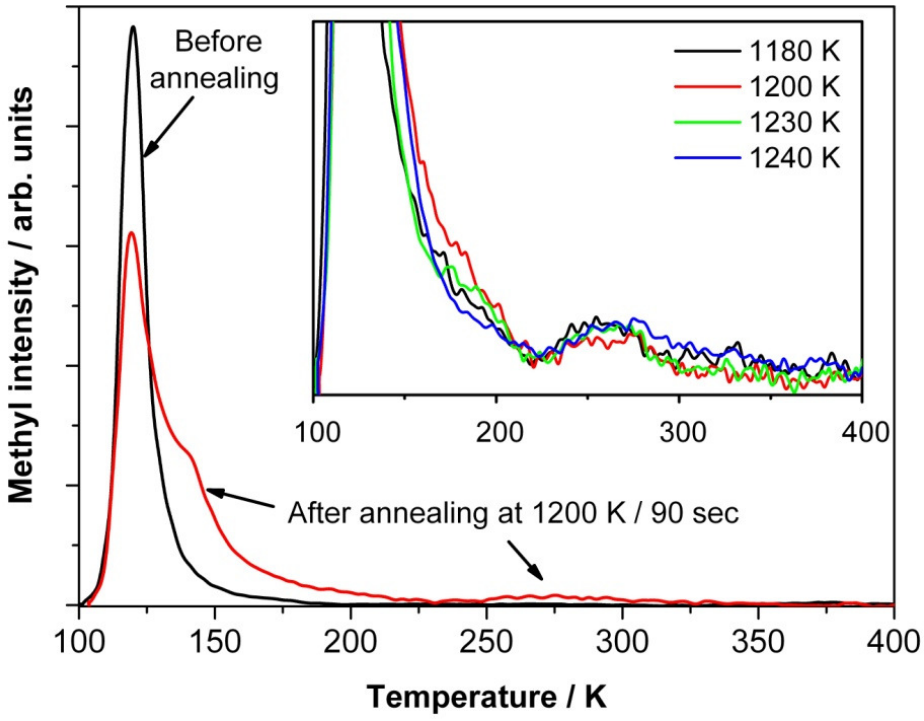

Figure 5.15 Thermal desorption spectra of 0.5 ML CD_3I from 10 MgO/Mo(100) surface before (black spectrum) and after (red spectrum) annealing at 1200 K. Inset: TPD spectra from surfaces annealed at different temperatures between 1080 K and 1240 K.

ing the surface at temperatures close to the thermal decomposition temperature of magnesia (Section 4.1.2).

Employing electron bombardment, the electron stimulated desorption of oxygen is the major process by which surface vacancies are created. In the electron bombardment experiments, a homebuilt electron gun (e^- gun) with an aperture of 10 mm diameter was positioned in the front of the surface. The kinetic energy and the intensity of the electrons were controlled by adjusting the acceleration voltage between the surface and the e^- gun as well as the current applied to the filament of the e^- gun. An amperemeter was employed to measure the intensity of the e^- current between the e^- gun and the sample.

In Figure 5.14 a TPD spectrum of CD_3I adsorbed on a defect-rich 10 ML MgO film on Mo(100) is compared to a TPD spectrum recorded under the same conditions, but from a defect poor MgO film. The sample surface was exposed to 4.5×10^{-2} C/cm^2, and the kinetic energy of the electrons was 200 eV. Comparing the spectra in Figure 5.14, it can be observed that after defect generation the methyl iodide desorption peak maximum shifts from 115 K to 129 K and the desorption peak appears broader. However, no distinct CD_3I desorption peak at higher temperatures, indicating a stronger type of interaction with the magnesia surface is observed. No other reaction products such as C_2H_6 are detected.

Concerning the photochemistry, no dramatic differences are observed between the real-time photodissociation of CD_3I adsorbed on defect poor and defect rich magnesia films produced by means of e^- bombardment. Just the methyl exponential rise signal at longer delay times exhibits a slightly larger time constant on defective films (defect rich τ_3 = 800 fs). However, this time constant becomes shorter when a second transient is recorded from the same surface and approaches the time constant obtained on a defect poor surface (defect poor τ_3 = 680 fs, cf. Figure 5.4) after the recording of a few transients. This indicates a change of the surface, i.e. potentially a “healing” of the surface defects with time.

The second method applied to produce defective magnesia films consists of surface annealing (see Section 4.1.2). Yan et al., determined the relative concentration of the F centers created by annealing the magnesia surface [160]. No defects were created up to 1070 K. Subsequently, the density of F centers increases with increasing annealing temperature. In our experiment, significant differences were observed in the TPD measurements from methyl iodide adsorbed on an as-prepared (defect poor) and on high temperature annealed (defect rich) magnesia films.

In Figure 5.15 TPD spectra recorded from 0.5 ML CD_3I on 10 ML MgO films on Mo(100) before and after annealing at 1200 K are presented (cf. also Section 5.1.1). As described in Section 5.1, methyl iodide binds only weakly to the magnesia surface and desorbs without decomposition below 180 K [211, 238]. If methyl iodide is adsorbed on MgO films on which surface defects were generated through thermal annealing two new distinct desorption features appear (see red spectrum in Figure 5.15). First, a shoulder around 140 K, which extends up to 220 K, appears at the low temperature desorption peak that also exists on defect-poor films. Second, a weak separated desorption peak at 270 K is observed. These de-

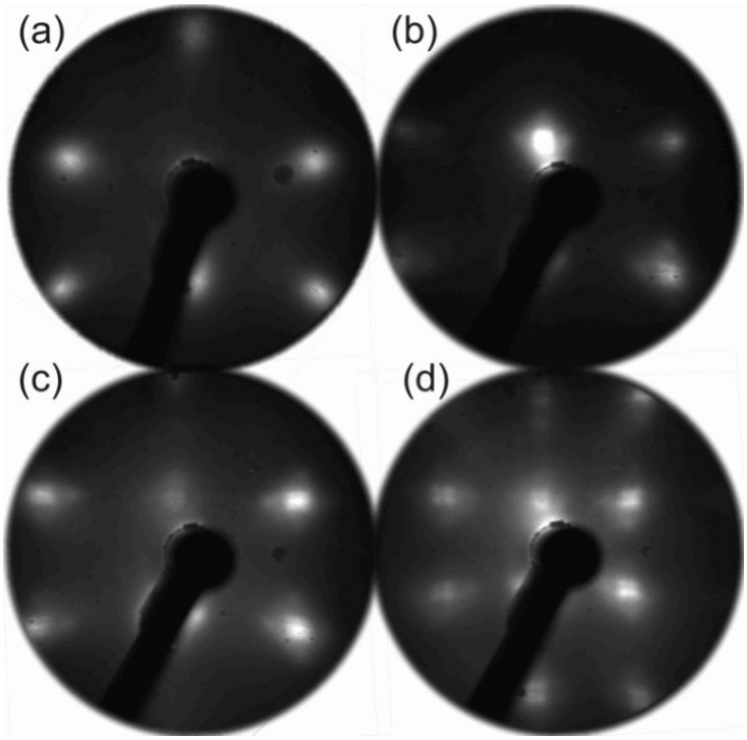

Figure 5.16 LEED images recorded from 10 ML MgO on Mo(100): (a) as prepared Ep = 78 eV; (b) after annealing at 1210 K, Ep = 78 eV; (c) annealed at 1210 K, Ep = 87 eV; (d) annealed at 1210 K, Ep = 150 eV.

sorption characteristics do not change, if the annealing temperature is varied between 1180 K and 1240 K as can be seen from the inset in Figure 5.15.

Figure 5.16 displays LEED images obtained from the same MgO/Mo(100) surfaces (before and after annealing at 1200 K) employed in the TPD spectra shown in Figure 5.15. Upon annealing at 1200 K, the simple 1×1 LEED pattern of the as-prepared surface changes. Characteristic crosses appear around each fundamental spot in LEED (cf. Section 4.1.2) indicating the formation of mosaics spanned between a dislocation network that relaxes the strain in the oxide layer. Consequently, a surface with an increased global roughness is created. Such defect structures present stronger binding sites to the CD_3I molecules which are likely to be responsible for the higher temperature desorption features in Figure 5.15.

The femtosecond photodissociation dynamics of methyl iodide adsorbed at 90 K on a 10 ML MgO film annealed at 1200 K is presented in Figure 5.17. In contrast to the CD_3^+ transient signals measured from a defect-poor magnesia surface (Figure 5.4), the peak structure at early pump-probe delay times is very weak in Figure 5.17a compared to the exponential growth component at later delay times. Moreover, the intensity ratio of the peak structure to the exponential growth structure in the transient methyl signal was found to depend on the methyl iodide coverage (see Figure 5.17). Such a coverage dependent variation of the peak structure intensity relative to the exponential growth component intensity and also to the total CD_3^+ transient signal has never been observed on defect-poor MgO/Mo(100) substrates. Ap-

parently, on the defect-rich, annealed MgO surface the detection of the methyl iodide transition state dynamics by means of one pump plus two probe photons is suppressed, but the REMPI sampling of the emerging methyl fragments is not affected.

A possible explanation might be the strong interaction between the adsorbed methyl iodide molecules and the surface defects, which leads to a considerable distortion of the excited electronic states of methyl iodide rendering the detection via equation (5.1) unfavorable at the employed laser wavelength.

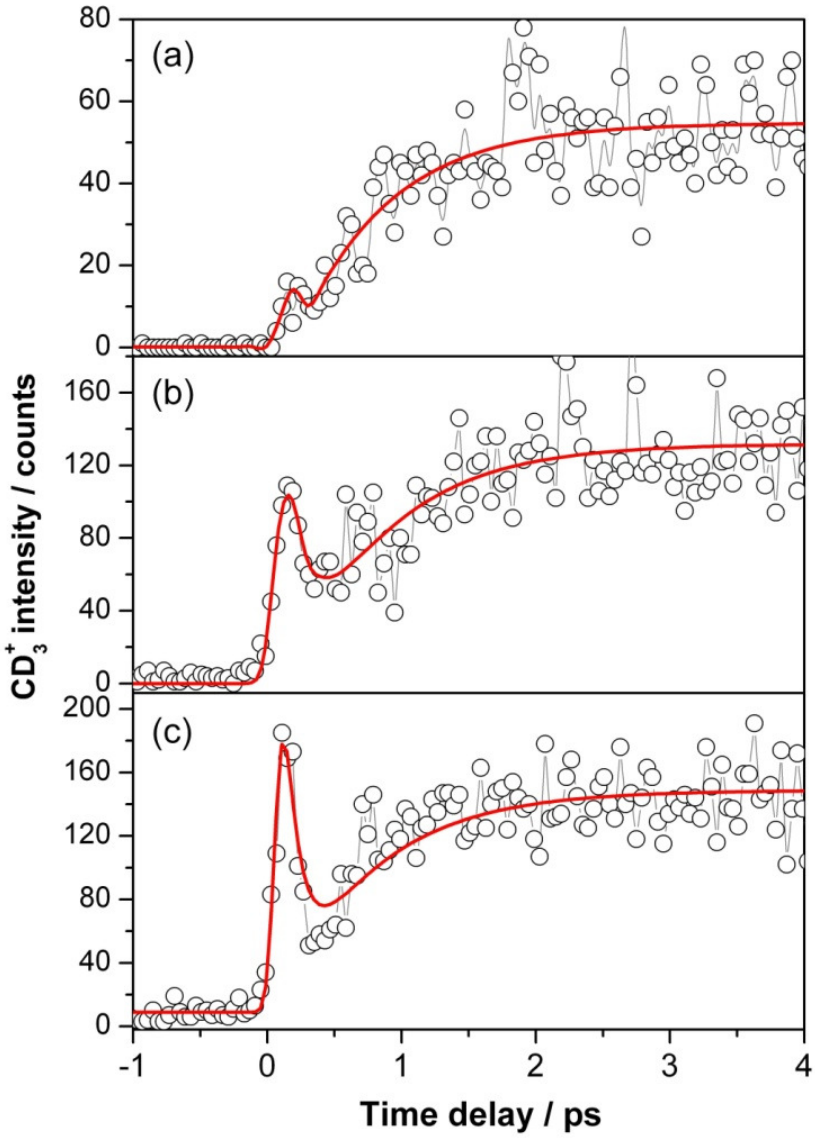

Figure 5.17 Femtosecond dynamics of the surface photodissociation reaction of methyl iodide on a defect-rich MgO film prepared by thermal annealing. The transients were obtained by recording the methyl cation signal intensity as a function of the pump-probe delay time for different methyl iodide coverages: (a) 0.2 ML; (b) 0.5 ML; (c) 0.6 ML. The solid lines are the best fits of the sum of the exponential `rise and decay` and the `delayed exponential rise` model to the experimental data (open circles). Pump pulse: 266 nm, 2 mW/cm²; probe pulse: 333.9 nm, 400 mW/cm².

The observation that on the defect-rich, annealed magnesia films the peak structure in the transient methyl data at early delay times increases in relative intensity with the methyl iodide coverage (see Figure 5.17), indicates that the molecules adsorb first at defect sites, like steps, corners, and vacancies. At higher coverages also the defect-free areas of the magnesia surface become decorated and the resulting transient signal gradually starts to resemble the one obtained from the defect-poor surfaces (cf. Figure 5.3). Interestingly, the obtained time constants of the kinetic model do not differ significantly for the defect-poor and the defect-rich annealed magnesia films.

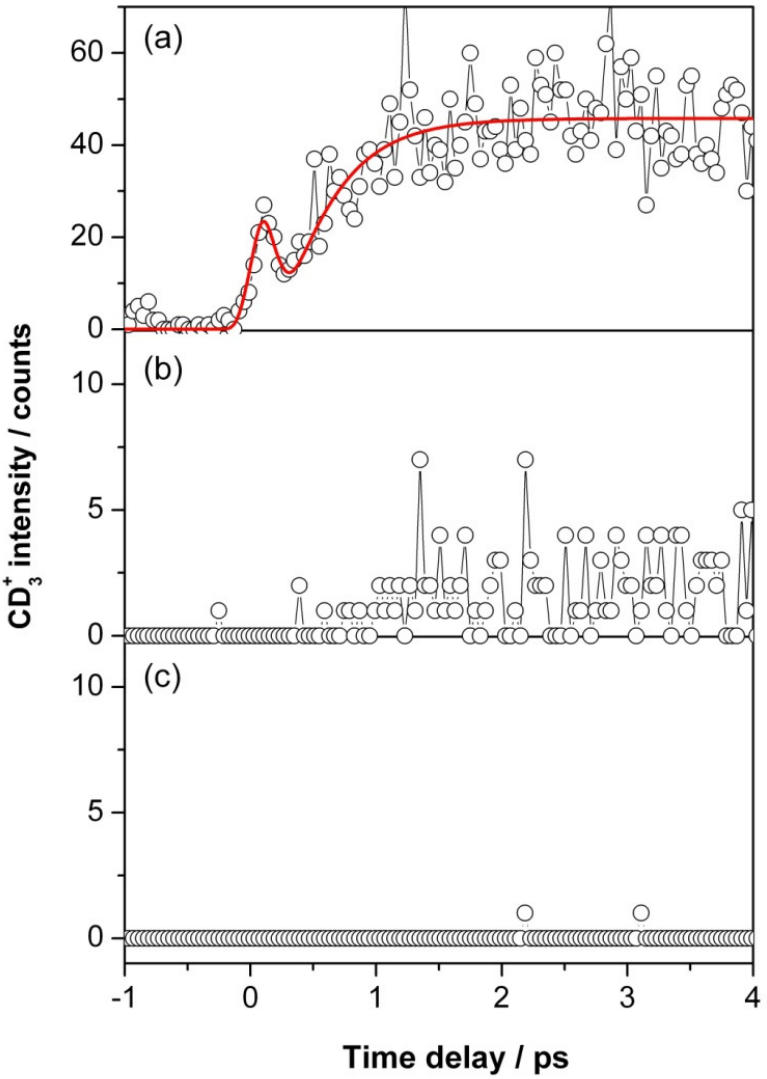

Figure 5.18 Fs time-resolved methyl signal emerging from the photodissociation of CD_3I on defect-rich, annealed 10ML MgO on Mo(100) obtained at different temperatures: (a) 90 K, (b) 160 K, and (c) 250 K. The open circles represent the experimental data whereas the solid line is the best fit of the sum of the exponential `rise and decay` and the `delayed exponential rise` model to the experimental data. In all transients the CD_3I coverage was 0.25 ML. Pump pulse: 266 nm, 2 mW/cm²; probe pulse: 333.9 nm, 400 mW/cm².

As the methyl iodide molecules adsorbed on defect sites have higher desorption temperatures than molecules on the defect-free areas, transient CD_3 signals recorded at elevated surface temperatures should selectively reveal the dissociation dynamics of CD_3I on the defect sites. According to the TPD spectra of CD_3I on defect-rich, annealed magnesia films (cf. Figure 5.15) the majority of CD_3I on defect-free areas should be desorbed at 150 K and the molecules remaining on the surface at higher temperatures are likely to be bound exclusively to defect sites. Figure 5.18 displays transient methyl fragment signals recorded at different surface temperatures on a defect-rich, annealed MgO film. Figure 5.18a shows the transient recorded at 90 K for reference. At a surface temperature of 160 K (Figure 5.18b) the total signal intensity is considerably reduced. Nevertheless, it is quite apparent that the peak structure corresponding to the detection of the dissociative transition state is completely missing. At 250 K no signal is detected anymore, although the molecules corresponding to the 270 K TPD peak in Figure 5.15 (red spectrum) should still remain on the surface. Possible reasons might be that the molecules cannot be excited at these adsorption sites or that the fragments are trapped at the surface and are not detectable with the employed probe laser wavelength.

The previous results show that the methyl iodide adsorption and dissociation dynamics on the magnesia surface is apparently more influenced when the magnesia surface contains defects generated by thermal annealing procedure in contrast to defects generated by electron bombardment. For the interpretation of these results, the theoretical investigation performed by Pacchioni and coworkers is helpful [239]. Computational simulations of MgO crystals [239] show that the F centers at low coordinated sites are more stable than the high coordinated vacancies. This is directly connected to the energy required to remove an oxygen atom from magnesia. Therefore, F centers located at corners are more stable than the F centers located at steps. The stability decreases further for defects on terraces, and the most unstable F centers are located in bulk. This trend is also valid for F^+centers. According to the investigation of Pacchioni et al. [239], a higher density of stable F centers are expected on our MgO/Mo(100) surfaces annealed around 1200 K, due to its increased global roughness. On the other hand, magnesia surfaces bombarded with electrons contain just unstable F centers located at high coordinated sites. Hence, their influence on methyl iodide photodissociation dynamics is weak and disappears with time.

5.2 Methyl iodide on gold

5.2.1 Temperature programmed desorption and reaction

Figure 5.19 shows a series of TPD spectra recorded after dosing different amounts of CD_3I molecules at 90 K onto a 10 ML Au film grown on Mo(100). Similar to the TPD investigation of methyl iodide on Au(100) [59] and Au(111) [240] surfaces that have been reported in the literature, we found that most of the first layer desorbs without fragmentation. At submonolayer coverage just one desorption peak which shifts to lower temperature with increasing coverage appears in the TPD spectra. This desorption feature has been observed for CH_3I [211] (see also Section 5.1) and CH_3Br [241] (see also Section 6.1) on MgO, CH_3Br on LiF [52], CH_3Cl on Pd(100) [242], CH_3Cl, CH_3Br and CH_3I on GaAs(110) [212, 243] and is attributed to the adsorbate-adsorbate repulsion, that results from the interaction between the static dipole moments of adsorbed molecules. Due to this lateral repulsion between the adsorbates, the activation energy for desorption decreases with increasing coverage (cf. Section 2.2.3). The completion of the first monolayer of CD_3I molecules appears for doses just below 4.75 L, in agreement with the previous investigations on Au(100) [59]. The peak below 140 K in Figure 5.19 is due to the multilayer desorption. Higher coverages were not investigated in this experiment.

About 4% of the CD_3I molecules of the first layer dissociate and produce ethane. The inset in Figure 5.19 shows the evolution of the ethane signal in the temperature programmed

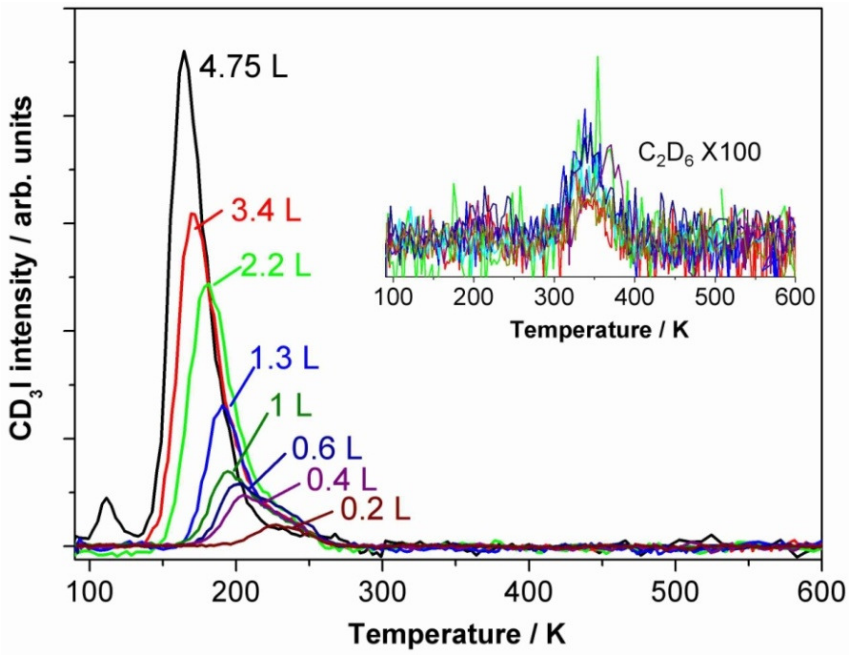

Figure 5.19 Temperature programmed desorption/reaction spectra of CD_3I on a 10 ML Au film on Mo(100). Shown is the CD_3I molecular desorption for different coverages. The numbers indicated at the spectra represent the CD_3I exposure in units of Langmuir The inset displays the C_2D_6 signal evolution.

reaction of CD_3I molecules on the 10 ML Au film on Mo(100). The ethane signal starts just below 300 K, extends up to 400 K and presents a maximum at 350 K. Based on similar results for Au(100) [59] and Au(111) [240], the ethane formation is interpreted to be a consequence of methyl iodide dissociation followed by the coupling between the methyl radicals. Since the ethane appearance temperature is higher than the ethane molecular desorption (below 100 K), it was concluded that the ethane formation is the rate-determining step as opposed to the desorption [59]. Furthermore, it can be assumed that the methyl iodide molecules involved in the thermal reaction dissociate close to ethane appearance temperature (300 K). The remaining iodine atoms resulting from dissociation should desorb from the surface as atoms at temperatures higher than 650 K [244] (not investigated here). The intensity of the ethane signal saturates at a CD_3I coverage corresponding to an exposure of about 0.75 L in agreement with the previous investigation of Yang et al. [59]. No other thermal reaction products were detected.

5.2.2 Photoemission spectroscopy

Fs-laser 2PPS was employed as an additional technique to characterize the CD_3I molecules adsorbed on an Au film on Mo(100). Figure 5.20 displays photoemission spectra recorded from a 10 ML Au film on the Mo(100) surface and from 1 L CD_3I adsorbed on a 10 ML Au film on Mo(100). The spectra in Figure 5.20 are presented on the initial state energy scale ($E_F = 0$) and were recorded at the excitation wavelengths of 333 nm (50 nJ, Figure 5.20a) and 266 nm (80 nJ, Figure 5.20b). The two-photon photoemission spectra from Au films on Mo(100) were already discussed in Section 4.2.1.

After dosing 1 L CD_3I on the gold surface, the shape of the photoemission spectrum does not change with respect to the bare surface, but the work function decreases by about 0.4 eV and the photoemission yield increases. Furthermore, we observed also a variation of the work function with the CH_3I coverage. This is in agreement with the previous publications, which report a decrease of the work function upon adsorption of methyl halide molecules on the metal surfaces (CH_3Cl, CH_3Br and CH_3I on Ag(111) [245], CH_3I on Pd(100) [246, 247], CH_3I on Au(100) [59], CH_3Cl on Pt(111) [248, 249], and CH_3I on Cu(110) [250]).

Yang and coworkers observed that the work function of the Au(100) surface decrease gradually by increasing the methyl iodide coverage [59]. The work function reached the lowest value ($\Delta\Phi$ 1 eV) for exposures of 5 L, and remained constant up to exposures of 15 L. The work function subsequently increased with increasing the methyl iodide coverage. Yang et al., attributed this behavior to the adsorbates dipole-dipole interaction. Based on a local potential model, a localized work function change and a localized ejection of photoelectrons is assumed [251]. In this model, the work function change can be expressed as $\Delta\Phi = C\mu\Theta$, where C is a constant, μ is the dipole moment and Θ is the adsorbate coverage ($0 < \Theta < 1$). The decrease of the work function up to monolayer coverage indicates that the adsorbed CD_3I molecules have a positive outward dipole moment. At higher methyl iodide coverage, due to the

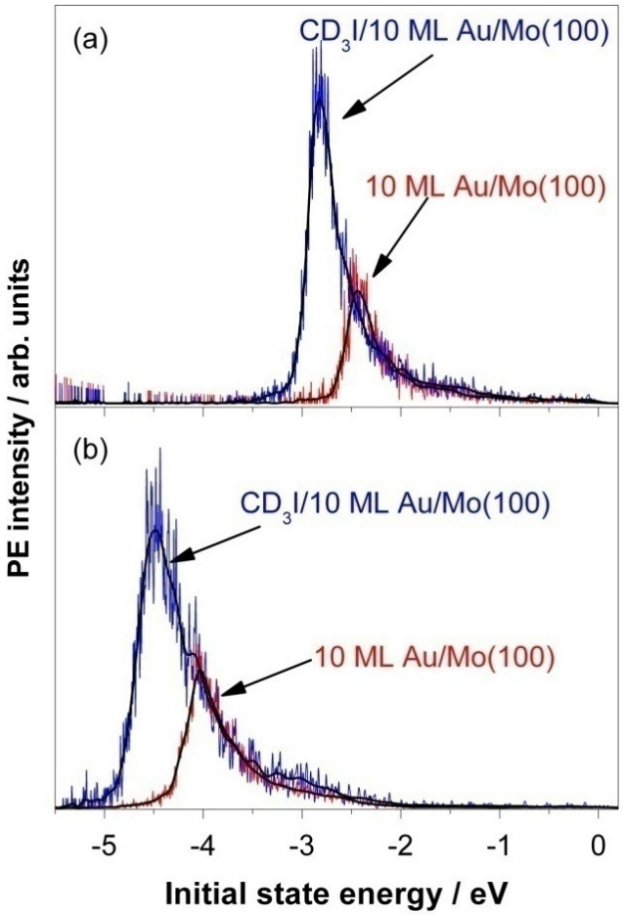

Figure 5.20 One color femtosecond two-photon photoemission spectra recorded from a 10 ML Au film on Mo(100) before and after deposition of 1 L CD_3I . The spectra were recorded at wavelengths of (a) 333 nm and (b) 266 nm.

lateral interaction between neighboring adsorbates, a dipole depolarization occurs and consequently an increase of the surface sample work function occurs. The constant value of the work function at intermediate coverage (5-15 L exposure) was attributed to the simultaneous formation of a metastable state and of multilayers, which have opposite effects [59]. Thus, the work function change of the Au surface after adsorption of CD_3I gives information concerning the orientation of the adsorbate molecules.

Figure 5.21 shows a series of photoemission transients recorded from a 10 ML Au film on Mo(100) on which different amounts of CD_3I have been deposited. The left part shows the integral transient photoemission signal, while the right part displays just the transient photoemission signal originating from the states located from E_F to 0.5 eV above E_F. The pump and probe wavelengths were 266 nm (80 nJ) and 333 nm (50 nJ), respectively. The transient photoemission signal (Figure 5.21a, left hand side) consists of a peak structure centered at 0 fs. Increasing the CD_3I coverage on the Au film, this peak structure (Figure 5.21b-e, left hand side) remains centered at 0 fs, but it becomes intensive and broader.

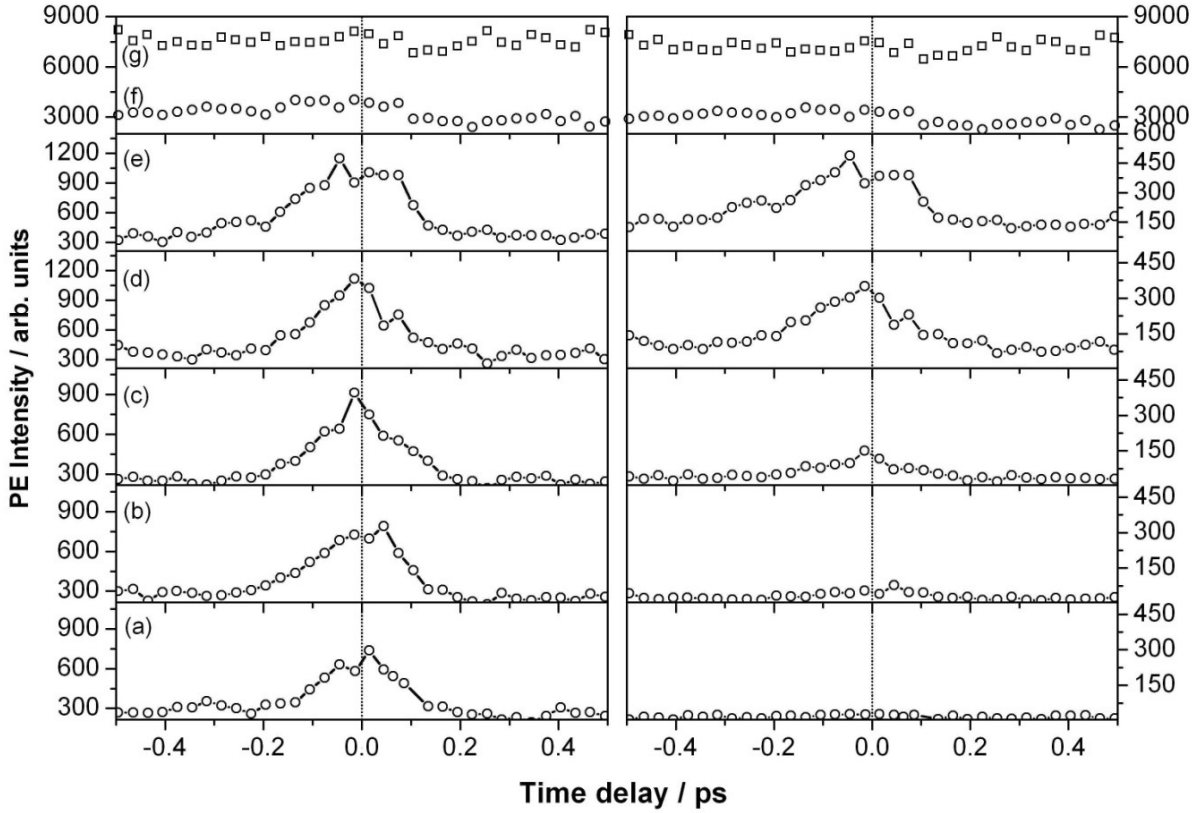

Figure 5.21 Two-photon photoemission transients recorded from 10 ML Au film on Mo(100) dosed with different CD_3I amounts: (a) 0 L; (b) 0.25 L; (c) 0.5 L; (d) 0.75 L; (e) 1 L; (f) 1.2 L; (g) 1.5 L;. The left part shows the total photoemission transient signal, while the right part displays just the transient photoemission signal originating from the states located from E_F to 0.5 eV above E_F.

For CD_3I exposures larger than 1 L the total photoemission signal increases, but the time dependent peak structure disappears (cf. Figure 5.21f,g, left hand side). The same transient photoemission behavior is observed when just the states located from E_F to 0.5 eV above E_F are monitored (cf. Figure 5.21b-g, right hand side), but the increase of the transient photoemission intensity with increasing CD_3I coverage is more apparent.

The gradual increase of the photoemission signal in Figure 5.21 with increasing CD_3I coverage is attributed to the gradual decrease of the surface work function. At CD_3I exposures up to 1 L, the transient peak structure in Figure 5.21 becomes broader with increasing adsorbate coverage. As shown by Cao et al. [134] the lifetime of the electronic states above E_F increase gradually from E_{VAC} to E_F. The temporal broadening of the 2PPS transient signal in Figure 5.21b-e is attributed to the surface work function reduction induced by the adsorbed molecules, which facilitates the excitation of the long lifetime intermediate states closer to E_F. The loss of the transient signal (peak structure) in Figure 5.21f,g is caused by the lowering of the work function value to less than 4.66 eV. Consequently, the major part of the photoemission signal is produced in a single-photon excitation process at 266 nm.

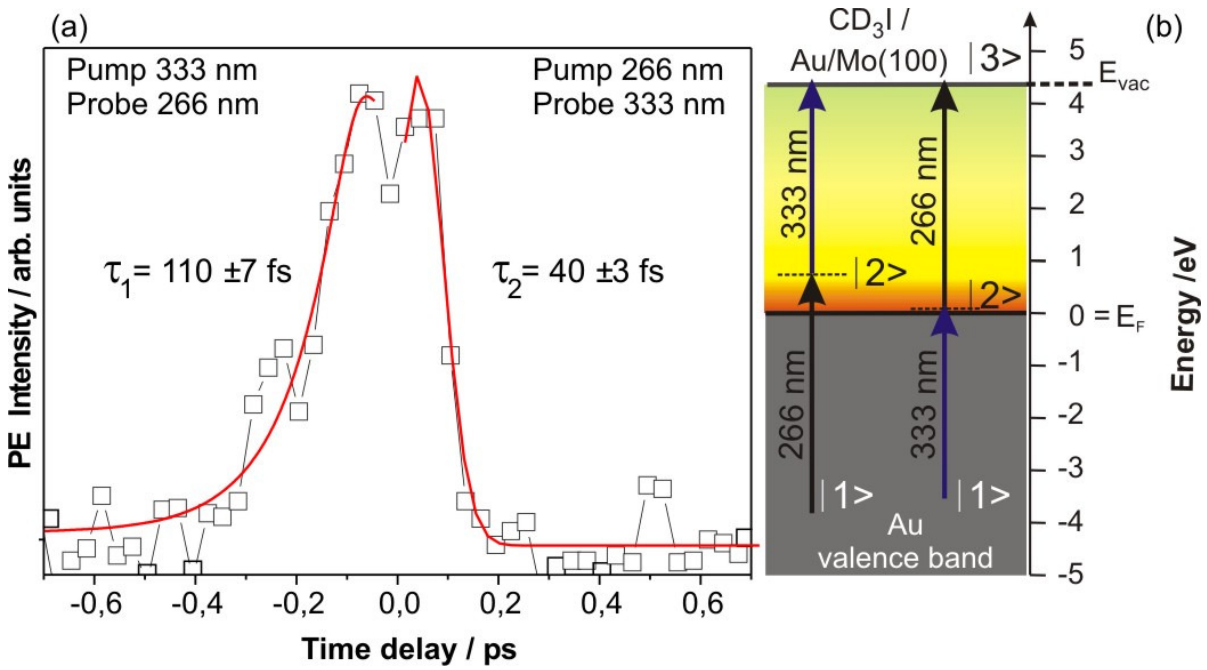

Figure 5.22 (a) Enlarged view of the photoemission transient signals presented in Figure 5.21e (right side). The solid lines represent the best fit of the experimental data with a first-order exponential decay function convoluted with the Gaussian autocorrelation function (cf. Section 3.5.4.2). (b) Schematic energy level diagram illustrating the assignment of the different excitation processes that lead to the observed transient signal. |1>, |2>, |3> *represent the initial, the intermediate, and the final electronic states involved in this pump-probe experiment.*

In Figure 5.22a an enlarged view of the photoemission transient signal presented in Figure 5.21e (right side) is displayed. At negative time delay, the intermediate states above the Fermi level are populated by the photons having the energy of 3.72 eV (333 nm, pump). Subsequently these states are probed by the photons with an energy of 4.66 eV (266 nm, probe). At positively time delay the sequence of the laser pulses is exchanged (266 nm pump and 333 nm probe). Both pump-probe schemes are presented in Figure 5.22b. Due to the long lifetime of the intermediate states that can be probed at a wavelength of 266 nm with respect to 333 nm, an asymmetric transient peak shape is observed with a longer decay time constant (τ_1) at negative delay times (see the values of τ_1 and τ_2 in Figure 5.22). This effect is more pronounced when just the low energy electrons are gated (cf. Figure 5.21 - right side).

5.2.3 Methyl iodide photochemistry on gold

5.2.3.1 Methyl iodide photodissociation on a gold surface

CD_3I was adsorbed at submonolayer coverage on a 10 ML Au film on Mo(100) and irradiated using the same laser parameters as in the previously described experiments, i.e. pump beam: 266 nm, 80 fs, *p*-polarized, 1-2 mW/cm^2; and probe beam: 333.4 nm, 80 fs, p-polarized, 600 mW/cm^2. However, neither photodissociation products, nor the parent molecule were detected independent on the pump-probe delay time.

Similar results were reported by White and coworkers for methyl iodide adsorbed on Pt(111) [252-255]. In their work, methyl iodide molecules adsorbed on the metal surfaces were exposed to the full spectrum of a Hg arc lamp. The photodissociation and the desorption of the molecules from the surface was subsequently monitored by means of X-ray photoemission spectroscopy. White and coworkers measured that only 10% of the first CH_3I layer adsorbed on Pt(111) substrate dissociated, if the sample was irradiated for 120 minutes with a 100 W Hg arc lamp [253]. In contrast, a facile cleavage of the second layer was observed.

According to vibrational spectroscopy investigations, the methyl iodide molecules adsorb on a Pt(111) surface with the halogen atom bound to the surface and with the C-I axis considerably tilted away from the surface normal [221]. On Au(100), even an adsorption geometry with the C-I axis almost parallel to the surface plane is expected for CH_3I at submonolayer coverages [59]. Under these circumstances, the ground state of the CH_3I molecule is weakly perturbed from the gas-phase, but the excited state is strongly bound to the metal surface, which facilitates the recapturing of the ground state before the C-I bond stretches considerably. This means that after excitation, the molecule will almost instantaneously relax back to the ground state and the molecular dissociation will be quenched.

In contrast to CH_3I, the photodissociation of the first monolayer of CH_3Br and CH_3Cl is easily promoted on the Pt(111) surface [248, 255-257]. Also on the Ag(111) surface the methyl iodide molecules adsorbed at monolayer coverage are photolyzed at slower rate compared to multilayer coverages, indicating a substantial quenching of the photodissociation when the molecules are in contact with the metal substrate as well [258, 259].

5.2.3.2 Trapping of the I atoms at the surface subsequent to CD_3I photodissociation on Au

Figure 5.23 displays the time evolution of the CD_3^+ signal during continuous admission of CD_3I to a 10 ML Au film on Mo(100). The surface temperature was held at 120 K to ensure a maximum CD_3I coverage of just about one monolayer (cf. Figure 5.19 and Ref [59]). In the beginning (period A in Figure 5.23), the surface was continuously irradiated by the laser beams. An increase of the CD_3^+ signal intensity was observed starting after a few tens of seconds. The saturation of the CD_3^+ signal appeared close to 2000 s. The CD_3^+ signal up to 2000 s was approximated with an exponential rise function. The obtained time constant was $\tau_A = 410 \pm 20$ s. After 2000 s (period B in Figure 5.23), the CD_3I admission was stopped, but the surface was further irradiated by the laser beams. The CD_3^+ signal immediately starts to decrease. This decay is best fitted by a second order exponential decay function. The time constants of the fast and slow decaying parts are $\tau_{B1} = 55 \pm 5$ s and $\tau_{B2} = 300 \pm 100$ s, respectively. After 3000 s the CD_3I gas admission was restarted (period C in Figure 5.23). and the CD_3^+ signal exhibits an abrupt increase. The best fit to this signal with an exponential rise function gives a time constant of $\tau_C = 75 \pm 22$ s.

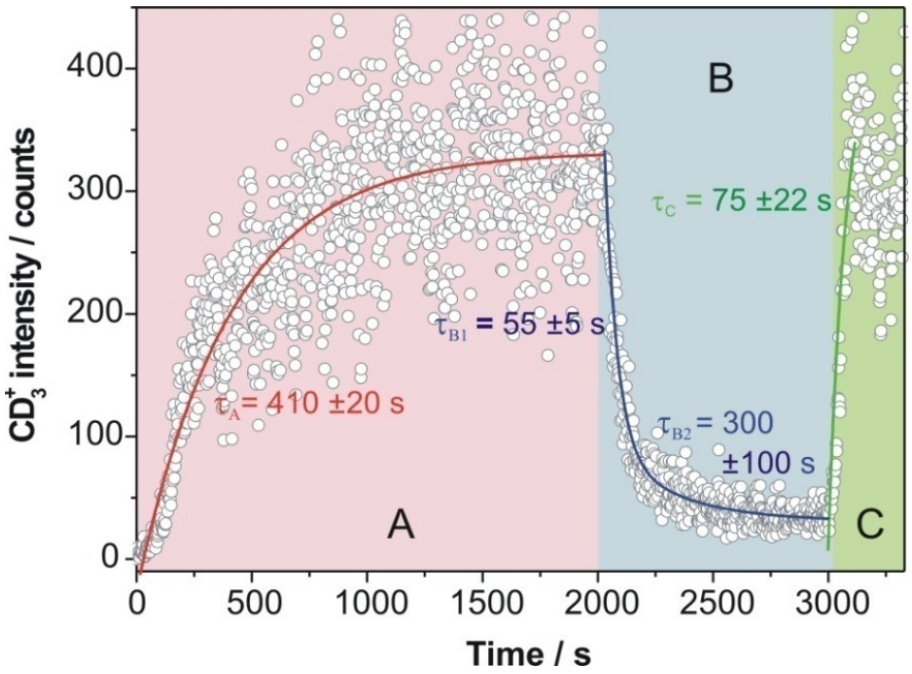

Figure 5.23 Time evolution of the integral CD_3^+ intensity (open circles) during the continuous admission of CD_3I to a 10 ML Au film on Mo(100). The surface temperature was 120 K. At 2000 s the gas admission was stopped for 1000 s. The solid lines represent the best fits to the different parts of the measured data (A, B and C) with exponential growth and decay functions, respectively (see text for more details). Pump pulse 266 nm, 2 mW/cm²; probe pulse 333.9 nm, 600 mW/cm²; pump-probe delay time 130 fs.

The rise of the CD_3^+ signal in Figure 5.23 (period A) cannot be attributed to the continuous accumulation of CD_3I molecules on to the surface, since the saturation of the monolayer is expected within less than 10 s. Moreover, a subsequent irradiation of a new (but already covered with CD_3I) surface area, of the same sample, gave a similar exponential rise of the CD_3^+ signal. Therefore, it must be assumed that the result shown in Figure 5.23 indicate a change in the in the nature of the surface during laser irradiation. As discussed in the previous section, just a small amount of C-I bond cleavage of CH_3I at monolayer coverage on Pt(111) was observed after a long time (120 min) irradiation with a 100 W Hg arc lamp [253, 260]. In the present experiment a much more intense light source, i.e. a femtosecond laser, was employed. Therefore, in our experiment the dissociation of the CD_3I adsorbed at monolayer coverage on Au can be assumed to occur at a faster rate (on the time scale of tens of seconds in contrast to tens of minutes). According to the adsorption geometry and binding energy of methyl iodide molecules on the Au surface [59], we expect the trapping of the iodine atoms at surface subsequent to CD_3I photodissociation. Consequently, during the laser irradiation of the sample an iodine film might be formed between the Au surface and the subsequently adsorbed CD_3I molecules. On this iodine film, the photodissociation of the CD_3I molecules should not be quenched anymore. The suggestion of the formation of an iodine layer in the

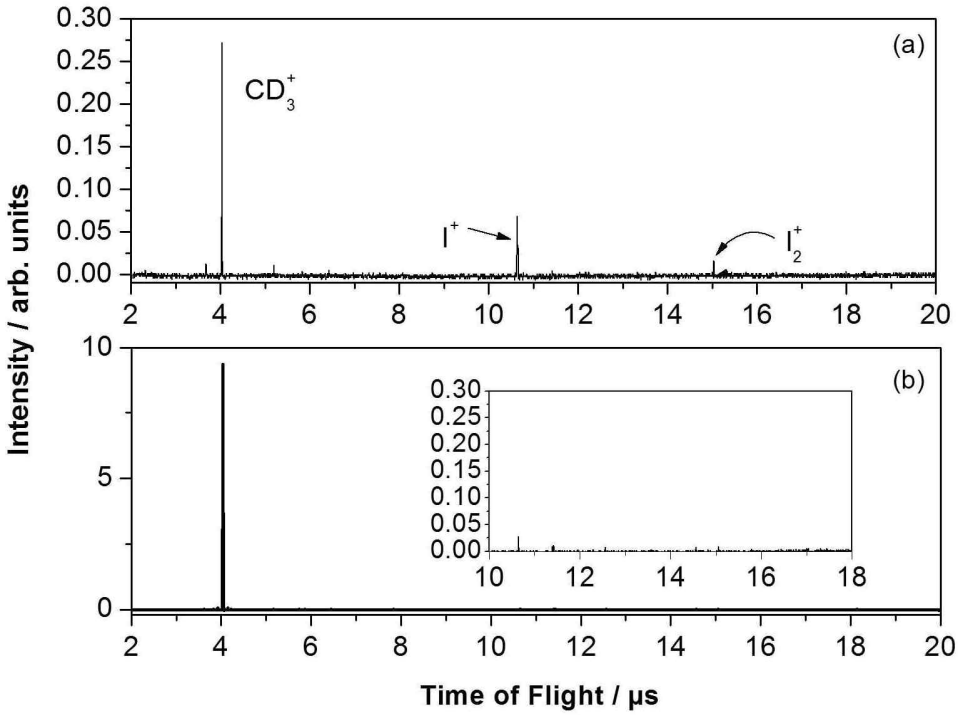

Figure 5.24 Mass spectra recorded at (a) 150 K and (b) 100 K from the same surface sample as in Figure 5.25 period C, after 3500 s. The inset presents a zoom in to the mass spectrum (b). During the recording of the mass spectra, CD_3I was continuously dosed on to the surface. The laser parameters were: pump pulse 266 nm, 2 mW/cm²; probe pulse 333.9 nm, 600 mW/cm²; pump-probe delay time at 130 fs.

present experiment is supported by the investigations of White and coworkers, who observed that the CH_3I photodissociation on a Pt(111) surface pre-covered with a monolayer of iodine atoms was not quenched as well [260].

The rise time of the CD_3^+ signal in Figure 5.23 (period A) should be related to the formation of the iodine layer. Once the sample is modified, i.e. the transformation $CD_3I/10\ ML\ Au/Mo(100) \xrightarrow{LASER} CD_3I/I/10\ ML\ Au/Mo(100)$ is completed, the laser can induce the dissociation and fragment desorption of an significant part of the adsorbed molecules. The dissociated and desorbed amount of CD_3I molecules is immediately restored, due to the continuously admission and a stable methyl desorption signal is established at the end of period A in Figure 5.23.

In Figure 5.23 (period B), the fast decaying part is attributed to the dissociation of the uppermost CD_3I molecules, weakly adsorbed on the iodine spacer layer. The slowly decaying part in period B, could be attributed to the dissociation of strongly bound CD_3I molecules, possibly surrounded by iodine atoms. To the end of period B in Figure 5.23 it can be expected that the sample surface consists mostly of iodine atoms adsorbed on the gold film on Mo(100).

The considerably faster rise of the methyl signal in period C of Figure 5.23, when the gas admission was restarted, compared to the one obtained in the beginning of the experiment

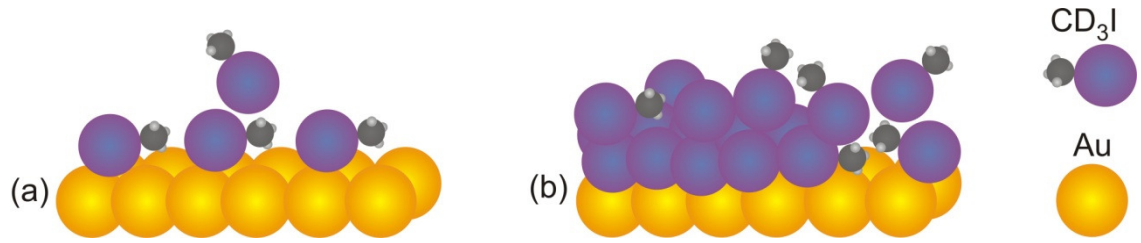

Figure 5.25 (a) Schematic representation of >1 ML CD_3I adsorbed Au surface. (b) Formation of an iodine spacer between the Au substrate and the adsorbed CD_3I molecules subsequent to continuous gas admission and laser irradiation of the surface.

(see period A in Figure 5.23), supports the assumption that a change of the surface sample composition after laser irradiation during continuous methyl iodide admission has occurred. The CD_3^+ signal in period C is attributed to the dissociation of CD_3I molecules adsorbed on the new iodide film formed during previous laser irradiation. The fast rises of the CD_3^+ signal than reflects the time needed to saturate this iodine film surface with CD_3I molecules. The maximum CD_3^+ signal intensities reached in both period B and C coincide. The exact values of the time constants presented in Figure 5.23 depend of course strongly on the laser intensity. In particular the rise time in period A can be strongly enhanced by a reduced laser intensity.

In Figure 5.24 mass spectra recorded from the surface sample used in Figure 5.23 after 3500 s are shown. At a surface temperature of 150 K (Figure 5.24a), signals corresponding to atomic and molecular iodine are detected apart from the methyl mass peak. For comparison, in Figure 5.24b a mass spectrum recorded at a surface temperature of 100 K is shown. When the sample is held at 100 K the methyl peak intensity is about 35 times higher than at 150 K due to the CD_3I multilayer formation. In contrast, at 100 K, the intensity of the atomic iodine is less than a quarter and the intensity of molecular iodine is less than a half of the intensity measured at 150 K. The higher amount of iodine atoms and molecules detected at a surface temperature of 150 K, when the CD_3I coverage could not exceed the monolayer (cf. Figure 5.1), also supports the assumption that iodine atoms are trapped on the gold surface, which can also be desorbed by laser irradiation under these conditions. In contrast, at multilayer coverages, the atomic and molecular iodine desorption is suppressed.

Based on these results, a schematic representation of gold surface prepared with CD_3I molecules before and after prolonged laser irradiation is proposed in Figure 5.25. As already mentioned, the first CD_3I layer is adsorbed on the gold surface with the C-I axis almost parallel with the surface (Figure 5.25a). In the second and multilayer, the average molecular orientation is neither flat nor upright but with the C-I bond tilted from the surface normal [59]. After extended laser irradiation of the CD_3I/Au/Mo(100) surface sample and continuously CD_3I admission, the formation of an iodine film at the surface occurs. The possibility of iodine islands formation and intercalation of CD_3I between the iodine fragments is not excluded (cf. Figure. 5.25b).

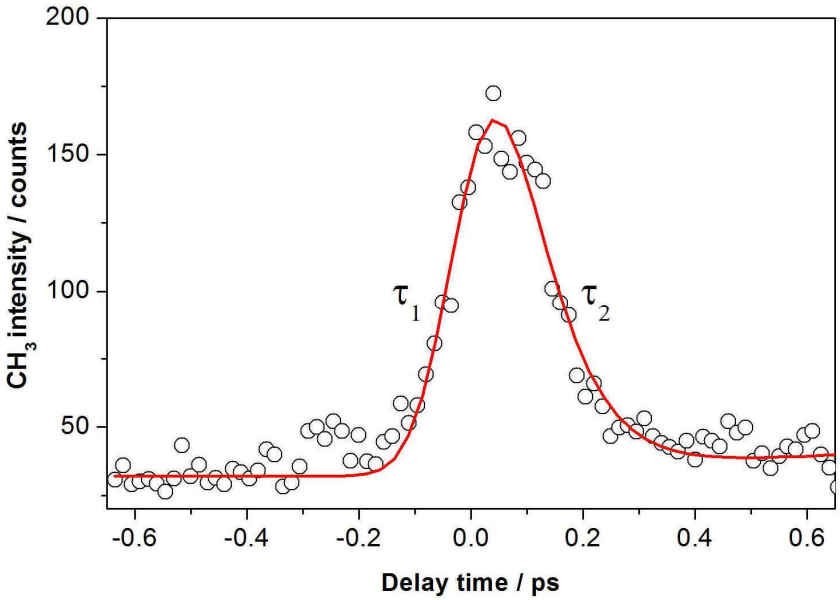

Figure 5.26 Femtosecond photodissociation reaction of multilayer methyl iodide adsorbed on 10 ML Au/Mo(100) recorded by monitoring the transient methyl cation signal intensity as a function of the pump-probe delay time (pump 266 nm, 2 mW/cm² and probe 333 nm 60 mW/cm²). The solid line is the best fit of an exponential 'rise and decay'-model to the experimental data yielding the indicated time constants τ_1 and τ_2.

The femtosecond photodissociation dynamics, of multilayer CD_3I adsorbed on the I/Au/Mo(100) surface was recorded by monitoring the transient methyl cation signal intensity as a function of the pump-probe delay. The result is shown in Figure 5.26. The CD_3^+ transient signal consists of a peak structure with a maximum at 50 fs. We attribute again the peak structure to the dynamics of the dissociating excited transition state of methyl iodide, which was directly ionized by the probe pulse by means of two photons at 333.9 nm immediately after A-band excitation by means of a single photon at 266 nm (cf. Scheme (5.1)). Subsequent rapid decomposition of the excited methyl iodide cation is proposed to lead to the observed methyl fragment signal. Fitting the experimental data with an exponential 'rise and decay'-model, the time constants of $\tau_1 = 60$ fs and $\tau_2 = 70$ fs for the rise and decay of the peak structure have been obtained.

5.3 Methyl iodide on magnesia supported gold nanoparticles

5.3.1 Methyl iodide adsorption on magnesia supported gold nanoparticles

The adsorption behavior of methyl iodide on magnesia supported gold nanoparticles was characterized by means of TPD measurements. The Au nanoparticles were grown by gold deposition at normal incidence with the gold evaporator as described in Section 3.3. As shown in Section 5.1.1, methyl iodide adsorbs molecularly on the magnesia surface and desorbs without decomposition [211, 238]. On the gold surface methyl iodide adsorbs molecularly too, and desorbs without decomposition to more than 95% (see Section 5.2.1). Detailed TPD investigations of the methyl iodide adsorbed on magnesia and gold surfaces at submonolayer coverages were already presented in this chapter (Section 5.1.1 and Section 5.2.1). On the MgO surface a single desorption peak with the intensity maximum around 140 K is observed for 0.25 ML CD_3I coverage as show in Figure 5.27a. When 0.12 ML gold is deposited on the

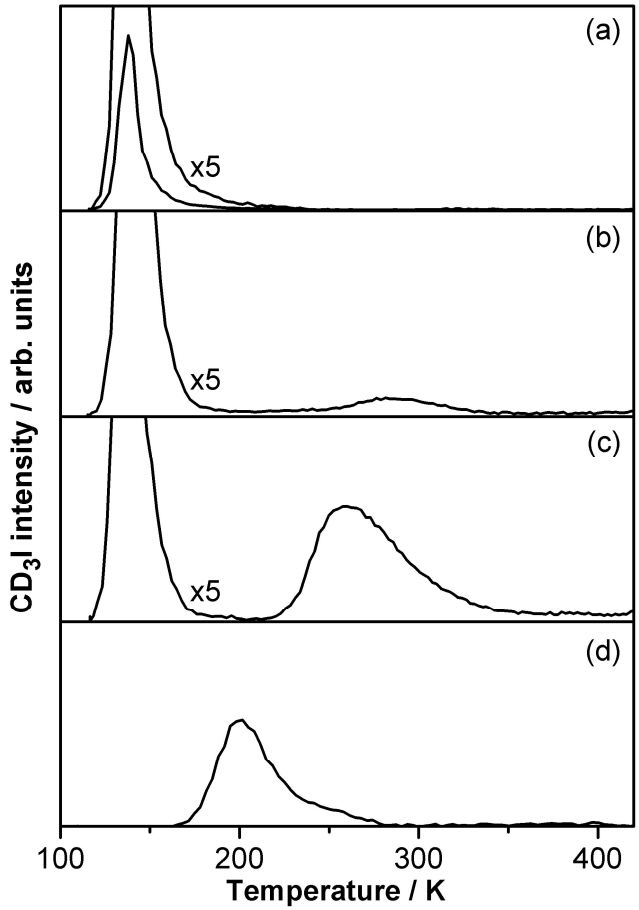

Figure 5.27 TPD spectra of 1 L (1 L = 0.25 ML [18]) CD_3I on a bare 10 ML MgO film on Mo(100) (a), on MgO supported gold nanoparticles generated by depositing different gold coverages ((b) 0.12 ML Au, (c) 0.90 ML Au), and on a 10 ML gold film on Mo(100) (d). The heating rate was 2 K/s.

magnesia thin film, a new distinct CD_3I desorption peak with a maximum located at 285 K appears in the TPD spectrum (Figure 5.27b). This new desorption peak is attributed to molecular methyl iodide desorption directly from the gold particles. Neither fragments nor new reaction products were detected.

With increasing gold coverage the peak at 140 K remains unchanged, but the peak representing the desorption from gold particles shifts to lower temperatures. Figure 5.27c displays the TPD spectrum obtained from an MgO film covered with 0.9 ML Au (cf. Section 4.3). Here, the desorption peak maximum from gold particles is located at 260 K. The coverage dependent adsorption energy (reflected in the temperature shift of the TPD peak) points toward a change in the morphology and the electronic structure of the supported gold. Consequently, larger nanoparticles are assumed to be formed at 0.9 ML Au coverage. Thus, the shift of the methyl iodide desorption peak at elevated temperatures can be attributed to the adsorption on different size gold nanoparticles.

The integrated TPD peak areas of the CD_3I desorption from gold and from magnesia, respectively, further support the coverage dependent nanoparticle growth (the monolayer saturation coverage for magnesia and gold are identical [59, 211]): for 0.12 ML Au coverage the fraction of desorbing molecules from gold (12%) to the gold coverage is about unity, whereas for 0.9 ML Au coverage 50% of the desorbing molecules originate from the gold leading to a much smaller value for this fraction (0.45). This indicates that some of the gold is no longer available for surface CD_3I adsorption and might be rather incorporated into larger gold nanoparticles. Finally, in Figure 5.27d the TPD of 1 L CD_3I on a 10 ML Au film on Mo(100) is presented (same spectrum as in Figure 5.19). Now, the maximum of the desorption peak has shifted further down to 200 K.

5.3.2 Photodissociation dynamics

Two distinct desorption peaks of molecular methyl iodide were identified corresponding to molecules bound to magnesia and more strongly bound to gold, respectively (cf. Figure 5.27). This permits to selectively investigate the photoreaction of methyl iodide on the gold particles by choosing the appropriate temperature at which all molecules have been desorbed from MgO but not yet from the gold particles.

The ultrafast photodissociation dynamics of methyl iodide absorbed on magnesia covered with gold particles is presented in Figure 5.28 for different substrate temperatures. Shown are the results for a sample containing 0.12 ML Au on MgO/Mo(100). All transients were recorded with the same laser parameters, i.e., pump beam: 266 nm, 80 fs, *p*-polarized, 1 mW/cm^2; and probe beam: 333.4 nm, 80 fs, *p*-polarized, 400 mW/cm^2. The open circles in Figure 5.28 represent the transient CD_3^+ signal obtained at 90 K. It consists of a peak starting at zero delay time with a maximum reached around 130 fs and a subsequent delayed exponential rise. The major contribution to this signal is from the photodissociation of CD_3I adsorbed on MgO (see Section 5.1.2). The methyl transient recorded at 150 K surface temperature is represented by the open squares in Figure 5.28. This transient has a similar appearance as the

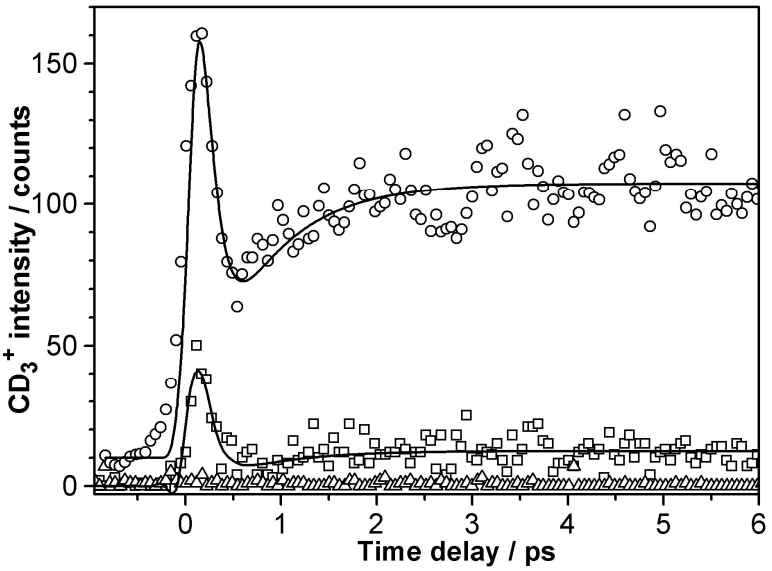

Figure 5.28 Femtosecond dynamics of the surface photodissociation reaction recorded by monitoring the transient methyl cation signal intensity as a function of the pump-probe delay time at different temperatures (0.12 ML Au on MgO/Mo(100)). Circles:90 K; squares: 150 K; and triangles: 170 K. The solid lines represent the fit of a peak with delayed exponential rise model to the experimental data [3]. The obtained time constants are presented in the text.

90 K transient, but with a lower intensity. Fitting the experimental data recorded at 90 K and 150 K by a peak in conjunction with an exponential rise model (solid lines in Figure 5.28) results in the same time constants for both temperatures as for bare MgO substrate (cf. Figure 5.4). Further heating to 170 K leads to the disappearance of the transient signal. Above 180 K the TPD data indicate (cf. Figure. 5.27) that all CD_3I molecules are adsorbed just on gold. However, no photodesorption of CD_3 fragments could be detected at this temperature. The same behavior was observed for all investigated gold coverages.

These observations are also reflected in the photodissociation mass spectra recorded from CD_3I on magnesia supported Au nanoparticles. Figure 5.29 displays a series of mass spectra recorded at 2 ps pump-probe delay time from CD_3I adsorbed on 0.12 ML Au deposited on MgO/Mo(100) for different substrate temperatures. At 90 K both CD_3^+ and I_2^+ are present in mass spectrum. With increasing the surface temperature their intensity decreases and at 170 K all ion signals completely disappear from the mass spectrum.

Consequently, it has to be concluded that the initial excitation does not lead to photodissociation in the case of CD_3I adsorbed on gold particles. This result can be rationalized by considering previous experiments with methyl iodide adsorbed at submonolayer coverages on Pt(111) [255], Ag(111) [259], and Au(100) (see Section 5.2), respectively. In these cases, the molecules are adsorbed with the C-I axis lying almost parallel to the substrate surface. Under this circumstance, the ground state of the molecules is weakly perturbed from the gas-phase, but the excited state is strongly bound to the metal which facilitates the recapturing of the

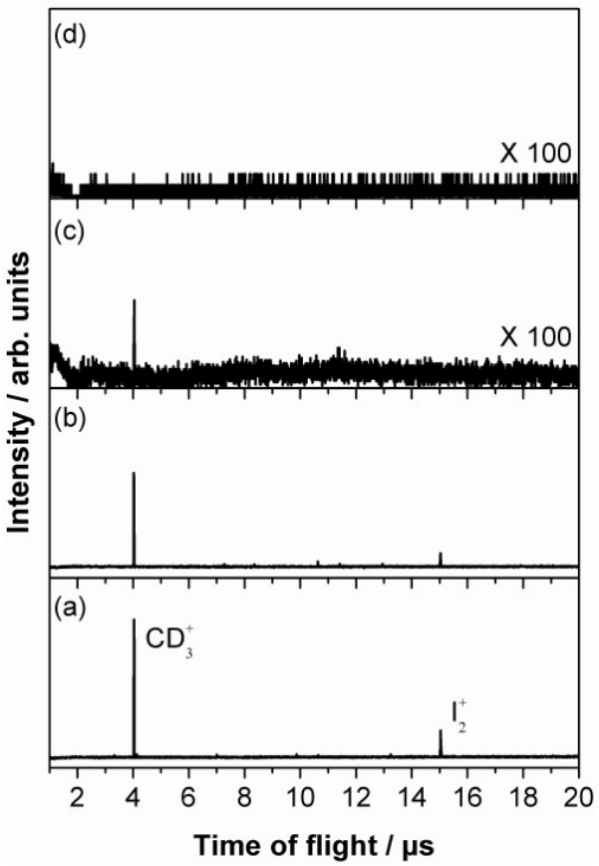

Figure 5.29 Mass spectra recorded from methyl iodide adsorbed on magnesia supported Au nanoparticles (12% ML Au deposition) at different temperatures: (a) 90 K; (b) 110 K; (c) 150 K; (d) 170 K. All spectra were recorded at 2 ps pump-probe delay time.

ground state before the C-I bond stretches considerably. This means that after excitation, the molecule will almost instantaneously relax back into the electronic ground state and the molecular dissociation will be quenched. Potential excitation mechanism on nanoparticles might also include photoelectron attachment processes (cf Section 3.4) as observed for metal and semiconducting substrates [261].

5.3.3 Methyl iodide reactivity with very small gold clusters

Since the methyl iodide molecules could not be photodissociated neither on the gold nanoparticles nor on gold films, an additional experiment was performed with very small gold clusters consisting of few atoms deposited on a magnesia surface. For this purpose, Au_n^+ (n = 1, 2, 3), produced by the cluster source, were deposited on the magnesia surface (10 ML MgO on Mo(100)) at 90 K by means of soft-landing, as described in Chapter 2. In all experiments the gold coverage was about 0.02 ML. However, the methyl iodide photodissociation dynamics on magnesia prepared with Au_n^+ (n = 1, 2, 3) clusters appeared to be similar to the results shown in Figure 5.28. In contrast to the experiments with gold nanoparticles (Figure 5.27) no

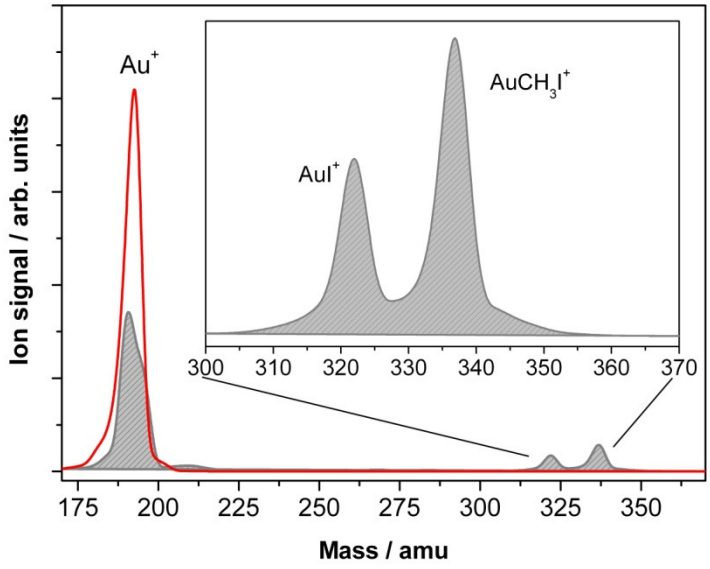

Figure 5.30 (solid line) Gas-phase mass spectrum of Au_1^+; (solid line, filled spectrum) Product ion mass spectrum between CH_3I and Au_1^+ in the presence of He buffer gas. The inset displays an enlarged view of the product mass spectrum between 300 and 370 amu.

distinct methyl iodide desorption peak from these small mass-selected Au clusters was observed in the TPD spectra.

In order to understand the absence of the methyl iodide signal in TPD measurements from magnesia supported mass-selected Au_n^+ (n = 1, 2, 3) clusters, an additional experiment was preformed. In this experiment, the gas-phase reaction between mass-selected small gold cluster cations and methyl iodide was investigated. Figure 5.30 shows the mass spectra of Au_1^+ before and after the reaction with CH_3I. For this experiment, the Au_1^+ clusters were let to react in the transfer quadrupole (Figure 2.1) filled with 2×10^{-2} mbar He and 2×10^{-3} mbar CH_3I and the reaction products were detected in the gas-phase reaction chamber [262]. The reaction products were $Au_1CH_3I^+$ and Au_1I^+. This means that the gold monomer reacts at room temperature within a very short time with CH_3I and breaks the C-I bond. The same behavior is expected also for gold dimers and trimers [262]. More detailed gas-phase reactivity measurements were performed in the case of CH_3Br (see Chapter 6).

Based on both surface and gas-phase experiments shown above, it might be assumed that the small Au clusters deposed on magnesia surface breaks the C-I bond of the methyl iodide molecules. This could give a reasonable explanation to the TPD experiments, where no methyl iodide molecular desorption was observed from small mass selected gold clusters (Au_{1-3}) deposited on magnesia. Also the C-I bond breakage produced by the small Au clusters could explain the absence of the CD_3^+ fragments in the SFsMS investigation of CD_3I adsorbed on Au_{1-3} clusters on MgO/Mo.

5.4 Conclusions

In this chapter the adsorption and the ultrafast photoinduced chemistry of methyl iodide adsorbed on magnesia, on a gold film, and on magnesia supported nanoparticles and small gold clusters was presented.

The adsorption behavior of methyl iodide molecules on the various substrates was investigated by means of TPD spectroscopy. On a magnesia surface methyl iodide adsorbs molecularly and desorbs without decomposition below 170 K. Also on a gold surface the major part of the methyl iodide adsorbs molecularly and desorbs without decomposition below 300 K. Only about 4% of the first layer dissociates and produces ethane. The desorption temperature from magnesia supported gold clusters depends on the gold coverage and hence on the cluster size.

By means of surface SFsMS, the direct time-resolved monitoring of the surface reaction transition state and product formation dynamics was accomplished. On the basis of the time-, mass-, and velocity-resolved product detection it was possible to elucidate the complex dynamics of a photoinduced surface reaction.

On magnesia films grown on a molybdenum single crystal, methyl iodide molecules were dissociated by direct photoexcitation leading to the formation of methyl and iodine fragments which were detected in real-time by multiphoton ionization at surface. Moreover, the ultrafast bimolecular reaction dynamics of iodine atoms generated by photodissociation of CD_3I adsorbed on the magnesia surface was measured. By changing the magnesia film thickness or composition, the electronic structure of the methyl iodide adsorbates is altered, which is also reflected in the transient measurements.

No photoreaction products were detected from methyl iodide adsorbed on an extended gold surface and on magnesia supported gold nanoparticles. This observation was attributed to an ultrafast electronic relaxation of the excited molecules on the noble metals that preceded the molecular dissociation.

On small mass-selected Au clusters, consisting of just few atoms deposited on MgO/Mo(100), a strong CH_3I-Au interaction occurs that might lead to molecular fragmentation upon adsorption.

6 Methyl bromide

In this chapter, the adsorption behavior and the photodissociation dynamics of methyl bromide molecules adsorbed at submonolayer coverage on surfaces consisting of magnesia, gold and magnesia supported gold clusters is presented. Similar to methyl iodide (cf. Chapter 5), the methyl bromide adsorption behavior on the different substrates was studied by means of temperature programmed desorption. The real-time photodissociation dynamics of methyl bromide molecules on the surface was investigated by monitoring the emerging transient methyl cation signal. Power dependence measurements were employed to provide insights into the mechanisms of initial photoexcitation of the adsorbed molecules and the detection of the methyl fragment. Significant differences were observed in the methyl bromide photodissociation dynamics on magnesia, gold films, and magnesia supported gold nanoparticles.

6.1 Methyl bromide on magnesia

6.1.1 Temperature programmed desorption

TPD investigations were performed to characterize the adsorption behavior of methyl bromide on the magnesia surface. Figure 6.1 displays a series of TPD spectra recorded after dosing different amounts of CH_3Br on an 8 ML MgO/Mo(100) surface at 90 K. No evidence for methyl bromide dissociation subsequent to adsorption on the MgO/Mo(100) substrate was found. No reaction products such as ethane or molecular bromide, which could be formed due to methyl bromide dissociation on surface, were observed. Hence, methyl bromide adsorbs molecularly on the MgO/Mo(100) surface and desorbs without decomposition.

Similar to CH_3I adsorbed on magnesia, the maximum of the desorption signal in Figure 6.1 shifts to lower temperatures with increasing coverage. The same behavior has been observed previously for CH_3Br adsorbed on bulk MgO(100) [241, 263] and on LiF(100) [52] and it has been interpreted in terms of a repulsive adsorbate-adsorbate interaction between the adsorbate molecules which tend to wet the surface uniformly rather than form 3D islands.

The inset in Figure 6.1 shows the desorption energy of CH_3Br molecules from the MgO surface as a function of the coverage, calculated by means of the simple Redhead approximation (see Section 2.2.3) assuming a frequency factor of 10^{-12} Hz. The desorption energy change smoothly from 0.36 eV for 0.075 ML (0.3 L) to 0.32 eV for 0.375 ML (1.5 L)

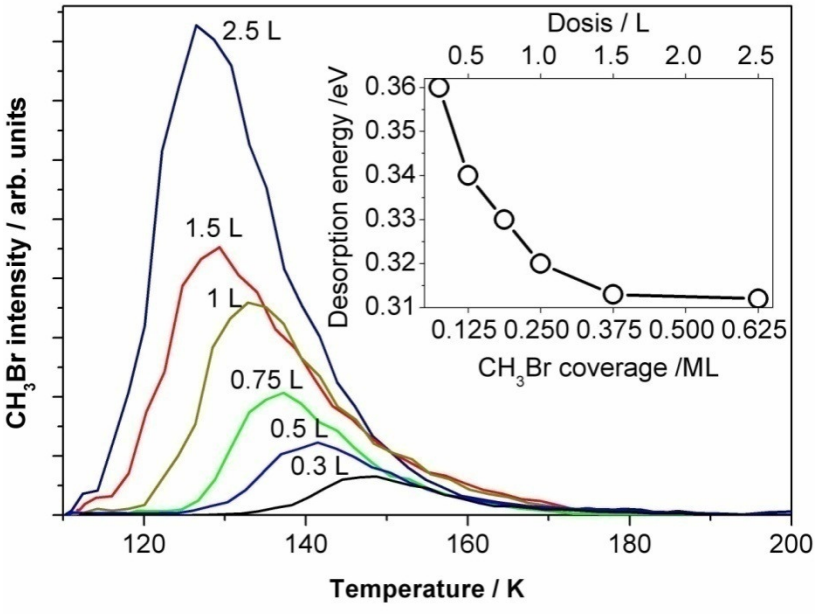

Figure 6.1 TPD spectra of the CH_3Br molecular desorption from submonolayer coverages on MgO(100) ultra-thin films grown on Mo(100). The spectra were obtained with a heating rate of 2 K/s. The numbers indicated at the spectra represent the CH_3Br exposure in units of Langmuir. In this adsorption system 1 L corresponds to a coverage of 0.25 ML [241, 263]. Inset: Desorption energy of CH_3Br molecules from the MgO surface as a function of the coverage, calculated by means of the simple Redhead approximation.

and stay almost constant (within 0.01 eV) for larger coverages up to 0.625 ML (2.5 L) indicating a normal (non repulsive) first order desorption behavior.

6.1.2 Real-time photodissociation dynamics

In contrast to methyl iodide, which was extensively studied in the past, few reports are available on the methyl bromide photodissociation. Previous investigations [42, 43] assumed that the potentials of methyl bromide and methyl iodide molecules are similar, but due to the shorter C-Br bond length (1.939 Å) of methyl bromide with respect to the C-I bond length (2.1396 Å) of methyl iodide, the A-band maximum of CH_3Br shifts to higher energy. The A-band, i.e., the first absorption continuum, of CH_3Br can be accessed in the 170-270 nm spectral range with an absorption maximum around 200 nm [97, 264-266].

In the gas-phase, the photodissociation of the methyl bromide molecule was investigated by means of time-of-flight mass spectrometry and photofragment imaging employing excitation wavelengths of 193 nm and 222 nm [42], 205 nm [43], 215.9 nm [44], 213 – 235 nm [45], 218 – 245 nm [46], 240 nm, and 280 nm [47].

Similar to methyl iodide, the excitation of methyl bromide to the of A-band leads to two dissociative channels: (i) the `Br-channel` giving rise to methyl and a bromine atom in the ground state, i.e. $CH_3 + Br(^2P_{3/2})$ and (ii) the `Br*-channel` giving rise to methyl and a bromine atom in the spin-orbit excited state, i.e. $CH_3 + Br(^2P_{1/2})$. Five dissociative states are correlated with these two channels. Using the Mulliken`s notation [213, 267, 268], these states are labeled in ascending energy order $^3Q_2$, $^3Q_1$, $^3Q_{0+}$, $^3Q_{0-}$, and $^1Q_1$. The $^3Q_1$ and $^1Q_1$ states can be accessed from the ground state via single photon excitation in a perpendicular electric dipole transition and they adiabatically correlate with the Br-channel. The $^3Q_{0+}$ state can be accessed in a parallel transition by single photon excitation and it is correlated with the Br*-channel. The single photon excitation of the $^3Q_2$ and $^3Q_{0-}$ states is electric dipole forbidden. Also similar to methyl iodide [38, 269-271], a curve crossing occurs in the case of methyl bromide between the $^1Q_1$ and $^3Q_{0+}$ states [40, 272]. This crossing is possible because these states have different symmetries. However, in contrast to the methyl iodide molecule, where the A-band absorption occurs mainly via a parallel transition to the $^3Q_{0+}$ state which correlates with I*, in the case of methyl bromide, magnetic-circular-dichroism investigations show that the $^1Q_1$ state is more strongly populated than the $^3Q_1$ and $^3Q_{0+}$ [273] states.

The adsorption and photodissociation of methyl bromide molecules were studied on several insulating substrates including MgO(100) [241], NaCl(100) [52], and LiF(100) [52, 274], on semiconducting GaAs(110) [212, 261, 275], on metallic substrates like Pt(111) [253, 255-257], Ag(111) [245, 259], Ni(100) [276], and polycrystalline W [277]. Neither in the gas-phase nor on the surface, was the photodissociation of methyl bromide molecules investigated with time-resolved methods previously.

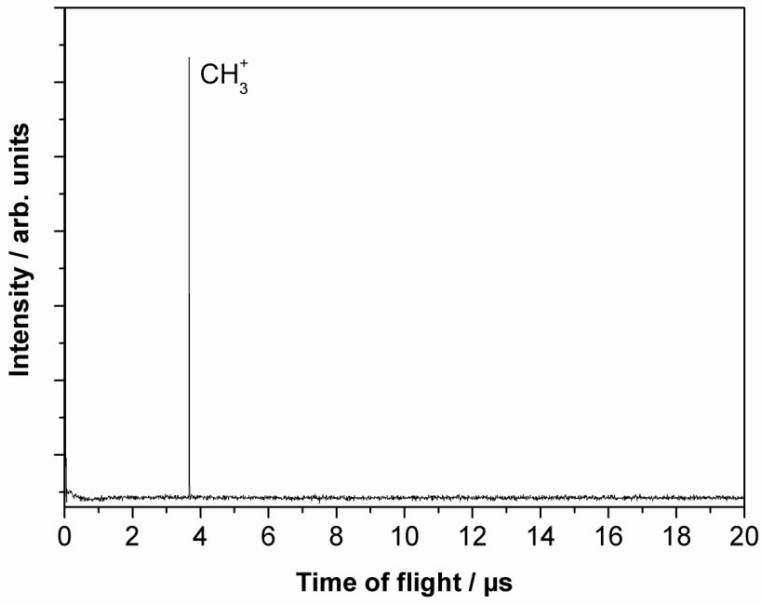

Figure 6.2 Time-of-flight mass spectrum obtained from methyl bromide adsorbed at submonolayer coverage on 8 ML MgO/Mo(100) by excitation with 266 nm and probed with 333.4 nm at 2 ps pump-probe delay time.

Figure 6.2 shows a time-of-flight mass spectrum obtained at 2 ps pump-probe delay time from methyl bromide adsorbed at submonolayer coverage on MgO/Mo(100). The pump laser wavelength and power were 266 nm and 6 mW/cm², respectively. The probe laser (600 mW/cm²) was tuned to the center wavelength of 333.4 nm to sensitively detect the methyl fragments through (2+1)-REMPI via the $3p^2A_2'$ Rydberg state [102]. The only reaction product observed in the mass spectrum was the methyl fragment. No other reaction products were observed independent on laser intensity or pump-probe delay time.

In order to monitor in real-time the photodissociation dynamics of methyl bromide molecules adsorbed at submonolayer coverage on the magnesia surface, the methyl cation signal intensity was recorded as a function of the pump-probe delay time. Figure 6.3 shows the CH_3^+ transient signal obtained from 0.25 ML CH_3Br adsorbed on 8 ML MgO on Mo(100). No transient signal was observed up to 150 fs. Subsequently, the CH_3^+ signal presented an exponential rise with a maximum reached after about 1.2 ps. Fitting the experimental data by a ´delayed exponential rise´-model, a time constant $\tau = 320 \pm 60$ fs was obtained for the rise of the methyl signal.

Before the discussion of the dynamic processes that are correlated with the CH_3Br photodissociation on MgO, the initial excitation mechanism has to be clarified. This is more complicated in the case of methyl bromide than for methyl iodide since the absorption cross-section of CH_3Br at 266 nm ($\sigma = 0.0551$ cm^2) is considerably lower than at the A-band center around 200 nm ($\sigma = 79$ cm^2) [266]. For this purpose, power dependence measurements were performed on the pump laser beam. Figure 6.4 shows the CH_3^+ yield at 2 ps time delay as

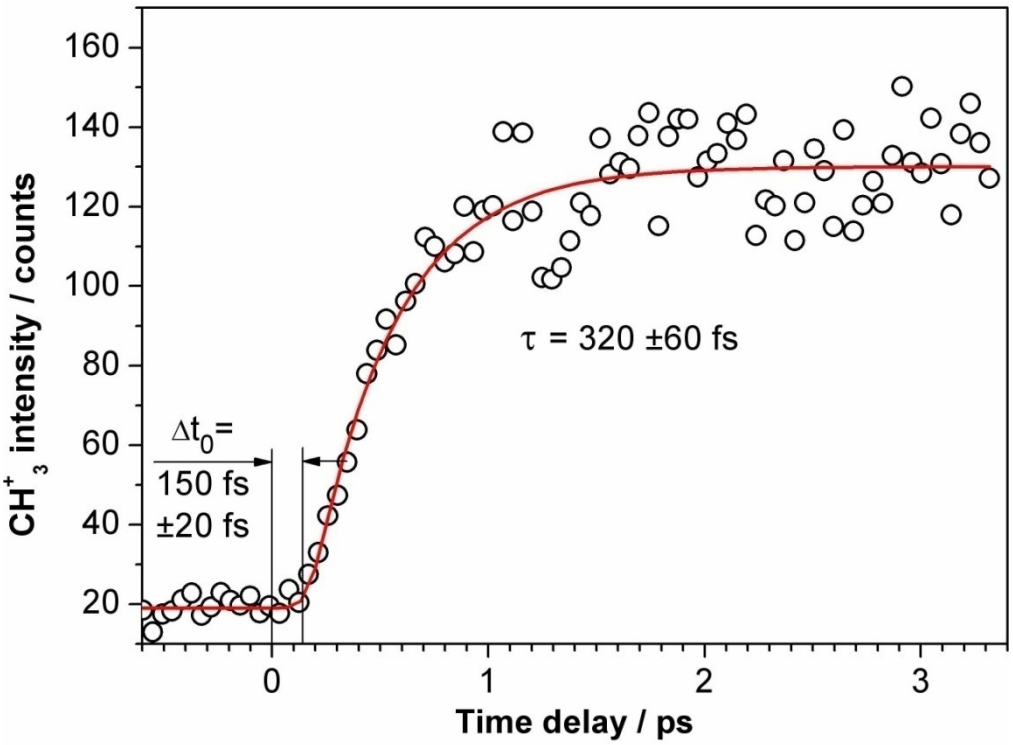

Figure 6.3 Transient obtained by monitoring the methyl cation signal as a function of the pump-probe delay time. Each data point of one single transient represents the sum over the ion count yield from 2500 pump and probe laser exposures to a 0.25 ML methyl bromide preparation. Five single transients were averaged to improve the signal-to-noise ratio. The transient signal was obtained with 6 mW/cm² pump and 600 mW/cm² probe laser power. The solid line is the best fit of the ´delayed exponential rise´-model to the experimental data. The initial coherent delay Δt_0 and the time constant τ of the 'delayed exponential rise'-component are indicated in the graph.

a function of the pump laser power. It shows that the photodissociation process requires more then a single photon. The slope value of 1.8 ±0.2 of a linear fit to the measured power dependence data in a double logarithmic plot indicates that the photodissociation is most likely initiated by two pump photons (cf. Figure 6.3b).

The prospective dissociative pathways due to an excitation with two photons at a central wavelength of 266 nm will be discussed on the basis of the available potential energy curves of the CH_3Br molecule. Figure 6.5a displays the diabatic potential energy curves corresponding to the $^1A_1$ ground state and to the A-band of a free methyl bromide molecule. In addition, in Figure 6.5b the 5s – 5p Rydberg states are shown with consideration of spin - orbit interactions. Note that the C-Br distance in Figure 6.5 is given in atomic units[7]. When spin-orbit interaction is included (see Figure 6.5b), the ^3E state becomes[8]: $^3Q_2$ ($\Omega = 2$),

[7] 1 au = 5.291 772 108(18)×10^{-11} m

[8] In Mullikan's notation ^XE becomes $^XQ_\Omega$, where Ω = 0, 1, 2 is the projection of the total angular momentum (orbital + spin)

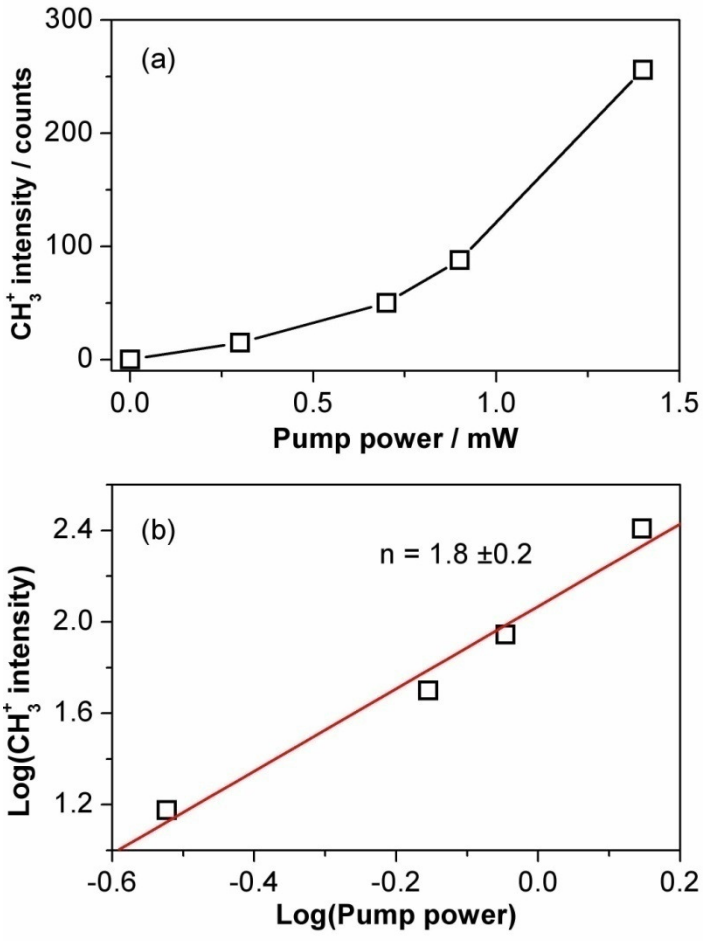

Figure 6.4 Methyl cation signal intensity as a function of the pump laser power at 2 ps pump-probe delay time: (a) as measured; (b) double logarithmic representation.

$^3Q_1(\Omega = 1)$, $^3Q_{0-}$ ($\Omega = 0$; A_2 - symmetry), $^3Q_{0+}$ ($\Omega = 0$; A_1 - symmetry) and the ^1E state becomes $^1Q_1$ ($\Omega = 1$). The $^3A_1$ state give rise to two states corresponding to $\Omega = 0$ and $\Omega = 1$.

The most probable two-photon excitation channel of the CH_3Br molecule which leads to dissociation is indicated in Figure 6.5a by the vertical arrows. According to Ref. [40], the $^3A_1$ dissociative state can be accessed near the C-Br equilibrium distance by two-photon excitation at 266 nm. This excitation would initiate a dissociation process comparable to the one that has been observed for methyl iodide on magnesia thin films (cf. Chapter 5). In addition, at 9.3 eV (2×266 nm) above the ground state, the 5p Rydberg states are located (cf. Figure 6.5b). The dissociation directly from these Rydberg states is excluded because these states do not have a repulsive character. However, theoretical investigations indicate [41] that a crossing between a particular state of the 5p Rydberg series and a repulsive valence-character state (corresponding to $^3A_1$) is avoided and thus a potential barrier is generated through which tunneling and consequently transition from a Rydberg to a valence state can occur. This pho-

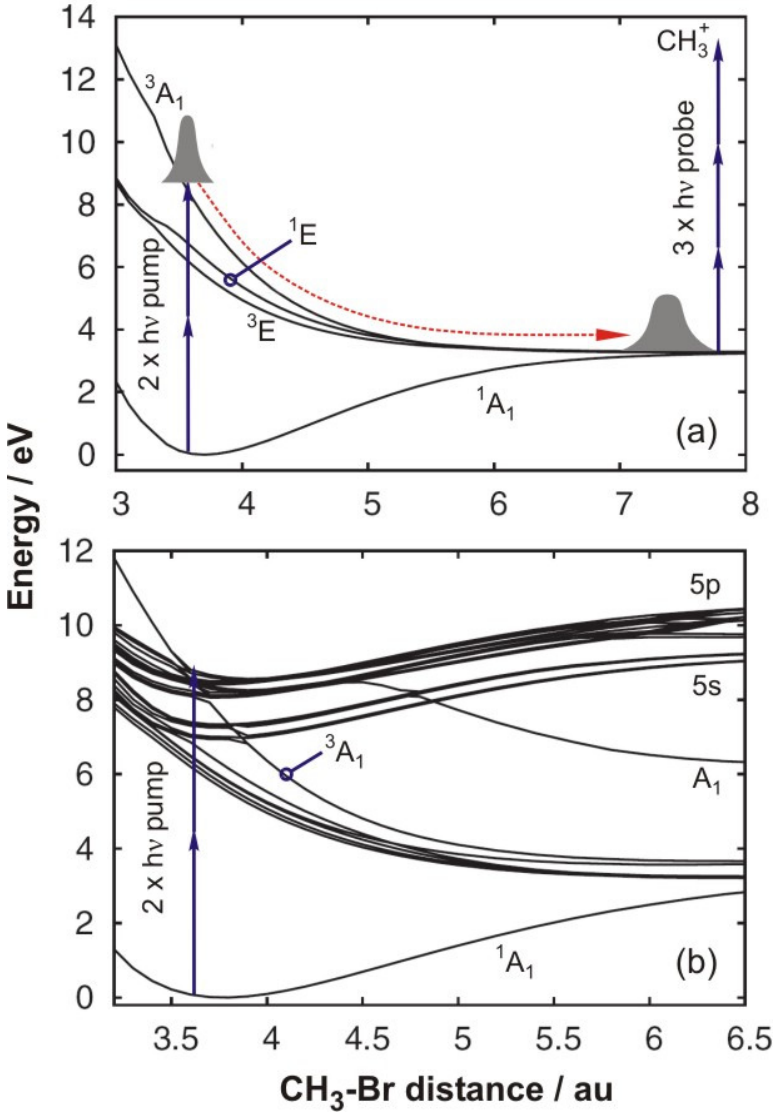

Figure 6.5 Potential energy curves of the free CH_3Br molecule. (a) Ground state ($^1A_1$) and A-band (^3E, ^1E, $^3A_1$) (adapted from [40]); (b) Ground state ($^1A_1$), A-band and the 5s – 5p Rydberg states with consideration of spin–orbit interaction (adapted from [41]). The dashed arrows illustrate the propagation of the wave packet. The vertical arrows represent the excitation and the detection laser pulses.

todissociation channel is also excluded because of the predicted long lifetime of the Rydberg states of about 10 ps [41] which would be reflected in the appearance time of the CH_3^+ reaction products. Our data presented in Figure 6.3 show, however, a methyl appearance time of only about 320 fs. Consequently, we conclude that the excitation of CH_3Br molecules at 266 nm by means of a two-photon transition most likely leads to A-band dissociation via the $^3A_1$ state, always under the assumption that the gas-phase potentials of CH_3Br are only weakly perturbed on the MgO surface.

The emerging methyl radicals are subsequently detected via (2+1) REMPI at wavelength of 333.4 nm according to the schema:

$$CH_3Br_{ads} \xrightarrow{2\times 266\ nm} CH_3B^*_{ads} \rightarrow CH_3 + Br \xrightarrow{(2+1)\times 333.4\ nm} CH_3^+ + Br \qquad (6.1)$$

The time constant of $\tau = 320 \pm 60$ fs, obtained from the fitting of the experimental data by a ´delayed exponential rise´-model (cf. Figure 6.3) is considerably shorter compared to the one obtained for the exponential rise of the CH_3^+ signal in the case of CH_3I photodissociation on MgO (680 ±50 fs, see Section 5.1). Similar to CH_3I/MgO, the initial coherent delay of $\Delta t_0 =$ 150 ±50 fs (cf. Figure 6.3) of the methyl ion signal is proposed to reflect the liberation of the methyl fragments from the molecular force field and from the force field of the magnesia surface. The subsequent growth of the methyl signal with a time constant of $\tau = 320 \pm 60$ fs is consequently interpreted as the average life time of all trajectories leading form the initial excitation to the release of the methyl fragment.

As previously mentioned, no direct measurement of the CH_3Br photodissociation time, has been performed until now. However, based on the method provided by Sander and Wilson [278] to calculate the lifetime of a dissociative state using the anisotropy parameter β which is deduced from the angular distribution of the photofragments, Gougousi et al. [46], estimated that the lifetime of the CH_3Br A-band is 120 ±40 fs. If this method is applied to CH_3I, an upper limit for the lifetime of the A-band of 70 fs can be estimated [279]. This means that in the gas-phase the methyl bromide A-band photodissociation takes longer than the methyl iodide A-band photodissociation. However, in the present investigation the methyl bromide appears to photodissociate faster than methyl iodide, if adsorbed on MgO.

By means of angular resolved time-of-flight mass spectrometry, Polanyi and coworkers have investigated the 193 nm photodissociation of CH_3Br adsorbed on a bulk MgO(100) surface [241]. Depending on the coverage, this experiment indicates that the emerging methyl photofragments can be either directly liberated into the gas-phase or they can lose a significant part of their total kinetic energy released from the A-band photodissociation in a collision process with neighboring molecules. This later mechanism exclusively occurs at submonolayer coverage, where all escaping methyl fragments have to experience a collision with adjacent molecules because of an adsorption geometry in which the C-Br axis is nearly parallel to the surface. These results by Polanyi and coworkers [241] provide the basis for a reasonable explanation why the methyl photofragment appearance time on MgO, measured in our experiment, is much faster for methyl bromide (320 ±60 fs) compared to methyl iodide (680 ±50 fs) despite of the theoretical prediction of a longer dissociation time for free CH_3Br. The different appearance time can be connected to the different adsorption geometries of the methyl halide molecules on the magnesia surface. As discussed in Chapter 5, methyl iodide molecules are proposed to be adsorbed with the methyl-end heading toward the surface. This leads to a trapping of the methyl group between the MgO surface and the I atom subsequent to the photodissociation. Due to the resulting “chattering” motion, the liberation of the methyl fragment from the surface takes a considerable time in the case of methyl iodide. In contrast, according to Polanyi and coworkers [241], the methyl bromide molecules are adsorbed with their C-Br axis

almost parallel to the MgO substrate. Therefore, the methyl photofragment can escape much easier and faster, suffering in most case only one collision with the adjacent molecule, which would explain the faster appearance time of 320 ±60 fs for CH_3Br.

6.1.3 Influence of the magnesia film thickness on the methyl bromide photodissociation dynamics

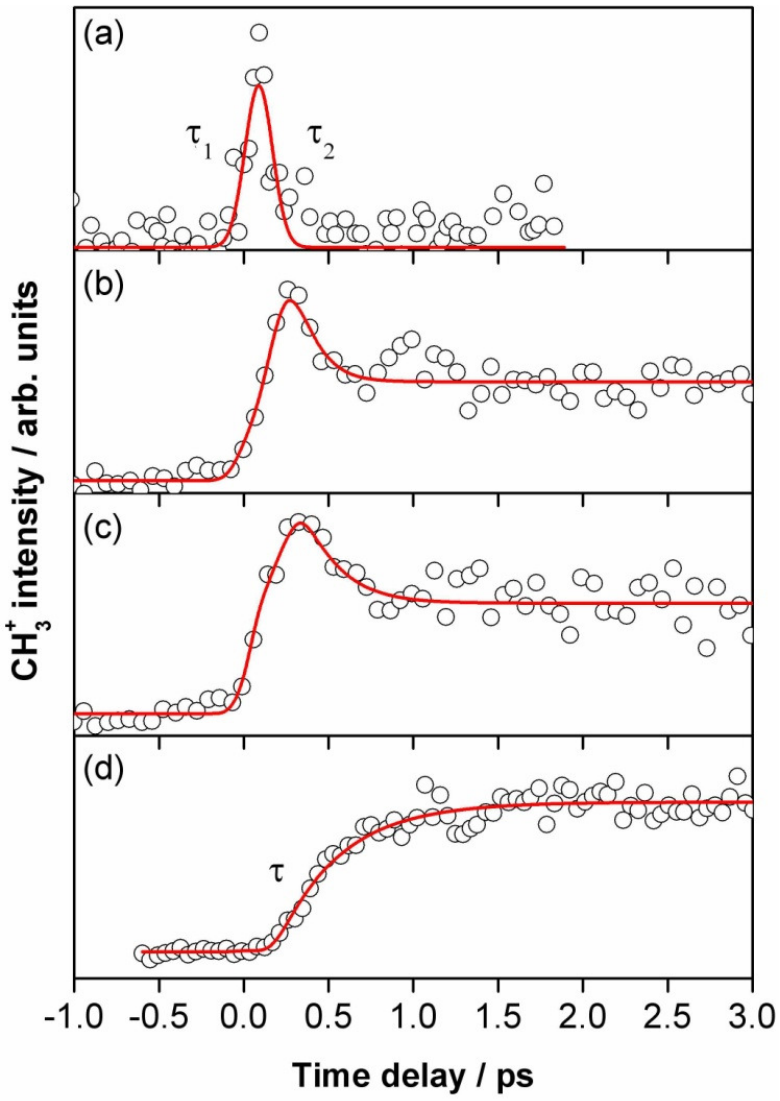

Figure 6.6 Time-resolved photodissociation dynamics of 0.25 ML CH_3Br adsorbed on Mo(100) and on MgO films of different thickness grown on Mo(100): (a) bare Mo(100); (b) 1.5 ML MgO; (c) 3 ML MgO; (d) 10 ML MgO. Five single transients were averaged in each case to improve the signal-to-noise ratio. The transient signals were obtained with 1 mW/cm² pump and 200 mW/cm² probe laser power in the case of (a) and with 6 mW/cm² pump and 600 mW/cm² probe laser power in the case of (b-d). The solid line is the best fit of an appropriate model to the experimental data (see text for more details). The rise and decay time constants of the peak structure are labeled τ_1 and τ_2. The rise time constant of the methyl cation signal on 10 ML MgO film on Mo(100) is labeled τ.

Small, but apparent changes were observed in the photodissociation dynamics of methyl iodide molecules adsorbed on MgO films of various thickness on Mo(100) (cf. Section 5.1.3). These changes might indicate a different interaction of the adsorbed molecules by changing the thickness of MgO film. A similar experiment was performed in the case of CH_3Br adsorbed on MgO films on Mo(100), in order to study how the magnesia thickness influences the photodissociation dynamics of the CH_3Br molecules and consequently to obtain new insights into the interaction between the substrate and the adsorbed CH_3Br molecules. Figure 6.6 displays transients obtained by monitoring the methyl cation signal as a function of the pump-probe delay time from surface samples consisting of submonolayer methyl bromide (0.25 ML) adsorbed on bare Mo(100) and on 1.5 ML, 3 ML, and 10 ML MgO films on Mo(100).

The methyl cation transient signal recorded from the CH_3Br photodissociation on the bare Mo(100) substrate exhibits a peak structure with a maximum at about 90 fs (cf. Figure 6.6a). Fitting the experimental data by an `exponential rise and decay` model gives similar time constants of $\tau_1 = \tau_2 = 75 \pm 10$ fs for the rise and the decay component of the observed peak, respectively. No transient signal is observed for a pump-probe time delay longer than 300 fs.

On the Mo(100) covered with a magnesia films with a thickness of 1.5 ML, the CH_3Br photodissociation leads to a CH_3^+ transient signal, which displays a rise starting at zero time delay, followed by a decay (peak structure). Subsequently the signal does not reach the initial value measured at negative delay times. An apparent offset is observed which stays constant at longer positive delay times (see Figure 6.6b). Fitting of an `exponential rise and decay` model with offset at long delay times to the experimental data give a time constant $\tau_1 = 100 \pm 10$ fs for the rise and $\tau_2 = 110 \pm 10$ fs for the decay of the peak structure, respectively. The maximum of the peak structure is located at 265 fs.

The CH_3^+ transient signal recorded from the CH_3Br photodissociation on a 3 ML MgO film on Mo(100) (see Figure 6.6c) displays a similar shape as the CH_3^+ transient recorded from 1.5 ML MgO film on Mo(100) (Figure 6.6b), but with different time constants. In this case (Figure 6.6c) the peak structure exhibits a maximum at 320 fs and its rise and decay time constants are $\tau_1 = 120 \pm 10$ fs and $\tau_2 = 170 \pm 15$ fs, respectively.

In Figure 6.6d the CH_3^+ transient signal obtained from CH_3Br adsorbed at submonolayer coverage (0.25 ML) on a 10 ML MgO film is shown as a reference. The interpretation of this transient signal was discussed the previous section.

For the interpretation of the transient signals measured on thinner MgO films and on Mo(100) (Figure 6.6a-c) a perturbation of the electronic structure of the adsorbed CH_3Br molecules by the molybdenum substrate is proposed. Such a perturbation of the electronic structure of the adsorbed molecules on metal surfaces is well characterized in the literature [72, 280]. In particular, the perturbation of the electronic structure of methyl halides after adsorption on different metal single crystals was evidenced through a red-shift of their absorption spectra (see Refs. [103, 260] and references therein).

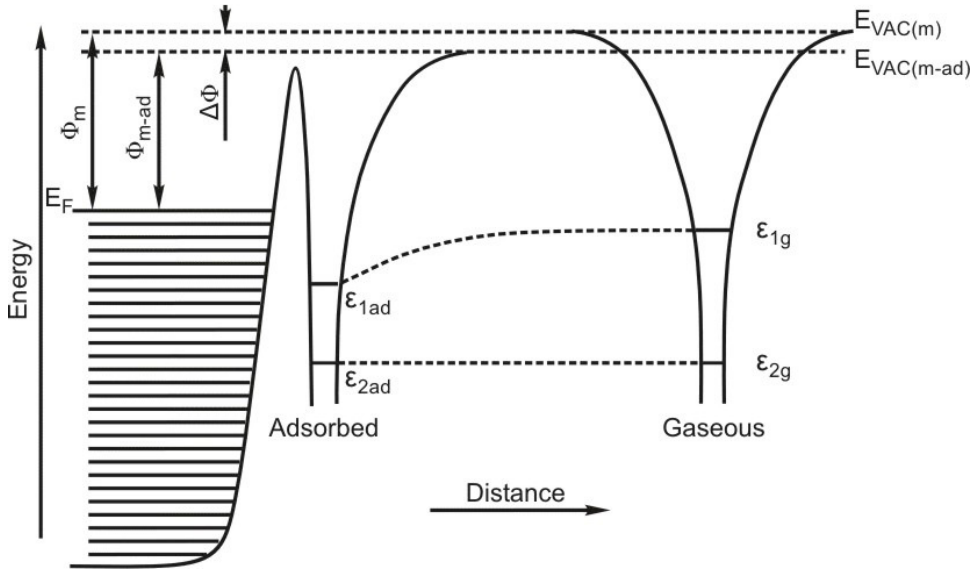

Figure 6.7 Schematic energy diagram of the orbitals of a hypothetical molecule as a function of distance between the molecule and a metallic surface. ε_{1g} *,* ε_{2g} *and* ε_{1ad} *,* ε_{2ad} *are the orbital (1 and 2) energies of the free and of the adsorbed molecule, respectively. The vacum energies and the work functions of the bare metal surface and the metal-adsorbate complex are labeled by* $E_{VAC(m)}$*,* $E_{VAC(m-ad)}$ *and* Φ_m*,* Φ_{m-ad}*, respectively. (Adapted from Ref. [72])*

Figure 6.7 displays a schematic energy diagram of the orbitals of a hypothetical molecule as a function of the distance between the molecule itself and the metallic surface. Upon adsorption, the interaction of the orbital 1 with the metal electrons may induce a decrease of the orbital energy from ε_{1g} to ε_{1ad} (bonding shift). Varying the distance between the molecule and the metal substrate by an insulating spacer (in our case by the MgO film), the orbital energy can be tuned between its energy when the molecule is free and when it is adsorbed directly on the metal surface. The orbital 2 may not be involved in the bond formation and consequently no energy shift of this orbital ($\varepsilon_{2g} = \varepsilon_{2ad}$) is expected to occur after adsorption on the surface. As a consequence of the interaction of the molecule with the metal surface, the work function of the surface is changed by $\Delta\Phi$[9].

As mentioned in Chapter 2, two possible pathways are assumed for the dissociation of a molecule adsorbed on a surface, i.e. (i) direct photodissociation, when the light excites strictly the adsorbed molecule and (ii) substrate excitation, when the light is absorbed by the substrate and the resulting hot carriers induce the dissociation. In Figure 6.8 possible photo-excitation channels for methyl bromide adsorbed on an insulating and on a metallic surface are illustrated in conjunction with the detection mechanisms of the emerging methyl radicals. Directly on the molybdenum substrate the electronic structure of the CH_3Br molecule is as-

[9] The variation of the work function of different metal substrates upon adsorption of methyl halide molecules was discussed in Section 5.2.2

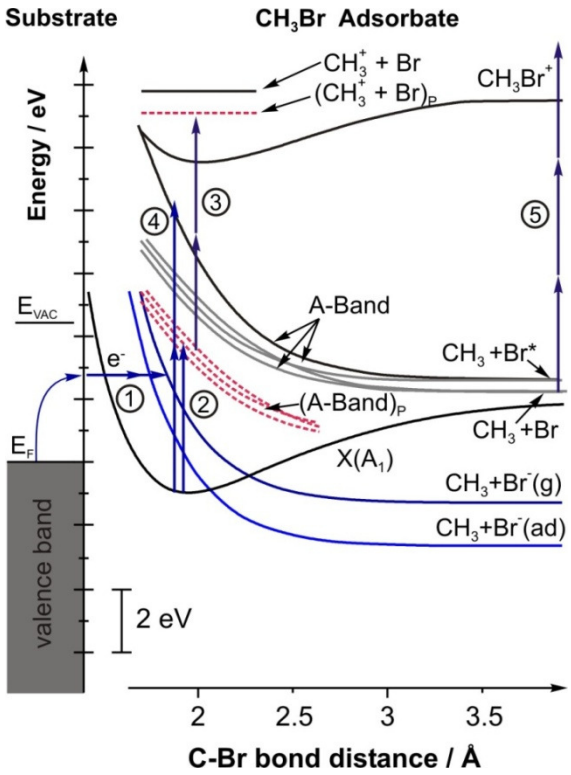

Figure 6.8 Potential energy diagram for CH_3Br adsorbed on a solid surface. The potentials and relative energies were adapted from references [40, 41, 44, 256, 257, 275]. The numbers of the excitation mechanisms refer to the discussion in the text. The electronic levels proposed to be involved in the excitation and detection mechanism on metal surface are highlighted by the dashed red lines.

sumed to be strongly perturbed, such that the A-band might be accessible by a single pump photon. In the case of CH_3Br molecules adsorbed on Mo(100), using the typical pump and probe laser intensities as for CH_3Br adsorbed on MgO/Mo(100), an intense CH_3^+ signal can be detected, but no temporal evolution of this signal is observed. Therefore, in order to be able to record the CH_3^+ transient signal from CH_3Br adsorbed on Mo(100) shown in Figure 6.6a, the intensities of the pump and probe laser beams had to be reduced. This indicates that the number of photons involved in the dissociation of the CH_3Br molecules adsorbed on Mo(100) and in the detection of CH_3^+ (Figure 6.6a) is lower than the number of photons employed to dissociate CH_3Br (2×hν 266 nm) and to detect the emerging CH_3^+ (3×hν 333.4 nm) on MgO (Figure 6.6d and Figure 6.3).

The possibility of substrate excitation via a DEA process (process 1 in Figure 6.8) is very likely for CH_3Br on Mo(100). However, DEA cannot be responsible for the measured dynamics shown in Figure 6.6a. In a DEA process, a substrate electron attaches to an adsorbed molecule, which consequently is transformed into an anion. However, anion states of methyl halide molecules are not stable [281] and the CH_3Br anion will rapidly dissociate along the repulsive potential curve (process 1 in Figure 6.8). The detection of the emerging

methyl radicals subsequent to DEA would involve three photons for the ionization to CH_3^+. Moreover, after dissociation, the liberated methyl radicals should be detected also at later (ps) delay times (as has been observed on magnesia).

Also the direct transition of CH_3Br from the anionic state to a dissociative cationic state can be ruled out because this process would involve at least three probe photons as well (see Figure 6.8). Therefore, the CH_3^+ transient peak structure observed in Figure 6.6a is assumed to have the same origin as the CD_3^+ transient peak obtained in the case of the CD_3I photodissociation on Mo(100) (see Section 5.1.3) and that the excitation and CD_3^+ detection proceeds according to:

$$CH_3Br_{ads} \xrightarrow[266\ nm]{1\times h\nu} CH_3Br^*_{ads} \xrightarrow[333.4\ nm]{2\times h\nu} CH_3Br^{+*} \rightarrow CH^+_{3\ g} + Br_{ads} \qquad (6.2)$$

One photon with a central wavelength of 266 nm excites the adsorbed CH_3Br molecules, probably to the A-band which is accessible in the case of CH_3Br on Mo(100). Subsequently, two photons with 333.4 nm wavelength are necessary to ionize the excited molecule which decomposes yielding CH_3^+ (processes 2 and 3 in Figure 6.8).

If the mechanism in Equation (6.2) is assumed to be responsible for the observed CD_3^+ transient signal in Figure 6.6a and if a single pump photon leads to A-band excitation of CH_3Br on the metal surface, than a rough calculation yields that the A-band must be lowered by about 1.5 ±0.1 eV for CH_3Br on Mo(100) with respect to the free molecule. This result is in agreement with the investigations of White and coworkers [259], in which a red shift of 1.5 eV was observed for the A-band of CH_3Br molecules adsorbed at monolayer coverage on Ag(111).

On magnesia films with a thickness of 1.5 and 3 ML, the peak structure in the CH_3^+ transient signal is assumed to have the same origin as the CH_3^+ peak structure observed from CH_3Br adsorbed directly on the Mo(100) substrate. In contrast, the CH_3^+ transient signal obtained at later pump-probe time delay (cf. Figure 6.6 from 0.5 to 5 ps) which is observed only on magnesia surfaces is suggested to be due to the two-photon dissociation of the methyl bromide molecules (process 4 in Figure 6.8) followed by (2+1) REMPI detection of the methyl fragments (process 5 in Figure 6.8).

6.2 Methyl bromide adsorption and photodissociation on gold

6.2.1 Temperature programmed desorption

The adsorption behavior of methyl bromide on a gold surface was investigated by means of TPD spectroscopy. The gold substrate was prepared as described in Section 4.2. During the CH_3Br deposition, the Au/Mo(100) surface was held at 90 K. A series of TPD spectra obtained from different CH_3Br coverages on a gold surface are displayed in Figure 6.9. For a coverage of 0.15 ML the CH_3Br desorption begins around 150 K and extends to 310 K with an intensity maximum at about 275 K. For a coverage of 0.6 ML CH_3Br, a decrease of the maximum desorption temperature to about 235 K is observed. Additionally, a new desorption feature appears below 200 K. When 1.2 ML CH_3Br is dosed on to the Au film, a distinct desorption peak at 120 K is observed apart from the desorption peak observed at lower coverages, now with the maximum shifted to 205 K.

No investigations of the adsorption of methyl bromide molecules on a gold surface have been reported so far in the literature. The interpretation of the features displayed in Figure 6.9 is therefore based on TPD experiments with methyl halide molecules adsorbed on different substrates, which have been reported in the literature (see Section 5.2.1 and Section 6.2.1). The desorption peak above 170 K is assigned to the molecular desorption of CH_3Br molecules from the gold surface. Its shift to lower temperature with increasing adsor-

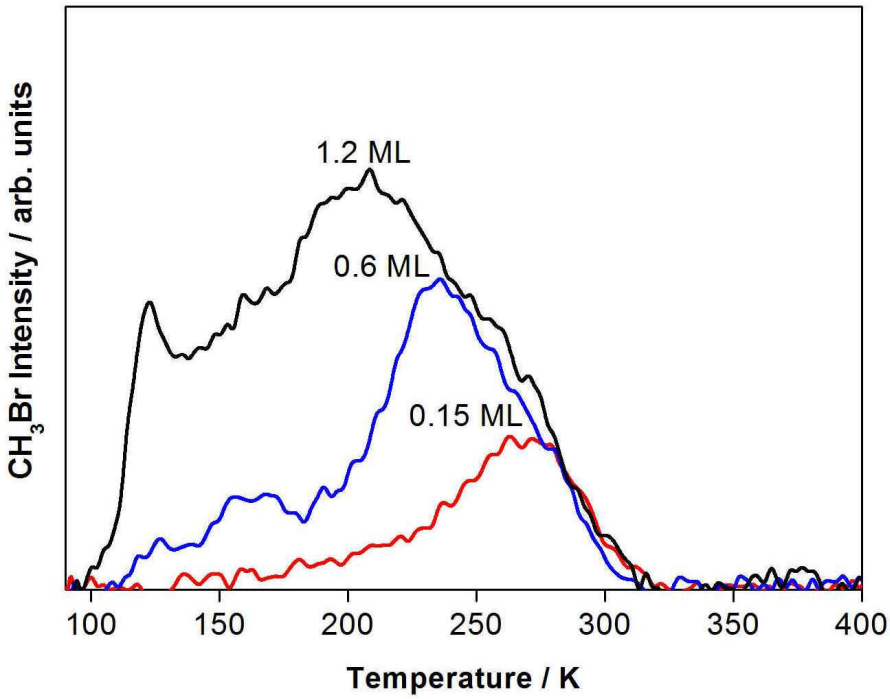

Figure 6.9 TPD spectra of CH_3Br adsorbed on a 10 ML Au film on Mo(100). The spectra were obtained with a heating rate of 2 K/s. The numbers indicated at the spectra represent the CH_3Br coverage in monolayer equivalent.

bate coverage is attributed to a repulsive desorption which is caused by the interaction between the static dipole moments of the adsorbed molecules. A similar desorption characteristic was observed for submonolayer coverages of CH_3Br on Ru(001) [282]. The distinct peak at 122 K is assigned to the onset of the CH_3Br multilayer desorption [282]. In contrast to methyl iodide adsorbed on a gold surface, no thermal induced reaction products of CH_3Br such as methane or ethane were detected. As well, no evidences for methyl bromide dissociation subsequent to adsorption on the Au substrate were found.

6.2.2 Photodissociation dynamics

In contrast to submonolayer methyl iodide molecules adsorbed on a gold surface, which do not photodissociate (cf. Section 5.2), submonolayer methyl bromide adsorbed on the same substrate can be easily photodissociated.

Figure 6.10 displays a mass spectrum recorded from submonolayer (0.25 ML) CH_3Br adsorbed on 10 ML Au/Mo(100). The spectrum was recorded at 90 K. The pump and probe wavelengths were 266 nm and 333.4 nm, respectively. The pump-probe delay time was fixed to 140 fs. As can be seen from Figure 6.10, the only observed photoreaction product was CH_3^+. Mass spectra taken under different experimental conditions, i.e. different pump-probe delay times, laser intensities, coverages, and temperatures, do not lead to the detection of other reaction products.

The real-time photodissociation dynamics of CH_3Br adsorbed at submonolayer coverage on an Au film on Mo(100) is shown in Figure 6.11. Similar to the real-time photodissociation of submonolayer CD_3I and CH_3Br molecules on the Mo(100) substrate, the CH_3^+ tran-

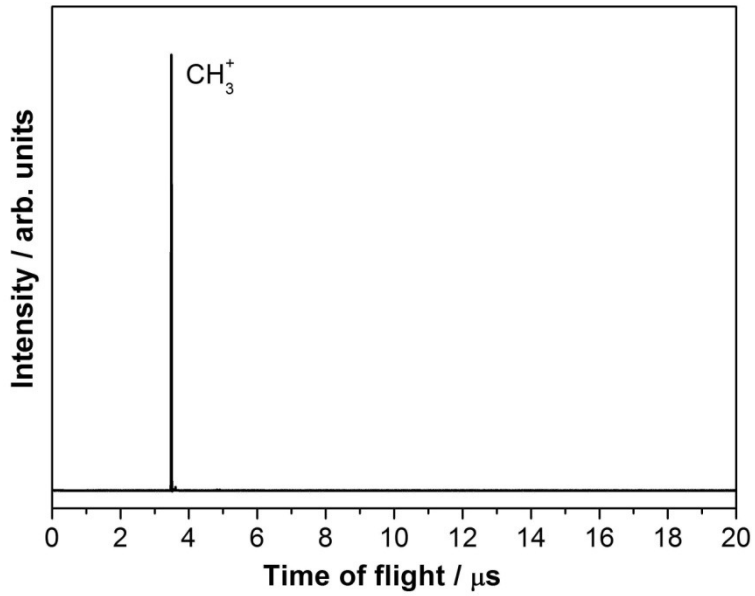

Figure 6.10 Time-of-flight mass spectrum obtained from 0.25 ML methyl bromide adsorbed on a 10 ML Au film on Mo(100) at 140 fs pump-probe delay time (266 nm pump and 333.4 nm probe).

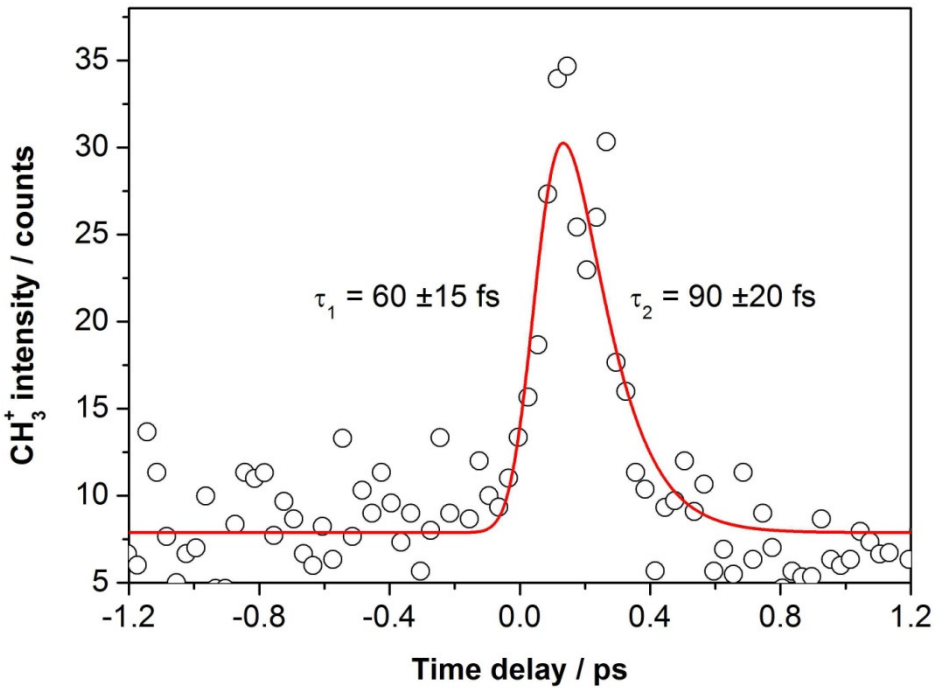

Figure 6.11 Femtosecond photodissociation dynamics of CH_3Br molecules adsorbed on Au(100)/Mo(100) recorded by monitoring the CH_3^+ signal as a function of the pump-probe time delay. The surface temperature was 150 K. The solid line is the best fit of an exponential 'rise and decay'-model to the experimental data yielding the indicated time constants τ_1 and τ_2. For the transient shown four single transients were averaged to improve the signal-to-noise ratio. The transient was obtained with 2 mW/cm² pump (266 nm) and 200 mW/cm² probe (333.4 nm) laser power.

sient signal in Figure 6.11 exhibits a peak structure starting at 0 fs. No CH_3^+ transient signal was detected for reaction times longer than 600 fs. The measured data were fitted by an 'exponential rise and decay' model (convoluted with the laser cross correlation). The determined rise and decay time constants were τ_1 = 60 ±15 fs and τ_2 = 90 ±20 fs, respectively. The maximum of the peak structure is located at 140 ±20 fs. The error of ±20 fs in determining the maximum intensity was determined from several transients recorded under similar conditions, i.e. similar substrate preparation, molecular coverage, and laser parameters. The other errors in determining the time constants were acquired directly from the fitting procedure.

Laser power dependence measurements indicate that the mechanism of the CH_3Br photodissociation on the Au film is similar to the cases of CH_3I and CH_3Br photodissociation on Mo(100) (cf. Schema (6.2)). The pump and probe power dependences of the CH_3^+ signal intensity at 140 fs pump-probe delay time are depicted in Figures 6.12a and 6.12b in a double logarithmic representation. The slope of the double logarithmic representation is an indication for the number of photons involved in the respective processes.

From Figure 6.12a it can be seen that one pump photon is needed to excite the adsorbed CH_3Br molecules. This observation that CH_3Br adsorbed on Au can be excited by means of a single photon with a central wavelength of 266 nm to a dissociative state, which is

most likely the A-band, strongly indicates that the Au substrate induces a red-shift of the CH_3Br A-band by at least 1.5 ±0.1 eV (see also the discussion in Section 6.1.2). Similar results were reported in the literature for CH_3Br adsorbed on Ag(111) [259] and Mo(100).

Figure 3.12b shows that a quadratic power dependence has been measured for the probe laser beam. This indicates that two probe photons are most likely required to generate the ionized methyl fragments. Therefore, the interpretation of the detection mechanism is similar to the one found for CD_3I on Mo(100) (cf. Section 5.1.3) and CH_3Br on Mo(100) (cf. Section 6.1.3). Namely, the excited adsorbate molecules are ionized by non-resonant two photons of 333.4 nm wavelength and decompose yielding the CH_3^+ fragment.

The fact that the CH_3^+ signal in Figure 6.11 does not show any transient evolution at negative delay times excludes the possibility that the 333.4 nm laser pulse acts as a pump excitation. As previously mentioned, the maximum intensity of the CH_3^+ transient peak obtained from CH_3Br photodissociation on gold surface is located at 140 fs. The CH_3^+ transient signal recorded from the CH_3Br photodissociation on the Mo(100) exhibited also a peak structure, but with the maximum intensity located at 90 fs pump-probe delay time. This clearly indicates that CH_3Br interacts differently with the molybdenum and gold surfaces.

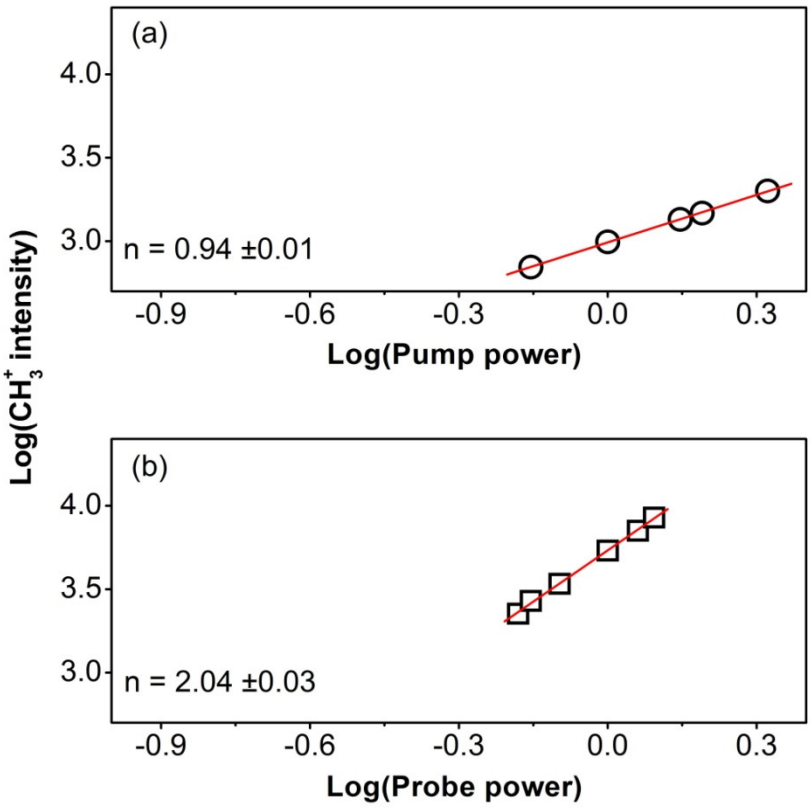

Figure 6.12 Intensity of the CH_3^+ signal as a function of (a) pump power; (b) probe power. Both measurements (a) and (b) were performed for a pump-probe delay time of 140 fs. The straight lines represent the linear fits to the experimental data yielding the indicated slopes n.

6.3 Methyl bromide adsorption and photodissociation on magnesia supported gold clusters

6.3.1 Temperature programmed desorption

The adsorption and the thermally induced reaction of CH_3Br on magnesia supported gold particles was characterized by means of TPD. The experiment was performed at a fixed molecule coverage of 0.25 ML. The gold nanoparticles were grown by thermal evaporation (cf. Section 4.3). During the deposition the MgO/Mo(100) substrate was held at 90 K.

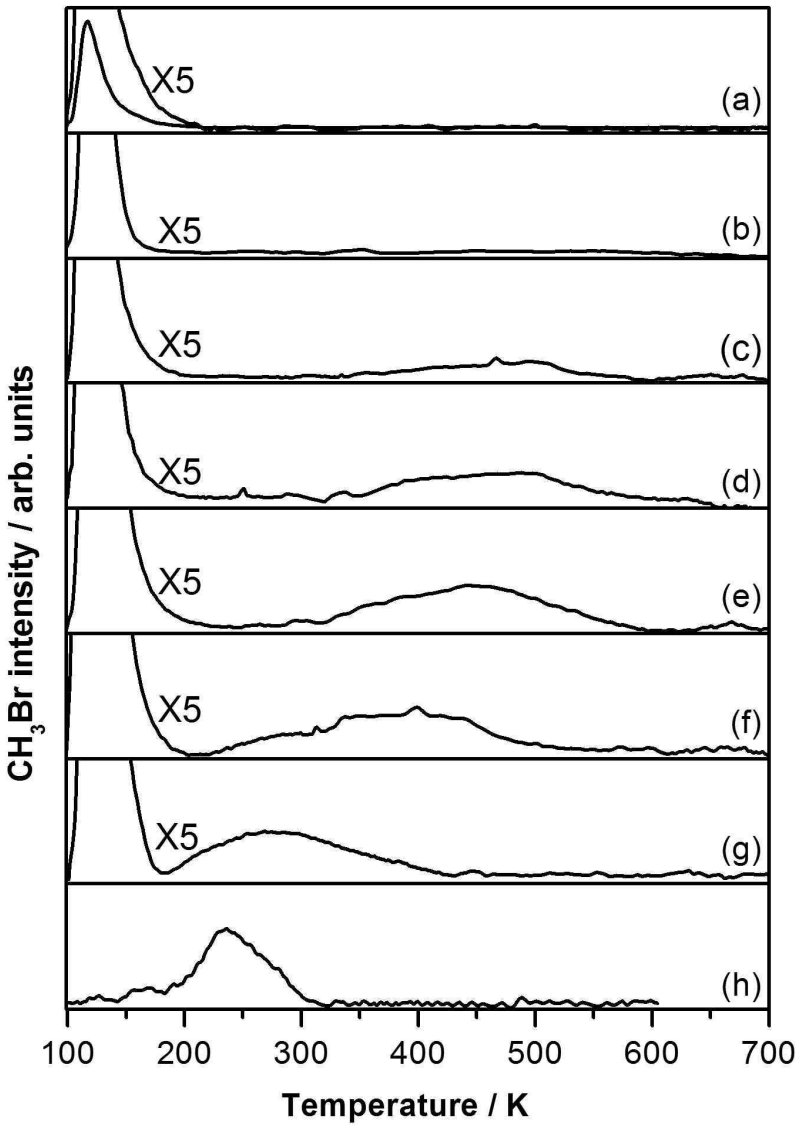

Figure 6.13 Temperature programmed desorption spectra of 1 L (0.25 ML) CH_3Br on (a) 10 ML MgO film on Mo(100); (b-f) MgO supported gold nanoparticles generated by thermal evaporation ((b) 0.07 ML Au; (c) 0.1 ML Au; (d) 0.13 ML Au; (e) 0.45 ML Au; (f) 1 ML Au; (g) 3 ML Au), (h) 10 ML gold film on Mo(100). The heating rate was 2 K/s.

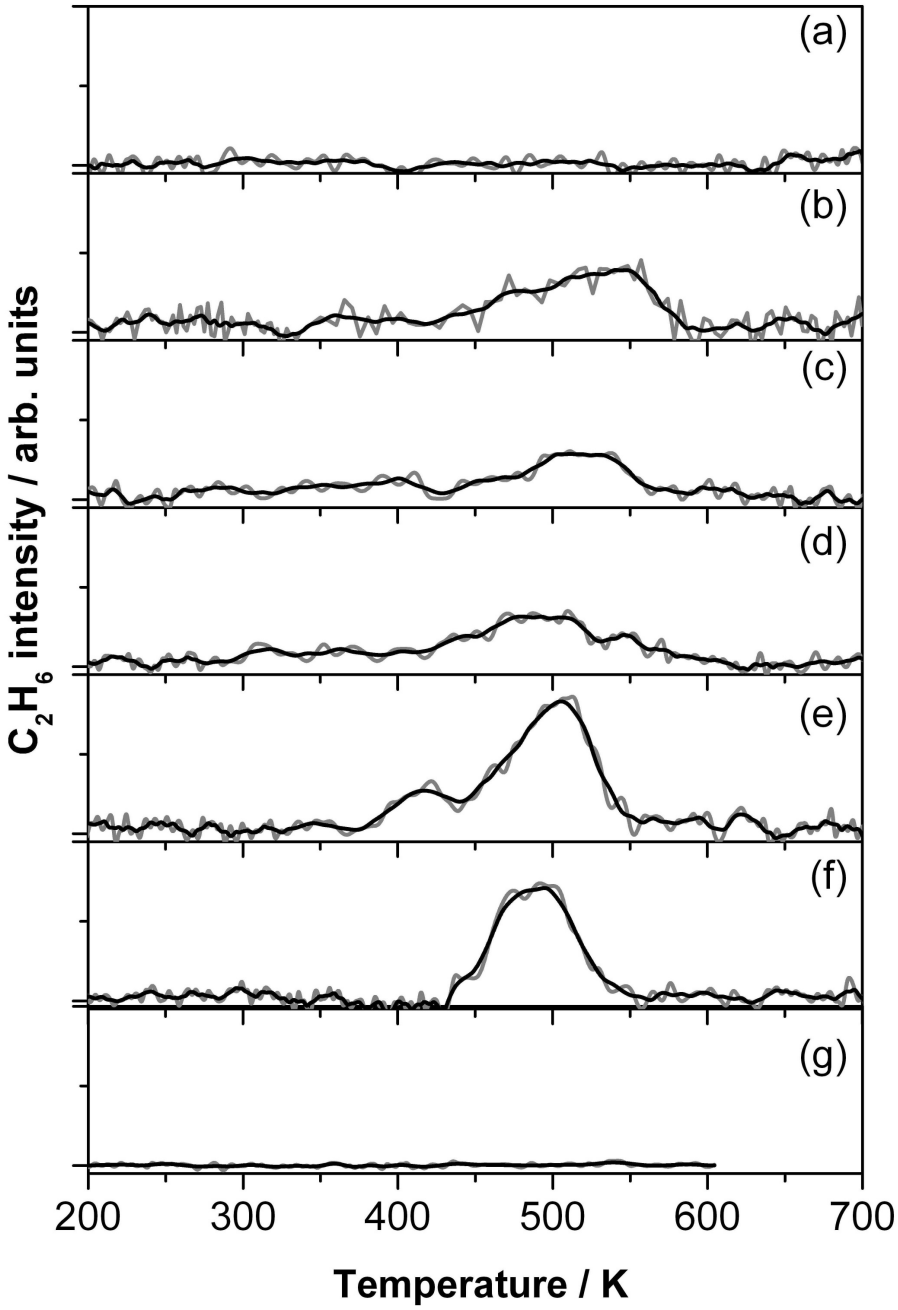

Figure 6.14 Temperature programmed reaction of 1 L CH_3Br on different substrates studied by monitoring the C_2H_6 product signal (a) 10 ML MgO film on Mo(100); (b-f) MgO supported gold nanoparticles generated by thermal evaporation ((b) 0.1 ML Au; (c) 0.13 ML Au; (d) 0.45 ML Au; (e) 1 ML Au; (f) 3 ML Au); (g) 10 ML gold film on Mo(100). The thin gray lines represent the measured data; bold black lines were obtained by applying a low pass FTT filter to the data. The heating rate was 2 K/s.

Figure 6.13 shows the CH_3Br TPD spectra recorded from 0.25 ML CH_3Br on bare magnesia, magnesia supported gold clusters, and an Au surface. On the bare magnesia and the bare gold surface we observed that CH_3Br molecules adsorb molecularly and desorb without decomposition. A detailed TPD investigation of CH_3Br adsorbed on both magnesia and gold surface

were presented in Section 6.1.1 and Section 6.2.1, respectively. On the bare magnesia surface a single desorption peak below 180 K was detected (Figure 6.13a). A similar TPD spectrum to the one obtained from the bare magnesia surface is obtained from 0.07 ML Au on magnesia. After deposition of 0.1 ML Au on the magnesia thin film a new distinct desorption peak appears in the TPD spectrum in Figure 6.13c apart from the CH_3Br desorption below 180 K. This new desorption feature extends from 350 K to about 550 K with a maximum around 490 K and it is attributed to the molecular desorption of CH_3Br molecules from the magnesia supported gold clusters. Increasing the gold coverage to 0.13 ML (Figure 6.13d) leaves this new desorption peak essentially unchanged in shape, position and intensity. A further successive increase in the Au coverage (Figure 6.13e - 6.13f) results in a shift of this CH_3Br desorption peak originating from the Au particles to lower temperatures. At the highest investigated Au coverage of 3 ML, the maximum of the CH_3Br desorption from the Au particles is located at 270 K and the TPD peak narrows to a width of about 140 K (Figure 6.13g).

The temperature shift of the TPD peak indicates a change of the CH_3Br adsorption energy with coverage which points toward a change in the morphology and/or in the electronic structure of the supported gold nanoparticles. Therefore, the shift of the methyl bromide desorption peak is attributed to the CH_3Br adsorption on gold nanoparticles with different size (see also Section 5.3.1 and Ref [283]). The broad temperature range in which desorption of CH_3Br from the Au particles occurs might be due to multiple adsorptions at different sites on the nanoparticles.

Apart from the molecular desorption of CH_3Br from magnesia supported Au nanoparticles, the thermal reaction leading to C_2H_6 formation was observed. Figure 6.14 shows the temperature programmed reaction/desorption of ethane from magnesia surfaces covered with different amounts of gold. The C_2H_6 signal intensity axis in Figure 6.14 is enhanced by a factor of 100 with respect to the CH_3Br signal intensity axis in Figure 6.13. No ethane signal was detected from bare magnesia surfaces (Figure 6.14a). For a gold coverage of 0.1 ML a broad ethane desorption peak appears with the maximum intensity at about 550 K (Figure 6.14b). This TPD peak shifts to lower temperatures with increasing the gold coverage (Figure 6.14c-f). For the highest studied Au coverage of 3 ML, the desorption maximum is located at 490 K. No ethane signal was detected from bare Au surfaces (Figure 6.14g). From the TPD series in Figure 6.14 it can be also observed that the maximum ethane production is obtained from a magnesia surface covered with 1 ML Au.

6.3.2 Photodissociation dynamics

The photodissociation dynamics of methyl bromide on magnesia supported gold nanoparticles was studied with SFsMS by monitoring the emerging methyl cation signal as a function of the pump-probe time delay. The results are presented in Figure 6.15. The transients were recorded

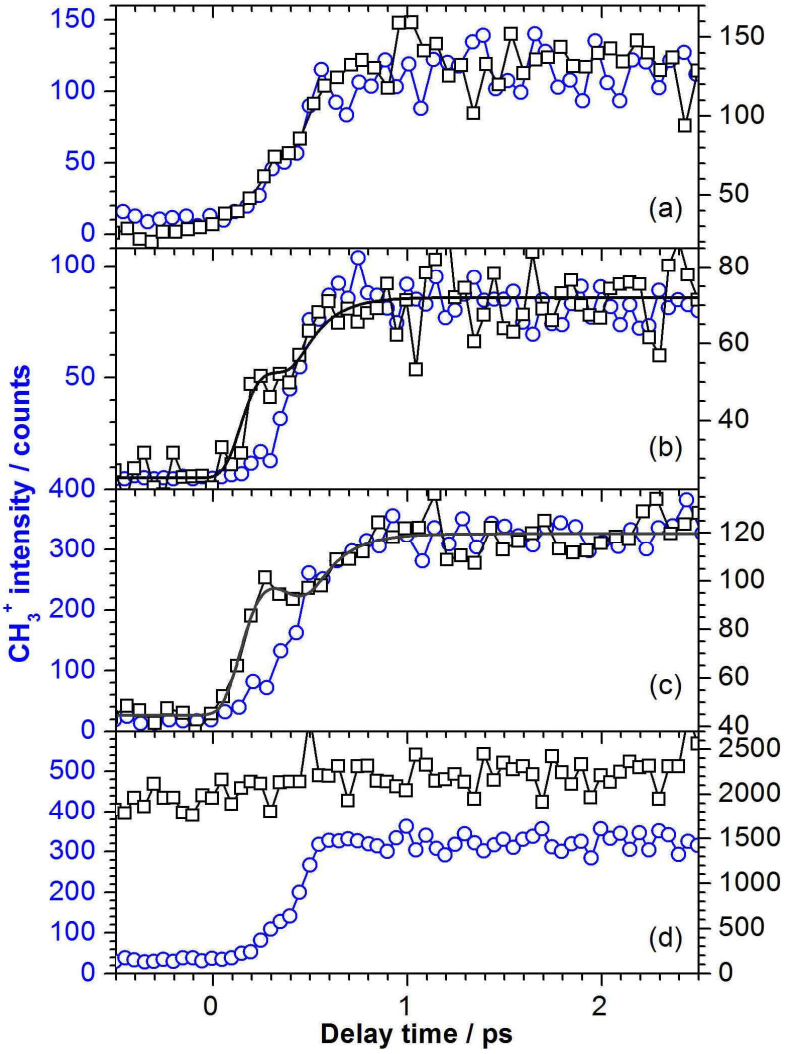

Figure 6.15 Femtosecond time-resolved pump-probe mass signals of methyl cations detected after photodissociation of CH_3Br adsorbed on the bare MgO/Mo(100) substrate (blue circles) and from CH_3Br adsorbed on tha same MgO/Mo(100) surface covered by gold particles (black squers). The gold coverages are (a) 0.065 ML Au; (b) 0.10 ML Au; (c) 0.13 ML Au; (d) 0.15 ML Au. The transient signals were obtained with 6 mW/cm² pump (266 nm) and 600 mW/cm² probe laser power (333 nm). The solid lines are the best fit of a ´peak´ in conjunction with a ´delayed exponential rise´ model to the experimental data. The vertical scale on the left hand side indicates the methyl cation intensity measured from the CH_3Br photodissociation on the bare MgO/Mo(100). The vertical scale on the right hand side represents the methyl cation intensity measured from the CH_3Br photodissociation on the MgO/Mo(100) surface covered by gold particles.

from MgO surfaces prepared with a series of different amounts of gold between 0.065 ML and 0.15 ML. For reference, in each case a CH_3^+ transient was recorded from the bare magnesia surface just before gold deposition. Subsequently, the MgO surface was cleaned by heating to 800 K and the desired amount of gold was deposited at a surface temperature of 90 K. Then CH_3Br was deposited again and the transients shown in Figure 6.15 (blue circles) were recorded. The methyl bromide coverage (0.25 ML) was kept constant for all recorded transient signals. Also the laser parameters were kept approximately constant during the acquisition of the data shown in Figure 6.15.

On the bare magnesia thin film, the transient methyl signal exhibits a single exponential rise with a time constant of 320 ±60 fs and an initial delay of 150 ±50 fs (see also Figure 6.3). The transient methyl signal obtained from the photodissociation of CH_3Br on magnesia covered by 0.065 ML Au (Figure 6.15a - black squares) is essentially similar to the one obtained from the bare MgO surface (Figure 6.15a - blue circles). After deposition of 0.01 ML Au on the magnesia surface, the transient methyl signal also exhibits an exponential rise, but in addition it displays a peak structure with a maximum at 240 fs (Figure 6.15b - black squares). Fitting an exponential 'rise and decay' in conjunction with a 'delayed exponential rise' model (convoluted with the laser cross correlation) to the experimental data (Figure 6.15b - black squares) gave 190 ±30 fs for the rise of the peak structure. For the subsequent exponential rise at longer delay times, the time constant matched with the one obtained from the bare MgO surface.

Figure 6.15c (black squares) shows the transient methyl signal obtained from the photodissociation of CH_3Br on magnesia covered by 0.13 ML Au. In this transient signal a peak structure at early delay times is even more apparent with an intensity maximum at 270 fs followed by an exponential rise. The best fit with the same model as in Figure 6.15b to the experimental data (Figure 6.15c - black squares) gave similar time constants of 200 ±30 fs for the rise and the decay components of the observed peak. For the subsequent exponential rise at longer delay times, the time constant matched again with the one obtained from bare MgO surface.

The photodissociation of CH_3Br on MgO/Mo(100) covered by 0.15 ML Au leads to a dramatic increase of the methyl cation signal intensity (about 2200 counts (Figure 6.15d-black squares) compared to about 350 counts on the bare magnesia surface (Figure 6.15d-blue circles)). However, no time dependence of the CH_3^+ signal is observed anymore.

For the interpretation of the transient data in Figure 6.15, the size dependent structure of the gold clusters on MgO is considered, which has been investigated previously by STM and EPR [201, 210] (cf Section 4.3.2).

The CH_3^+ transient peak structure observed in Figure 6.15b,c appears only on magnesia substrates prepared with gold particles (coverages between 0.1 and less than 0.15 ML). Therefore, it has to be assigned to the dissociation of methyl bromide molecules adsorbed on the gold clusters. It is assumed that the CH_3^+ transient peak structure observed at 240 fs to 270 fs in Figure 6.15b,c has the a similar excitation and detection mechanism as for CH_3Br on the extended Au surface (cf. Figure 6.11), which is described by the reaction schema (6.2).

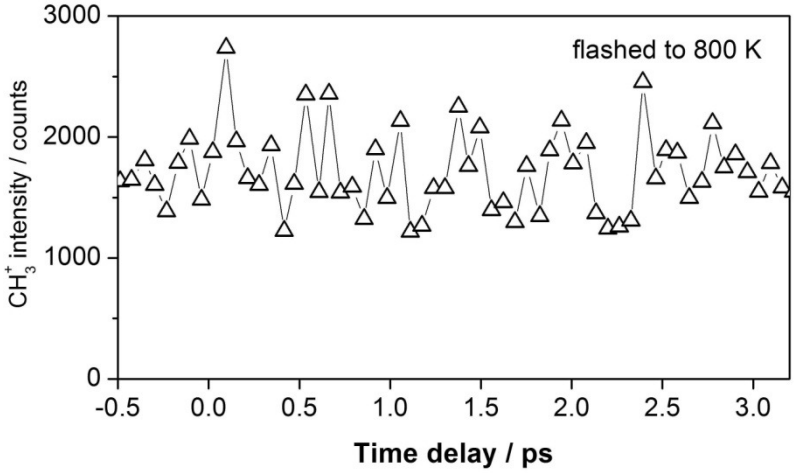

Figure 6.16 Femtosecond pump-probe signal of methyl cations from 0.13 ML Au/MgO/Mo(100) previously flashed to 800 K. The transient signal was obtained with 6 mW/cm² pump (at 266 nm) and 600 mW/cm² probe laser power (at 333.4 nm).

According to the STM and EPR investigations of magnesia supported gold particles performed by Freund and coworkers [201, 210], up to a gold coverage of 0.06 ML Au on 8 ML MgO/Mo(100) at 90 K, mostly gold atoms are expected on the surface. Consequently, it can be assumed that in the case of Figure 6.15a (0.65 ML) the surface is still mostly covered by isolated gold atoms and very small clusters consisting of just few atoms from which no photodissociation/desorption signal (no peak structure) is observed. This conclusion is further supported by an experiment in which mass-selected Au atoms produced by the cluster source (cf. Section 2.3.2) were deposed on 8 ML MgO/Mo(100) surface by means of softlanding (Au coverage was about 0.03 ML). In this experiment, no CH_3^+ transient peak structure was observed.

For gold coverages above 0.06 ML, small Au particles are expected on the magnesia surface. Apparently, in contrast to magnesia supported Au atoms and very small clusters, the CH_3Br photodissociation on these Au particles on MgO/Mo(100) leads as presented in Figure 6.15b,c to the appearance of the CH_3^+ transient peak structure.

The dramatic increase of the methyl cation signal intensity detected from the magnesia surface covered by 0.15 ML Au (Figure 6.15d) is suggested to be due to the photodissociation on even bigger Au particles, which might have electronic and/or geometric structures different from the Au particles obtained at lower coverages. Hypothetical, the dramatic increase of the methyl cation signal observed in Figure 6.15d might be due to the predominant formation of compact 3D gold particles at a coverage above 0.15 ML.

STM investigations of Freund and coworkers indicated that 3D Au particles are also formed, if MgO samples with gold coverages below 0.06 ML (which consist of isolated Au atoms at low temperatures) were annealed to 300 K [201]. Therefore, in order to confirm the hypothesis that larger 3D particles are responsible for the change of the methyl signal at coverages above 0.15 ML Au (Figure 6.15d), the magnesia sample with 0.13 ML Au (Figure 6.15c) was briefly heated to 800 K to induce the formation of larger 3D Au particles. Subse-

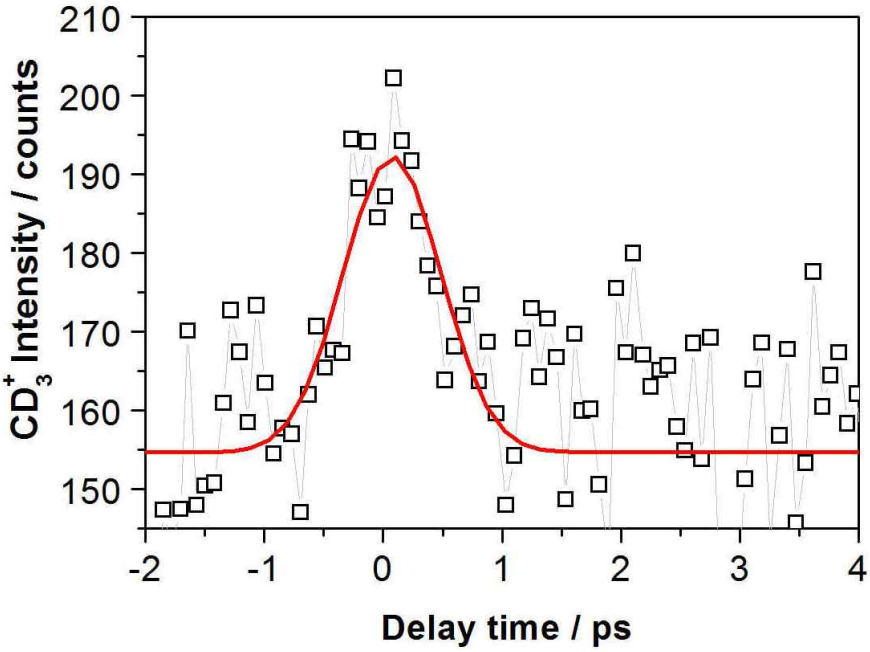

Figure 6.17 Femtosecond time-resolved signal intensity of methyl cation signal detected from a MgO/Mo(100) surface coverd by 0.13 ML Au and anneald at 800 K. The open symbols are the measured data, while the solid line is a gaussian fit to the experimental data, drown to gude the eye. The transient signal was obtained with 2 mW/cm² pump (at 266 nm) and 200 mW/cm² probe laser power (at 333 nm).

quently, CH_3Br molecules were deposited again and a photodissociation transient was recorded at 90 K. The result is displayed in Figure 6.16. Indeed, the peak structure (and exponential rise) measured before the annealing (Figure 6.15c) is not observed anymore. Instead, an intense methyl signal is obtained that does not exhibit any time dependence, similar to the case of 0.15 ML coverage in Figure 6.15d. This result supports the hypothesis that the presence of a considerable fraction of larger 3D Au nanoparticles is responsible for the different signal in Figure 6.15d. In other words, a transition from small, mostly 2D Au particles to 3D particles is expected to occur at a coverage of about 0.15 ML.

Reducing the intensity of both pump and probe laser pulses by a factor of three, a time dependent measurement of CH_3Br photodissociation on the surface shown in Figure 6.16 was possible. The result is shown in Figure 6.17. The methyl cation transient signal presents a broad peak (1.1 ps FWHM) structure with a maximum located at about 0 fs. Due to the high noise level, only a Gaussian function (solid line in Figure 6.17) was drawn to guide the eye. The reduced laser intensity used to record the methyl transient signal and the shape of this transient signal (peak structure in Figure 6.17) further indicates a similar excitation and detection mechanism as for CH_3Br adsorbed on the extended Au surface.

6.3.3 Gas-phase reactivity measurements

In the previous section it was shown that neither thermal desorption (cf. Figure 6.13) nor photodissociation (cf. Figure 6.15) could be detected from CH_3Br adsorbed on magnesia supported gold atoms and small clusters. This could be attributed to a very strong interaction be-

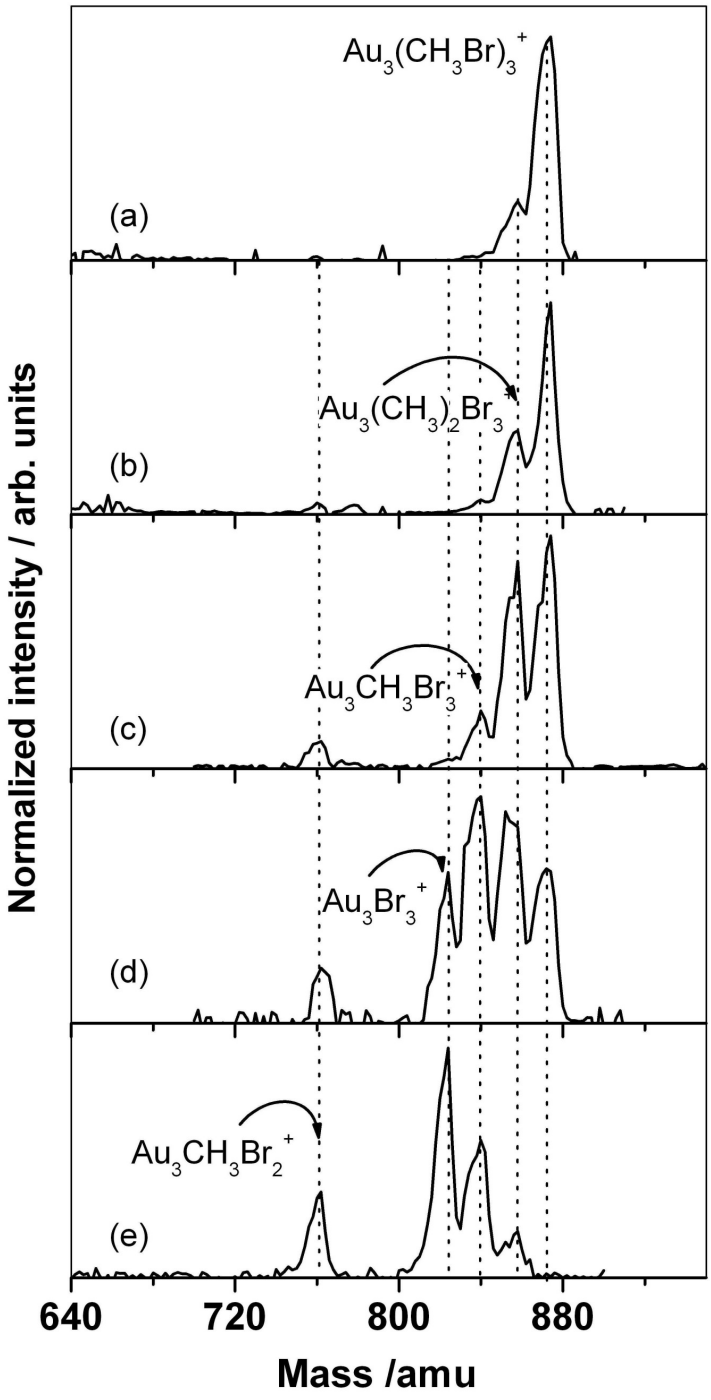

Figure 6.18 Gas-phase product ion mass spectra of gold trimers cations with methyl bromide in a rf-octopole ion trap at 300 K for different reaction times: (a) 10 ms; (b) 100 ms; (c) 500 ms; (d) 1 s; (e) 5 s.

tween the CH_3Br molecules and the Au atoms (or small Au clusters) on the magnesia surface. In order to shed light on the nature of the interaction between CH_3Br and Au atoms and small Au clusters, gas-phase reactivity measurements between small mass-selected gold clusters and methyl bromide molecules were performed [262]. The reactivity measurements were carried out in an rf-octopole ion trap filled with 1 Pa of helium buffer gas (see Section 2.3.2). The additional partial pressure of CH_3Br reactive gas was 0.1 Pa. The trapping time of the clusters in the rf-octopole and hence the reaction time was accurately determined by controlling the electrostatic fields at the entrance and exit lenses of the trap.

Figure 6.19 shows the product ion mass spectra of gold trimer cations with methyl bromide at 300 K for different reaction times. For the shortest reaction time of 10 ms, a small peak corresponding to $Au_3(CH_3)_2Br_3^+$ was observed apart of the predominant mass peak of $Au_3(CH_3Br)_3^+$. Increasing the reaction time to 100 ms the $Au_3(CH_3)_2Br_3^+$ signal slightly increased and small contributions from $Au_3CH_3Br_3^+$ and $Au_3CH_3Br_2^+$ were observed. At 500 ms, the $Au_3(CH_3)_2Br_3^+$, $Au_3CH_3Br_3^+$ and $Au_3CH_3Br_2^+$ reaction product intensities increased and $Au_3Br_3^+$ was detected. For a reaction time of 1 s, all above mentioned reaction products coexisted, but the relative intensity of $Au_3(CH_3Br)_3^+$ apparently decreased. At 5 s, the longest investigated reaction time, the $Au_3(CH_3Br)_3^+$ vanished, and Au_3Br_3 reached the highest intensity.

Figure 6.19 clearly shows that methyl bromide molecules react at room temperature with Au_3^+. The maximum number of adsorbed CH_3Br molecules coincides with the number of Au atoms of the cluster. A sequential dissociation reaction of the adsorbed molecules is observed with increasing reaction time, such that for longer reaction times the Au_3Br_3 product dominates.

Detailed gas-phase investigations of the reactions between CH_3Br and Au_n^+ (n = 1, 2, 5, 7) show that the trend observed for gold trimers, i.e. progressive loss of the methyl radical with increasing the reaction time, is observed on all studied gold cluster sizes [262].

Based on the present surface and gas-phase observations, it seems reasonable to assume that Au atoms and small Au cluster consisting of just few atoms supported on a magnesia surface induce a dissociation of the C-Br bond of the adsorbed CH_3Br molecules. This might be the reason why mainly bromine atoms are expected to be adsorbed on the Au atoms and small Au cluster after CH_3Br dissociation, which cannot be photodesorbed. Consequently, neither CH_3^+ transient signal nor CH_3Br thermal desorption was observed from thin magnesia films covered with less than 0.06 ML.

6.4 Conclusions

The adsorption behavior of methyl bromide molecules on the different surfaces consisting of ultra-thin magnesia films, gold, and magnesia supported gold clusters and nanoparticles was investigated by means of TPD. The TPD experiments show that the methyl bromide molecules are weakly adsorbed on the magnesia surface because the complete desorption occurs at temperatures below 180 K. In contrast to magnesia, the interaction of CH_3Br with a gold surface is considerably stronger. Depending on CH_3Br coverage, the TPD spectra display two

distinct desorption peaks characteristic for monolayer and multilayer desorption. On the magnesia surface covered with gold nanoparticles, a separate peak corresponding to the desorption from Au particles is observed apart from the direct desorption from the magnesia surface. This peak shifts to higher temperatures with decreasing the gold amount deposited on the surface, indicating that the CH_3Br - Au interaction increases with decreasing particle size.

On all employed surfaces, the time-resolved photodissociation dynamics of the adsorbed CH_3Br molecules was investigated by monitoring the methyl cation intensity as a function of the pump-probe delay time by means of SFsMS. Suggestions for the excitation and the detection mechanisms were deduced with the help of power dependence measurements and by employing the available potential energy diagrams. In contrast to 8 - 10 ML MgO/Mo(100) where the electronic structure of the CH_3Br adsorbates is likely to be similar to that of the free molecules, on metal surfaces, a strong perturbation of the electronic structure was evidenced. A similar perturbation of the electronic structure can be also induced either by the molybdenum substrate, when the CH_3Br molecules are adsorbed on magnesia films with a thickness of 1 - 3 ML, or by the gold particles deposited on the magnesia films.

The observation that neither molecular desorption nor photoproducts of the methyl bromide were detected for the smallest gold cluster sizes was attributed to dissociative adsorption as verified by complementary experiments with gas-phase gold clusters.

7 Methyl halide adsorption and surface femtochemistry: Comparison and conclusions

The goal of this final chapter is to summarize the conclusions from the experimental findings through a short comparison between the methyl iodide and the methyl bromide electronic structure, adsorption behavior and femtochemistry on ultra-thin magnesia films, on a gold surface and on magnesia supported gold clusters and nanoparticles. Also in this chapter, the viability of the novel surface pump-probe laser mass spectrometry technique is emphasized and further possible applications are discussed.

7.1 Electronic structure

In Figure 7.1 the relevant potential energy curves of methyl iodide and methyl bromide ground state and A-band are displayed. The potentials of methyl bromide and methyl iodide are similar, but due to the shorter C-Br bond length (1.939 Å) of methyl bromide with respect to the C-I bond length (2.1396 Å) of methyl iodide, the A-band (first adsorption continuum) maximum of CH_3Br is shifted to higher energy [42, 43]. The A-band adsorption maximum of methyl iodide and methyl bromide molecules are located at 4.7 eV and 6.2 eV, respectively [265, 266].

The photodissociation of the free methyl iodide molecule via A-band excitation occurs within less than 100 fs (see the discussion in Section 5.1.2, the most recent contributions [30, 31] and references therein). The real-time photodissociation of methyl bromide via excitation to the A-band was not directly measured until now. However, the lifetime of the methyl bromide A-band was estimate to be about 120 ±40 fs [46].

7.2 Adsorption behavior

By means of temperature programmed desorption spectroscopy insights into the adsorption behavior of the methyl halide molecules on different substrates have been obtained.

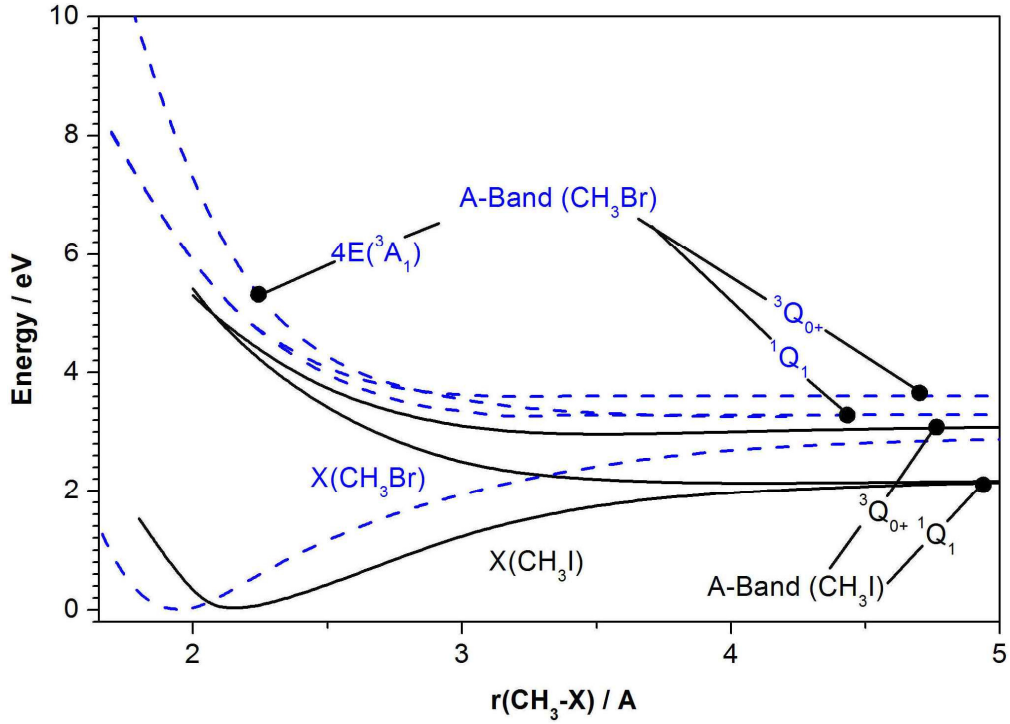

Figure 7.1 Potential energy diagram of free methyl iodide (solid lines) and methyl bromide molecules (dashed lines) adapted from Ref. [38-41].

7.2.1 Adsorption on MgO films on Mo(100)

Both methyl iodide and methyl bromide molecules displayed similar adsorption characteristics on magnesia thin films:

(i) They adsorbed molecularly on the surface and desorbed without decomposition.

(ii) The molecules interacted weakly with the surface, i.e. they are physisorbed because the complete desorption occurs at temperatures below 180 K.

(iii) The recorded TPD spectra showed that the desorption maximum is shifted to lower temperatures with increasing coverage. This observation was interpreted as the consequence of a repulsive adsorbate-adsorbate interaction due to the permanent dipole moment of the molecules aligned parallel to each other. Consequently, the methyl halide molecules tend to wet the surface uniformly rather than to form 3D islands.

(iv) The complete coverage of the surface with molecules was accomplished for doses of about 4 L.

7.2.2 Adsorption on Au films on Mo(100)

In contrast to magnesia, the methyl halide molecules were more strongly bound to the gold substrate. The desorption temperatures were between 150 and 250 K for methyl iodide and between 150 and 300 K for methyl bromide. However, similar to magnesia the molecules were almost exclusively found to adsorb molecularly and to desorb without decomposition. At submonolayer coverage, the TPD spectra showed that the maximum of the desorption signal was shifted to lower temperatures with increasing coverage, which was again attributed to the repulsive interaction of the adsorbed molecules.

On the gold surface, about 4% of the first methyl iodide molecular layer dissociated and produced ethane. The ethane signal appeared in the TPD spectra at temperatures between 300 and 400K. In contrast, no thermal induced reaction products were detected from methyl bromide adsorbed on gold surface.

7.2.3 Adsorption on magnesia supported gold clusters

The TPD spectra of methyl iodide and methyl bromide molecules adsorbed on the magnesia surfaces decorated with gold nanoparticles exhibited a separate peak apart from the peak corresponding to the direct desorption from magnesia, which was assigned to the desorption from Au nanoparticles. This TPD peak corresponding to the desorption from Au nanoparticles shifted to lower temperatures with increasing the amount of gold deposited on the surface. This indicated that the CH_3X-Au (X = I, Br) interaction decreased with increasing particle size. Consequently, the coverage dependent adsorption energy (reflected in the temperature shift of the TPD peak) might be assigned to a change in the morphology and/or the electronic structure of the supported Au nanoparticles.

The interaction with the gold nanoparticles was found to be stronger in the case of methyl bromide compared to methyl iodide. This was reflected by the molecular thermal de-

sorption, which occurred, e.g., for an initial coverage of 0.1 – 0.13 ML at 450 K for CH_3Br, but at 300 K for CD_3I.

Neither fragments nor new reaction products were detected from methyl iodide adsorbed on Au nanoparticles. In contrast, a small fraction of methyl bromide molecules were found to dissociate on the Au nanoparticles and produces ethane. The ethane thermal desorption signal gradually shifted to lower temperatures (from 550 K to 490 K) with increasing cluster size.

In both investigated systems, no methyl halide molecular signal was detected in the TPD experiments if the magnesia surface was prepared with less than 0.065 ML Au. In this case, Au atoms and small Au clusters are expected to exist on the magnesia surface (cf. Section 4.3.2). Supplementary gas-phase reactivity experiments indicated that the methyl halide molecules dissociate upon adsorption on small Au clusters.

7.3 Photochemistry

The novel investigation method of surface pump-probe fs-laser mass spectrometry was applied to monitor the photoinduced reaction on methyl halide molecules adsorbed on different substrates consisting of magnesia, gold, and magnesia supported small gold clusters and nanoparticles.

7.3.1 Photochemistry on MgO films on a Mo(100)

Both methyl iodide and methyl bromide molecules adsorbed at submonolayer coverage on the magnesia surface were photodissociated with laser light with a central wavelength of 266 nm. The photodissociation of methyl iodide proceeded via the absorption of a single photon almost at the center of the A-band. In contrast, for the fragmentation of the methyl bromide molecule, power dependence measurements showed that two photons are required.

Employing time-delayed multiphoton ionization, the dynamics of the surface photoinduced reaction was detected with femtosecond resolution. For the detection step the probe laser pulse wavelength was tuned to 333.4 or to 333.9 nm in order to sensitively detect the CH_3 or the CD_3 radical, respectively by means of 2+1 REMPI.

7.3.1.1 8-10 ML MgO/Mo(100)

In the case of methyl iodide the methyl cation transient signal consisted of a peak starting at zero delay time with a maximum at about 130 fs and a subsequent delayed exponential rise. The peak structure with rise and decay time constants of about 90 ±10 fs each was associated with the lifetime of the transition state of the dissociating methyl iodide, which was excited to the A-band by a single pump photon transition. This transition state was detected via two-photon ionization by the probe laser pulse. Subsequently, instantaneous ion fragmentation lead to the observed methyl ion fragments. The delayed exponential rise of the methyl ion signal at positive delay time (with an initial coherent delay of 170 fs and exponential rise time

constant 680 fs) was assigned to the (2 + 1) REMPI detection of the methyl radical emerging from the A-band dissociation of the adsorbed methyl iodide molecules.

In the case of methyl bromide, the methyl cation transient signal started after 150 fs delay time and showed just an exponential rise with a time constant of 320 $\pm$60 fs. This transient signal was also attributed to the direct REMPI detection of the emerging neutral methyl fragments reflecting the dynamics of their liberation from the force fields in coherent motion along the dissociative potential energy surfaces.

Comparing the rise time constants of the methyl signal, a smaller value (320 $\pm$60 fs) was obtained for the appearance of the methyl fragments for methyl bromide than for methyl iodide (680 $\pm$50 fs) on MgO. This is in disagreement with the gas-phase calculation which estimated a longer dissociation time for CH_3Br than for CH_3I. This discrepancy might be attributed to the adsorption geometry of the methyl halide molecules on the magnesia surface. Methyl iodide molecules are considered to adsorb with the methyl-end toward the surface [238], which is proposed to lead to a chattering motion of the methyl group between the MgO surface and the I atom after photoexcitation and before dissociation. On the other hand, methyl bromide molecules have been reported to posses an adsorption geometry in which the C-Br axis is nearly parallel to the surface [241]. Therefore, in the case of CH_3Br the methyl fragment suffers mostly only one collision with the adjacent molecules and is easier released than in the case of methyl iodide.

Subsequent to the photodissociation of methyl iodide and simultaneously with the desorption of the methyl fragments, the bimolecular reaction of the emerging ground state and spin-orbit excited iodine atoms on the surface was probed by detecting molecular iodine in the electronically excited B-state. In contrast to methyl iodide, no bromine molecules were detected subsequent to CH_3Br photodissociation on the MgO surface.

7.3.1.2 Mo(100) and 1-6 ML MgO/Mo(100)

The interaction of the methyl iodide molecule with the Mo(100) surface was found to be different with respect to the interaction with the MgO films of variable thickness on Mo(100). This was indicated by: (i) the shift of the peak structure assigned to the detection of the dissociating transition state of the excited methyl iodide molecules observed in the methyl transient signal from methyl iodide photodissociation on bare Mo(100) and on MgO films of variable thickness; and (ii) the detection of I_2 just from MgO films thicker than 3 ML.

Also apparent differences were observed in the case of the methyl bromide photodissociation dynamics on magnesia films of variable thickness. On 1 to 3 ML MgO films, the appearance of a peak structure in the methyl cation transient signal at early pump-probe delay time was attributed to the detection of the dissociating transition state of excited methyl bromide molecules. For thicker MgO films the peak structure disappeared. A perturbation of the electronic structure of the adsorbed CH_3Br molecules by the molybdenum substrate was consequently proposed to be responsible for the transient peak structure detected on 1 to 3 ML MgO films.

7.3.2 Photochemistry on Au films on Mo(100)

Independent on the laser parameters, methyl iodide molecules adsorbed at submonolayer coverage on a gold film could not be photodissociated. This was proposed to be due to the fact that the ground state of the CH_3I molecule, which is adsorbed with the C-I axis almost parallel to the surface, is weakly perturbed compared to the gas-phase, but the molecule excited state is strongly bound to the metal. This facilitates the recapturing of the ground state after photoexcitation and before the C-I bond stretches considerably. Consequently, after excitation, the molecules almost instantaneously relax back into the ground states and the molecular dissociation is quenched. On a Pt(111) surface, the lifetime of the excited methyl iodide molecule was estimated to be shorter than 5-10 fs [255]. Furthermore, it was found that the photodissociation of CH_3I molecules adsorbed on an iodine film on the gold surface or at multilayer coverage is not quenched anymore.

In contrast to CH_3I it was demonstrated that CH_3Br molecules adsorbed at submonolayer coverage on a gold surface dissociate subsequent to laser irradiation. The time-resolved investigation in conjunction with power dependence measurements show that the detected methyl fragment signal was due to a direct photodissociation process. The excitation of the adsorbed CH_3Br molecules and the detection of the methyl cation signal involved a single pump photon at 266 nm and two probe photons at 333.4 nm, respectively.

7.3.3 Photochemistry on Magnesia supported gold clusters

7.3.3.1 Small gold clusters and nanoparticles

Both methyl iodide and bromide molecules interact strongly with small gold clusters supported on the magnesia surface. This strong interaction was confirmed by the TPD investigations where no molecular desorption was observed and by the SFsMS measurements, where no methyl cation transient signal from small gold clusters was detected. As indicated by the complementary gas-phase measurements, gold atoms and small gold clusters consisting of just few atoms break the C-X (X = I, Br) bond of the adsorbed methyl halide molecules. Just in the case of CH_3Br adsorbed on gold particles formed by deposition of 0.10 to 0.13 ML Au on magnesia, a methyl cation transient signal was observed. In this case a lowering of the A-band and of the excited cationic states of the CH_3Br molecules by the Au agglomerates was proposed.

7.3.3.2 3D gold nanoparticles

Similar to the extended gold surface, methyl iodide molecules adsorbed on 3D gold nanoparticles cannot be photodissociated. The absence of the photofragments was attributed to an ultrafast electronic relaxation preceding the molecular dissociation. In contrast, methyl bromide molecules adsorbed on 3D gold nanoparticles can be photodissociated and the transient evolution of the methyl fragment could be monitored.

Table 7.1 summarizes the adsorption and the photodissociation characteristics observed for the investigated methyl halides molecules on substrates consisting of magnesia, magnesia supported gold clusters and gold surface.

	Magnesia surface	Magnesia supported gold clusters		Gold surface
		Au_1,Au_2, Au_3 up to small 2D clusters	3D nanoparticles	
CH_3I and CD_3I	● Desorption below 180 K. ● Adsorb molecularly on the surface and desorb without decomposition. ■ Repulsive adsorbate-adsorbate interaction between the molecules at submonolayer coverage. ■ The methyl iodide molecules are adsorbed parallel to each other.	● Strong interaction. ■ Breaking of the C-I bond of the adsorbed methyl iodide molecules by the gold clusters.	● Desorption temperatures between 200 and 320 K. ● Adsorb molecularly and desorb without decomposition.	● Distinct desorption peaks for submonolayer (150 – 250 K) and multilayer coverage (under 150 K). ● About 4% of the first methyl iodide layer dissociate and produce ethane.
	● Photoinduced dissociation via A-band by a single photon at 266 nm. ● Time-resolved detection of the CH_3 and I fragments via multiphoton ionization at surface. ● Bimolecular reaction of the iodine atom fragments and time-resolved detection of I_2 reaction product. ■ The methyl iodide molecules are adsorbed with the methyl-end to the surface. ■ After photoexcitation the emergent methyl fragment collide with the surface.	● No CH_3I photodissociation. ■ The C-I bonds of the CH_3I molecules are split by the gold clusters.	● No CH_3I photodissociation. ■ Ultrafast electronic relaxation preceding the molecular dissociation	● No CH_3I photodissociation. ■ Ultrafast electronic relaxation preceding the molecular dissociation

Table 7.1 Continued on the next page.

	Magnesia surface	Magnesia supported gold clusters		Gold surface
		Au_1,Au_2, Au_3 up to small 2D clusters	3D nanoparticles	
CH_3Br	● Adsorb molecularly and desorb without decomposition. ● Desorption below 180 K. ■ Repulsive adsorbate-adsorbate interaction between the molecules at submonolayer coverage.	● Strong interaction. ■ Breaking of the C-Br bond of the adsorbed methyl bromide molecules by the gold clusters.	● Desorption at temperatures between 200 and 550 K. ● Few percent of the adsorbed molecules dissociate and produce ethane.	● Distinct desorption peaks for submonolayer (150 – 300 K) and multilayer coverage (under 150 K). ● Adsorb molecularly and desorb without decomposition. ■ Repulsive adsorbate-adsorbate interaction between the molecules at submonolayer coverage.
	● Photodissociation produced by two photons at 266 nm. ● Time-resolved detection of the CH_3 fragment via (2+1) REMPI at surface. ■ Methyl bromide molecules are adsorbed parallel with the surface. ■ After photoexcitation the methyl fragment collide with the adjacent molecule and subsequently is released in the gas-phase.	● No CH_3Br photodissociation. ■ Breaking of the C-Br bond of the adsorbed methyl bromide molecules by the gold clusters.	● Photodissociation and time-resolved detection of the CH_3^+ fragment via multiphoton ionization at surface ■ Strong perturbation of the CH_3Br electronic structure.	● Photodissociation and time-resolved detection of the CH_3^+ fragment via multiphoton ionization at surface ■ Photoinduced dissociation via A-band by a single 266 nm photon.

Table 7.1 Comparison and summarization of the adsorption (green background) and photodissociation (blue background) characteristics of the investigated methyl halide molecules on different supports. The filled circles represent the experimental observations, while the the filled squares represent the interpretations of the experimental data.

7.4 Conclusions and future directions

The findings presented in this thesis demonstrate the potential of the new experimental technique of surface femtosecond laser mass spectrometry to reveal the detailed dynamics of a wide variety of uni- and bimolecular surface-aligned reactions. The unique possibility to measure directly the surface transition state and product formation dynamics is of importance to the revelation of even complex reaction mechanisms in surface chemistry and heterogeneous catalysis.

Possible further experiments employing the SFsMS technique to reveal the molecular reaction dynamics could focus on elementary bimolecular reactions of two different molecules on an insulating surface.

(i) The reaction of hydrogen with carbon dioxide on a magnesia surface:

$$H + CO_2 \rightarrow OH + CO \tag{7.1}$$

HI and CO_2 molecules are coadsorbed on the surface. The bimolecular reaction of $H + CO_2$ should be started on the surface via HI photodissociation by the pump laser pulse. The reaction dynamics will be monitored by detecting the OH radicals via REMPI by means of the probe laser pulse. It should be mentioned that the HI photodissociation [284, 285] and OH detection by means of REMPI [286-288] have been investigated in the past. The dynamics of the $H + CO_2$ reaction has been theoretically studied on a LiF surface by Guo, Schatz and coworkers as well [289, 290].

(ii) The reaction between the iodine and bromine atoms on a magnesia surface:

$$CH_3I + CH_3Br \xrightarrow{266\ nm} 2CH_3 + IBr \tag{7.2}$$

Methyl iodide and methyl iodide molecules are coadsorbed on the surface. The pump laser pulse at a central wavelength of 266 nm starts the reaction by dissociating the methyl halide molecules (as described in Chapter 5 and Chapter 6). The reaction dynamics will be monitored by detecting the IBr product via REMPI by means of the probe laser pulse.

Also of potential interest might be the photoinduced bimolecular reactions on oxide supported metal clusters, because the metal clusters could influence the electronic structure of an adsorbed molecule (as shown in this work) and consequently they could make possible the excitation and/or the detection of the reaction intermediates and products in the wavelength range produced by our laser system.

Zusammenfassung

Ziel dieser Arbeit war die Untersuchung der chemischen Reaktionsdynamik von auf Festkörperoberflächen adsorbierten Molekülen in Echtzeit über den direkten Nachweis von Reaktionszwischen- und Endprodukten. Um dieses Ziel zu erreichen, wurde eine neue experimentelle Technik entwickelt. Der neuartige experimentelle Ansatz ermöglicht die zeitaufgelöste Untersuchung photoinduzierter Oberflächenreaktionsdynamik mittels Multi-Photonen-Ionisierung von Übergangszuständen, Zwischenprodukten und Endprodukten direkt auf der Oberfläche in einem Laser-massenspektrometrischen Pump-Probe-Verfahren.

Um die Zweckdienlichkeit dieser neuen Technik zu demonstrieren wurden die photoinduzierten Reaktionen von Methyliodid- und Methylbromidmolekülen untersucht, die in Submonolagen-Bedeckungen (i) auf Magnesiumoxidfilmen, (ii) auf Goldoberflächen und (iii) auf Goldclustern und –Nanopartikeln auf Magnesiumoxid adsorbiert waren.

Die verwendeten Oberflächen wurden mittels Auger-Elektronenspektroskopie, der Beugung niederenergetischer Elektronen, Photoelektronenspektroskopie und temperaturprogrammierter Desorptionsspektroskopie charakterisiert. Zusätzlich zu diesen Standardanalyseverfahren wurde erstmalig die Femtosekunden-Laser- Photoemissionsspektroskopie verwendet, um die elektronische Struktur eines hochschmelzenden Metalles zu untersuchen, das mit ultradünnen Magnesiumoxidfilmen variabler Schichtdicke bedeckt ist, und um Goldcluster zu studieren, die auf Magnesiumoxidfilmen deponiert wurden.

Auf einer Magnesiumoxid-Oberfläche adsorbierte Methyliodid Moleküle wurden photonisch in das dissoziative A-Band angeregt und zerfielen daraufhin innerhalb von 300 fs. Anschließend an die Dissoziation des Methyliodids und gleichzeitig mit der Desorption der Methylfragmente wurde die bimolekulare Reaktion der entstehenden Iod Atome im Grund- und im Spin-Bahn-angeregten Zustand durch die Detektion von molekularem Iod im elektronisch angeregten B-Zustand nachgewiesen. Es konnte gezeigt werden, daß diese Iod-Moleküle metastabil sind und induziert durch die Gegenwart der Oberfläche auf der Zeitskala von Picosekunden prädissoziieren.

Auf einer Goldoberfläche und auf Magnesiumoxid-geträgerten Gold-Nanopartikeln erfuhren die angeregten Methyliodid-Moleküle eine ultraschnelle Rückkehr in den Grundzustand, bevor sich die C-I Bindung wesentlich ausdehnen konnte. Daraus ergab sich nach der Molekülanregung eine nahezu sofortige Relaxation in den Grundzustand und damit eine Unterdrückung der molekularen Dissoziation.

Auf Magnesiumoxid adsorbierte Methylbromid-Moleküle dissoziierten schneller als Methyliodid-Moleküle. Zudem konnten nach dem lichtinduzieren Zerfall von Methylbromid Zerfall auf Magnesiumoxid keine Brommoleküle nachgewiesen werden.

Im Gegensatz zu Methyliodid konnte gezeigt werden, daß angeregte Methylbromid-Moleküle auf der Goldoberfläche und auf Magnesiumoxid-geträgerten Gold-Nanopartikeln

dissoziieren. Die zeitaufgelösten Messungen ließen eine durch Gold induzierte Störung der elektronischen Struktur der adsorbierten Methylbromid-Moleküle erkennen. Es wurde beobachtet, daß sich die Stärke dieser Störung mit der Größe der Goldpartikel änderte.

Schließlich wurde die Beobachtung, daß im Fall der kleinsten Goldcluster keine Photoprodukte der Methylhalogenide nachgewiesen wurden, durch dissoziative Adsorption erklärt, was mittels ergänzender Gasphasen-Experimente mit kleinen Gold Clustern bestätigt werden konnte.

Bibliography

[1] *Femtochemistry: Ultrafast Dynamics of the Chemical Bond* 20th Century Chemistry, ed. A.H. Zewail. Vol. 1 &2 (World Scientific, Singapore, 1994).

[2] *Femtosecond Chemistry*. ed. J. Manz and L. Wöste. Vol. 1 & 2. (VCH, Weinheim, 1995).

[3] M. Dantus and A. Zewail, Chem. Rev. **104**, 1717 (2004).

[4] *Femtochemistry and Femtobiology: Ultrafast Events in Molecular Science*. ed. M. Martin, M.M. Martin, and J.T. Hynes. (Elsevier, 2004).

[5] A. H. Zewail, J. Phys. Chem. A **104**, 5660 (2000).

[6] G. Ertl, Angew. Chem. Int. Ed. **47**, 3524 (2008).

[7] J. C. Polanyi, Acc. Chem. Res. **5**, 161 (1972).

[8] J. C. Polanyi, Angew. Chem. **99**, 981 (1987).

[9] Y. T. Lee, Angew. Chem. **99**, 967 (1987).

[10] D. R. Herschbach, Angew. Chem., 1251 (1987).

[11] R. D. Levine and R. B. Bernstein, *Molecular Reaction Dynamics*. (Oxford University Press, Oxford, 1988).

[12] J. C. Polanyi and A. H. Zewail, Acc. Chem. Res. **28**, 119 (1995).

[13] J. C. Polanyi and Y. Zeiri, *Dynamics of Adsorbate Photochemistry*, in *Laser Spectroscopy and Photochemistry on Metal Surfaces*, H.-L. Dai and W. Ho, Editors. 1995, World Scientific Publishing: Singapore. p. 1241.

[14] C. Frischkorn and M. Wolf, Chem. Rev. **106**, 4207 (2006).

[15] H.-L. Dai and W. Ho, eds. *Laser Spectroscopy and Photochemistry on Metal Surfaces*. Advanced Series in Physical Chemistry, ed. C.Y. Ng. 1995, World Scientific: Singapore.

[16] H. Petek and S. Ogawa, Annu. Rev. Phys. Chem. **53**, 507 (2002).

[17] W. Ho, Surf. Sci. **363**, 166 (1996).

[18] J. A. Misewich, A. Kalamarides, T. F. Heinz, U. Hofer, and M. M. T. Loy, J. Chem. Phys. **100**, 736 (1994).

[19] P. Szymanski, A. L. Harris, and N. Camillone, J. Phys. Chem. C **112**, 15802 (2008).

[20] M. Bonn, S. Funk, C. Hess, D. N. Denzler, C. Stampfl, M. Scheffler, M. Wolf, and G. Ertl, Science **285**, 1042 (1999).

[21] I. M. Lane, D. A. King, Z.-P. Liu, and H. Arnolds, Phys. Rev. Lett. **97**, 186105 (2006).

[22] J. A. Prybyla, H. W. K. Tom, and G. D. Aumiller, Phys. Rev. Lett. **68**, 503 (1992).

[23] M. Bauer, C. Lei, K. Read, R. Tobey, J. Gland, M. M. Murnane, and H. C. Kapteyn, Phys. Rev. Lett. **87**, 025501 (2001).

[24] A. Fohlisch, P. Feulner, F. Hennies, A. Fink, D. Menzel, D. Sanchez-Portal, P. M. Echenique, and W. Wurth, Nature **436**, 373 (2005).

[25] C. D. Lindstrom and X. Y. Zhu, Chem. Rev. **106**, 4281 (2006).

[26] C. Reuß, I. L. Shumay, U. Thomann, M. Kutschera, M. Weinelt, T. Fauster, and U. Höfer, Phys. Rev. Lett. **82**, 153 (1999).

[27] P. Szymanski, S. Garrett-Roe, and C. B. Harris, Prog. Surf. Sci. **78**, 1 (2005).

[28] C. Hu, S. Pei, Y.-L. Chen, and K. Liu, J. Phys. Chem. A **111**, 6813 (2007).

[29] G. Li and H. J. Hwang, J. Chem. Phys. **124**, 244306 (2006).

[30] R. de Nalda, J. Dura, A. Garcia-Vela, J. G. Izquierdo, J. Gonzalez-Vazquez, and L. Banares, J. Chem. Phys. **128**, 244309 (2008).

[31] R. de Nalda, J. G. Izquierdo, J. Dura, and L. Banares, J. Chem. Phys. **126**, 021101 (2007).

[32] L. R. Khundkar and A. H. Zewail, Chem. Phys. Lett. **142**, 426 (1987).

[33] J. L. Knee, L. R. Khundkar, and A. H. Zewail, J. Chem. Phys. **83**, 1996 (1985).

[34] D. Zhong, P. Y. Cheng, and A. H. Zewail, J. Chem. Phys. **105**, 7864 (1996).

[35] D. Zhong and A. H. Zewail, J. Phys. Chem. A **102**, 4031 (1998).

[36] K. J. Taylor, C. L. Pettiette-Hall, O. Cheshnovsky, and R. E. Smalley, J. Chem. Phys. **96**, 3319 (1992).

[37] A. B. Alekseyev, H.-P. Liebermann, and R. J. Buenker, J. Chem. Phys. **126**, 234103 (2007).

[38] A. B. Alekseyev, H.-P. Liebermann, R. J. Buenker, and S. N. Yurchenko, J. Chem. Phys. **126**, 234102 (2007).

[39] M. Tadjeddine, J. P. Flament, and C. Teichteil, Chem. Phys. **118**, 45 (1987).

[40] C. Escure, T. Leininger, and B. Lepetit, J. Chem. Phys. **130**, 244305 (2009).

[41] C. Escure, T. Leininger, and B. Lepetit, J. Chem. Phys. **130**, 244306 (2009).

[42] G. N. A. Van Veen, T. Baller, and A. E. De Vries, Chem. Phys. **92**, 59 (1985).

[43] W. P. Hess, D. W. Chandler, and J. W. Thoman Jr, Chem. Phys. **163**, 277 (1992).

[44] V. Blanchet, P. C. Samartzis, and A. M. Wodtke, J. Chem. Phys. **130**, 034304 (2009).

[45] M. L. Lipciuc and M. H. M. Janssen, J. Chem. Phys. **127**, 224310 (2007).

[46] T. Gougousi, P. C. Samartzis, and T. N. Kitsopoulos, J. Chem. Phys. **108**, 5742 (1998).

[47] J. G. Underwood and I. Powis, Phys. Chem. Chem. Phys. **1**, 747 (2000).

[48] K. A. Briggman, P. C. Stair, and E. Weitz, Chem. Phys. Lett. **334**, 1 (2001).

[49] D. H. Fairbrother, K. A. Briggman, P. C. Stair, and E. Weitz, J. Phys. Chem. **98**, 13042 (1994).

[50] D. H. Fairbrother, K. A. Briggman, P. C. Stair, and E. Weitz, J. Chem. Phys. **102**, 7267 (1995).

[51] D. H. Fairbrother, K. A. Trentelman, P. G. Strupp, P. C. Stair, and E. Weitz, J. Vac. Sci. Technol. A **10**, 2243 (1992).

[52] S. J. Garrett, D. V. Heyd, and J. C. Polanyi, J. Chem. Phys. **106**, 7834 (1997).

[53] J. Kutzner, G. Lindeke, K. H. Welge, and D. Feldmann, J. Chem. Phys. **90**, 548 (1989).

[54] K. A. Trentelman, D. H. Fairbrother, P. G. Strupp, P. C. Stair, and E. Weitz, J. Chem. Phys. **96**, 9221 (1992).

[55] K. A. Trentelman, H. Fairbrother, P. C. Stair, P. G. Strupp, and E. Weitz, J. Vac. Sci. Technol. A **9**, 1820 (1991).

[56] J.-Y. Fang and H. Guo, J. Chem. Phys. **101**, 5831 (1994).

[57] J. V. Setzler, Z. H. Huang, and H. Guo, J. Chem. Phys. **103**, 4300 (1995).

[58] H. Guo and G. C. Schatz, Chem. Phys. Lett. **184**, 245 (1991).

[59] M. X. Yang, S. K. Jo, A. Paul, L. Avila, B. E. Bent, and K. Nishikida, Surf. Sci. **325**, 102 (1995).

[60] H. Haberland, *Clusters of Atoms and Molecules: Theory, Experiment and Clusters of Atoms*. Springer Series of Chemical Physics ed. Vol. I. (Springer Verlag, Berlin, 1994).

[61] *The chemical physics of solid surfaces*. Atomic clusters: From gas phase to deposited, ed. D.P. Woodruff. Vol. 12. (Elsevier, Amsterdam, 2007).

[62] P. Fayet, F. Granzer, G. Hegenbart, E. Moisar, B. Pischel, and L. Wöste, Phys. Rev. Lett. **55**, 3002 (1985).

[63] R. L. Whetten, D. M. Cox, D. J. Trevor, and A. Kaldor, Phys. Rev. Lett. **54**, 1494 (1985).

[64] L. Holmgren, M. Andersson, and A. Rosén, Surf. Sci. **331-333**, 231 (1995).

[65] P. B. Armentrout, Annu. Rev. Phys. Chem. **52**, 423 (2003).

[66] T. M. Bernhardt, U. Heiz, and U. Landman, *Nanocatalysis* Nanoscience and Technology, ed. U. Heiz and U. Landman. (Springer Verlag, Berlin, 2007).

[67] W. A. de Heer, *Confinement and size effects in free metal clusters*. Metal clusters at surfaces: structure, quantum properties, physical chemistry ed. K.-H. Meiwes-Broer. (Springer Verlag, Berlin, 2000).

[68] T. Gleitsmann, *PhD Thesis: Untersuchung des Einflusses von Fehlstellen und monodispersen Silberclustern auf die elektronischen und optischen Eigenschaften ultradün-*

ner Oxidfilme mittels einer neuen Zweiphotonen Photoemissionapparatur. (Universität Ulm, Ulm, 2007).

[69] T. M. Bernhardt, Int. J. Mass Spectrom. **243**, 1 (2005).

[70] M. E. Vaida, *Master Thesis: Design and construction of a low energy ion guiding system for softl landing experiments with mass selected metal clusters.* (West University of Timisoara, Timisoara, 2004).

[71] V. S. Smentkowski and J. T. Yates, J. Vac. Sci. Technol. A **14**, 260 (1996).

[72] G. Ertl and J. Küppers, *Low energy electrons and suface chemistry*. 2nd ed. (WCH, Weinheim, 1985).

[73] M. P. Seah and W. A. Dench, Surf. Interf. Anal. **1**, 2 (1979).

[74] J. W. Niemantsverdriet, *Spectroscopy in catalysis: An introduction*. (VCH, Weinheim, 1995).

[75] P. Auger, J. Phys. Radium. **6**, 1382 (1925).

[76] J. J. Lander, Phys. Rew. **91**, 1382 (1953).

[77] M. Henzler, Appl. Surf. Sci. **11/12**, 450 (1982).

[78] A. Einstein, Ann. Phys. Leipzig **322**, 132 (1905).

[79] N. Gall, E. Rutkov, A. Tontegode, and M. Usufov, Tech. Phys. **44**, 1066 (1999).

[80] A. Hotzel, *PhD thesis: Femtosekunden Elektronendynamik der Adsorbat bedeckten Cu(111)-Oberfläche.* (FU Berlin, Berlin, 1999).

[81] L. Chan and G. L. Griffin, Surf. Sci. **145**, 185 (1984).

[82] M. Vollmer and F. Träger, Surf. Sci. **187**, 445 (1987).

[83] A. M. d. Jong and J. W. Niemantsverdriet, Surf. Sci. **233**, 355 (1990).

[84] R. Keller, F. Nöhmayer, P. Spädtke, and M.-H. Schönenberg, Vacuum **34**, 31 (1984).

[85] K. J. Boyd, A. Lapicki, M. Aizawa, and S. L. Anderson, Nucl. Instrum. Methods Phys. Res., Sect. B **157**, 144 (1999).

[86] K. J. Boyd, A. Lapicki, M. Aizawa, and S. L. Anderson, Rev. Sci. Instrum. **69**, 4106 (1998).

[87] B. Krämer, *Diploma Thesis: Der "Phasenraumkompressor": Eine neuartige Methode zur Erzeugung eines intensiven Strahls von Metallclusterionen*. (Freien Universität Berlin, Berlin, 1993).

[88] P. F. Moulton, Opt. News **8**, 9 (1982).

[89] P. F. Moulton, J. Opt. Soc. Am. B **3**, 125 (1986).

[90] P. Albers, E. Stark, and G. Huber, J. Opt. Soc. Am. B **3**, 134 (1986).

[91] *Tsunami, Operation Manual* (Spectra Physics, 1994).

[92] K. Onda, B. Li, and H. Petek, Phys. Rev. B **70**, 045415 (2004).

[93] B. Schröder, Optical and Quantum Electronics **15**, 57 (1983).

[94] C. Rulliére, *Femtosecond Laser Pulses-Principles and Experiments.* (Springer Verlag, Berlin- Heidelberg 1998).

[95] G. Stibenz, *Diploma Thesis: Konstruction eines Flugzeit-Massenspektrometers zur Untersuchung von laserinduzierten Desorptionsvorgängen an Oberflächen*. (FU Berlin, Berlin, 2002).

[96] W. C. Wiley and I. H. McLaren, Rev. Sci. Instrum. **26**, 1150 (1955).

[97] W. S. Felps, K. Rupnik, and S. P. McGlynn, J. Phys. Chem. **95**, 639 (1991).

[98] P. Avouris and R. E. Walkup, Annu. Rev. Phys. Chem. **40**, 173 (1989).

[99] J. W. Gadzuk, Annu. Rev. Phys. Chem. **39**, 395 (1988).

[100] P. Nordlander and J. C. Tully, Phys. Rev. Lett. **61**, 990 (1988).

[101] P. D. Johnson, A. J. Viescas, P. Nordlander, and J. C. Tully, Phys. Rev. Lett. **64**, 942 (1990).

[102] J. W. Hudgens, T. G. DiGiuseppe, and M. C. Lin, J. Chem. Phys. **79**, 571 (1983).

[103] X. L. Zhou, X. Y. Zhu, and J. M. White, Surface Science Reports **13**, 73 (1991).

[104] Y. H. Cheng, H. Kupfer, F. Richter, and A. M. Paraian, Applied Surface Science **200**, 117 (2002).

[105] J. D. E. McIntyre, *Advances in electrochemistry and electrochemical engineering*. ed. C.W. Tobias. Vol. 9. (Wiley, New York, 1973).

[106] X. Y. Zhu, J. M. White, M. Wolf, E. Hasselbrink, and G. Ertl, Chem. Phys. Lett. **176**, 459 (1991).

[107] *Handbook of optical constants of solids*. (Academic Press, Boston, 1991).

[108] J. D. E. McIntyre and D. E. Aspnes, Surface Science **24**, 417 (1971).

[109] W. N. Hansen, J. Opt. Soc. Am. **58**, 380 (1968).

[110] Z. C. Ying and W. Ho, J. Chem. Phys. **93**, 9077 (1990).

[111] S. A. Buntin, L. J. Richter, D. S. King, and R. R. Cavanagh, J. Chem. Phys. **91**, 6429 (1989).

[112] J. A. Prybyla, T. F. Heinz, J. A. Misewich, M. M. T. Loy, and J. H. Glownia, Phys. Rev. Lett. **64**, 1537 (1990).

[113] P. M. Johnson and C. E. Otis, Annu. Rev. Phys. Chem. **32**, 139 (1981).

[114] R. O. Loo, H. P. Haerri, G. E. Hall, and P. L. Houston, J. Chem. Phys. **90**, 4222 (1989).

[115] M. H. M. Janssen, D. H. Parker, G. O. Sitz, S. Stolte, and D. W. Chandler, J. Phys. Chem. **95**, 8007 (1991).

[116] W. K. Bischel, P. J. Kelly, and C. K. Rhodes, Phys. Rev. A **13**, 1817 (1976).

[117] R. P. Saxon and J. Eichler, Phys. Rev. A **34**, 199 (1986).

[118] M. P. J. van der Loo and G. C. Groenenboom, J. Chem. Phys. **123**, 074310 (2005).

[119] W. M. McClain, J. Chem. Phys. **55**, 2789 (1971).

[120] R. G. Bray and R. M. Hochstrasser, Molec. Phys. **31**, 1199 (1976).

[121] K.-m. Chen and E. S. Yeung, J. Chem. Phys. **69**, 43 (1978).

[122] D. H. Parker, R. Pandolfi, P. R. Stannard, and M. A. El-Sayed, Chem. Phys. **45**, 27 (1980).

[123] R. D. Jones and P. R. Callis, Chem. Phys. Lett. **144**, 158 (1988).

[124] D. M. Sammeth, S. S. Siewert, L. H. Spangler, and P. R. Callis, Chem. Phys. Lett. **193**, 532 (1992).

[125] C. A. Taatjes, J. W. G. Mastenbroek, G. van den Hoek, J. G. Snijders, and S. Stolte, J. Chem. Phys. **98**, 4355 (1993).

[126] G. O. Sitz, A. C. Kummel, and R. N. Zare, J. Vac. Sci. Technol. A **5**, 513 (1987).

[127] D. C. Jacobs, K. W. Kolasinski, R. J. Madix, and R. N. Zare, J. Chem. Phys. **87**, 5038 (1987).

[128] I. Powis and J. F. Black, J. Phys. Chem. **93**, 2461 (2002).

[129] A. T. J. B. Eppink and D. H. Parker, J. Chem. Phys. **110**, 832 (1999).

[130] J. Durá, R. d. Nalda, J. Álvarez, J. G. Izquierdo, G. A. Amaral, and L. Bañares, ChemPhysChem **9**, 1245 (2008).

[131] D. H. Fairbrother, K. A. Trentelman, P. G. Strupp, P. C. Stair, and E. Weitz, J. Vac. Sci. Technol. A **10**, 2243 (1992).

[132] K. A. Trentelman, D. H. Fairbrother, P. G. Strupp, P. C. Stair, and E. Weitz, J. Chem. Phys. **96**, 9221 (1992).

[133] M. E. Vaida, T. M. Bernhardt, C. Barth, F. Esch, U. Heiz, and U. Landman, Phys. Status Solidi B, In press (2010).

[134] J. Cao, Y. Gao, H. E. Elsayed-Ali, R. J. D. Miller, and D. A. Mantell, Phys. Rev. B **58**, 10948 (1998).

[135] T. Gleitsmann, M. E. Vaida, T. M. Bernhardt, V. Bonačić-Koutecký, C. Bürgel, A. E. Kuznetsov, and R. Mitrić, Eur. Phys. J. D **45**, 477 (2007).

[136] M. E. Vaida, T. Gleitsmann, R. Tchitnga, and T. M. Bernhardt, J. Phys. Chem. C **113**, 10264 (2009).

[137] O'Conner, *Time-correlated single photon counting*. 1970).

[138] S. Berge, P. O. Gartland, and B. J. Slagsvold, Surf. Sci. **43**, 275 (1974).

[139] S. Schintke and W.-D. Schneider, J. Phys.: Condens. Matter **16**, R49 (2004).

[140] H.-J. Freund and D. W. Goodman, *Ultrathin Oxide Films. In Handbook of Heterogeneous Catalysis*. ed. G. Ertl, E. Knözinger, and F. Schüth. Vol. 3. (Wiley-VCH, Weinheim, 2008).

[141] S. S. P. Parkin, C. Kaiser, A. Panchula, P. M. Rice, B. Hughes, M. Samant, and S.-H. Yang, Nat Mater **3**, 862 (2004).

[142] V. E. Henrich and P. A. Cox, *The Surface Science of Metal Oxides*. (Cambridge University Press, Cambridge, 1996).

[143] U. Heiz and U. Landman, *Nanocatalysis*. (Springer-Verlag, Berlin, 2007).

[144] S. C. Street, C. Xu, and D. W. Goodman, Annu. Rev. Phys. Chem. **48**, 43 (1997).

[145] U. Heiz and W.-D. Schneider, J. Phys. D **33**, R85 (2000).

[146] M.-C. Wu, J. S. Corneille, C. A. Estrada, J.-W. He, and D. Wayne Goodman, Chem. Phys. Lett. **182**, 472 (1991).

[147] M.-C. Wu, J. S. Corneille, J.-W. He, C. A. Estrada, and D. W. Goodman, J. Vac. Sci. Technol. A **10**, 1467 (1992).

[148] U. Heiz, F. Vanolli, L. Trento, and W. D. Schneider, Rev. Sci. Instrum. **68**, 1986 (1997).

[149] M. Sterrer, E. Fischbach, M. Heyde, N. Nilius, H.-P. Rust, T. Risse, and H.-J. Freund, J. Phys. Chem. B **110**, 8665 (2006).

[150] V. M. Bermudez and V. H. Ritz, Surf. Sci. **82**, L601 (1979).

[151] H. Namba, J. Darville, and J. M. Gilles, Surf. Sci. **108**, 446 (1981).

[152] V. E. Henrich, G. Dresselhaus, and H. J. Zeiger, Phys. Rew. B **22**, 4764 (1980).

[153] D. M. Roessler and W. C. Walker, Phys. Rew. **159**, 733 (1967).

[154] S. Benedetti, H. M. Benia, N. Nilius, S. Valeri, and H. J. Freund, Chem. Phys. Lett. **430**, 330 (2006).

[155] S. Benedetti, P. Torelli, S. Valeri, H. M. Benia, N. Nilius, and G. Renaud, Phys. Rev. B **78**, 195411 (2008).

[156] M. C. Gallagher, M. S. Fyfield, L. A. Bumm, J. P. Cowin, and S. A. Joyce, Thin Solid Films **445**, 90 (2003).

[157] M. Dynna, J. L. Vassent, A. Marty, and B. Gilles, J. Appl. Phys. **80**, 2650 (1996).

[158] J. Wollschläger, D. Erdös, and K. M. Schröder, Surf. Sci. **402-404**, 272 (1998).

[159] J. Wollschläger, D. Erdös, H. Goldbach, R. Höpken, and K. M. Schröder, Thin Solid Films **400**, 1 (2001).

[160] Z. Yan, S. Chinta, A. A. Mohamed, J. P. Fackler, and D. W. Goodman, J. Am. Chem. Soc. **127**, 1604 (2005).

[161] L. Giordano, F. Cinquini, and G. Pacchioni, Phys. Rev. B **73**, 045414 (2006).

[162] G. Pacchioni, L. Giordano, and M. Baistrocchi, Phys. Rev. Lett. **94**, 226104 (2005).

[163] A. Mönnich, J. Lange, M. Bauer, M. Aeschlimann, I. A. Nechaev, V. P. Zhukov, P. M. Echenique, and E. V. Chulkov, Phys. Rev. B **74**, 035102 (2006).

[164] D. Ochs, W. Maus-Friedrichs, M. Brause, J. Günster, V. Kempter, V. Puchin, A. Shluger, and L. Kantorovich, Surf. Sci. **365**, 557 (1996).

[165] H.-J. Freund and G. Pacchioni, Chem. Soc. Rev. **37**, 2224 (2008).

[166] H. M. Benia, N. Nilius, and H. J. Freund, Surf. Sci. **601**, L55 (2007).

[167] T. Gleitsmann, M. E. Vaida, T. M. Bernhardt, V. Bonačić-Koutecký, C. Bürgel, A. E. Kuznetsov, and R. Mitrić, Eur. Phys. J. D **45**, 477 (2007).

[168] P. K. d. Boer and R. A. d. Groot, J. Phys.: Condens. Matter **10**, 10241 (1998).

[169] S. Schintke, S. Messerli, M. Pivetta, F. Patthey, L. Libioulle, M. Stengel, A. De Vita, and W.-D. Schneider, Phys. Rev. Lett. **87**, 276801 (2001).

[170] L. Plucinski, Y. Zhao, B. Sinkovic, and E. Vescovo, Phys. Rev. B **75**, 214411 (2007).

[171] S. Valeri, S. Altieri, A. di Bona, P. Luches, C. Giovanardi, and T. S. Moia, Surf. Sci. **507-510**, 311 (2002).

[172] C. Barth and C. R. Henry, J. Phys. Chem. C **113**, 247 (2009).

[173] C. Zhang, B. Yoon, and U. Landman, Journal of the American Chemical Society **129**, 2228 (2007).

[174] R. Mamy, Surf. Sci. **322**, 337 (1995).

[175] G. V. Hansson and S. A. Flodström, Phys. Rev. B **18**, 1572 (1978).

[176] M. Sagurton, M. Strongin, F. Jona, and J. Colbert, Phys. Rev. B **28**, 4075 (1983).

[177] M. Strongin, M. El-Batanouny, and M. A. Pick, Phys. Rev. B **22**, 3126 (1980).

[178] B. E. Koel, R. J. Smith, and P. J. Berlowitz, Surf. Sci. **231**, 325 (1990).

[179] C. Park, E. Bauer, and H. Poppa, Surf. Sci. **154**, 371 (1985).

[180] P. J. Berlowitz and D. W. Goodman, Langmuir **4**, 1091 (1988).

[181] F. Soria and H. Poppa, J. Vac. Sci. Technol. **17**, 449 (1980).

[182] G. A. Attard and D. A. King, Surf. Sci. **222**, 360 (1989).

[183] A. Pavlovska, M. Paunov, and E. Bauer, Thin Solid Films **126**, 129 (1985).

[184] D. Wu, W. K. Lau, Z. Q. He, Y. J. Feng, M. S. Altman, and C. T. Chan, Phys. Rev. B **62**, 8366 (2000).

[185] K. L. Man, Y. J. Feng, and M. S. Altman, Physical Review B (Condensed Matter and Materials Physics) **74**, 085420 (2006).

[186] J. R. Cerdá, F. Soria, F. J. Palomares, and P. L. de Andres, Surf. Sci. **269-270**, 713 (1992).

[187] K. L. Man, Y. J. Feng, and M. S. Altman, Phys. Rev. B **74**, 085420 (2006).

[188] K. L. Man, Y. J. Feng, C. T. Chan, and M. S. Altman, Surf. Sci. **601**, L95 (2007).

[189] Z. Q. Wang, Y. S. Li, C. K. C. Lok, J. Quinn, F. Jona, and P. M. Marcus, Solid State Communications **62**, 181 (1987).

[190] S. H. Lu, Z. Q. Wang, S. C. Wu, C. K. C. Lok, J. Quinn, Y. S. Li, D. Tian, F. Jona, and P. M. Marcus, Phys. Rev. B **37**, 4296 (1988).

[191] D. Tian, R. F. Lin, F. Jona, and P. M. Marcus, Solid State Communications **74**, 1017 (1990).

[192] T. K. Yamada, A. L. Vázquez de Parga, M. M. J. Bischoff, T. Mizoguchi, and H. van Kempen, Surf. Sci. **600**, 1048 (2006).

[193] C. Kittel, *Introduction to Solid State Physics*. (Wiley, New York, 1976).

[194] H. M. Benia, X. Lin, H. J. Gao, N. Nilius, and H. J. Freund, J. Phys. Chem. C **111**, 10528 (2007).

[195] S. Abbet, K. Judai, L. Klinger, and U. Heiz, Pure Appl. Chem. **74**, 1527 (2002).

[196] M. Sterrer, M. Yulikov, E. Fischbach, M. Heyde, H.-P. Rust, G. Pacchioni, T. Risse, and H.-J. Freund, Angew. Chem. **45**, 2630 (2006).

[197] M. Sterrer, E. Fischbach, T. Risse, and H.-J. Freund, Phys. Rev. Lett. **94**, 186101 (2005).

[198] P. Frondelius, H. Hakkinen, and K. Honkala, New J. Phys. **9**, 339 (2007).

[199] T. Kizuka and N. Tanaka, Phys. Rev. B **56**, R10079 (1997).

[200] O. Meerson, G. Sitja, and C. R. Henry, Eur. Phys. J. D **34**, 119 (2005).

[201] M. Sterrer, T. Risse, M. Heyde, H.-P. Rust, and H.-J. Freund, Phys. Rev. Lett. **98**, 206103 (2007).

[202] A. Sanchez, S. Abbet, U. Heiz, W. D. Schneider, H. Hakkinen, R. N. Barnett, and U. Landman, J. Phys. Chem. A **103**, 9573 (1999).

[203] B. Yoon, H. Hakkinen, U. Landman, A. S. Worz, J.-M. Antonietti, S. Abbet, K. Judai, and U. Heiz, Science **307**, 403 (2005).

[204] H. Häkkinen, S. Abbet, A. Sanchez, U. Heiz, and U. Landman, Angew. Chem. **42**, 1297 (2003).

[205] K. Honkala and H. Hakkinen, J. Phys. Chem. C **111**, 4319 (2007).

[206] C. Harding, V. Habibpour, S. Kunz, A. N.-S. Farnbacher, U. Heiz, B. Yoon, and U. Landman, J. Am. Chem. Soc. **131**, 538 (2009).

[207] P. Stracke, S. Krischok, and V. Kempter, Surf. Sci. **473**, 86 (2001).

[208] S. Krischok, P. Stracke, and V. Kempter, Appl. Phys. A **82**, 167 (2006).

[209] P. Schwerdtfeger and G. A. Bowmaker, J. Chem. Phys. **100**, 4487 (1994).

[210] M. Yulikov, M. Sterrer, T. Risse, and H. J. Freund, Surf. Sci. **603**, 1622 (2009).

[211] V. P. Holbert, S. J. Garrett, J. C. Bruns, P. C. Stair, and E. Weitz, Surf. Sci. **314**, 107 (1994).

[212] P. H. Lu, P. J. Lasky, Q. Y. Yang, and R. M. Osgood, Chem. Phys. **205**, 143 (1996).

[213] R. S. Mulliken, J. Chem. Phys. **8**, 382 (1940).

[214] J.-Y. Fang and H. Guo, Chem. Phys. Lett. **235**, 341 (1995).

[215] K. Q. Lao, M. D. Person, P. Xayariboun, and L. J. Butler, J. Chem. Phys. **92**, 823 (1990).

[216] R. Schinke, *Photodissociation Dynamics*. (Cambridge University Press, Cambridge, 1995).

[217] D. P. Zhong, P. Y. Cheng, and A. H. Zewail, J. Chem. Phys. **105**, 7864 (1996).

[218] D. Zhong, T. M. Bernhardt, and A. H. Zewail, J. Phys. Chem. A **103**, 10093 (1999).

[219] G. A. Capelle and H. P. Broida, J. Chem. Phys. **58**, 4212 (1973).

[220] E. D. Potter, Q. Liu, and A. H. Zewail, Chem. Phys. Lett. **200**, 605 (1992).

[221] M. A. Henderson, G. E. Mitchell, and J. M. White, Surf. Sci. **184**, L325 (1987).

[222] M. X. Yang, S. K. Jo, A. Paul, L. Avila, B. E. Bent, and K. Nishikida, Suf. Sci. **325**, 102 (1995).

[223] H. Grönbeck, J. Phys. Chem. B **110**, 11977 (2006).

[224] P. Frondelius, A. Hellman, K. Honkala, H. Häkkinen, and H. Grönbeck, Phys. Rev. B **78**, 085426 (2008).

[225] A. Kolmakov, J. Stultz, and D. W. Goodman, J. Chem. Phys. **113**, 7564 (2000).

[226] C. Tegenkamp, H. Pfnur, W. Ernst, U. Malaske, J. Wollschlager, D. Peterka, K. M. Schroder, V. Zielasek, and M. Henzler, J. Phys.: Condens. Matter **11**, 9943 (1999).

[227] J. Kramer, W. Ernst, C. Tegenkamp, and H. Pfnür, Surf. Sci. **517**, 87 (2002).

[228] M.-C. Wu, C. M. Truong, and D. W. Goodman, Phys. Rev. B **46**, 12688 (1992).

[229] D. Peterka, C. Tegenkamp, K. M. Schröder, W. Ernst, and H. Pfnür, Surf. Sci. **431**, 146 (1999).

[230] Y. Chen, H. T. Tohver, J. Narayan, and M. M. Abraham, Phys. Rev. B **16**, 5535 (1977).

[231] J. L. Boldu, M. M. Abraham, and Y. Chen, Phys. Rev. B **19**, 4421 (1979).

[232] E. Giamello, A. Ferrero, S. Coluccia, and A. Zecchina, J. Phys. Chem. **95**, 9385 (2002).

[233] C. Di Valentin, A. Del Vitto, G. Pacchioni, S. Abbet, A. S. Worz, K. Judai, and U. Heiz, J. Phys. Chem. B **106**, 11961 (2002).

[234] C. Di Valentin, G. Pacchioni, S. Abbet, and U. Heiz, J. Phys. Chem. B **106**, 7666 (2002).

[235] M. Sterrer, M. Heyde, M. Novicki, N. Nilius, T. Risse, H.-P. Rust, G. Pacchioni, and H.-J. Freund, J. Phys. Chem. B **110**, 46 (2005).

[236] L. Giordano, U. Martinez, G. Pacchioni, M. Watkins, and A. L. Shluger, J. Phys. Chem. C **112**, 3857 (2008).

[237] D. Ricci, G. Pacchioni, P. V. Sushko, and A. L. Shluger, Surf. Sci. **542**, 293 (2003).

[238] M. E. Vaida, P. E. Hindelang, and T. M. Bernhardt, J. Chem. Phys. **129**, 011105 (2008).

[239] G. Pacchioni and P. Pescarmona, Surf. Sci. **412-413**, 657 (1998).

[240] A. M. Paul and B. E. Bent, J. Catal. **147**, 264 (1994).

[241] S. J. Garrett, D. V. Heyd, and J. C. Polanyi, J. Chem. Phys. **106**, 7847 (1997).

[242] A. Berko, W. Erley, and D. Sander, J. Chem. Phys. **93**, 8300 (1990).

[243] P. J. Lasky, P. H. Lu, M. X. Yang, R. M. Osgood, B. E. Bent, and P. A. Stevens, Surf. Sci. **336**, 140 (1995).

[244] A. Neumann, K. Christmann, and T. Solomun, Surf. Sci. **287-288**, 593 (1993).

[245] X. L. Zhou, F. Solymosi, P. M. Blass, K. C. Cannon, and J. M. White, Surf. Sci. **219**, 294 (1989).

[246] F. Solymosi, I. Kovács, and K. Révész, Catal. Lett. **27**, 53 (1994).

[247] F. Solymosi and K. Révész, Surf. Sci. **280**, 38 (1993).

[248] S. K. Jo, X. Y. Zhu, D. Lennon, and J. M. White, Surf. Sci. **241**, 231 (1991).

[249] S. K. Jo and J. M. White, J. Phys. Chem. **94**, 6852 (2002).

[250] E. T. Jensen, Surf. Sci. **528**, 204 (2003).

[251] J. Küppers, F. Nitschké, K. Wandelt, and G. Ertl, Surf. Sci. **87**, 295 (1979).

[252] S. A. Costello, B. Roop, Z. M. Liu, and J. M. White, J. Phys. Chem. **92**, 1019 (2002).

[253] Z. M. Liu, S. Akhter, B. Roop, and J. M. White, J. Am. Chem. Soc. **110**, 8708 (1988).

[254] Z. M. Liu, S. A. Costello, B. Roop, S. R. Coon, S. Akhter, and J. M. White, J. Phys. Chem. **93**, 7681 (2002).

[255] B. Roop, K. G. Lloyd, S. A. Costello, A. Campion, and J. M. White, J. Chem. Phys. **91**, 5103 (1989).

[256] V. A. Ukraintsev, T. J. Long, T. Gowl, and I. Harrison, J. Chem. Phys. **96**, 9114 (1992).

[257] V. A. Ukraintsev, T. J. Long, and I. Harrison, J. Chem. Phys. **96**, 3957 (1992).

[258] K. Domen and T. J. Chuang, J. Chem. Phys. **90**, 3332 (1989).

[259] X. L. Zhou and J. M. White, Surf. Sci. **241**, 270 (1991).

[260] X.-L. Zhou and J. M. White, *Laser spectroscopy and photochemistry on metal surfaces*. ed. H.-L. Dai and W. Ho. Vol. 5. (World Scientific, Singapore, 1995).

[261] R. Osgood, Chem. Rev. **106**, 4379 (2006).

[262] D. Popolan, *PhD Thesis: Size and composition dependent reaction kinetics and femtosecond photodissociation dynamics of noble metal cluster complexes*. (University of Ulm, Ulm, 2010).

[263] D. V. Heyd, *PhD Thesis: Photodissociation of methyl brornide adsorbed on LiF(001), NaCl(001), and MgO(001).* (University of Toronto, Toronto, 1997).

[264] L. T. Molina, M. J. Molina, and F. S. Rowland, J. Phys. Chem. **86**, 2672 (2002).

[265] W. B. DeMore, S. P. Sander, D. M. Golden, R. F. Hampson, M. J. Kurylo, C. J. Howard, A. R. Ravishankara, C. E. Kolb, and M. J. Molina, *Chemical kinetics and photo-*

chemical data for use in stratospheric modeling, Evaluation No. 11. (JPL Publication 94-26, Jet Propulsion Laboratory, Pasadena, CA, 1994).

[266] S. P. Sander, R. R. Friedl, A. R. Ravishankara, D. M. Golden, C. E. Kolb, M. J. Kurylo, M. J. Molina, G. K. Moortgat, H. Keller-Rudek, B. J.Finlayson-Pitts, P. H. Wine, R. E. Huie, and V. L. Orkin, *Chemical Kinetics and Photochemical Data for Use in Atmospheric Studies, Evaluation No. 15*. (JPL Publication 06-2, Jet Propulsion Laboratory, Pasadena, CA, 2006).

[267] R. S. Mulliken, Phys. Rev. **61**, 277 (1942).

[268] R. S. Mulliken and E. Teller, Phys. Rev. **61**, 283 (1942).

[269] S. Yabushita and K. Morokuma, Chem. Phys. Lett. **153**, 517 (1988).

[270] Y. Amatatsu, S. Yabushita, and K. Morokuma, J. Chem. Phys. **104**, 9783 (1996).

[271] D. Xie, H. Guo, Y. Amatatsu, and R. Kosloff, J. Phys. Chem. A **104**, 1009 (2000).

[272] D. Ajitha, M. Wierzbowska, R. Lindh, and P. A. Malmqvist, J. Chem. Phys. **121**, 5761 (2004).

[273] A. Gedanken and M. D. Rowe, Chem. Phys. Lett. **34**, 39 (1975).

[274] E. B. D. Bourdon, J. P. Cowin, I. Harrison, J. C. Polanyi, J. Segner, C. D. Stanners, and P. A. Young, J. Phys. Chem. **88**, 6100 (2002).

[275] N. Camillone Iii, K. A. Khan, P. J. Lasky, L. Wu, J. E. Moryl, and J. R. M. Osgood, J. Chem. Phys. **109**, 8045 (1998).

[276] X.-L. Zhou and J. M. White, Surf. Sci. **194**, 438 (1988).

[277] X. L. Zhou, C. Yoon, and J. M. White, Surf. Sci. **206**, 379 (1988).

[278] R. K. Sander and K. R. Wilson, J. Chem. Phys. **63**, 4242 (1975).

[279] M. Dzvonik, S. Yang, and R. Bersohn, J. Chem. Phys. **61**, 4408 (1974).

[280] M. Henzler and W. Göpel, *Oberflächenphysik des Festkörpers*. (B. G. Teubner, Stuttgart, 1991).

[281] J. Kim, J. A. Kelley, P. Ayotte, S. B. Nielsen, G. H. Weddle, and M. A. Johnson, J. Am. Soc. Mass Spectrom. **10**, 810 (1999).

[282] T. Livneh and M. Asscher, Langmuir **14**, 1348 (1998).

[283] M. E. Vaida and T. M. Bernhardt, Eur. Phys. J. D **52**, 119 (2009).

[284] N. F. Scherer, C. Sipes, R. B. Bernstein, and A. H. Zewail, J. Chem. Phys. **92**, 5239 (1990).

[285] V. J. Barclay, W.-H. Hung, J. C. Polanyi, G. Zhang, and Y. Zeiri, Faraday Discuss **96**, 129 (1993).

[286] M. Collard, P. Kerwin, and A. Hodgson, Chem. Phys. Lett. **179**, 422 (1991).

[287] E. de Beer, M. P. Koopmans, C. A. de Lange, Y. Wang, and W. A. Chupka, J. Chem. Phys. **94**, 7634 (1991).

[288] M. E. Greenslade, M. I. Lester, D. C. Radenovic, A. J. A. van Roij, and D. H. Parker, J. Chem. Phys. **123**, 074309 (2005).

[289] J. V. Setzler, J. Bechtel, H. Guo, and G. C. Schatz, J. Chem. Phys. **107**, 9176 (1997).

[290] J. V. Setzler, H. Guo, and G. C. Schatz, J. Phys. Chem. B **101**, 5352 (1997).

Curriculum Vitae

PERSONAL DATA

NAME:	Mihai-Emilian Vaida
BIRTH DATE / PLACE:	22 Jul 1979 / Deva, Romania
MARITAL STATUS:	Single
NATIONALITY:	Romanian

EDUCATION:

1986-1990	Elementary School “Sc. Generala Nr. 1” , Deva, Romania
1990-1994	Elementary School “Liceul Sabin Dragoi” , Deva, Romania
1994-1998	High School “Grup Scolar Industrial Energetic ”, Deva Romania
1998	Graduation: high school graduation “Diploma de Bacalaureat”

ACADEMIC STUDIES:

10.1998-06.2002	Studies of physics at the Faculty of Physics, West University of Timisoara, Romania
06.2002	Graduation: Diploma in Physics “Diploma de Licenta”
10.2002-06.2004	Master degree at the Faculty of Physics, West University of Timisoara, Romania and in the Physics Department, Free University of Berlin
06.2004	Graduation at West University of Timisoara, Romania: Master of Science “Diploma de Studii Aprofundate”
10.2004-04.2006	PhD studies in the group of Prof. Dr. L. Wöste Physics Department, Free University of Berlin
04.2006	PhD studies in the group of Prof. Dr. T. M. Bernhardt, Institute of Surface Chemistry and Catalysis, University of Ulm

FURTHER WORK, RESEARCH AND TEACHING EXPERIENCE:

1999-2000	Technician in the X-Ray Laboratory, West University of Timisoara, Romania

10.2001-05.2002	Preparation of the Diploma Thesis at Condensed Matter Research Institute of Timisoara, Romania
03.2003 –08.2004	Tutor; Preparation of physical experiments for students at Faculty of Medicine, Free University of Berlin
10.2007-2009	Supervising tutor for physical-chemistry laboratory experiments "Praktikumsbetreuer" at University of Ulm

SCHOLARSHIPS:

10.2002-08.2003	Erasmus-Socrates scholarship at Freie Universität Berlin
10.2003-10.2004	European Mobility Scheme for Physics Students (EMSPS) scholarship at Free University of Berlin
10.2004-05.2007	DAAD scholarship at Free University of Berlin and University of Ulm

List of publications

T. M. Bernhardt, J. Hagen, L D. Socaciu, R. Mitrić, Andreas Heidenreich, J. Le Roux, D. Popolan, M. Vaida, L.Wöste, V. Bonačić-Koutecký, and Joshua Jortner, *Femtosecond Time-Resolved Geometry Relaxation and Ultrafast Intramolecular Energy Redistribution in Ag_2Au,* ChemPhysChem, **6**, 243 (2005)

L. D. Socaciu-Siebert, J. Hagen, J. Le Roux, D. Popolan, M. Vaida, Š. Vajda, T. M. Bernhardt and L. Wöste, Ultrafast nuclear dynamics induced by photodetachment of Ag_2^- and $Ag_2O_2^-$: oxygen desorption from a molecular silver surface, Phys . Chem. Chem. Phys . **7**, 2706 (2005)

T. Gleitsmann, M. E. Vaida, T.M. Bernhardt, V. Bonačić-Koutecký, C. Bürgel, A.E. Kuznetsov, and R. Mitrić, *Mass-selected Ag_3 clusters soft-landed onto MgO/Mo(100): femtosecond photoemission and first-principles simulation,* Eur. Phys. J. D **45**, 477 (2007)

M. E. Vaida, P. E. Hindelang, and T. M. Bernhardt, *Femtosecond real-time probing of transition state dynamics in a surface photoreaction: Methyl desorption from CH_3I on MgO(100),* J. Chem. Phys. **129**, 011105 (2008)

M. E. Vaida and T. M. Bernhardt, *Adsorption and photodissociation dynamics of methyl iodide on magnesia supported gold nanoparticles*, Eur. Phys. J. D **52**, 119 (2009)

M. E. Vaida, T. Gleitsmann, R. Tchitnga, and T. M. Bernhardt, *Femtosecond-laser photoemission spectroscopy of Mo(100) covered by ultrathin MgO(100) films of variable thickness, J. Phys. Chem. C*, **113***,* 10264 (2009*)*

M.E. Vaida and T.M. Bernhardt, *Surface-aligned femtochemistry: Real-time dynamics of photoinduced I_2 formation from CD_3I on MgO(100)*, Chem. Phys. Chem. **11**, 804 (2010)

M. E. Vaida and T. M. Bernhardt, *Femtosecond photoemission and photodesorption from magnesia supported gold clusters*, Phys. Status Solidi B **247**, 1139 (2010).

M. E. Vaida, T. M. Bernhardt, C. Barth, F. Esch, U. Heiz, and U. Landman, *Ultrathin magnesia films as support for molecules and metal clusters: Tuning reactivity by thickness and composition,* Phys. Status Solidi B **247**, 1001 (2010), – ***Feature article***.

M. E. Vaida and T. M. Bernhardt, *Surface pump-probe femtosecond-laser mass spectrometry: Time-, mass-, and velocity-resolved detection of surface reaction dynamics,* Rev. Sci. Instrum., Submitted (2010).

Publications in preparation

M. E. Vaida, T. M. Bernhardt, *Photodissociation dynamics of methyl bromide adsorbed on an MgO(100) ultrathin films of variable thickness on Mo(100).*

M. E. Vaida, T. M. Bernhardt, *Size dependent femtosecond photodissociation dynamics of methyl bromide on magnesia supported gold clusters.*

M. E. Vaida, T. M. Bernhardt, *Femtosecond two-photon photoemission spectroscopy of methyl iodide adsorbed on Au(100).*

M. E. Vaida, T. Gleitsmann, D. Popolan, S. Lang, G. Stibenz, B. Stegemann, L. Wöste, T.M. Bernhardt, *Novel apparatus for femtosecond reaction dynamics studies on mass-selected free and deposited metal clusters.*

M. E. Vaida, T. M. Bernhardt, *Methyl iodide and methyl bromide adsorption and photodissociation dynamics on gold films grown on molybdenum single crystal.*

Conferance Contributions

2005

DPG – Frühjahrstagung, Berlin, Germany (March 2005):
M. Vaida, T. Gleitsmann, B. Stegemann, T. M. Bernhardt and L. Wöste, *Two-photon-photoemission spectroscopy of suported silver clusters*

International Workshop on Ultrafast Time-Resolved Soft X-Ray Science, Berlin-Zeuthen, Germany (April 2005):
M. E. Vaida, T. Gleitsmann, B. Stegemann, T. M. Bernhardt and L. Wöste, *Two-photon-photoemission spectroscopy of silver oxide layers grown on an insulating MgO thin film on Mo(100).*

International Workshop on Ultrafast Time-Resolved Soft X-Ray Science, Berlin-Zeuthen, Germany (April 2005):
D. M. Popolan, S. M. Lang, J. Hagen, L. D. Socaciu-Siebert, M. E. Vaida, B. Schmidt, T. M. Bernhardt, and L. Wöste, *Structural Dynamics and Reaction Kinetics of Small Bimetallic Silver-Gold Clusters*

ECOS 23 - European Conference on Surface Science, Berlin, Germany (September 2005):
T. Gleitsmann, M. E. Vaida, B. Stegemann, T. M. Bernhardt and L. Wöste, *Excited electronic state structure of thermally annealed silver oxide layers on MgO investigated by Two-Photon-Photoemission Spectroscopy.*

ECOS 23 - European Conference on Surface Science, Berlin, Germany (September 2005):
T. M. Bernhardt, T. Gleitsmann, M. E. Vaida, B. Stegemann, and L. Wöste, *Structural and optical properties of thin film nano-materials built from mono-disperse metal clusters.*

2006

DPG – Frühjahrstagung, Frankfurt am Main, Germany (March 2006):
Mihai Vaida, Tobias Gleitsman, Ludger Wöste and Thorsten M. Bernhardt, *Laser induced desorption of organometallic molecules from metallic and insulating surfaces monitored via time-of-flight mass spectrometry.*

ISSPIC XIII – International Symposium on Small Particles and Inorganic Clusters, Göteborg, Sweden (July 2006):
M. E. Vaida, T. Gleitsmann and T. M. Bernhardt, *Laser induced desorption of organometallic molecules from solid state surfaces monitored via time-of-flight mass spectrometry*

ISSPIC XIII – International Symposium on Small Particles and Inorganic Clusters, Göteborg, Sweden (July 2006):
T. Gleitsmann, M. E. Vaida and T. M. Bernhardt, *The role of annealing to the structure of ultrathin Magnisia films for cluster deposition.*

2007

Trends in Nanoscience, Irsee, Germany (February 2007):
T. Gleitsmann, M. E. Vaida, R. Tchitnga and T. M. Bernhardt, *Electronic properties of silver nanoclusters on oxides supports: Fluorescence microscopy and femtosecond two-photon photoemission spectroscopy.*

S^3C – Symposium on Size Selected Clusters, Brand, Austria (March 2007):
M. E. Vaida, T. Gleitsmann and T. M. Bernhardt, *Temperature dependent femtosecond two-photon photoemission from ultra-thin MgO films.*

S^3C – Symposium on Size Selected Clusters, Brand, Austria (March 2007):
D. M. Popolan, M. Vaida, and T. M. Bernhardt, *The Effect of Gold Doping on the Reactivity of Free Silver Clusters: Comparison of Ag_3^+ and Ag_2Au^+-*

DPG – Frühjahrstagung, Regensburg, Germany (March 2007):
T. Gleitsmann, M. E. Vaida and T. M. Bernhardt, *Temperature dependent femtosecond two-photon photoemission from ultrathin MgO films.*

DPG – Frühjahrstagung, Düsseldorf, Germany (March 2007):
D. M. Popolan, M. Vaida, and T. M. Bernhardt, *The Effect of Gold Doping on the Reactivity of Free Silver Clusters: Comparison of Ag_3^+ and Ag_2Au^+.*

2008

DPG – Frühjahrstagung, Berlin, Germany (March 2008):
M. Vaida, P. E. Hindelang, *R. Tchitnga* and T. M. Bernhardt, *Observing photo-induced chemical reaction on surface in real-time.*

International conference on clusters at surface, Warnemünde, Germany (May 2008):
M. Vaida, and T. M. Bernhardt, *Investigation of ultra-fast chemical reactions on surfaces: Oxides, metals and oxide supported metal clusters.*

Summer School – Structural Dynamics. Methods and Applications, Vilamoura, Portugal (June 2008):
M. Vaida, P. E. Hindelang, *R. Tchitnga* and T. M. Bernhardt, *Real-time observation of photo-induced uni- and bimolecular chemical reaction on surfaces.*

ISSPIC XIV – International Symposium on Small Particles and Inorganic Clusters, Valladolid, Spain (September 2008):
M. Vaida, and T. M. Bernhardt, *A new technique for monitoring ultra-fast photo-induced chemical reactions on oxides, metals and oxide supported metal clusters.*

UCP – International Workshop on Ultrafast Chemical Physics, Glasgow, Scotland (October 2008):

M. Vaida, and T. M. Bernhardt, *Investigation of ultra-fast chemical reactions on insulating and metallic surfaces.*

2009

S^3C – Symposium on Size Selected Clusters, Brand, Austria (March 2009):

M. Vaida, and T. M. Bernhardt, Adsorption *and photodissociation dynamics of methyl iodide molecules on magnesia supported gold clusters.*

FEMTO IX – Femtochemistry, Femtobiology and Femtophysics - Frontiers in Ultrafast Science and Technology, Beijing, China (August 2009):

M. Vaida, and T. M. Bernhardt, *Surface-aligned femtochemistry of methyl halides on oxide surfaces in comparison to metals and oxide supported metal clusters.*

Bunsen Colloquium Microscopic Views on Interface Phenomena - From Surface Science to Fuel Cell Catalysis, Reisensburg Castle, Günzburg, Germany (December 2009):

M. Vaida, and T. M. Bernhardt, *The femtochemistry of methyl halide molecules adsorbed on oxides, metals and oxide supported metal clusters.*

2010

Gordon Research Conferences - Ultrafast Phenomena in Cooperative Systems, Galveston, Texas, USA (February 2010):

M. Vaida, and T. M. Bernhardt, *Real-time observation of ultrafast photoinduced reaction dynamics of methyl halide molecules at surfaces.*

Acknowledgements

I would like to express my gratitude to a number of people and foundations for supporting this work.

My special thanks are addressed to **Prof. Dr. L. Wöste** for offering me an exciting opportunity to get involved at the frontiers of science and to start my PhD in his research group.

This thesis would not have been possible without the help, support and patience of my supervisor **Prof. T. Bernhardt**. I want to thank him for giving me the chance to continue the PhD research in his group in Ulm. He is one of the most enthusiastic people I have met. His enormous optimism and encouraging words helped me a lot during the time. I will never forget how fascinating he found every newly recorded transient signal, even when the signal to noise ratio was 2/1, and every mass spectrum even if it doesn't contain more than a single peak. I would also like to thank him for the opportunity to take part at many conferences and consequently to discuss our results with the leaders in the field of Femtochemistry, Surface Science and Cluster Science. I thank him for careful reading of this thesis too.

I am grateful to my colleagues **Sandra**, **Bruno**, **Robert** and in particular to **Tobias** for the help and for the great time inside and outside the laboratory.

I want to present my gratitude to **Prof. J. Behm** and to all members of the Institute of Surface Chemistry and Catalysis for their help and friendly manners.

I would like to thank **T. Häring** and **G. Bräth** for their technical support.

I am grateful to **Deutscher Akademischer Austausch Dienst** for the fellowship, and for the financial support from **Deutsche Forschungsgemeinschaft** through the priority programs SPP 1153 ‘Clusters at surfaces’, SFB 569 ‘Hierarchical structure formation and function in organic-inorganic nano-systems’ and through the grant BE2475/3. Both priority programs SPP 1153 and SFB 569 also provided a rich and valuable scientific forum for my work.

I am deeply grateful to my family for the support and encouragement throughout my studies.

In the end, I would like to thank **Denisia**, not only for her help in producing mass-selected metal clusters or for the very helpful gas-phase reactivity measurements, but also for her personal support and great patience at all times.

Erklärung

Hiermit erkläre ich, Mihai Emilian Vaida, dass ich die vorliegende Dissertation selbständig verfasst habe. Ich habe keine anderen als die angegebenen Quellen und Hilfsmittel benutzt und habe wörtliche oder sinngemäße Zitate als solche gekennzeichnet.

Ulm, den 27. 05. 2010

Mihai Emilian Vaida